UNIVERSITY CARLOS III OF MADRID

DEPARTMENT OF CONTINUUM MECHANICS AND STRUCTURAL ANALYSIS

UNDERGRADUATE THESIS PROJECT

NUMERICAL ANALYSIS ON THE FORMATION OF PLASTIC INSTABILITIES UNDER DYNAMIC TENSION

AUTHOR: CARLOS VELA ARROJO
DIRECTORS: Dr. JOSÉ ANTONIO RODRÍGUEZ MARTÍNEZ
Dr. ÁNGEL ARIAS HERNÁNDEZ

LEGANÉS, JULY 2010

UNDERGRADUATE THESIS PROJECT

NUMERICAL ANALYSIS ON THE FORMATION OF PLASTIC INSTABILITIES UNDER DYNAMIC TENSION

Author: Carlos Vela Arrojo

Directors: Dr. José Antonio Rodríguez Martínez

Dr. Ángel Arias Hernández

Grading Board signatures

President:

Member:

Member:

Secretary:

Grade:

Leganés, th of , 2010.

A mis padres y a mi hermano

AGRADECIMIENTOS

Me gustaría comenzar con una grandísimo agradecimiento a mis directores de este proyecto. A Ángel Arias tengo que agradecerle lo muchísimo que ha confiado en mi todos estos años y su cercanía, gracias a la cual he sentido su apoyo e interés constante en lo que hago. A José Antonio Rodríguez le agradezco infinitamente la oportunidad que me ha dado de trabajar junto a él todos estos meses, el tiempo que me ha dedicado y el esfuerzo realizado no tiene precio. Son innumerables las horas que ha dedicado a enseñarme todo lo que sé y agradezco de forma especial su preocupación constante en asegurar la calidad final de este proyecto.

A mis padres les debo todo. Sin ellos este trabajo no habría sido posible y me causa muchísima admiración el gran esfuerzo que han realizado en que llegara este momento. Su apoyo y cariño ha resultado fundamental durante todos estos años.

A mi hermano por su admiración y porque con sus bromas y "piques" me lleva empujando hacia la mejora toda la vida.

A mis amigos de toda la vida por su apoyo y porque su confianza siempre me ha dado esa fuerza extra para seguir trabajando. Agradezco de forma especial su sufrimiento durante mis épocas de exámenes. Sus consejos siempre serán muy bienvenidos. En particular me gustaría agradecer a Alberto, Victor y Álvaro su interés constante en la evolución de este último curso.

A mis amigos de la Universidad por haberme dado la oportunidad de conocerles mejor. Ellos tienen parte de responsabilidad en la consecución de este trabajo y son una fuente de consejos que agradezco y valoro enormemente.

A Jacobo, Manuel, Héctor, Susana y Leticia por demostrarme de una manera tan clara su amistad y su apoyo en los momentos complicados estos últimos años.

A mi abuela Julia por tener tan claro que iba a llegar aquí.

A mi abuela Florencia por su enorme apoyo. ¡Y porque tenía más ganas de que llegara este momento que yo!

A Yara porque sin ella esto no hubiera sido posible. Por ser mi pilar más sólido durante todos estos años. Su capacidad para escuchar y apoyarme en los momentos más complicados no será nunca suficientemente agradecida. ¡Y por aguantar mis insufribles charlas en momentos difíciles!

¡Muchísimas gracias a todos por estar a mi lado!

"If you believe in yourself and have the courage, the determination, the dedication, the competitive drive and if you are willing to sacrifice the little things in life and pay the price for the things that are worthwhile, it can be done."
Vince Lombardi

ABSTRACT

In this undergraduate thesis project, a numerical analysis regarding the plastic instabilities formation in metallic alloys subjected to dynamic loads is developed. These kinds of studies have an important interest in several industrial sectors due to the localization processes during deformation have influence on the capacity of a metal for energy absorption under dynamic solicitations.

First of all, the influence of strain rate sensitivity on plastic instabilities formation has been studied. For this, a dynamic tension numerical model with specimens of aluminum 7075 has been built. The fundamental role of the strain rate sensitivity as homogenizing agent of the material behavior has been proven. Moreover, it has been found that an increment in the strain rate sensitivity causes a delay in the localization process, increasing the capacity of the material for absorbing energy.

On the other hand, the importance of the strain hardening on flow localization has been studied. For this, a numerical model of the ring expansion test using specimens of austenitic steel 301Ln2B has been built. It has been proven that there exists a certain value of the strain hardening for which strain localization never takes place. As the strain rate sensitivity, the strain hardening acts as homogenizing agent of the material behavior, increasing the capacity of the material for absorbing energy under dynamic conditions.

Finally, with the fundamental objective of advancing in the understanding of the effects previously presented, the role of the constitutive relation on the material behavior predictions under impact solicitations has been studied. For this purpose, three different physical-based constitutive relations have been used to model the behavior of OFHC copper specimens subjected to the dynamic tension and ring expansion tests. It has been proven that even when constitutive descriptions with similar background are used, the predictions they provide regarding the capacity of the material for energy absorption under dynamic conditions are different. It has been confirmed that both the definition of the strain rate sensitivity and the strain hardening of each constitutive description determines in a notable way the predictions of the numerical model.

RESUMEN

En este proyecto fin de carrera se ha llevado a cabo un estudio numérico sobre la formación de inestabilidades plásticas en aleaciones metálicas sometidas a cargas dinámicas. Este tipo de estudios suscita un gran interés en diversos sectores industriales ya que los procesos de localización de deformación en metales condicionan la capacidad de los mismos para absorber energía bajo solicitación dinámica.

En primer lugar se ha estudiado la influencia de la sensibilidad a la velocidad de deformación en la generación de inestabilidades plásticas. Para ello se ha desarrollado un modelo numérico del ensayo de tracción dinámica aplicado a probetas de aluminio 7075. Se ha probado el papel fundamental de la sensibilidad a la velocidad de deformación como agente homogeneizador del comportamiento mecánico del material. Así, un incremento en la sensibilidad a la velocidad de deformación causa un retardo en la localización de la deformación aumentando la capacidad del material para absorber energía.

Por otro lado, se ha estudiado la importancia que el endurecimiento por deformación tiene en el proceso de localización de la deformación. Para ello se ha construido un modelo numérico del ensayo de expansión radial de anillo aplicado a probetas de acero 301Ln2B. Se ha probado que para niveles de endurecimiento por deformación superiores a un cierto valor umbral no se produce la localización del flujo de tensión. Al igual que la sensibilidad a la velocidad de deformación, el endurecimiento por deformación actúa como agente estabilizador del comportamiento del material, incrementando su capacidad para absorber energía en condiciones dinámicas.

Finalmente, y con el objetivo fundamental de avanzar en el entendimiento de los efectos expuestos previamente, se ha analizado el papel que la ley de endurecimiento tiene en las predicciones del comportamiento frente a impacto de un cierto material. A este efecto se han utilizado tres ecuaciones constitutivas de fundamentación física para simular la respuesta de probetas de cobre OFHC sometidas a tracción dinámica y expansión radial de anillo. Se ha demostrado que incluso utilizando ecuaciones constitutivas de similar fundamentación, éstas predicen valores diferentes sobre la capacidad del material para absorber energía en condiciones dinámicas. Se ha constatado que la definición tanto de la sensibilidad a la velocidad de deformación como del endurecimiento por deformación de cada una de las relaciones utilizadas condicionan de manera notable las predicciones del modelo numérico.

Contents

CHAPTER 1

MOTIVATION AND OBJECTIVES

ABSTRACT

Studying the behaviour of metallic alloys when they are subjected to mechanical loads has an increasing interest in many industrial fields nowadays. When a certain structure has to be designed, it is necessary the correct knowledge about how the structure will respond under these mechanical loads. Thus, in this chapter is described the motivation followed in this work. The main objectives of this document are explained and the methodology utilized along all the chapters is established. Finally, the original contributions achieved with this work are discussed. The most important goal is increasing the knowledge about the behaviour of metallic alloys under high rate loading conditions.

1 MOTIVATION AND OBJECTIVES

1.1 Motivation

The study of structures for absorbing energy at low and medium impact velocities (crashworthiness), or to protect against impacts at very high velocity has a huge interest nowadays. This kind of structures are used in many different industries. Some examples are the automotive industry, the aerospace industry, the naval industry, the civil engineering industry or the high-speed machining industry among others, Fig. 1-1. These structures are usually built with metallic alloys. In spite of the knowledge about the behaviour of these materials has increased in a very important way during last decades, it is not fully known how these materials behave when they are subjected to aggressive loading conditions. Thus, it is clear that the study mentioned before requires overcoming some problems with a high technological and scientific relevance.

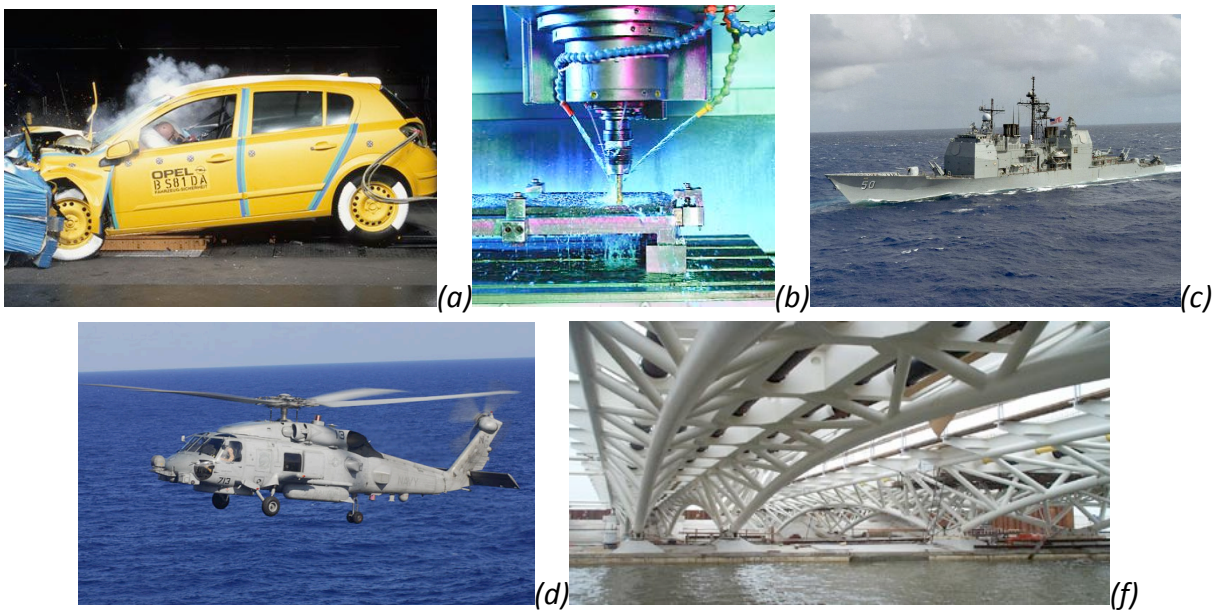

Fig. 1-1. Engineering applications which require a deep study of metallic alloys behaviour under wide range of temperatures and strain rates. (a) Automobile industry (Crashworthiness), (b) High-speed machining, (c) Naval industry, (d) Aerospace industry and (f) Civil engineering industry.

As an illustrative example, in the transport industry, energy absorption tests like the ones called crashworthiness *(*Fig. 1-1-*a)* are currently essential for the automobiles design approvals. These studies are also pertinent for civil engineering structures. Despite the fact that this kind of structures are not commonly subjected to dynamic loads, in the design stage should be taken into account impact loads such as explosions, penetration by fragments or collision due to dropped objects [Rusinek and Zaera 2007]. Other field in which the study of the materials under dynamic loading is very important is the high-speed machining industry. Due to the high speed at which these processes work, the material behaviour differs considerably from the general knowledge we have under static-loading conditions.

Thus, a common characteristic of all the processes described above is that in the end the material fails due to the extreme loading conditions at which it is subjected. In the Solid Mechanics field, it is considered that the failure is produced when the material breaks and stops satisfying its final structural function. However, before this failure happens, material properties such as the resistance, ductility or toughness decrease. During this stage, the material is plastically deformed. Several authors have investigated the behaviour of metallic alloys during this stage [Follansbee 1986, Regazzoni et al. 1987, Follansbee and Kocks 1988, Zerilli and Armstrong 1992, Huang et al. 2009] concluding that plastic instabilities formation plays a prominent role in the deformation and failure of engineering materials under dynamic solicitations.

In the present work the formation of these plastic instabilities under dynamic conditions has been studied. Understanding formation and propagation of instabilities in materials offers significant stops towards optimizing material's behavior under dynamic loading conditions. Thus, in order to evaluate the suitability of a certain metal to be used for energy absorption under dynamics conditions, plastic instabilities formation should be analyzed.

Typically, in order to define the behaviour of a material, a constitutive relation is used. This is a mathematical expression that relates the stress of the material with variables like the strain, temperature and strain rate at which it is subjected, Eq. 1-1.

$$\bar{\sigma} = \bar{\sigma}\left(\bar{\varepsilon}^{P}, \dot{\bar{\varepsilon}}^{P}, T\right) \qquad \textit{Eq. 1-1}$$

where, $\bar{\sigma}$ is an equivalent stress, $\bar{\varepsilon}^{P}$ is an equivalent plastic strain, $\dot{\bar{\varepsilon}}^{P}$ is an equivalent plastic strain rate and T is the temperature.

Because of in the equations which rule this kind of models not only the stress term appears but also its derivatives, it is clear the importance of the correct definition of the strain rate sensitivity *(first derivative of the equivalent stress respect with the equivalent strain rate)* and the strain hardening *(first derivative of the equivalent stress respect with the equivalent plastic strain)*. The analysis developed in this project has determined how the definition of these two mechanical properties of metals influences on the plastic instabilities formation predictions.

Thus, several authors have developed constitutive descriptions in order to properly define metallic alloys behaviour. In this work, some of them are analyzed and compared.

The final purpose of this project is advancing in the understanding of the plastic instabilities formation under dynamic loading conditions. There are several ways to proceed in order to reach this objective. First of all, using analytical solutions for the problem analyzed. In some particular cases, exact solutions of the Solid Mechanics' equations exist due to the boundary conditions of the problem. In these cases, the solution of the flow stress in the material during the test development is known. However, this technique is rarely applicable because there are few problems that could be solved in this way. Most of

the times, boundary conditions make impossible the use of this technique because of the equations cannot be analytically solved. An alternative way to proceed is developing experiments under a wide range of dynamic loading conditions. This technique allows to obtain high amount of empirical data that later on have to be used to develop a deep analysis. Although the use of experiments is always required (*at least to check predictions obtained with other methods)* it is not generally feasible developing this kind of studies using only experimental techniques due to the huge cost intrinsically related to the experiments. Finally, nowadays another method to carry out this analysis is using numerical techniques. Among all of them, the **FEM** *(Finite Element Method)* is commonly used to study this type of problems. The **FEM** is a numerical technique for finding approximate solutions of the partial differential equations as well as of integral equations which rule the model. The **FEM** is a good choice for solving partial differential equations over complicated domains *(like cars and oil pipelines)*, when the domain changes *(as during a solid state reaction with a moving boundary)*, when the desired precision varies over the entire domain, or when the solution lacks smoothness.

Therefore, the use of a **FE** code becomes very interesting. This makes the process much cheaper because a lot of different simulations can be carried out only changing some parameters. This advantage together with the huge advance in the computing science in last decades have pushed the use of these numerical tools both in the industry and researching fields. However, the use of these codes is not trivial. In order to model the behaviour of metallic alloys *(or other type of material)*, one of the main characteristics that users should introduce in the code is the constitutive description for the materials, which defines how the material behaves under certain loading conditions. Thus, a good knowledge of the material behaviour is required to obtain suitable results. Then, the constitutive description should have been proven to represent accurately the material behaviour in terms of plastic instabilities formation under wide range of loading conditions if the results provided by the numerical simulations with a **FE** code are considered. Finally, it is important to take into account that with experimental techniques is not possible to directly measure the stress state of the material where plastic instabilities are taking place. Therefore, the use of numerical tools is essential for this purpose.

Thus, in this project has been attempted to offer a complete approach of high rate behaviour of metallic alloys. The purpose has been advancing in the knowledge about the relation between deformation mechanisms and absorption of energy in metallic alloys subjected to dynamic loading conditions by means of the determination of the causes which control instabilities formation under these solicitations.

1.2 Objectives

The main objective followed with the present work is:

- Advancing in the present knowledge related to the plastic instabilities formation in some materials commonly used in the industry.

For this purpose, a **FE** code will be used. This analysis will provide a wide view of the processes behind the formation of the instabilities, which are responsible of failure in metals subjected to dynamic loading conditions.

Other more specific objectives are the followings:

- Studying the effect of strain rate sensitivity on plastic instabilities formation of metallic alloys. The Finite Element (**FE**) code used has been ABAQUS/Explicit.
- Studying the effect of strain hardening on plastic instabilities formation of metallic alloys. Again, ABAQUS/Explicit has been the numeric tool used for this analysis.
- Comparing the effect that a different definition of the studied strain rate and strain sensitivity for a certain material has on the plastic instabilities formation using three advanced constitutive relations, which are supposed to represent correctly the material behaviour under wide range of loading conditions.

In Table 1-1, a complete summary of the project is shown. This includes the main important points treated in each one of the following chapters.

Problem	Unknowledge of the metallic alloys behaviour when they are subjected to dynamic loading conditions. Particularly, regarding the formation of plastic instabilities under high rate impact loads.		
Need	Studying how material characteristics like the strain rate sensitivity or the strain hardening influences the formation of these instabilities. Thus, advanced constitutive relations capable to represent appropriately this kind of effects have to be used.		
Chapter	3	4	5
Final purpose	Studying the effect of the strain rate sensitivity on plastic instabilities formation.	Studying the effect of the strain hardening on plastic instabilities formation.	Studying the effect of the definition of the strain rate sensitivity and strain hardening on plastic instabilities formation.
Constitutive relation used	Extended RK	Extended RK	Extended MRK, NNL and VA
Representative material utilized	AA 7075	301Ln2B	OFHC copper
Numerical configuration used	Dynamic Tension	Ring expansion	Dynamic tension and ring expansion

Table 1-1. Summary of the present project

1.3 General methodology

To perform the different studies of this work, some general methodology should be followed. In Fig. 1-2 is shown the methodology applied along the different chapters of this project.

First of all, the objective of the chapter is fixed. This is related to the influence of the definition of material mechanical properties *(strain rate sensitivity and strain hardening)* on plastic instabilities formation in metallic alloys subjected to dynamic loading conditions.

Then, an appropiate metal which shows changes in this characteristic under certain conditions is selected. This allows us to study the influence of these changes on the plastic instabilities formation in the material.

Later on, an advance constitutive relation is chosen based on the nature of the thermal activation processes into the material. The models selected have been validated under certain range of loading conditions. To ensure this issue, well-known constitutive descriptions present in the literature have been chosen in this project.

Once the constitutive relation has been selected, this is implemented into a **FE** code *(ABAQUS/Explicit)*. All the constitutive relations used in this work have been implemented into ABAQUS/Explicit **FE** code using the thermo-viscoplastic integration scheme for J2 plasticity proposed by Zaera and Fernández-Sáez [Zaera and Fernández-Sáez 2006] *(Appendix I)*.

After the implementation of the constitutive description into the built numerical model to use *(dynamic tension test or ring expansion test),* the numerical configuration is validated by means of comparing the numerical results and analytical predictions under different loading conditions included in the range in which the constitutive description is supposed to be valid. This analytical data is obtained by means of the implementation of the constitutive relation into a Fortran subroutine.

Once the numerical configuration is validated, numerical simulations are performed in order to obtain data at different impact velocities *(within the validated range of strain rates)*. Next, the numerical data extracted should be used to obtain conclusions about the relation between the plastic instabilities formation in the material and the effect studied.

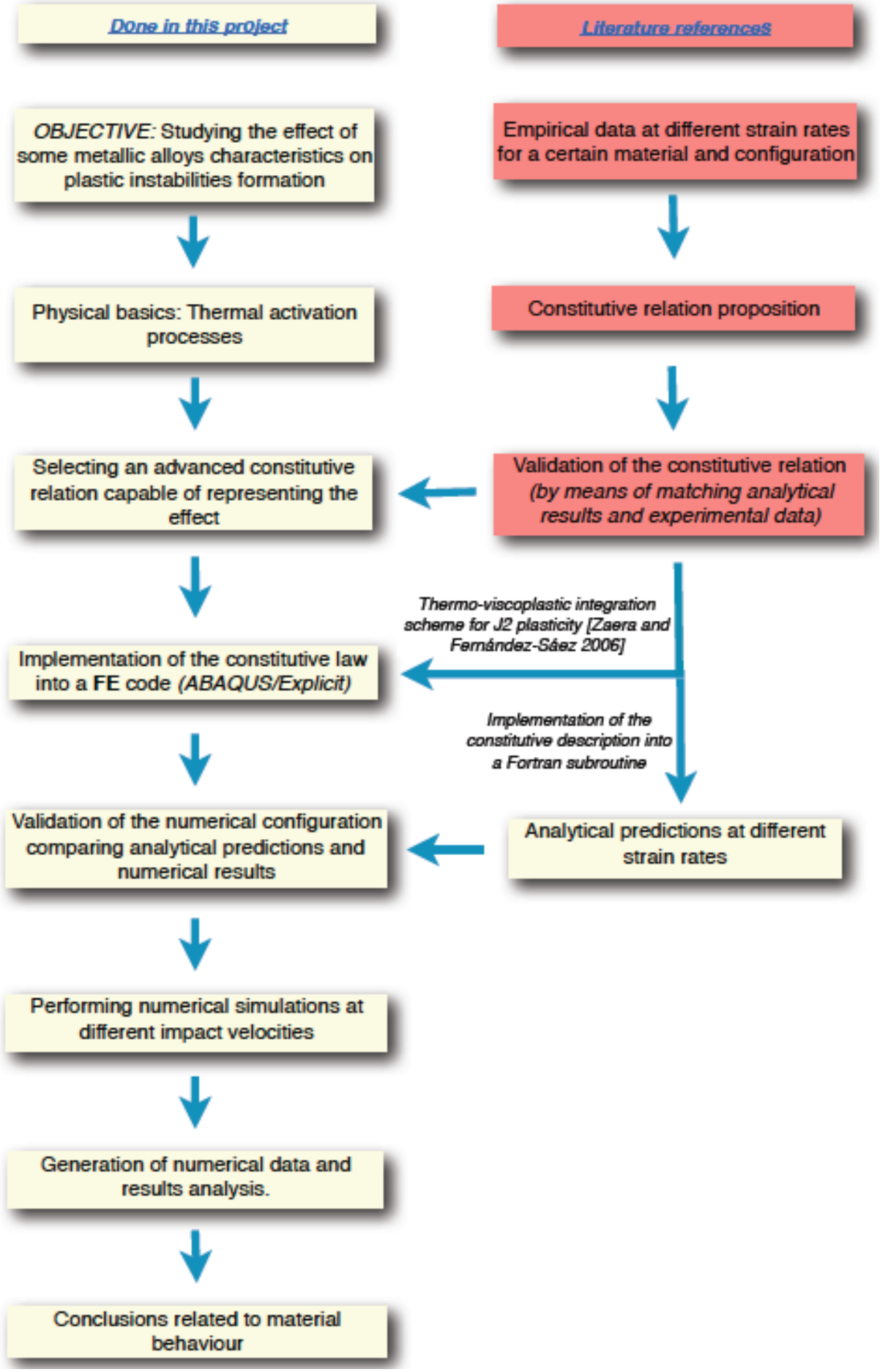

Fig. 1-2. General scheme of the methodology used in this project.

1.4 Original contributions

The original contributions of the present project are gathered in the following points:

- It has been studied the effect of the strain rate sensitivity on the plastic instabilities formation in metallic alloys. Particularly, the viscous drag effect *(sharply change in the strain rate sensitivity at high strain rates)* has been used for this purpose. It has been proven that not to take into account this strain rate sensitivity change results in significant different predictions regarding the plastic instabilities formation under dynamic loading.

- It has been studied the effect of the strain hardening on the plastic instabilities formation in metallic alloys. It has been proven that the strain hardening of the material plays a fundamental role on the formation of plastic instabilities. It has been also concluded that taking into account strain hardening effect reveals an increase in the material ductility. Then, strain sensitivity tends to stabilize the material.

- It has been proven that even when advanced constitutive descriptions are used to model the material behaviour under dynamic loading conditions, the different definition of the strain and strain rate sensitivity results in different predictions for the plastic instabilities formation in the material. The analysis revealed that the processes of strain localization and fragmentation occurring in the sample during loading are strongly influenced by the material modelling.

1.5 Contents

This work consists in six chapters.

In the present one a general description of the document is developed. Moreover, the objectives followed and the general methodology used along the work are described together with the original contributions of this project.

The second chapter is devoted to the constitutive modelling of metallic alloys. Thus, a general overview of metallic alloys behaviour is done. Furthermore, the constitutive relations that will be used later on are described and explained.

Chapters three, four and five form the core of the present dissertation. In the third chapter, the influence of the strain rate sensitivity on the flow localization is studied. For this purpose, an illustrative particular effect has been selected, the viscous-drag effect at high strain rates of deformation. A specific material that shows this effect will be used. This is the aluminium alloy **AA 7075**.

In the fourth chapter is studied the effect the strain sensitivity *(strain hardening)* has on plastic instabilities formation. The austenitic steel selected has been de **301Ln2B** because it shows this effect due to its specific properties.

The purpose of the fifth chapter is checking the importance of the two effects studied in chapters three and four. In this chapter will be studied the effect on the plastic instabilities formation of choosing different advanced constitutive relations under wide range of strain rates. Therefore, in spite of the fact of using advanced constitutive relations for modelling the thermo-viscoplastic behaviour of metallic alloys, their different definition of the strain and strain rate sensitivity provides differences in the behaviour predicted for the material. For this specific purpose, the material selected has been the **OFHC copper** due to there are several constitutive relations which have been proven to represent correctly its behaviour.

In the last chapter the conclusions obtained along the whole document are summarized and future researching lines are proposed.

Finally, the references used to develop this study together with some appendix that support specific aspects of this work are gathered.

1.6 Publications

Next, publications related to this undergraduate thesis project are listed:

AUTHORS: J. A. Rodríguez-Martínez, A. Rusinek, **C. Vela**, A. Arias, R. Zaera.

TITLE: Role of the strain rate sensitivity on the formation of plastic instabilities under dynamic tension.

STATE: In process

AUTHORS: C. Vela, J. A. Rodríguez-Martínez, A. Rusinek, A. Arias.

TITLE: The role of constitutive description on the strain localization process in the radial expansion of copper rings.

SUBMITTED TO JOURNAL: Internal Journal of Impact Engineering

CHAPTER 2

CONSTITUTIVE MODELLING OF METALLIC ALLOYS

ABSTRACT

In this chapter is carried out a brief discussion concerning different types of constitutive relations used to define metal behaviour. Moreover, general aspects in the behaviour of metallic materials are introduced. Particularly, the relation between macroscopic plasticity and dislocations moving through crystal lattice is discussed. This aspect has a strong importance in the contitutive descriptions that will be used later on. In addition, two of these constitutive descriptions are described, the Rusinek-Klepaczko *(RK)* and the Modified Rusinek-Klepaczko *(MRK)*. Furthermore, extensions to take into account the strain rate sensitivity change that some metals exhibits at high strain rates *(viscous-drag effect)* and to model the martensitic transformation in austenitic steels are discussed.

2 CONSTITUTIVE MODELLING OF METALLIC ALLOYS

2.1 Introduction

In order to represent accurately the thermo-viscoplastic behaviour of metallic alloys under different loading conditions, it is necessary to consider constitutive descriptions. These models represent the material behaviour relating mathematically the stress, temperature, strain rate and strain of the material.

The macroscopic constitutive descriptions can be split into two main groups [Rusinek et al. 2010]:

- **Phenomenological constitutive models**: These models propose mathematical expressions for the material flow stress based on empirical observations. They consist in mathematical functions with no physical meaning which fit experimental observations. These models have important advantages. For instance, they usually have a limited number of materials constants which involves an easy calibration of their values. Nevertheless, important drawbacks are present. Due to the lack of physical background, the use of these models is restricted to a short range of loading conditions (the range of temperatures and strain rates in which the constitutive description is applicable is limited) and furthermore, they have a limited flexibility (the formulation is specific for certain groups of materials). Some examples are the Cowper-Symonds [Cowper and Symonds 1952], the model of El-Magd [El-Magd 1994] or the Johnson-Cook model [Johnson and Cook 1983].

- **Physical-based constitutive relations**: These models account for physical aspects of the material behaviour. Most of them are founded on the thermodynamics and kinetics of slip theory [Kocks et al. 1975]. In comparison with phenomenological models previously mentioned, they usually have larger number of material constants and their determination procedure follows physical assumptions. In contrast, they allow for an accurate definition of the material behaviour under wide range of loading conditions. Some examples of these kinds of models are the Voyiadjis-Almasri (*VA*) [Voyiadjis and Almasri 2008], the Nemat-Nasser and Li (*NNL*) [Nemat-Nasser and Li 1998] or the Rusinek-Klepaczko (*RK*) [Rusinek and Klepaczko 2001] constitutive descriptions.

2.2 Theoretical considerations

Macroscopic plasticity in metals is the result of dislocations moving through the crystal lattice. Two types of obstacles are encountered that try to prevent dislocation movements through the lattice: long-range and short-range barriers [Kocks et al. 1975, Voyiadjis and Almasri 2008]. Long-range obstacles are due to the structure of the material and cannot be overcome by introducing thermal energy through the crystal [Zerilli and Amstrong 1987]. They contribute to the flow stress with a component that is non-thermally activated (*athermal stress*). On the other hand, overcoming of short-range barriers can be assisted by

thermal energy [Zerilli and Amstrong 1987]. Thermal activation aids dislocation gliding, decreasing the intrinsic lattice friction in the case of **BCC** metals (overcoming Peierls stress) or decreasing the strength of obstacles in the case of most of the **FCC** metals (overcoming forests of dislocations). In both cases, thermal activation reduces the applied stress required to force the dislocation past obstacles. Thus, flow stress of a material *(using J2 theory)* can be decomposed into equivalent athermal stress σ_μ and equivalent thermal stress σ^* [Zerilli and Amstrong 1987, Follansbee and Kocks 1988, Voyiadjis and Almasri 2008].

A scheme of the evolution of stress components with temperature is shown in Fig. 2-1. At low temperatures, the flow stress decreases with temperature *(the slope of the curve in Fig. 2-1 is negative)*. This region is influenced by thermal and athermal stress components. The next region with increasing temperature is basically athermal. At very high temperatures, flow stress decreases again with increasing temperature. However, according to the considerations reported, for example in [Voyiadjis and Almasri 2008], not all metals have the three regions described here. Then, definition (and contribution to the overall flow stress) of thermal and athermal stress terms is dependent on the crystal structure of the material. The causes are related to available symmetries of the lattice, the nature of dislocation cores and the available slip systems [Lennon and Ramesh 2004]. In **BCC** metals, overcoming Peierls stress resistance is the main phenomenon involved in thermally activated processes. Consequently, the thermal component of the flow stress σ^*, can be defined independent of plastic strain [Zerilli and Amstrong 1987, Rusinek and Klepaczko 2001]. The yield stress of most **BCC** metals is strongly temperature and rate dependent [Zerilli and Amstrong 1987]. Strain hardening is primarily accomplished through long-range barriers such as grain boundaries, far-field forest of dislocations and other microstructural elements with far-field influence [Nemat-Nasser and Li 1998]. Temperature and deformation rate have relatively small effect on strain hardening, Fig. 2-2.

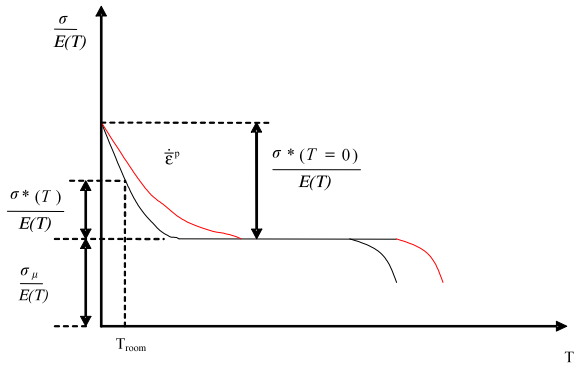

Fig. 2-1. Decomposition of macroscopic stress with temperature

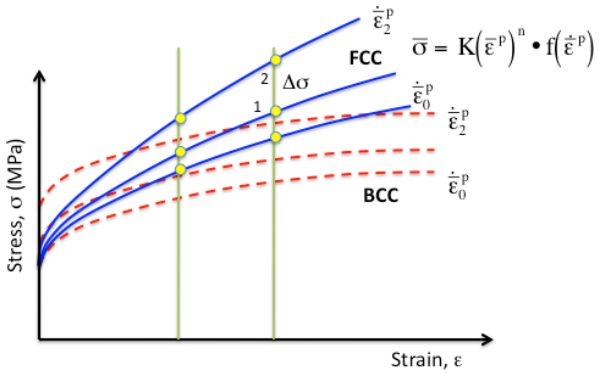

Fig. 2-2. Strain rate sensitivity definition for BCC and FCC metals. General case.

Peierls stress in many **FCC** metals is relatively unimportant. The rate-controlling mechanism is the overcoming of dislocation forests by individual dislocations [Voyiadjis and Abed 2005]. Thermal activation behaviour becomes dependent on the plastic strain $\sigma^* = \sigma^*\left(\bar{\varepsilon}^p, \dot{\bar{\varepsilon}}^p, T\right)\Big|_{FCC}$ [Zerilli and Amstrong 1987, Nemat-Nasser and Li 1998]. On the other hand, most of the **FCC** metals exhibit large strain hardening due to an increase in the amount of dislocation interactions with increasing strain. Strain hardening tends to be highly temperature and strain rate dependent, while the yield stress has reduced dependence on such effects, Fig. 2-2. In agreement with previous considerations, the Volume Thermally Activated (**VTA**) defined by Eq. 2-1 decreases with plastic strain for many **FCC** metals [Zerilli and Amstrong 1987] while it is independent of the deformation level for **BCC** metals.

$$V^* \approx kT \left.\frac{\partial \ln\left(\dot{\bar{\varepsilon}}^P\right)}{\partial \bar{\sigma}^*}\right|_T = kT\Psi_T \quad where \begin{cases} \left.\Psi\left(\dot{\bar{\varepsilon}}^P\right)\right|_T & for\ BCC \\ \left.\Psi\left(\bar{\varepsilon}^P, \dot{\bar{\varepsilon}}^P\right)\right|_T & for\ FCC \end{cases} \qquad \textit{Eq. 2-1}$$

where k is the Boltzmann's constant and T the absolute temperature.

Once the main physical aspects of the metals behaviour have been explained, it is possible to describe more appropriately the formulation of the constitutive models used in this dissertation. Two different constitutive descriptions have been selected due to their advantages. These constitutive descriptions are the *RK* constitutive relation, which is valid for metals without dependence of the plastic strain in the Volume Thermally Activated, and the *MRK*, appropriate for metals with dependence of the plastic strain in the Volume Thermally Activated. The number of material constants in these models is higher than most of phenomenological constitutive models but low in comparison with other physical-based constitutive relations. This aspect makes them very interesting for its use in order to model the behaviour of metallic alloys under dynamic loading conditions.

2.3 Constitutive modelling of metallic alloys without dependence of the plastic strain on the Volume Thermally Activated. The Rusinek-Klepaczko (RK) constituve relation

As it has been previously discussed, the *RK model (Rusinek-Klepaczko)* belongs to the physical-based constitutive relations. This is founded on the thermodynamics and kinetics of slip theory [Kocks et al. 1975], which is composed of a set of equations that relate activation energy ΔG, mechanical threshold stress $\hat{\sigma}^*$ (**MTS**), applied stress $\bar{\sigma}$, strain rate $\dot{\varepsilon}$, temperature T and determined physical material parameters.

Assuming the additive decomposition of the total stress, the equivalent Huber-Misses stress is decomposed into two parts. On the one hand, the internal stress σ_μ, which characterizes the strain hardening of the material. On the other hand, the effective stress, σ^*, which defines the thermal activation processes.

Then, the equation that defines the *RK* constitutive relation is, Eq. 2-2

$$\bar{\sigma}\left(\bar{\varepsilon}^p,\dot{\bar{\varepsilon}}^p,\mathrm{T}\right)=\frac{\mathrm{E(T)}}{\mathrm{E_0}}\left[\sigma_\mu\left(\bar{\varepsilon}^p,\dot{\bar{\varepsilon}}^p,\mathrm{T}\right)+\sigma^*\left(\dot{\bar{\varepsilon}}^p,\mathrm{T}\right)\right] \qquad \textit{Eq. 2-2}$$

In order to define the evolution of Young's modulus with temperature an additional term is present, acting as multiplicative factor of the stresses addition. This is modeled in the following way, Eq. 2-3:

$$\mathrm{E(T)}=\mathrm{E_0}\left\{1-\frac{\mathrm{T}}{\mathrm{T_m}}\exp\left[\theta^*\left(1-\frac{\mathrm{T_m}}{\mathrm{T}}\right)\right]\right\} \qquad \textit{Eq. 2-3}$$

where $\mathrm{E_0}, \mathrm{T_m}$ and θ^* denote respectively the Young's modulus at $\mathrm{T}=0\,\mathrm{K}$, the melting point and the characteristic homologous temperature. This expression allows for defining the thermal softening depending on the crystal lattice [Rusinek et al. 2009-b], Fig. 2-3. In the case of **FCC** metals, $\theta^* \approx 0.9$ as reported in [Rusinek et al. 2009-b].

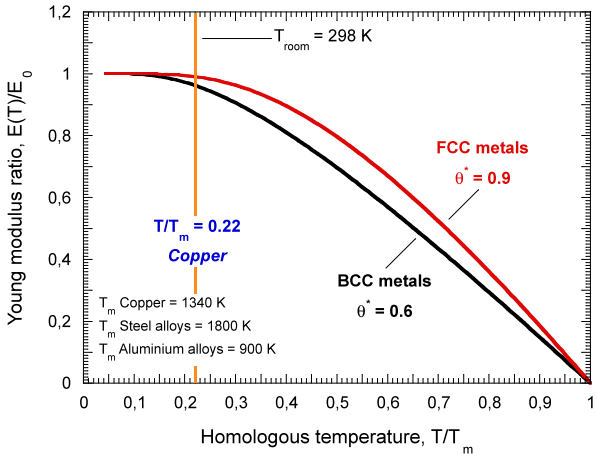

Fig. 2-3. Evolution of Young's modulus ratio with homologous temperature for different θ^* values [Rusinek et al. 2009-b].

The internal stress is defined by Eq. 2-4:

$$\bar{\sigma}_{\mu}\left(\bar{\varepsilon}_{p},\dot{\bar{\varepsilon}}_{p},T\right)=B(\dot{\bar{\varepsilon}}_{p},T)(\varepsilon_{0}+\bar{\varepsilon}_{p})^{n(\dot{\bar{\varepsilon}}_{p},T)} \qquad \textit{Eq. 2-4}$$

where the modulus of plasticity *B* defines rate and temperature sensitivities of strain hardening, *n* is the strain hardening exponent depending on strain rate and temperature and ε_0 is the strain level which defines the yield stress at specific strain rate and temperature.

The explicit formulations describing the modulus of plasticity and the strain hardening exponent are given, Eq. 2-5 and Eq. 2-6.

$$B\left(\dot{\bar{\varepsilon}}_{p},T\right)=B_{0}\left(\left(\frac{T}{T_{m}}\right)\log\left(\frac{\dot{\varepsilon}_{max}}{\dot{\bar{\varepsilon}}_{p}}\right)\right)^{-\nu} \qquad \textit{Eq. 2-5}$$

$$n\left(\dot{\bar{\varepsilon}}_{p},T\right)=n_{0}\left\langle 1-D_{2}\left(\frac{T}{T_{m}}\right)\log\frac{\dot{\bar{\varepsilon}}_{p}}{\dot{\varepsilon}_{min}}\right\rangle \qquad \textit{Eq. 2-6}$$

where B_0 is the material constant, ν is the temperature sensitivity, n_0 is the strain hardening exponent at $T=0\,K$, D_2 is a material constant, $\dot{\varepsilon}_{max}$ is the maximum strain rate accepted for a particular material and $\dot{\varepsilon}_{min}$ is the lowest limit of the model.

The McCauley operator is defined as follows, Eq. 2-7 :

$$\left\langle \bullet \right\rangle=\begin{cases} 0 & \text{if } \left\langle \bullet \right\rangle<0 \\ \bullet & \text{if } \left\langle \bullet \right\rangle>0 \end{cases} \qquad \textit{Eq. 2-7}$$

The effective stress is obtained using Arrhénius's relation, which couples temperature with strain rate, Eq. 2-8.

$$\sigma^{*}\left(\dot{\bar{\varepsilon}}^{p},T\right)=\sigma_{0}^{*}\left\langle 1-D_{1}\left(\frac{T}{T_{m}}\right)\log\left(\frac{\dot{\varepsilon}_{max}}{\dot{\bar{\varepsilon}}^{p}}\right)\right\rangle^{m^{*}} \qquad \textit{Eq. 2-8}$$

where σ_0^* is the effective stress at $T=0\,K$, D_1 is a material constant and m^* is the constant allowing to define the strain rate-temperature dependency.

In case of adiabatic conditions of deformation the constitutive relation is combined with the energy balance principle, Eq. 2-9. Such relation allows for an approximation of the thermal softening of the material by means of the adiabatic heating.

$$\Delta T\left(\bar{\varepsilon}^{p},\bar{\sigma}\right)=\frac{\beta}{\rho C_{p}}\int_{0}^{\bar{\varepsilon}_{max}^{p}}\bar{\sigma}\left(\bar{\varepsilon}^{p},\dot{\bar{\varepsilon}}^{p},T\right)d\bar{\varepsilon}^{p} \qquad \textit{Eq. 2-9}$$

where β is the Taylor-Quinney coefficient assumed as constant *(interesting considerations concerning the potential dependence on Taylor-Quinney coefficient on plastic deformation*

are reported in [Macdougal 2000]), ρ is the material density and C_p is the specific heat at constant pressure. Transition from isothermal to adiabatic conditions is assumed at $\dot{\bar{\varepsilon}}^p = 10\ s^{-1}$ in agreement with experimental observations and numerical estimations reported for example in [Oussouaddi and Klepaczko 1991, Rusinek et al. 2007].

Next, the *MRK* constitutive description is discussed. This constitutive relation is valid when the material exhibits dependence of the plastic strain on the Volume Thermally Activated (**VTA**). Thus, its formulation is different from the one commented above for the *RK* constitutive relation.

2.4 Constitutive modelling of metallic alloys with dependence of the plastic strain on the Volume Thermally Activated. The Modified Rusinek-Klepaczko (MRK) constituve relation

The *Modified Rusinek-Klepaczko (MRK)* constitutive relation is based on the original formulation proposed by Rusinek and Klepaczko (*RK*) [Rusinek et al. 2010, Rodríguez-Martínez 2010]. As it has been previously discussed, the original *RK* formulation has proven capacity for defining the thermo-viscoplastic behaviour of many metallic alloys without dependence of plastic strain on the Volume Thermally Activated (**VTA**). Thus, the *RK* model was modified in order to convert it in suitable for modeling determined **FCC** metals whose rate sensitivity is dependent on the plastic strain.

The *MRK* model, as well as the *RK* constitutive description, is based on the theory of thermodynamics and kinetics of slip [Kocks et al. 1975].

In the *MRK* constitutive relation, as well as in the original *RK* model, the equivalent Huber-Misses stress $\bar{\sigma}$ is decomposed into two stress terms, Eq. 2-10.

$$\bar{\sigma}\left(\bar{\varepsilon}^p, \dot{\bar{\varepsilon}}^p, T\right) = \frac{E(T)}{E_0} \cdot \left[\bar{\sigma}_\mu + \bar{\sigma}^*\left(\bar{\varepsilon}^p, \dot{\bar{\varepsilon}}^p, T\right)\right] \qquad \textit{Eq. 2-10}$$

Despite both *RK* and *MRK* constitutive descriptions are based in an additive decomposition of the total stress, there are high differences in the definition of each one of the stress terms present in the equation, as it will be shown later on.

The factor $E(T)/E_0$ defines the Young's modulus evolution with temperature and its formulation is identical that in the original *RK* constitutive relation, Eq. 2-3.

According to the considerations for most **FCC** metals reported for example in [Zerilli and Amstrong 1987, Follansbee and Kocks 1988, Voyiadjis and Abed 2005, Voyiadjis and Almasri 2008] could be assumed that the athermal stress, $\bar{\sigma}_\mu$, is independent of plastic strain. As it was previously discussed, the yield stress in these **FCC** metals may show reduced rate and temperature dependencies *(certain temperature effect is taken into account by the Young's modulus temperature dependent)*. In agreement with [Voyiadjis and Almasri 2008] the athermal stress will be just tied to the initial yield stress in the form, Eq. 2-11:

$$\overline{\sigma}_{\mu} = Y \qquad \textit{Eq. 2-11}$$

where Y is the flow stress on undeformed material.

The effective stress, $\overline{\sigma}^{*}$, is the flow stress component defining the rate dependent interactions with short-range obstacles. It denotes the rate controlling deformation mechanism from thermal activation. As it has been previously commented *(See Chapter 2.2)* at temperatures greater than 0 K, thermal activation assists the applied stress. It reduces the stress level required to force the dislocation past obstacles.

Based on such understanding of the material behaviour, Rusinek and Klepaczko [Rusinek and Klepaczko 2001] derived the following expression, Eq. 2-12.

$$\overline{\sigma}^{*}\left(\overline{\varepsilon}^{p},\dot{\overline{\varepsilon}}^{p},T\right) = \sigma_{0}^{*}\cdot\left\langle 1-\xi_{1}\left(\frac{T}{T_{m}}\right)\log\left(\frac{\dot{\varepsilon}_{max}}{\dot{\overline{\varepsilon}}^{p}}\right)\right\rangle^{1/\xi_{2}} \qquad \textit{Eq. 2-12}$$

where ξ_1 and ξ_2 are material constants describing temperature and rate sensitivities of the material, T_m is the melting temperature and $\dot{\varepsilon}_{max}$ is the maximum strain rate level for a particular material.

As it was previously discussed, in many **FCC** metals the thermal activation processes have strain dependence. In agreement with the considerations reported in [Zerilli and Amstrong 1987, Voyiadjis and Abed 2005] such dependence may be formulated in the form of Eq. 2-13:

$$\sigma_{0}^{*} = \sigma_{0}^{*}\left(\overline{\varepsilon}^{p}\right) = B\cdot\left(\overline{\varepsilon}^{p}\right)^{n} \qquad \textit{Eq. 2-13}$$

However, strain hardening is intrinsically dependent on strain rate and temperature. Based on the formulation reported in [Rusinek and Klepaczko 2001], a more suitable expression *(in comparison with* Eq. 2-13*)* was proposed, Eq. 2-14.

$$\sigma_{0}^{*}\left(\overline{\varepsilon}^{p},\dot{\overline{\varepsilon}}^{p},T\right) = B\left(\dot{\overline{\varepsilon}}^{p},T\right)\cdot\left(\overline{\varepsilon}^{p}\right)^{n\left(\dot{\overline{\varepsilon}}^{p},T\right)} \qquad \textit{Eq. 2-14}$$

Therefore, the expression Eq. 2-13 also becomes rate and temperature dependent. Thus, the model considers the dependences on strain and strain rate that the Mechanical Threshold Stress (**MTS**) exhibits in the case of some **FCC** metals [Follansbee and Kocks 1988], for example **OFHC Copper**. This definition is consistent with the dominance of the dislocation-obstacle interactions in the plastic deformation of polycrystalline **FCC** materials [Follansbee and Kocks 1988, Nemat-Nasser and Li 1998].

The modulus of plasticity *B*, defines rate and temperature sensitivities on strain hardening and *n* is the strain hardening exponent dependent on strain rate and temperature. The explicit formulations describing the modulus of plasticity and the strain hardening exponent are identical that in case of the original *RK* model. Thus, they are given by Eq. 2-5 and Eq. 2-6.

In the same way that for the *RK* model, in case of adiabatic conditions of deformation the constitutive relation is combined with the energy balance principle, Eq. 2-9.

Next, two extensions for these constitutive relations (*MRK* and *RK*) are introduced. These will allow taking into account some particular effects by the addition of one additional stress term to the equivalent Huber-Misses stress.

2.5 Extensions of the RK and MRK constitutive relations for defining viscous drag and martensitic transformation effects

In spite of the fact that both the *RK* and *MRK* constitutive description are based on physical aspects of the material behaviour, it has been proven that there exists some specific effects that cannot correctly represent. Then, some extensions have been reported [Rodríguez-Martínez et al. 2009, Rusinek and Rodríguez-Martínez 2009] in order to model these effects. They are valid both for *RK* and *MRK* models. Next, an extension to take into account the viscous drag effect at high strain rates and another to represent macroscopically the martensitic transformation in austenitic steels are introduced.

2.5.1 Constitutive modelling of viscous drag effect at high strain rates. The role of strain rate sensitivity

As it was explained in the introduction of this dissertation *(See Chapter 1.1),* one of the objectives followed with this work is studying the influence of the strain rate sensitivity on flow localization. For this purpose the viscous drag effect that some metallic alloys exhibit at high strain rates is used *(See* Table 1-1*).* Next, theoretical considerations regarding this material effect are discussed. Later on, the formulation used in [Rusinek and Rodríguez-Martínez 2009] to take into account this effect when using *RK* and *MRK* models is introduced.

2.5.1.1 Theoretical considerations

A common characteristic of many **FCC** metals is the appearance of a viscous drag component of the flow stress at high rates of deformation [Kapoor and Nemat-Nasser 1999]. For strain rate level varying from $10^3 \mathrm{s}^{-1} \leq \dot{\bar{\varepsilon}}^{\mathrm{p}} \leq 10^4 \mathrm{s}^{-1}$ the strain rate sensitivity of the material sharply increases, which involves an increase in the flow stress. This could be seen in Fig. 2-4.

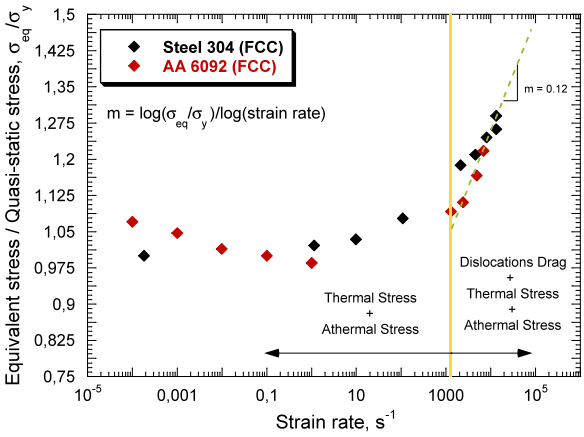

*Fig. 2-4. Evolution of the normalized equivalent stress with strain rate for different **FCC** metals [Follansbee 1986, Zhang et al. 2001**].***

This increase has been interpreted in different ways over the years. Some of them are based on a transition in rate controlling deformation mechanism from thermal activation at low strain rates to some form of dislocations' drag [Campbell and Ferguson 1970, Regazzoni et al. 1987]. On the other hand, other authors also account for the strain rate history effects and relate this phenomenon to the strain rate sensitivity of structure evolution.

The increase in the rate sensitivity of the material is of main relevance since it is assumed that this rate sensitivity acts homogenizing materials behaviour [Mercier and Molinari 2004], increasing their ductility [Hu and Daehn 1996] and delaying plastic localization [Rodríguez-Martínez 2010].

According to Campbell and Ferguson [Campbell and Ferguson 1970, Rusinek and Rodríguez-Martínez 2009, Rodríguez-Martínez 2010], when viscous drag effect takes place, the equivalent stress may be defined as follows, Eq. 2-15.

$$\bar{\sigma} = \bar{\sigma}_{\mu} + \bar{\sigma}^{*} + \bar{\sigma}_{vs} \qquad \textit{Eq. 2-15}$$

where $\bar{\sigma}_{vs}$ is the viscous drag component *(independent of temperature [Kapoor and Nemat-Nasser 1999])*. In the case of most of the **FCC** metals, the strain rate sensitivity cannot be defined using the models only based on an Arrhénius-type equation [Nemat-Nasser et al. 2001, Rusinek and Rodríguez-Martínez 2009, Rusinek et al. 2010].

For pure drag deformation mechanisms a simple description of the material behaviour can be derived.

The deformation rate is tied to the dislocations' velocity by the Orowan relationship, Eq. 2-16.

$$\dot{\bar{\varepsilon}}^{p} = \frac{\rho_{m} \cdot b \cdot v}{\bar{M}} \qquad \textit{Eq. 2-16}$$

where ρ_m is the mobile dislocations density, b is the Burgers vector, $\bar{M}$ is the Taylor factor and v is the dislocations velocity.

Moreover, Eq. 2-17 describes the relation between dislocations velocity and flow stress.

$$v = \frac{\sigma_{vs} \cdot b}{\bar{M} \cdot B} \qquad \textit{Eq. 2-17}$$

where B is the drag coefficient.

Combination of Eq. 2-16 and Eq. 2-17 leads to the linear relation between flow stress and strain rate commonly reported in the literature [Campbell and Ferguson 1970, Kapoor and Nemat-Nasser 1999, Rusinek and Rodríguez-Martínez 2009, Rodríguez-Martínez 2010], for defining the deformation drag mechanisms, Eq. 2-18.

$$\sigma_{vs} = \dot{\bar{\varepsilon}}^{p} \cdot \frac{B \cdot \bar{M}^2}{\rho_m \cdot b^2} \qquad \textit{Eq. 2-18}$$

It is assumed that the linear dependence of applied stress on strain rate occurs because of a corresponding increase in the average dislocation velocity. However, Kapoor and Nemat-Nasser [Kapoor and Nemat-Nasser 1999] observed that beyond a certain point the dislocations velocity no longer increases with strain rate, Fig. 2-5. Then, the increasing strain rate seems to be accommodated by an augment of the dislocations density; the material flow stress level remains constant [Kapoor and Nemat-Nasser 1999].

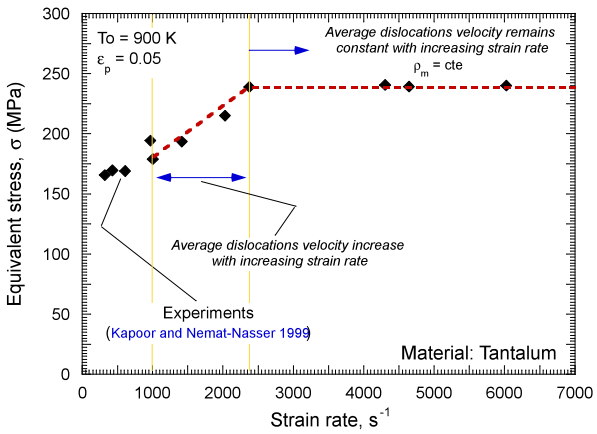

Fig. 2-5. Experimental data of the flow stress evolution with strain rate for Tantalum, for ε^p = 0.05 at T_0=900K. Definition of the stages of the viscous drag process [Kapoor and Nemat-Nasser 1999].

Regazzoni et al. [Regazzoni et al. 1987] suggested that the relation between dislocations velocity and stress is no longer linear at $v > v_s/3$, where v_s is the velocity at which dislocations move, limited by the shear waves velocity, $v_s = C_e$.

The formulation used to define the viscous drag component in the *RK* and *MRK* constitutive descriptions $\sigma_{vs}\left(\dot{\bar{\varepsilon}}^{p}\right)$ was originally introduced in [Kapoor and Nemat-Nasser 1999] and it has a semi-physical character. It comes from the relation between viscous drag,

strain rate and determined physical material parameters given by Eq. 2-18 [Nemat-Nasser et al. 2001].

Thus, based on experimental observations, Kapoor and Nemat-Nasser [Kapoor and Nemat-Nasser 1999] set the following relations, Eq. 2-19 and Eq. 2-20.

$$\bar{\sigma}_{vs}\left(\dot{\bar{\varepsilon}}^{p}\right) = \chi \cdot \left[1 - \exp\left(-\alpha \cdot \dot{\bar{\varepsilon}}^{p}\right)\right] \qquad \textit{Eq. 2-19}$$

$$\alpha = \left(\frac{M^2 \cdot B}{\rho_m \cdot b^2 \cdot \tau_y}\right) \qquad \textit{Eq. 2-20}$$

where χ is a material constant, α represents an effective damping coefficient affecting the dislocation motion and τ_y is the athermal yield stress [Nemat-Nasser et al. 2001]. The value of τ_y could be assumed constant. This expression enables to define both stages of dislocations drag behaviour. First stage of flow stress linearly increasing with strain rate and subsequent stage of rate sensitivity no longer active.

In Fig. 2-6 is shown the evolution of the viscous drag component as a function of χ and α for different strain rate levels. Under a certain level of deformation rate $\dot{\bar{\varepsilon}}^{p} \leq 1000\ s^{-1}$ the viscous drag component is negligible no matter the value of the constants χ and α. In that case, the rate sensitivity is governed by the thermal activation mechanisms.

At higher strain rate level, $\dot{\bar{\varepsilon}}^{p} \geq 1000\ s^{-1}$, the flow stress due to viscous drag becomes relevant and it quickly increases with the rate of deformation. The increase of both material constants χ and α induces an augment on the flow stress.

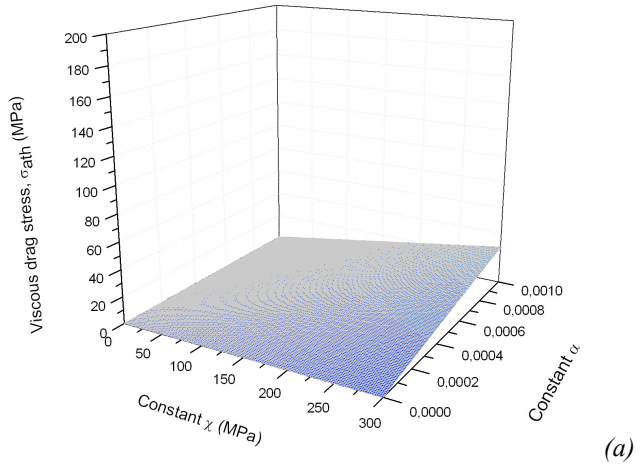

(a)

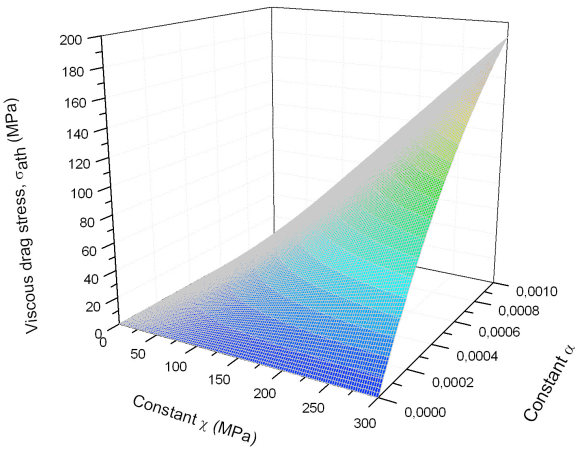

(b)

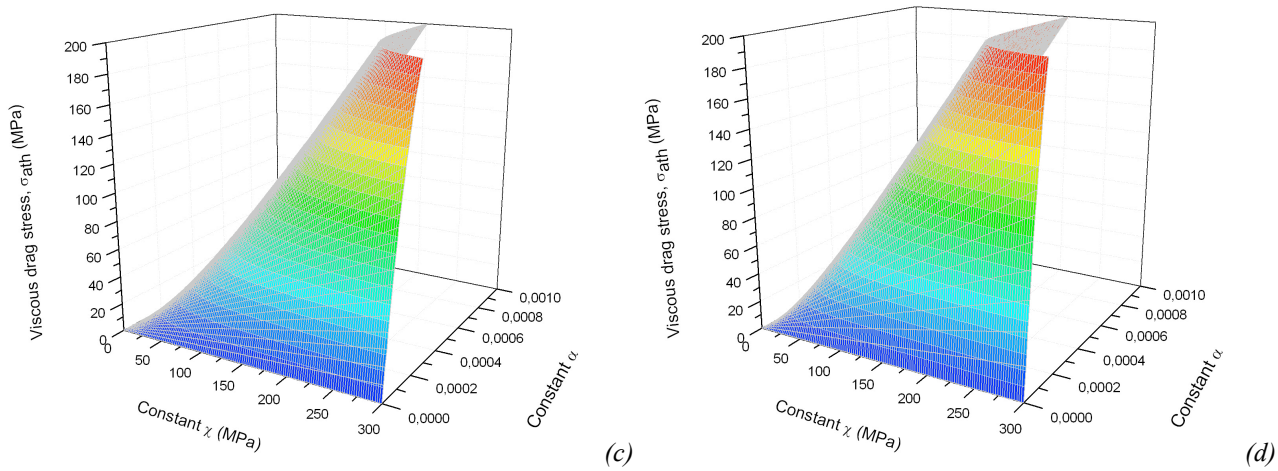

Fig. 2-6. Evolution of the viscous-drag component with χ and α for different strain rate levels. (a) 100 s^{-1}, (b) 1000 s^{-1}, (c) 5000 s^{-1}, (d) 10000 s^{-1} [Rusinek and Rodríguez-Martínez 2009].

Finally, it is necessary to take into account that the dislocation drag is not the only one mechanism controlling deformation at high strain rates, but it is superposed to the thermally controlled mechanisms [Follansbee 1986, Regazzoni et al. 1987], Fig. 2-7. In the presence of thermal activation only, the stress increases slowly with the logarithm of strain rate, whereas in the presence of dislocation drag only, the curve is steep and reaches the strain rate for the applied stress. The curve obtained when both thermally activated and drag mechanisms are operative follows the thermal activation curve at low stresses and the drag curve at high stresses [Regazzoni et al. 1987], Fig. 2-7.

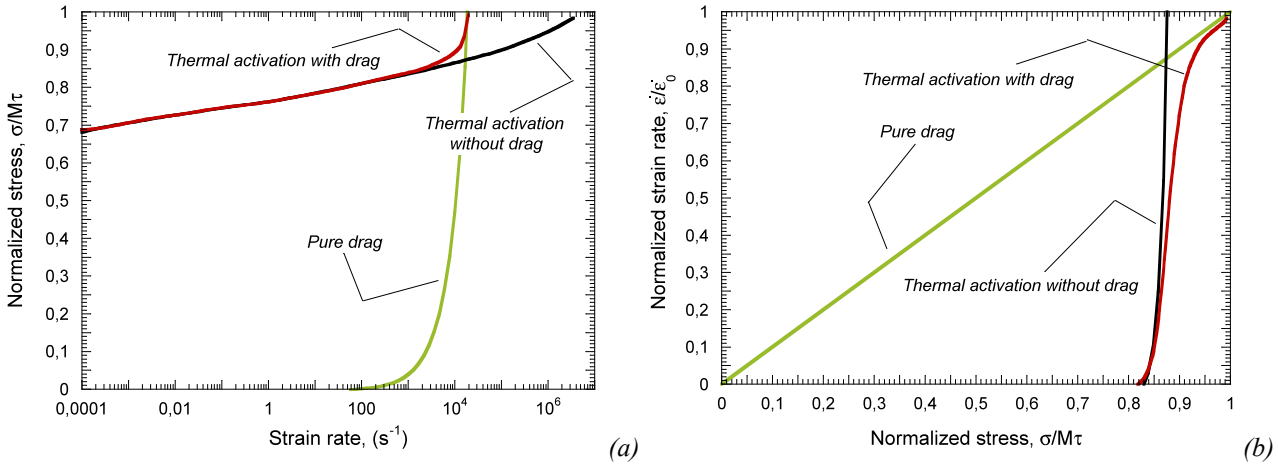

Fig. 2-7. Curves that represent the different flow stress evolution considering pure drag only, thermal activation only and both mechanisms simultaneously [Regazzoni et al. 1987].

2.5.1.2 Formulation

In order to define the viscous drag effect at high strain rates, an additional term is introduced in the formulation of the *RK or MRK* model for describing the equivalent Huber-Misses stress $\overline{\sigma}$ [Rusinek and Rodríguez-Martínez 2009] *(the formulation of both models is based on an additive decomposition of the total stress -See Chapters 2.3 and 2.4-)*. The updated formulation of the model is depicted in Eq. 2-21:

$$\bar{\sigma}\left(\bar{\varepsilon}^{p},\dot{\bar{\varepsilon}}^{p},T\right)=\frac{E(T)}{E_0}\left[\sigma_{\mu}+\sigma^{*}\right]+\sigma_{vs}\left(\dot{\bar{\varepsilon}}^{p}\right) \qquad \textit{Eq. 2-21}$$

In this work, the extended model to dislocations drag mechanisms has been implemented into ABAQUS/Explicit **FE** code using the integration scheme proposed by Zaera and Fernandez-Sáez [Zaera and Fernandez-Sáez 2006].

The procedure for calibration of the constitutive relation is reported in [Klepaczko et al. 2009] *(for the original RK)* and [Rusinek et al. 2010, Rodríguez-Martínez 2010] *(for the MRK)* taking into account the details discussed in [Rusinek and Rodríguez-Martínez 2009].

2.5.2 Constitutive modelling of phase transformation phenomena. The role of strain hardening

This another extension aplicable both for the *RK* and *MRK* constitutive descriptions will be used in Chapter 2 to study the strain hardening effect on plastic instabilities formation *(See objectives of Chapter 1.2)*. A effect showed in austenitic steels is used in order to study the influence of the strain sensitivity *(strain hardening)* on flow localization. This effect is the martensitic transformation phenomenon that these steels show from austenite to martensite under certain conditions in terms of stress, strain, strain rate and temperature. Firstly, theoretical considerations regarding this effect are discussed.

2.5.2.1 Theoretical considerations

In austenitic steels, martensitic transformation only occurs under some certain conditions of strain rates and initial temperatures. Thus, for these steels, martensitic transformation during plastic deformation strongly depends on temperature, Fig. 2-8.

As it could be seen in Fig. 2-8-a, the phase transformation can be split in three different parts depending on temperature. For low enough temperatures *(domain A in the figure),* martensitic transformation appears instantaneously without stress application. For higher temperatures *(domain B in the figure),* phase transformation needs plastic deformation to occur *(application of work)*. For very high temperatures ($T > M_f$) the rest of the austenite remains stable and no phase transformation is observed.

Nevertheless, not only temperature influences the process. Strain rate is also important for phase transformation. When austenitic steels are subjected to high enough strain rates loading, the adiabatic conditions of plastic deformation induce a high temperature increase in the material. Thus, phase transformation is slowed down or even eliminated. As it could be seen in Fig. 2-8-b, for a moderate strain rate of $\dot{\bar{\varepsilon}}^{p} \approx 500 s^{-1}$ the phase transformation does not appear at room temperature ($T = 298\,K$).

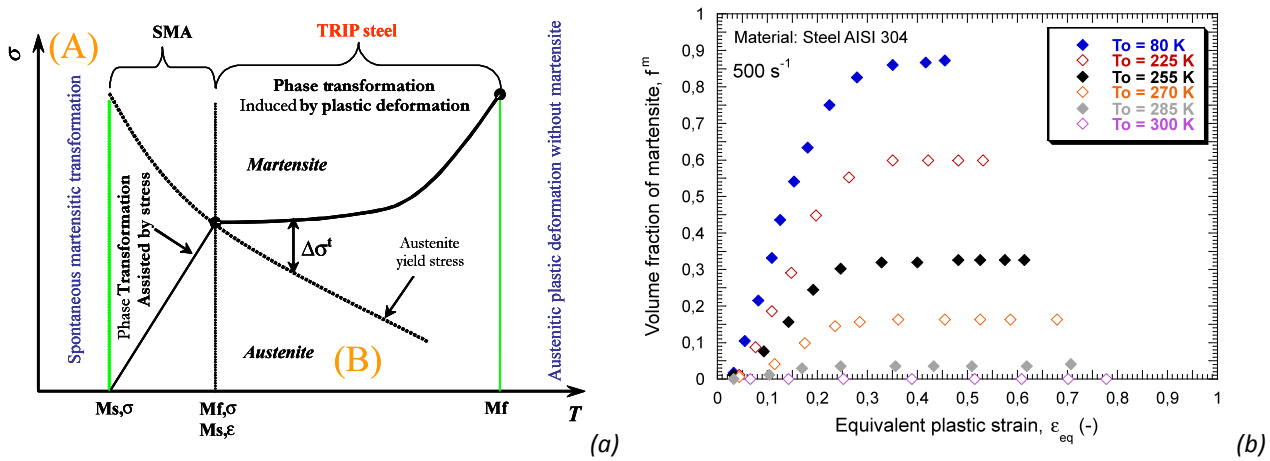

Fig. 2-8. (a) Schematic description of phase transformation; (b) Phase transformation with plastic deformation for different initial temperature in dynamic loading, 500 s^{-1} [Rodríguez-Martínez et al. 2008].

Martensitic transformation plays an important role in the industry. That is because with phase transformation the yield stress level is increased in comparison with steels without it *(yield stress for a martensitic steel is higher than the one for an austenitic steel)*. The way in which this technological operation is carried out is with the introduction of a plastic pre-strain into the steel sheet, Fig. 2-9-a. This operation is usually carried out by cold rolling. It allows avoiding failure in the sheet due to an excessive plastic deformation. Moreover, due to quasi-static bending processes applied to the steel sheet after pre-strain, in order to form a "U" shape, Fig. 2-9-b, additional phase transformation effect may appear.

For applications like crash box, it is necessary to define the behaviour of austenitic steels properly in a strain rate range of $0.001\ s^{-1} \le \dot{\bar{\varepsilon}}^{p} \le 10^{3}\ s^{-1}$. During dynamic loading, due to the high temperature increase by adiabatic heating, the austenite remains stable and no phase transformation is observed. Thus, the phase transformation must be introduced in modelling before the crash test application.

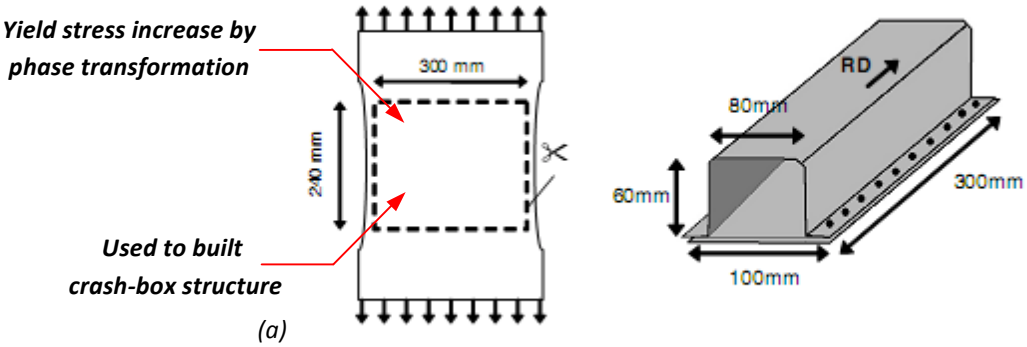

Fig. 2-9. Prestrain history; (a) specimen dimensions after pre-strain process, (b) U box after bending [Rodríguez-Martínez et al. 2008].

Thus, based on experimental observations the following formulation to define the yield stress increase due to the martensitic transformation phenomena was proposed [Rodríguez-Martínez et al. 2008], $\sigma_{T}\left(\bar{\varepsilon}^{p}, \dot{\bar{\varepsilon}}^{p}, T\right)$, Eq. 2-22:

$$\sigma_T\left(\bar{\varepsilon}^p,\dot{\bar{\varepsilon}}^p,T\right)=\sigma_0\cdot f\left(\bar{\varepsilon}^p,\dot{\bar{\varepsilon}}^p\right)\cdot g\left(T\right) \qquad \textit{Eq. 2-22}$$

The first multiplier σ_0 is a fitting parameter which allows defining the maximum of stress increase due to phase transformation, Fig. 2-10. This multiplicative factor could be estimated by mechanical testing. The value of σ_0 must be identified at the lowest temperature of interest or, if possible, at the lowest temperature of experimental data available. The best solution is performing mechanical testing at $T < M_S$. Thus, it corresponds to the maximum phase transformation observed and therefore to the maximum stress level exhibited by the material. The stress component $\sigma_T\left(\bar{\varepsilon}^p,\dot{\bar{\varepsilon}}^p,T\right)$ is split into two independent functions. One in order to take into account the effect of plastic strain and strain rate during phase transformation, $f\left(\bar{\varepsilon}^p,\dot{\bar{\varepsilon}}^p\right)$ and the other one to define the thermal contribution of the rate of phase transformation $g\left(T\right)$.

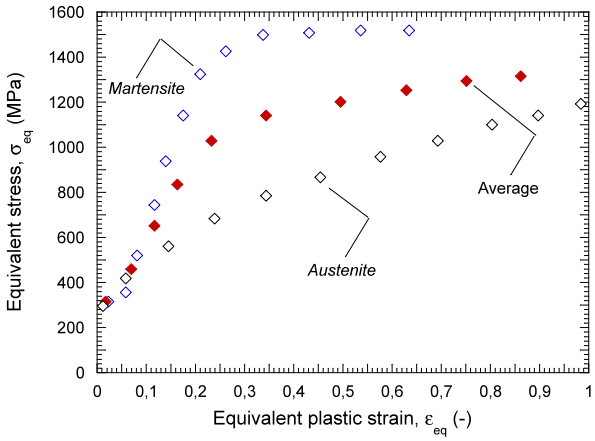

Fig. 2-10. Mechanical behaviour of different phases in steels [Rodríguez-Martínez 2010].

In case of adiabatic conditions the constitutive relation is coupled with heat equation as it has been previously discussed *(See Chapter 2.3).*

Next, the functions both for plastic strain and strain rate effects and for the temperature effect are described.

In order to define the influence of strain and strain rate in the phase transformation, the following function $f\left(\bar{\varepsilon}^p,\dot{\bar{\varepsilon}}^p\right)$ is applied, Eq. 2-23:

$$f\left(\bar{\varepsilon}^p,\dot{\bar{\varepsilon}}^p\right)=\left[1-\exp\left(-h\left(\dot{\bar{\varepsilon}}^p\right)\cdot\bar{\varepsilon}^p\right)\right]^{\xi} \qquad \textit{Eq. 2-23}$$

This expression is similar to the relation with logistic function used in [Pęcherski 1998] to propose phenomenological description of plastic softening of material during the development of multiscale shear banding.

As it could be seen, to approximate behaviour of an austenitic steel during the process of phase transformation, one function, $h\left(\dot{\bar{\varepsilon}}^p\right)$, and one material parameter, ξ, are

introduced. In agreement with experimental observations, $h\left(\dot{\bar{\varepsilon}}^p\right)$ is defined as being strain-rate dependent. Furthermore, due to the form of Eq. 2-23, as $h\left(\dot{\bar{\varepsilon}}^p\right)$ increases, $f\left(\bar{\varepsilon}^p, \dot{\bar{\varepsilon}}^p\right)$ increases too. A decrease of $h\left(\dot{\bar{\varepsilon}}^p\right)$ with plastic strain allows reducing the rate of the phase transformation by diminishing its intensity and delaying its starting point, Fig. 2-11-a. The coefficient ξ controls the strain level where the phase transformation is observed on the macroscopic scale by σ-ε form. The phase transformation starts at determined initiation point of strain, Fig. 2-11-b.

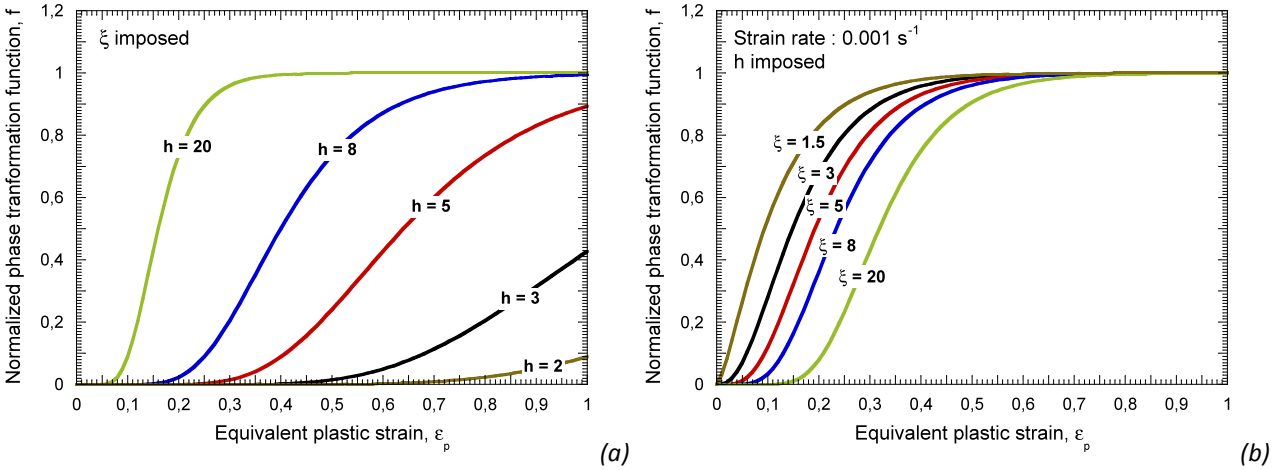

Fig. 2-11. Evolution of phase transformation function $f\left(\bar{\varepsilon}^p, \dot{\bar{\varepsilon}}^p\right)$ with equivalent strain, (a) at fixed strain rate levels for different values of the function h and (b) for different values of ξ [Rodríguez-Martínez et al. 2008].

The function $h\left(\dot{\bar{\varepsilon}}^p\right)$ is the responsible of defining the influence of the strain rate in the phase transformation process. The function proposed is defined as follows, Eq. 2-24:

$$h\left(\dot{\bar{\varepsilon}}^p\right) = \lambda_0 \exp\left(-\lambda \cdot \dot{\bar{\varepsilon}}^p\right) \qquad \textit{Eq. 2-24}$$

where λ_0 and λ are two shape fitting parameters which define the strain rate dependency on the phase transformation.

In Fig. 2-12 is observed that an increase of the parameter λ decreases the strain rate level where the phase transformation is annihilated. To identify this coefficient can be used the experimental data in terms of macroscopic behaviour on the form of σ-ε curve.

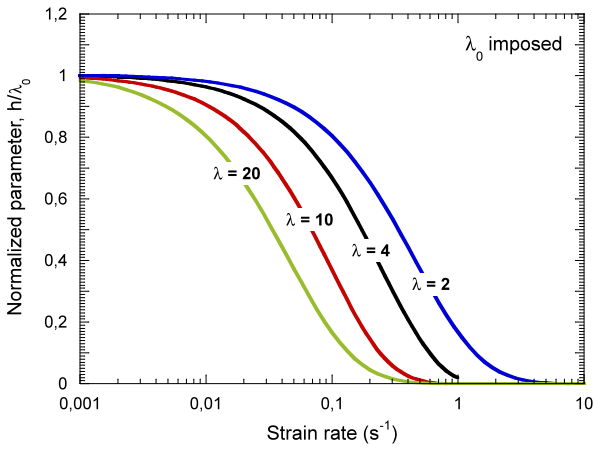

Fig. 2-12. Evolution of normalized parameter h/λ_0 with strain rate [Rodríguez-Martínez et al. 2008].

The function $g(T)$ is the responsible to define the effect of temperature in the phase transformation kinetics. Two different formulations were proposed in [Rodríguez-Martínez et al. 2008] to define this effect.

First of the proposed expressions, $g_1(T)$, Eq. 2-25, is based on the relation suggested by Johnson and Cook [Johnson and Cook 1983] and similar to the formulation used to describe phase transformation process, for example, by [Papatriantafillou et al. 2006].

$$\begin{cases} g_1(T) = 1 - \Theta^{\eta} & if\ T \le M_S \rightarrow g_1(T) = 1 \\ \Theta = \left(\dfrac{T - M_S}{M_D - M_S} \right) & if\ T \le M_D \rightarrow g_1(T) = 0 \end{cases} \qquad \textit{Eq. 2-25}$$

where $\Theta = (T - M_S)/(M_D - M_S)$ is the normalized temperature. T is the current temperature, M_S the martensite-start temperature and M_D is the temperature at which the martensite cannot be induced, no matter how much the austenite is deformed. Values for M_D and M_S are usually obtained from experiments in quasi-static conditions. Furthermore, the parameter η is the temperature sensitivity of the phase transformation process.

A parametric study was carried out in order to show the effect that the parameters involved in this formulation have on the kinetics of the phase transformation, Fig. 2-13-a. As it could be seen in the figure (Fig. 2-13-a), it allows for description of the intensity and level of phase transformation depending on the initial temperature, T_0, in qualitative agreement with experimental observations, Fig. 2-13-b, [Tomita and Iwamoto 1995].

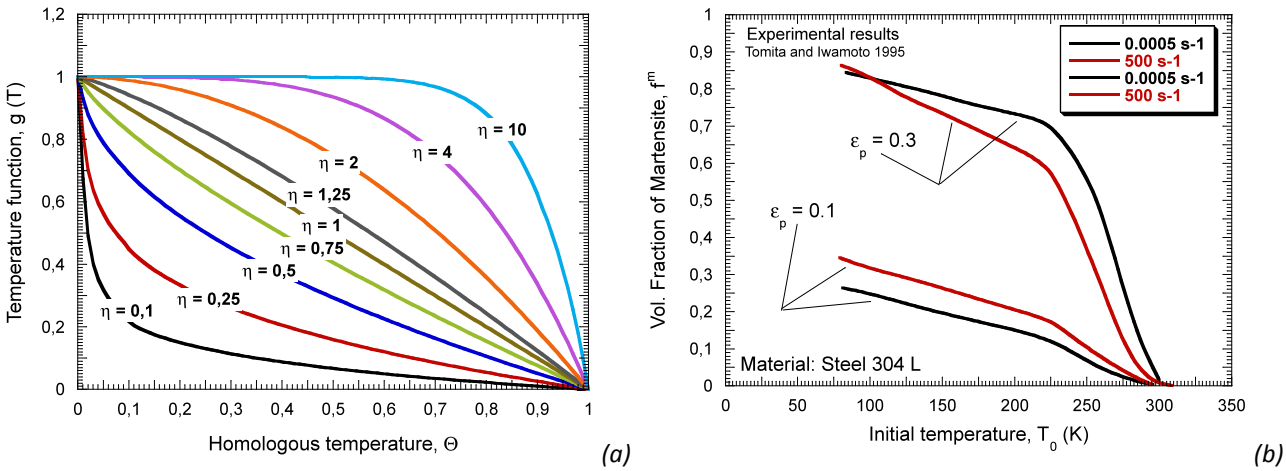

Fig. 2-13. (a) Evolution of temperature sensitivity with initial temperature for different values of η [Rodríguez-Martínez et al. 2008] . (b) Evolution of the martensite volume fraction with temperature [Tomita and Iwamoto 1995].

Second of the proposed expressions, $g_2(T)$, Eq. 2-26, is similar to that reported by [Mahnken et al. 2008].

$$g_2(T) = \exp\left[-\left(\frac{T}{M_D - T_0}\right)^{\alpha}\right] \qquad \textit{Eq. 2-26}$$

where T is the current temperature, T_0 and α are material constants to determine. In this case, the expression is dependend on M_D but not on M_S as for the previous equation Eq. 2-25. For a given value of M_D there is just one possible combination of the constants T_0 and α which fit the requirements of the phase transformation process, that is $if\ T \geq M_D \rightarrow g_2(T) = 0$. One example is shown in Fig. 2-14 for a given value of $M_D = 300\,K$.

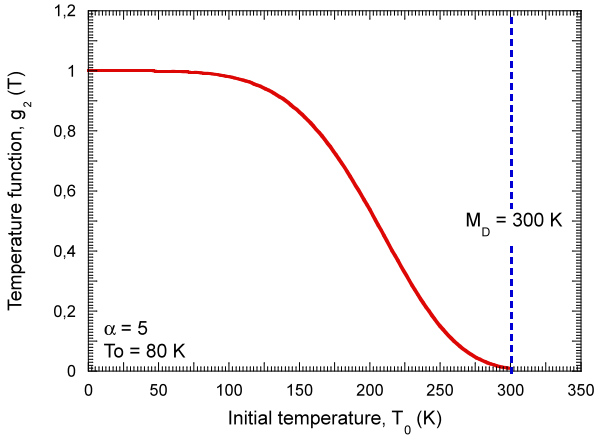

Fig. 2-14. Evolution of $g_2(T)$ function with temperature for a given value of M_D = 300 K [Rodríguez-Martínez et al. 2008].

2.5.2.2 Formulation

In this extended model, a third component $\sigma_T\left(\bar{\varepsilon}^p, \dot{\bar{\varepsilon}}^p, T\right)$ is added to the *RK or MRK* constitutive relations, which allows for an approximation of the phase transformation effect

using a phenomenological approach. The third component $\sigma_T\left(\bar{\varepsilon}^p, \dot{\bar{\varepsilon}}^p, T\right)$ depends on the plastic strain $\bar{\varepsilon}^p$, strain rate $\dot{\bar{\varepsilon}}^p$ and temperature T.

Thus, the general form of the *Extended RK* or *MRK* constitutive relation to phase transformation phenomena is given by Eq. 2-27.

$$\bar{\sigma}\left(\bar{\varepsilon}^p, \dot{\bar{\varepsilon}}^p, T\right) = \frac{E(T)}{E_0}\left[\sigma_\mu + \sigma^*\right] + \sigma_T\left(\bar{\varepsilon}^p, \dot{\bar{\varepsilon}}^p, T\right) \qquad \textit{Eq. 2-27}$$

Moreover, it is important to notice that the effect of the adiabatic temperature increase in dynamic conditions is taken into account in the model via the strain rate dependency on the flow stress.

The procedure for calibration of the constitutive relation is reported in [Klepaczko et al. 2009] *(for the original RK)* and [Rusinek et al. 2010, Rodríguez-Martínez 2010] *(for the MRK)* taking into account the details discussed in [Rusinek and Rodríguez-Martínez 2008] for the calibration of the additional terms for the strain hardening effect.

In the present work this extended model will be applied into a **FE** code, ABAQUS/Explicit using the integration scheme proposed by Zaera and Fernandez-Sáez [Zaera and Fernandez-Sáez 2006].

CHAPTER 3

INFLUENCE OF THE STRAIN RATE SENSITIVITY ON FLOW LOCALIZATION

ABSTRACT

The strain rate sensitivity of a certain metal has an important effect in the flow localization when the metal is dynamically loaded. In this chapter, a wide study of this phenomenon is conducted by application of the dynamic tension test configuration to **AA 7075** using ABAQUS/Explicit. In particular, the effect of the viscous drag is used as an effective example for demonstration of such behaviour. The viscous drag effect takes place when high strain rates of deformation are applied in the material. The effect of omitting the change in the strain rate sensitivity finishes with different localization predictions. The *Extended RK* model to viscous drag effect is used to perform this study. Finally, a parametric analysis is developed to check the effect each one of the parameters which define the viscous drag in this extended model has in the flow localization of the material.

3 INFLUENCE OF THE STRAIN RATE SENSITIVITY ON FLOW LOCALIZATION

3.1 Introduction

Aluminium alloys (**AA**) gather an increasing interest in several engineering fields because of their notorious mechanical properties. Certain types of **AA** exhibit flow stress level comparable to that showed by steel alloys traditionally used in industrial applications. Thus, the main advantage of **AA** respect to steel alloys is the improvement of the strength-to-weight ratio of structures. Due to this low density and remarkable mechanical properties, the use of **AA** is more and more extended in the current industry.

Dynamic behaviour of **AA** has particular relevance in aeronautical industry. Habitually, mechanical elements as fuselage or wings are subjected to impact tests in order to ensure their structural integrity under eventual crashes or accidents. During such loading condition the material is subjected to wide ranges of strain rate from quasi-static to high strain rates up to $\dot{\bar{\varepsilon}}^p \approx 10^4 s^{-1}$.

In that range of strain rates some **AA** exhibit some particular effects that strongly influence their thermo-viscoplastic behaviour. An example of these is the viscous drag effect. In the present work this effect will be extensively studied due to it usually appears in **AA** commonly used in the industry. The material taken for the application of the model is the **AA 7075**.

The structural relevance of aluminium components leads to the necessity of developing and studying advanced constitutive models allowing for an accurate definition of the **AA** behaviour at wide ranges of strain rates and temperatures.

Phenomenological constitutive descriptions like those due to Zerilli and Amstrong [Zerilli and Amstrong 1987] or Johnson and Cook [Johnson and Cook 1983] cannot define the material behaviour when complex phenomena like the viscous drag effect take place. Then, the use of advanced constitutive relations is necessary to perform the analysis. In this chapter will be studied the result of introducing an extension in the *RK* model *(Rusinek-Klepazkco)* in order to take into account the viscous drag effect at high strain rates.

In this work, a numerical analysis of the dynamic tension test is performed. For this, specimens of **AA 7075** subjected to high strain rates have been built in the numerical configuration. Conclusions relating the strain rate sensitivity of the material and plastic instabilities formation have been obtained.

3.2 Numerical model

The analysis developed in this chapter has been performed using the dynamic tension test configuration built in ABAQUS/Explicit.

Next, the numerical model used in this chapter is detailed. First of all, a general overview of the dynamic tension test is shown. Then, the numerical configuration used is described and the boundary conditions applied validated.

3.2.1 The dynamic tension test

The dynamic tension test has some particular characteristics that make its study very interesting. The main important one is the waves propagation which takes place in many industrial applications like the crash-box test or some machining operations. The effect that these waves effect plays on the material behavior has to be carefully studied.

This dynamic test is usually performed using hydraulic machine or Hopkinson bar. If this boundary value problem is considered, the strain rate applied to the material during testing can be assumed by Eq. 3-1.

$$\dot{\bar{\varepsilon}}^{p} = \frac{V_0}{L_t(t)} \qquad \textit{Eq. 3-1}$$

where $L_t(t)$ is the active part of the specimen as a function of time during the test.

In this test one specimen extreme is fixed while the other one is free. This extreme is impacted at a constant impact velocity V_0. Due to the impact on the specimen, a tensile wave is formed. When this wave reaches the opposite side of the specimen (the one that is fixed) is reflected with different direction but the same sign because of the boundary condition that is being applied. In the following figure, Fig. 3-1, is shown a scheme of the discussed process.

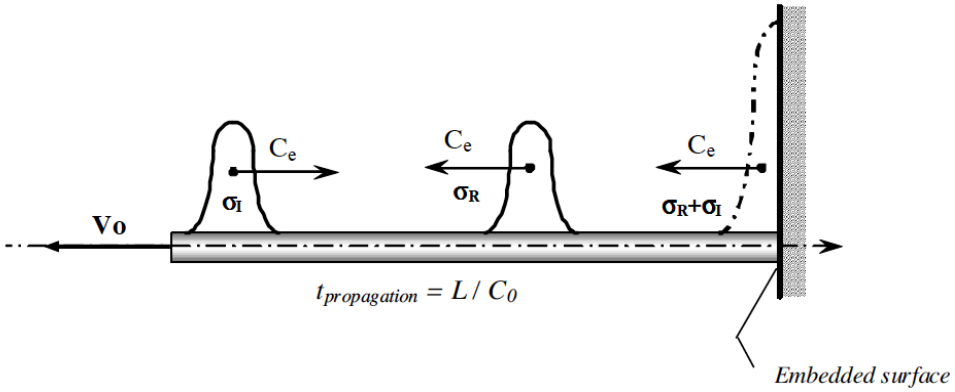

Fig. 3-1. Scheme of the wave effect in an elastic bar during a dynamic tension test.

The velocity of the waves in the specimen could be easily calculated. Assuming one-dimensional linear elasticity, the elastic waves speed is, Eq. 3-2:

$$C_e(T) = \left(\frac{E(T)}{\rho(T)} \right)^{1/2} \qquad \textit{Eq. 3-2}$$

where E(T) is the Young's modulus of the material and ρ(T) is the density. In a general case, these two material properties could be assumed as a function of the temperature. When a pure elastic wave is reflected, it is known that the intensity of this reflected wave is the same

as the original one. Thus, based on D'Alembert's wave propagation theory can be demonstrated that the stress level induced into the material is double of the original one.

Nevertheless the problem is more complex. The materials that will be analyzed show a thermo-viscoplastic behaviour. Thus, plastic wave propagation should also be taken into account. The plastic wave speed is defined as follows, Eq. 3-3.

$$C_p(\bar{\varepsilon}^p, \dot{\bar{\varepsilon}}^p, T) = \left(\frac{1}{\rho(T)} \cdot \frac{d\bar{\sigma}\left(\bar{\varepsilon}^p, \dot{\bar{\varepsilon}}^p, T\right)}{d\bar{\varepsilon}^p} \right)^{1/2} \qquad \textit{Eq. 3-3}$$

where the second term is the slope of the stress-strain curve in each point at a certain moment. This plastic wave speed does not only depend on the temperature, but also on the plastic strain and the strain rate of the material. It is important to notice that in such thermo-viscoplastic case, it is not possible to get analytical solutions for the flow localization. Then, it is necessary to develop experiments in order to define where plastic instability takes place.

This problem was studied by Clark and Wood [Clark and Wood 1957]. They reported some different cases of localization depending on the impact velocity, Fig. 3-2-b.

1. Quasi-static conditions: The plastic flow material is spread along the active part of the specimen due to the stress wave induced is much lower than that corresponding to the yield stress of the material. Necking appears in the middle of the active part of the specimen because of the smallest section of the specimen is located here. This is the so-called *geometrical instability*.

2. As impact velocity increases, the intensity of the reflected wave involves necking appearance in the active part of the specimen near the fixed extreme.

3. If the velocity still increases, a double necking in the specimen is formed. One of them in the impacted side due to the plasticity induced by the high impact velocity. The other one takes place in the fixed end because of the effect of the wave reflection, which induces faster trapping of plastic deformation.

4. With higher velocities, double necking still appears. However, the stress induced by the impact velocity is high enough to induce fast localization in the impacted end, precursor of failure.

5. Finally, for very high impact velocities only one necking appears again. This necking takes place in the impacted side of the specimen due to the stress wave produced by the impact induces the fast trapping of plastic deformation. This is, the velocity of the impacted end equals the plastic waves velocity. When this phenomenon appears, this velocity is called **CIV (Critical Impact Velocity)**. Then, the behaviour of the sample becomes unstable. Under these conditions, there is not equilibrium between input force (in the impacted end) and the force measured in the fixed end [Hu and Daehn

1996, Rusinek et al. 2005, Rodríguez-Martínez et al. 2009]. In such condition this **CIV** velocity becomes a limiting factor for material testing.

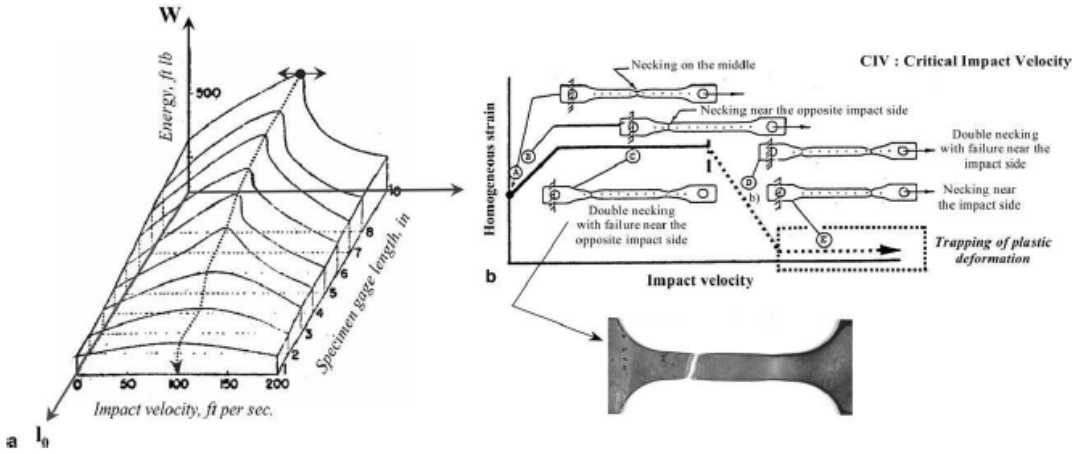

Fig. 3-2. (a) Schematic diagram showing influence of gage length and velocity of impact in total energy [Clark and Wood, 1957]. (b) Scheme of impact velocity effect on a dynamic necking [Clark and Wood, 1957].

According to Klepaczko [Klepaczko 2005] the **CIV** can be obtained integrating the wave celerity along strain. The expression for **CIV** can be split into two parts, Eq. 3-4.

$$\mathrm{CIV} = \int_0^{\varepsilon_e} \mathrm{C_e}\left(\mathrm{T}\right)\cdot \mathrm{d}\varepsilon + \int_{\varepsilon_e}^{\varepsilon_{pm}} \mathrm{C_p}\left(\overline{\varepsilon}_\mathrm{p}, \dot{\overline{\varepsilon}}_\mathrm{p}, \mathrm{T}\right)\cdot \mathrm{d}\overline{\varepsilon}_\mathrm{p} \qquad \textit{Eq. 3-4}$$

The fist term corresponds to the elastic range. In that term $C_e(T)$ is the elastic wave celerity *(in a general case may be dependent on temperature)* and ε_e is the elastic deformation corresponding to the yield stress at $\overline{\varepsilon}^{\mathrm{p}} = 0.$

The second term corresponds to the plastic range. In that term, $\mathrm{C_p}\left(\overline{\varepsilon}^{\mathrm{p}}, \dot{\overline{\varepsilon}}^{\mathrm{p}}, \mathrm{T}\right)$ is the plastic wave celerity dependent on strain hardening, strain rate and temperature. The upper limit of integration, ε_{pm}, may be considered as the plastic strain value corresponding to the instability criterion, $\mathrm{d}\overline{\sigma}/\mathrm{d}\overline{\varepsilon}_{pm} = \overline{\sigma}$ [Klepaczko 2005]. Another possibility is considering ε_{pm} as the plastic strain value corresponding the flow stress saturation, $\mathrm{d}\overline{\sigma}/\mathrm{d}\overline{\varepsilon}^{\mathrm{p}} = 0$ [Klepaczko 2005]. However, the use of one or another possibility could strongly modify the analytical prediction of the **CIV** for a determined material [Rodríguez-Martínez et al. 2009], Fig. 3-3. Moreover, the analytical solution of Eq. 3-4 depends on the constitutive relation used to define the material behaviour since $\mathrm{C_p}\left(\overline{\varepsilon}^{\mathrm{p}}, \dot{\overline{\varepsilon}}^{\mathrm{p}}, \mathrm{T}\right) \propto \overline{\sigma}_{eq}\left(\overline{\varepsilon}^{\mathrm{p}}, \dot{\overline{\varepsilon}}^{\mathrm{p}}, \mathrm{T}\right)$. In addition, the thermal coupling must be taken into account and then increase of temperature becomes dependent on plastic deformation $\mathrm{dT}/\mathrm{d}\overline{\varepsilon}^{\mathrm{p}} \neq 0$.

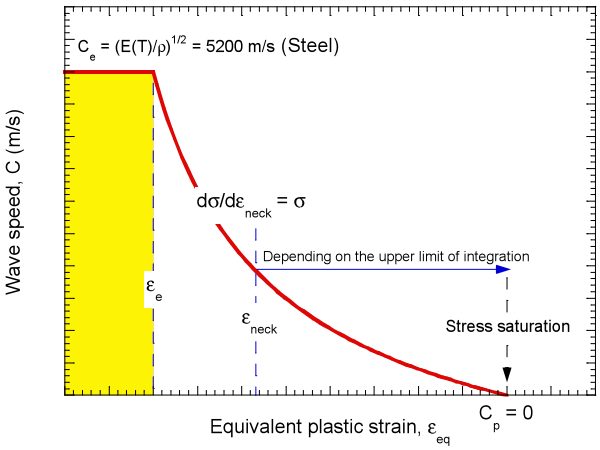

*Fig. 3-3. Schematic representation of the wave speed versus plastic strain for strain rate and temperature levels given. Influence of the upper limit of integration ε_{pm} on the **CIV** value [Rodríguez-Martínez et al. 2009].*

3.2.2 Numerical configuration

The geometry and dimensions of the specimen used in this chapter are based on a previous work due to Rusinek et al. [Rusinek et al. 2009-a]. Such geometry of specimen allows for observing well developed necking [Rusinek et al. 2009-a]. A scheme of the specimen is shown in Fig. 3-4. The thickness of the sample is t_s = 1.65 mm. Its impacted side is subjected to a constant velocity during the numerical simulation. The movements are restricted to the axial direction. The opposite impacted side is embedded. Such configuration idealizes the boundary conditions required for the test. It must be noted that during experiments may be difficult to obtain such arrangement *(the applied velocity may not be constant during the whole test, transversal displacements of the specimen may occur)*. However, this numerical configuration is suitable to control the level of strain rate on the active part of the specimen during the simulations.

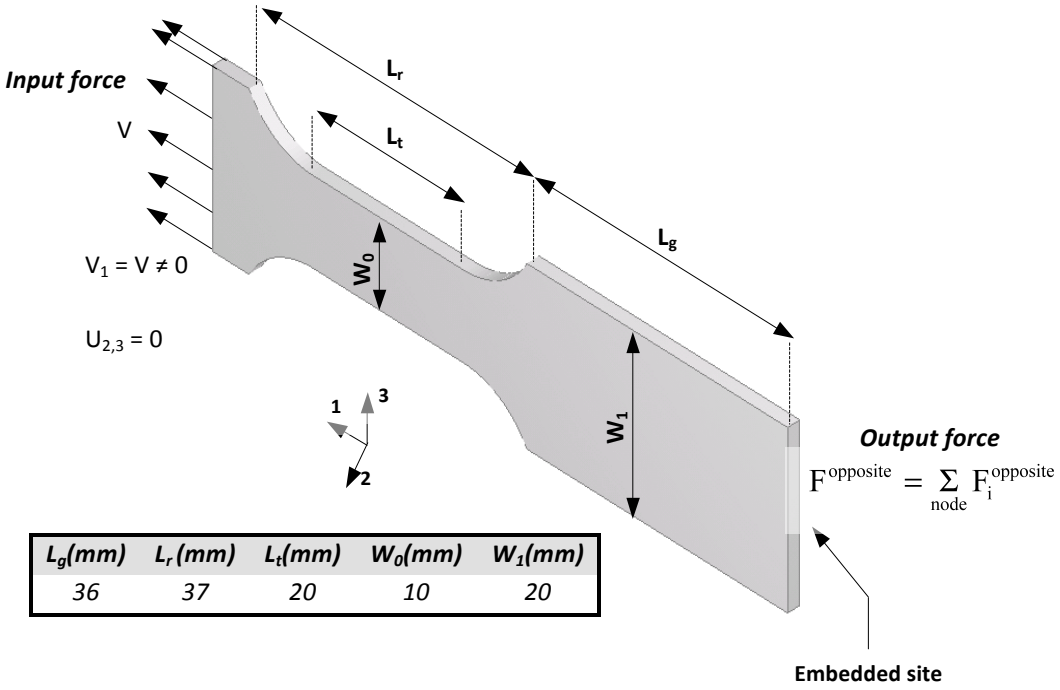

L_g(mm)	L_r(mm)	L_t(mm)	W_0(mm)	W_1(mm)
36	37	20	10	20

Fig. 3-4. Geometry and dimensions (mm) of the specimen used during simulations

The active part of the specimen has been meshed using hexahedral elements whose aspect ratio is close to 1:1:1 $\left(\approx 0.5 \cdot 0.5 \cdot 0.5\ \mathrm{mm}^3\right)$. This definition is in agreement with the considerations reported by Zukas and Scheffler [Zukas and Scheffler 2000]. Besides the active part of the specimen two transition zones are defined. These zones are meshed with tetrahedral elements, Fig. 3-5-a. Such transition zones allow for increasing the number of elements along the 3 axis of the specimen. This technique is used to get hexahedral elements in the outer sides of the sample maintaining the desired aspect ratio 1:1:1.

In Fig. 3-5-b triaxiality contours during numerical simulation are shown. It can be observed that the triaxiality value in the active part of the specimen is that corresponding to uniaxial tension state, $\sigma_{\text{triaxiality}} = 0.33$, then it is proved that boundary conditions applied to the simulations guarantee the tensile state in the active part of the specimen.

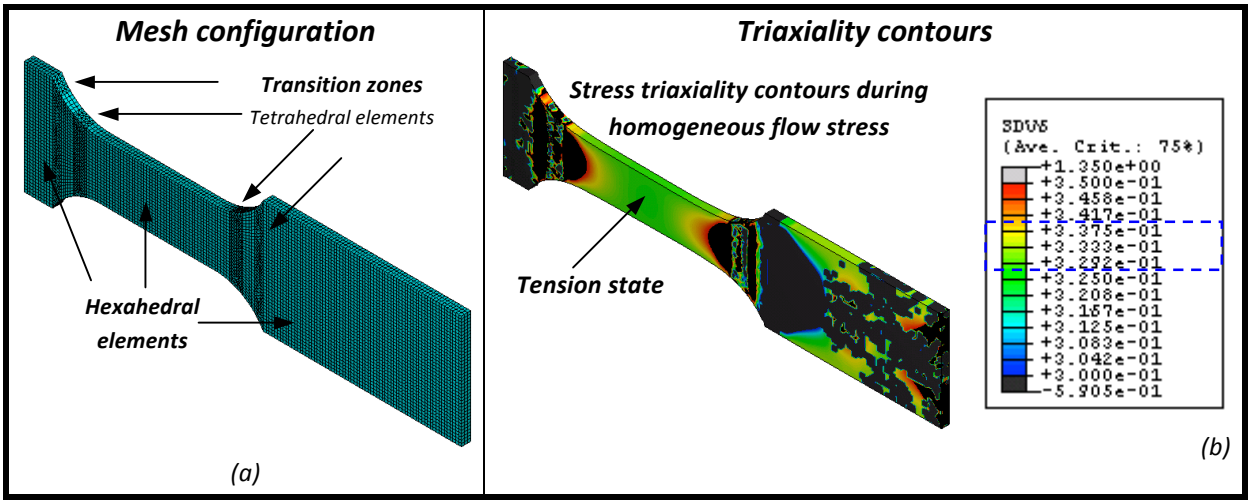

Fig. 3-5. (a) Mesh configuration used during numerical simulations. (b) Numerical estimation of the triaxiality contours during loading.

In agreement with previous works of Rusinek and Zaera [Rusinek and Zaera 2007], the failure criterion used has been the selection of a constant critical value for the strain. Moreover, because of in the present dissertation it has been studied the plastic instabilities of the material, this failure strain must be imposed with a value high enough to not disturb the plastic localization and necking progression in the sample. It is important to realize that this strain of instability depends on the definition of the material behaviour, this is the constitutive relation used.

During this work, results of simulations with the original and *Extended RK* model used here have been compared.

3.3 Application to AA 7075

The **AA** 7xxx series are alloyed with zinc, and can be hardened to the highest strengths of any **AA**. **AA 7075** is notable for its strength, with good fatigue strength and average machinability, but it is not weldable and has less resistance to corrosion than many other **AA**. It is widely used in the aeronautical industry for construction of aircraft structures,

such as wings and fuselages *(it is assumed that this material does not exhibit dependence of plastic strain on the Volume Thermally Activated* ***(VTA)*** *since its strain hardening remains approximately constant for different temperatures and strain rates [El-Magd and Abouridouane 2006, Rusinek and Rodríguez-Martínez 2009])*. Its main alloying elements are listed in Table 3-1.

Mn	Si	Cr	Ti	Fe	Mg	Zn	Ti	Cu
0.3	0.4	0.23	0.2	0.5	2.5	5.5	0.2	1.6

Table 3-1. Chemical composition of AA 7075 (% of wt)

Using the systematic procedure reported in [Rusinek and Rodríguez-Martínez 2009], the model has been calibrated for **AA 7075** using the experimental data reported in [El-Magd and Abouridouane 2006]. The following set of constants was found [Rusinek and Rodríguez-Martínez 2009], Table 3-2 and Table 3-3.

B_0 (MPa)	ν (-)	n_0 (-)	D_2 (-)	ε_0 (-)	σ_0^* (MPa)	m^* (-)	D_1 (-)	T_m (K)	$\dot{\varepsilon}_{min}$ (s^{-1})	$\dot{\varepsilon}_{max}$ (s^{-1})
790.3	-0.0002	0.1966	0.0555	0.018	196.57	1.2857	0.3	900	10^{-5}	10^{7}

Table 3-2. Constants determined for AA 7075 for RK model [Rusinek and Rodríguez-Martínez 2009].

χ (MPa)	α (-)
286.7	0.00005368

Table 3-3. Constants determined for AA 7075 for the viscous drag component of the Extended RK model [Rusinek and Rodríguez-Martínez 2009].

Conventional physical constants of aluminum alloys can be obtained from material handbooks, Table 3-4.

E_0 (GPa)	C_p ($Jkg^{-1}K^{-1}$)	β (-)	ρ (kgm^{-3})
70	900	0.9	2700

Table 3-4. Physical constants for aluminum alloys.

By application of the material constants listed above the flow stress of the material is defined as follows, Fig. 3-6. In Fig. 3-6 the overall stress is decomposed into its respective components. It is observed that the viscous drag term starts to contribute to the material stress level in the case of $\dot{\bar{\varepsilon}}^p \geq 1000\,s^{-1}$. For $\dot{\bar{\varepsilon}}^p = 5000\,s^{-1}$ the drag mechanisms show a contribution of approximately 10 % of the overall flow stress. Then, it can be assured that possible differences in the material behaviour using this *Extended RK* constitutive relation does not come from the additional stress level applied *(which will cause temperature increase).* This change only depends on the variation in the strain rate sensitivity of the material, this is the viscous drag effect.

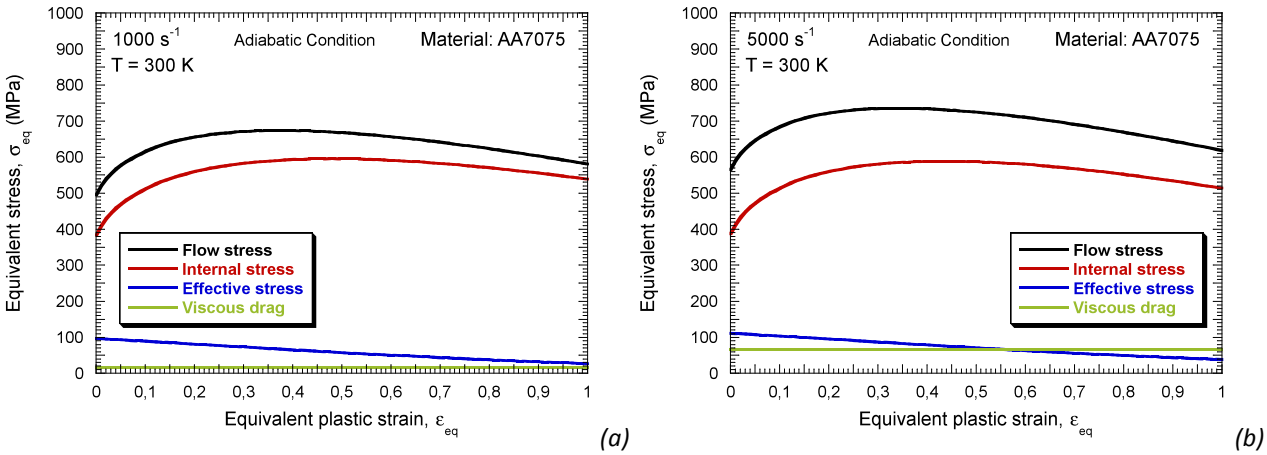

Fig. 3-6. Decomposition of the overall flow stress into its respective stress components at two different strain rates. (a) 1000 s^{-1}, (b) 5000 s^{-1} [Rusinek and Rodríguez-Martínez 2009].

Next, a validation of both constitutive descriptions (*RK* and *Extended RK*) is showed [Rusinek and Rodríguez-Martínez 2009]. The first step was to evaluate the predictions of the *Extended RK* model for different strain rate levels. For this purpose a comparison between model predictions and experimental data was carried out. In Fig. 3-7 is reported a satisfactory agreement between the model and the experiments from quasi-static loading to high strain rate $0.001\ s^{-1} \le \dot{\bar{\varepsilon}}^{p} \le 2529\ s^{-1}$.

Notice that the experimental data follows the model prediction up to certain plastic strain. This plastic strain corresponds with saturation stress stage ($d\bar{\sigma}/d\bar{\varepsilon}^{p} = 0$), which involves non-homogeneous behaviour *(open symbols in* Fig. 3-7*,* Fig. 3-8*).* In such a case, nucleation and growth of micro voids sharply decrease the flow stress. It must be noticed that the viscous drag component added to the *RK* model allows for correct definition of the material behaviour at high rate of deformation, Fig. 3-7-d.

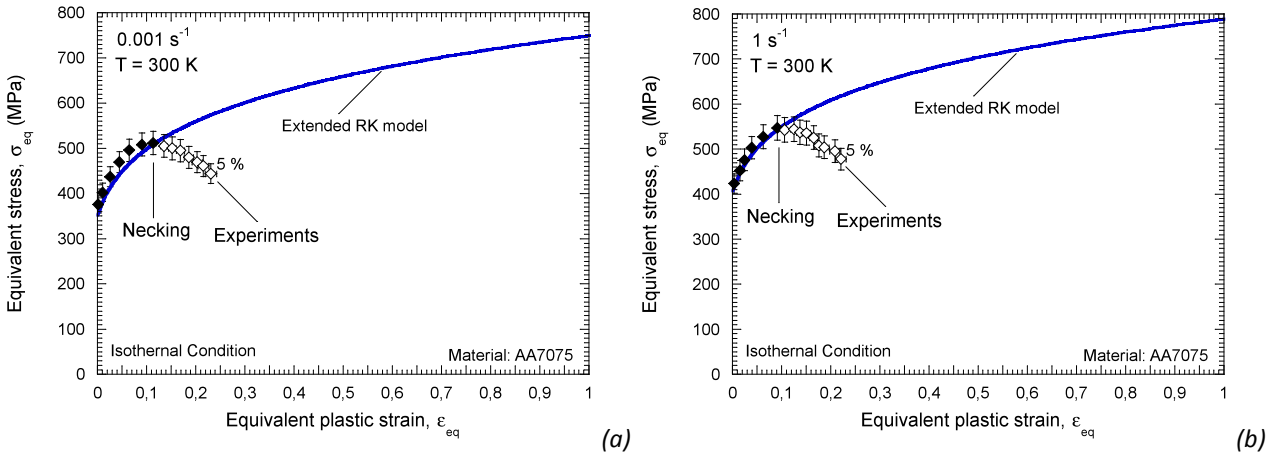

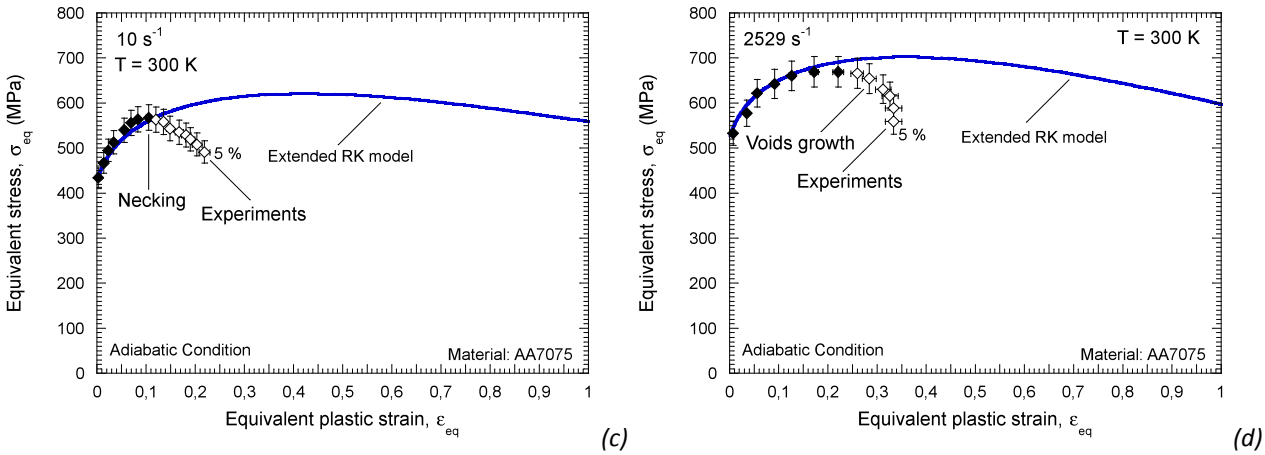

Fig. 3-7. Description of the flow stress evolution as a function of the plastic strain using Extended RK model and comparison with experiments at room temperature [El-Magd and Abouridouane 2006]. (a) 0.001 s^{-1}, (b) 1 s^{-1}, (c) 10 s^{-1} and (d) 2529s^{-1} [Rusinek and Rodríguez-Martínez 2009].

In Fig. 3-8 is shown a comparison between the original and *Extended RK* model studied in this work at different conditions. At first sight, the contribution of the viscous drag term may not look very important in the description of the material behaviour. For strain rates bellow $\dot{\bar{\varepsilon}}^{p}_{trans-drag}$ the difference between both models is negligible, Fig. 3-8-a. However, for high strain rates of deformation, Fig. 3-8-b, the predictions of the *Extended RK* formulation agree with experiments, while the original formulation clearly underestimates the material flow stress level. In addition, due to the athermal character of viscous drag formulation used, its contribution is revealed indispensable for describing the material behaviour at high temperatures, Fig. 3-8-c-d.

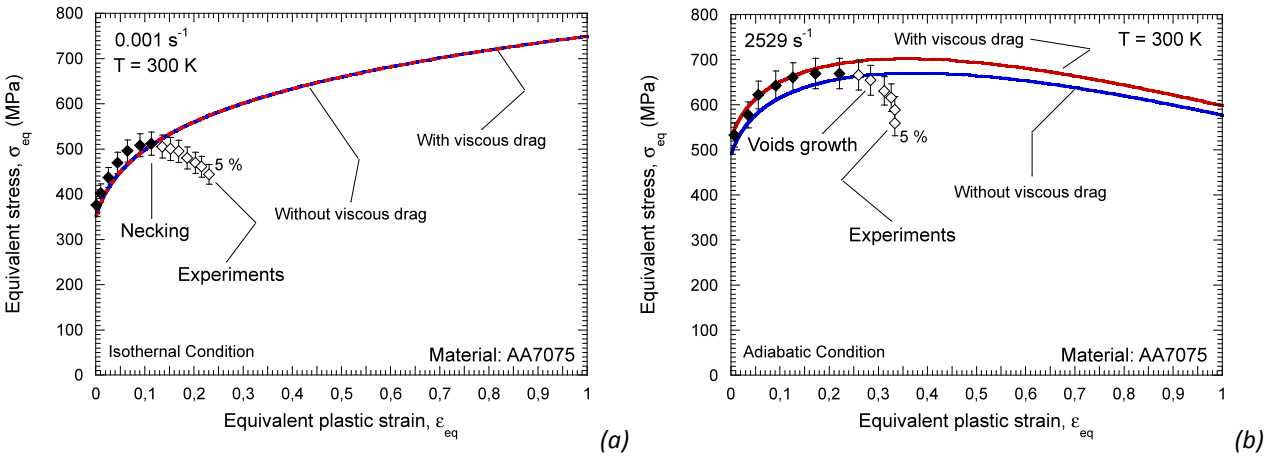

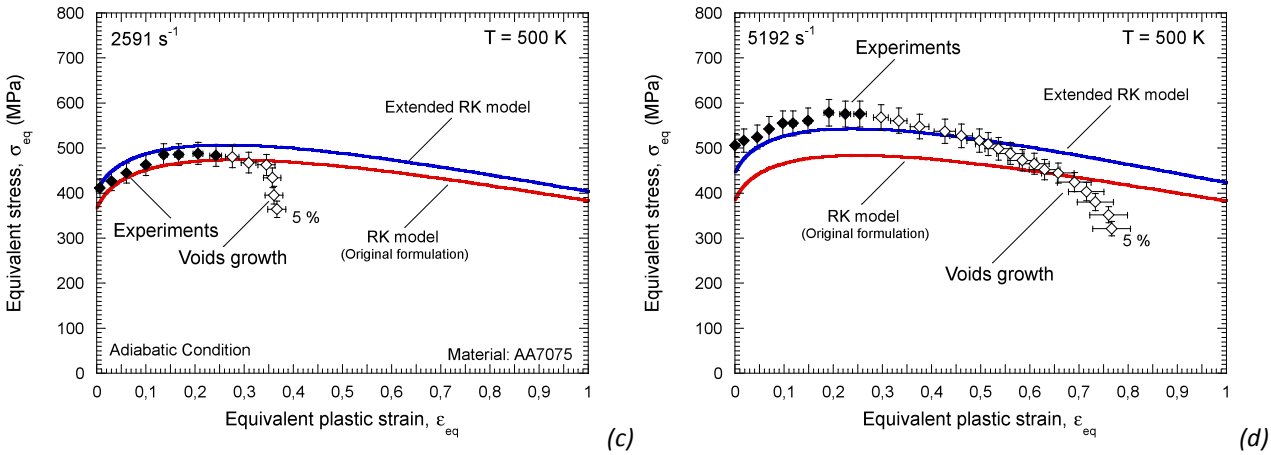

Fig. 3-8. Description of the flow stress evolution as a function of the plastic strain using RK and Extended RK models and comparison with experiments at room temperature and T_0 = 500 K [El-Magd and Abouridouane 2006] at different strain rates [Rusinek and Rodríguez-Martínez 2009].

The importance of taking into account the viscous drag effect is clearly showed in Fig. 3-9. When the $\dot{\varepsilon}^{p}_{trans-drag}$ is reached, dislocations drag drastically changes the material strain rate sensitivity, Fig. 3-9-a. If only the thermally actived deformation mechanisms are taken into account, the rate sensitivity remains approximately constant, Fig. 3-9. With the inclusion of the additional term for the viscous-drag, this strain rate sensitivity change is perfectly modeled. Furthermore, the viscous-drag term compensates the underestimation on the flow stress at high strain rates that would be obtained using just the Arrhenius's equation as the mechanism to describe the rate sensitivity of the material, Fig. 3-8-d. Dislocations drag and thermally actived deformation mechanisms are radically different and the implications that this fact may have on the response of the material under dynamic loading will be extensively investigated in this dissertation.

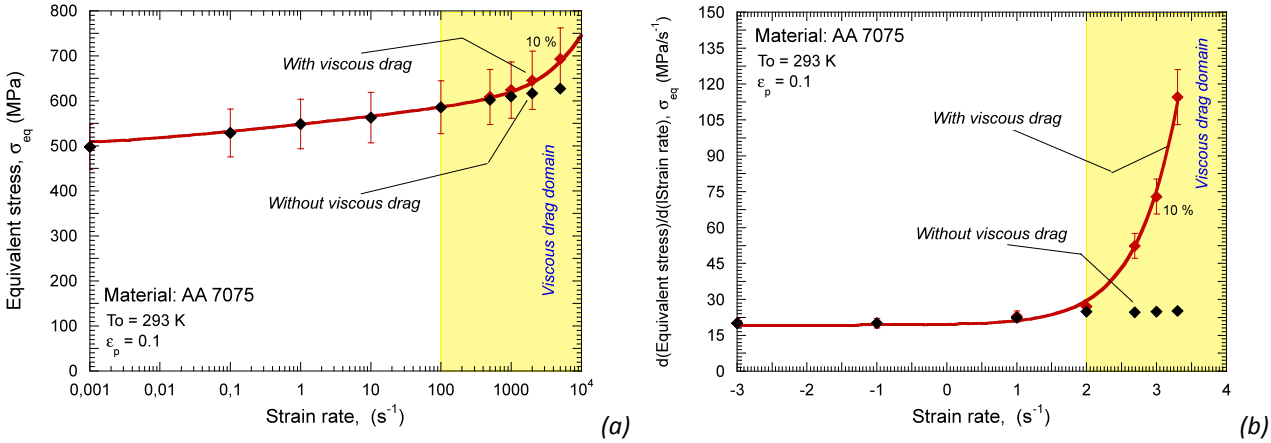

Fig. 3-9. (a) Flow stress evolution as a function of the strain rate of AA7075 predicted by original and Extended RK models and comparison with experiments at room temperature and ε_p=0.1 [El-Magd and Abouridouane 2006]. (b) Rate sensitivity of AA7075 predicted by original and Extended RK models [Rusinek and Rodríguez-Martínez 2009].

Thus, it is clear that the *Extended RK* constitutive relation provides a proper description of the thermo-viscoplastic behaviour of **AA 7075**. Next, a numerical analysis on the influence of the viscous drag term in the formation of plastic instabilities under dynamic tension is conducted. The methodology applied could be seen in Fig. 1-2 *(Section 1.3)*.

3.4 Analysis and results: the role of strain rate sensitivity

Next, the results and conclusions obtained from the numerical analysis developed in this chapter are described. First of all, a validation of the numerical model was performed. Once the model was validated, numerical simulations within wide range of impact velocities were carried out in order to obtain conclusions about the role of the strain rate sensitivity on flow localization under dynamic tension loading conditions.

3.4.1 Validation of the model

Simulations at different impact velocities were carried out in order to validate this numerical configuration. Stress and strain data were extracted from an integration point belonging to an element out of the necking zone *(placed on the active part of the specimen),* Fig. 3-10. There, the flow stress can be considered homogeneous, the strain rate remains *(approximately)* constant along the test and it agrees with the theoretical one. Then a proper comparison with the analytical predictions for an imposed rate level can be carried out.

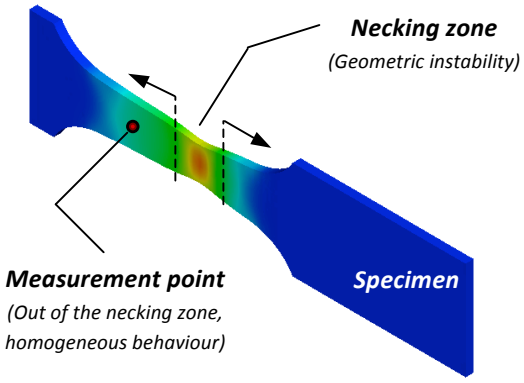

Fig. 3-10. Measurement point of stress-strain curves for model validation.

In Fig. 3-11 are shown the stress-strain curves for some of the simulations carried out. It is important to notice that the simulation results match the analytical predictions of the model at different impact velocities, both for the original and *Extended RK model.* It validates the boundary conditions applied in the numerical configuration as well as the implementation of the viscous drag term into the **FE** code.

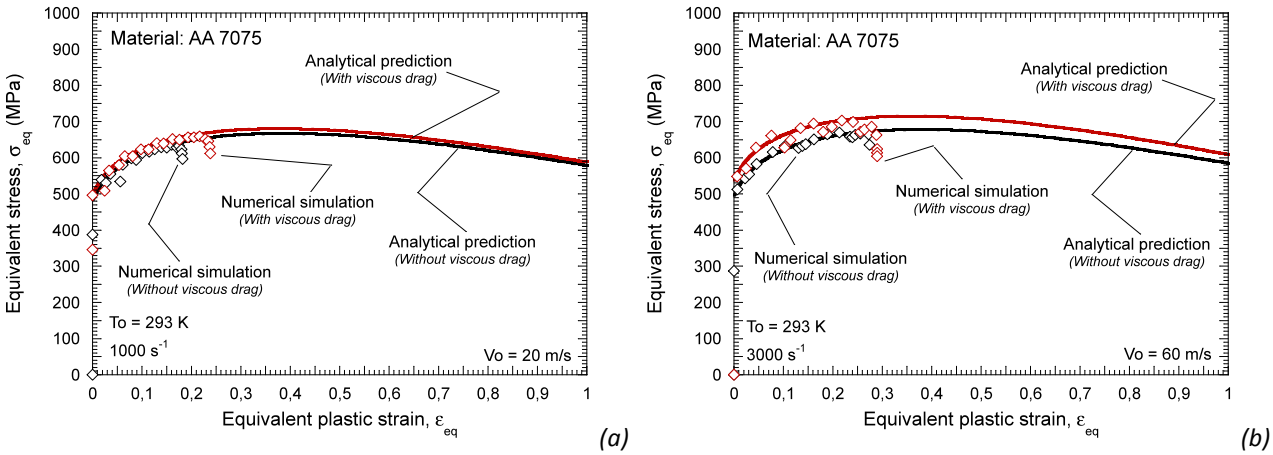

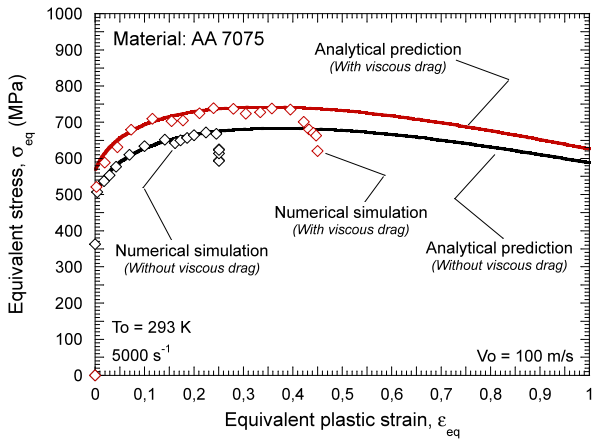

(c)

Fig. 3-11. Stress-strain curves (both simulation results and analytical predictions) for different impact velocities and both models (original and Extended RK). (a) 20 m/s, (b) 60 m/s and (c) 100 m/s.

Once the numerical configuration is validated, an analysis on the influence of dislocations drag effects on the flow stress localization in **AA 7075** is conducted.

3.4.2 Influence of viscous drag stress term on the dynamic behaviour of AA 7075

Numerical simulations within the range of impact velocities $5\,\mathrm{m/s} \le V_0 \le 140\,\mathrm{m/s}$ have been carried out. This interval of velocities corresponds to the theoretical *(homogeneous deformation)* range of strain rates $250\,\mathrm{s^{-1}} \le \dot{\bar{\varepsilon}}^{p} \le 7000\,\mathrm{s^{-1}}$.

Before discussing the implications that the addition of the viscous drag term has on the plastic instabilities formation it is necessary to check that the potential secondary effects induced by the addition of this stress term to the overall flow stress could be neglected. Such secondary effects refer to the increase of the flow stress which leads to the elevation of the material temperature *(due to adiabatic heating)* and to the subsequent potential modification of the strain hardening *(due to the material softening)*.

To check this issue, in Fig. 3-12 is shown that the increase in the flow stress involves an increase in the temperature of the material that can be considered negligible for the softening of it in all cases. Even in Fig. 3-12-b, where the strain rate is high and the addition of the viscous drag component is more important, the increase of temperature related to the viscous stress seems to be irrelevant.

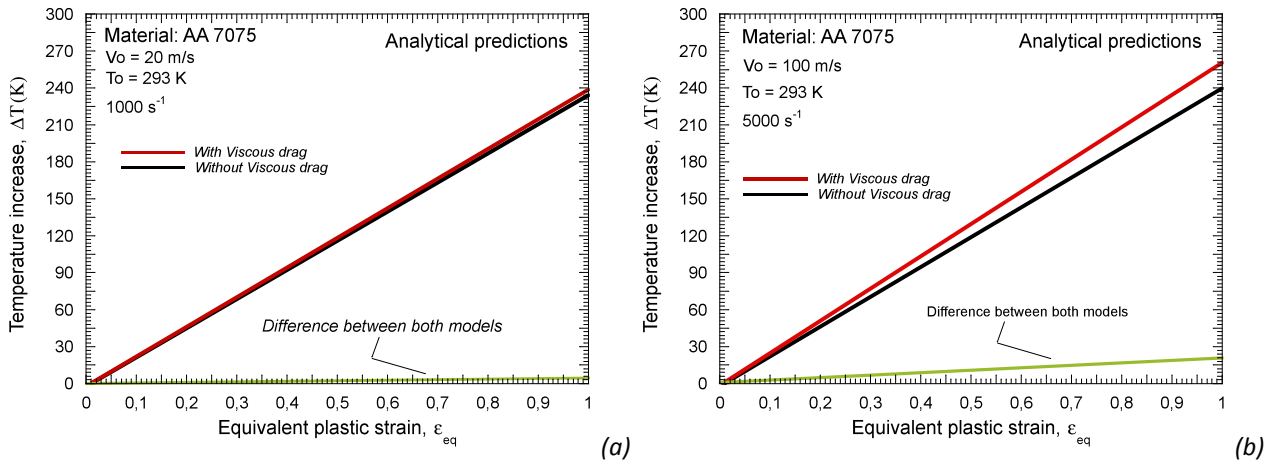

Fig. 3-12. Temperature increase for original and Extended RK models. (a) 1000 s^{-1}, (b) 5000 s^{-1}.

Moreover, if the increase in the softening of the material is almost negligible, the strain hardening should be similar for both models too. This fact is clearly showed in Fig. 3-13. Both for an impact velocity of V_0=20 m/s and V_0=100 m/s, the strain hardening of the **AA** using the original *RK* formulation (without viscous-drag term) and the *Extended RK* (with viscous-drag term) is approximately equal. This confirms that the difference in the material behaviour comes basically from the change in the strain rate sensitivity at high strain rates. In addition, a qualitative estimation of the strain at which plastic instability will occur can be seen in Fig. 3-13 by application of the Considere's criterion.

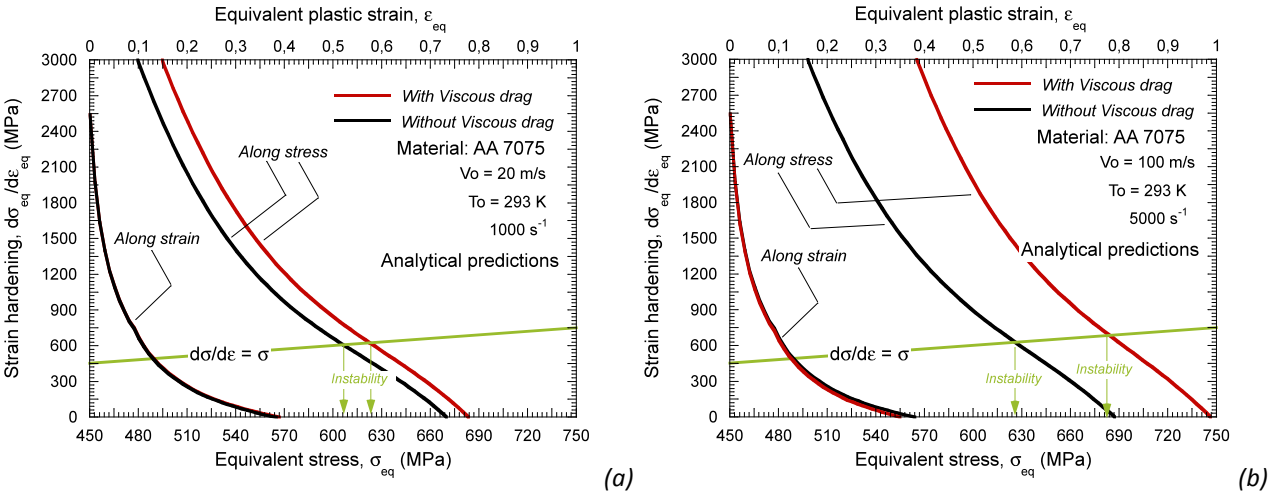

Fig. 3-13. Strain hardening evolution versus plastic strain and versus flow stress for original and Extended RK models. (a) V_0 = 20 m/s (1000 s^{-1}), (b) V_0 = 100 m/s (5000 s^{-1}).

A study to relate the influence of the viscous drag term on the strain of instability was performed. Strain data was extracted from elements located where the necking was formed. This data corresponds with the strain of an integration point where maximum localization takes place *(middle point of necking),* Fig. 3-14.

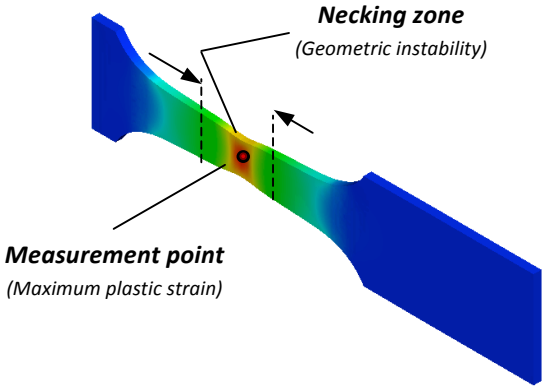

Fig. 3-14. Measurement point of local plastic strain.

The local value of strain is compared with the theoretical one corresponding to the whole specimen, Fig. 3-15. The onset of the plastic instability is clearly defined. It corresponds with the local strain at which local and global strains do not match [Triantafyllidis and Waldenmyer 2004], Fig. 3-15. The bifurcation point *(strain of instability)* is highly dependent on impact velocity, Fig. 3-15. Once instability takes place, small increments in the specimen deformation involve high increments in the local strain of the material in the necking zone of the specimen.

There are some points to comment regarding to the results presented in Fig. 3-15. First of all, in the *Extended RK* constitutive relation the strain of instability is always higher than in case of not taking the viscous-drag effect into account, Fig. 3-15. Second, the strain of instability increases with the strain rate, Fig. 3-15-e, but this increase is much more notable in case of considering the viscous-drag term, Fig. 3-15-c-d-e. Moreover, the behaviour of the **AA** under low rate loading conditions for both models is similar. However, if the loading conditions involve high strain rates of deformation in the material, the fact of not considering the viscous-drag term result in an inaccurate material behaviour modelling. Finally, the inclusion of the additional term to take into account the viscous-drag effect seems to slow down the instability progression with increasing strain rate sensitivity *(such consideration only can be postulated carefully since instability progression is also controlled by damage mechanics [Perzyna 2008] which is not being taken into account in our numerical model).*

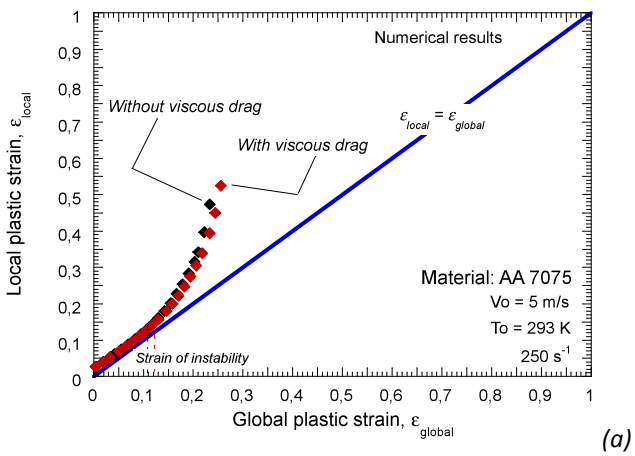

(a)

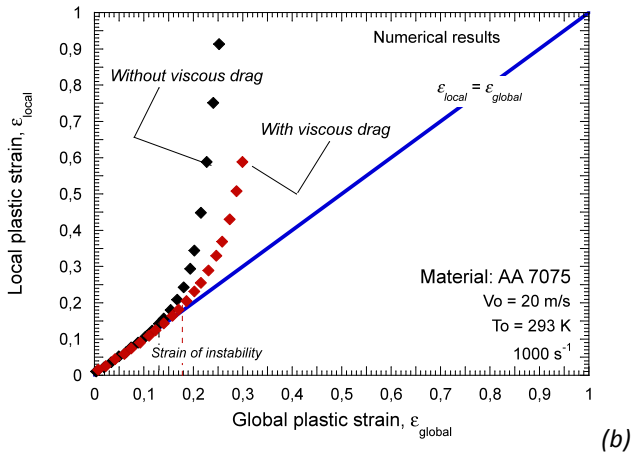

(b)

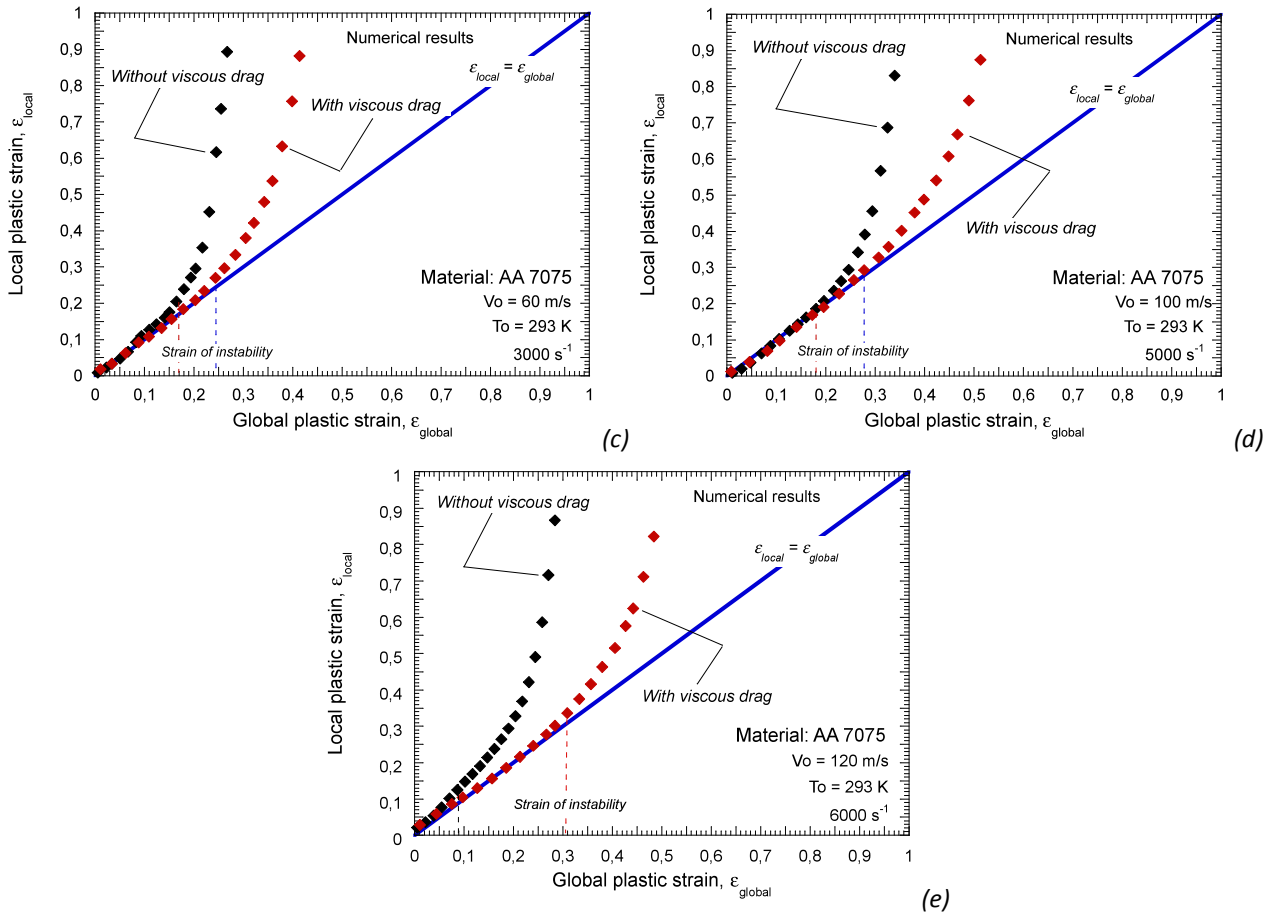

Fig. 3-15. Evolution of local plastic strain as a function of the global plastic strain for original and Extended RK models. (a) V_0=5 m/s, (b) V_0=20 m/s, (c) V_0=60 m/s, (d) V_0=100 m/s and (e) V_0=120 m/s.

Regarding previous results, some comments can be done:

- In agreement with the previous discussion, the plastic instability of metals increases with strain rate *(this is increasing the impact velocity)* [Hu and Daehn 1996]. Then, it could be said that higher strain rate sensitivity homogenizes the material behaviour retarding strain localization [Mercier and Molinari 2004].

- As it has been indicated in previous sections *(See Chapter 3.2.1)*, the dynamic tension test is ruled by the waves propagation. This is, there exists a certain impact velocity, called **C**ritical **I**mpact **V**elocity (**CIV**), at which the impact velocity equals the velocity of the plastic waves through the specimen. The **CIV** leads to fast localization and subsequent failure acting as a limiting factor for material testing [Klepaczko 2005, Rodríguez-Martínez et al. 2009]. Therefore, it is expected that in the simulations carried out in this work, the strain of instability will increase with impact velocity until *(approximately)* the **CIV** will be reached [Klepaczko 1998, Rusinek et al. 2005].

The differences in the strain of instability because of the viscous drag term are depicted in Fig. 3-16. Performing comparisons at impact velocities higher than 100 m/s does not provide useful conclusions due to at this velocity the **CIV** (**C**ritical **I**mpact **V**elocity) is reached when *original RK* constitutive relation is applied. Moreover, it must be pointed that the trends of the curves obtained here are in quite well agreement with those published by Hu and Dehn [Hu and Daehn 1996].

The rate sensitivity seems to play certain role in the **CIV** value. In Fig. 3-16 is observed that in the case of *original RK* model the **CIV** is reached, while in the case of using the extension to dislocations drag processes, the strain of instability is still increasing with the impact velocity. Then, the application of the additional stress component considerably increases the ductility of the material and delays the **CIV** appearance, Fig. 3-16.

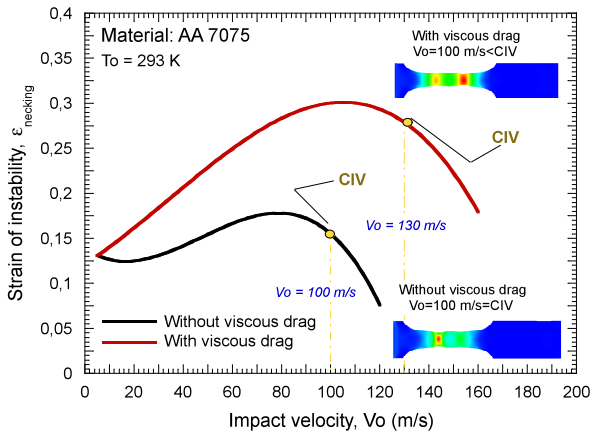

Fig. 3-16. Strain of instability versus impact velocity for original and Extended RK models.

The **CIV** showed in the previous figure, Fig. 3-16, has been estimated by comparison of input (at the impacted site, Fig. 3-4) and output (at the clamped site, Fig. 3-4) forces, Fig. 3-17. The **CIV** velocity is assumed to be the impact velocity at which both forces do not reach equilibrium as reported in [Rusinek et al. 2005, Rodríguez-Martínez et al. 2009].

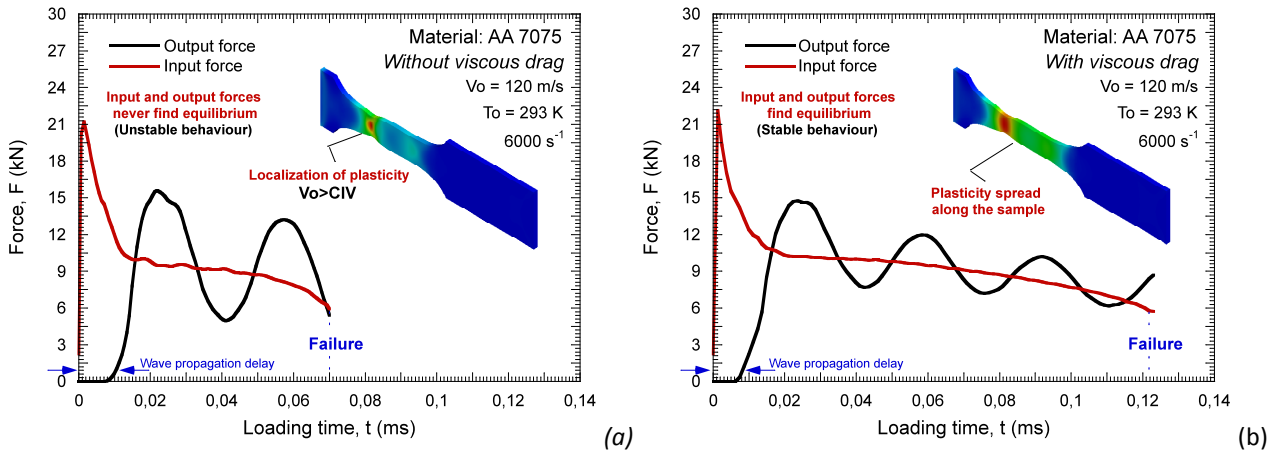

Fig. 3-17. Output and input forces for original and Extended RK models, V_0 = 120 m/s.

Moreover, as it has been previously explained *(See Chapter 3.2.1)*, an analytical solution for the **CIV** can be obtained [Taylor 1958, Klepaczko 2005], Eq. 3-4'.

$$\mathrm{CIV} = \int_0^{\varepsilon_e} C_e \, d\varepsilon + \int_{\varepsilon}^{\varepsilon_{pm}} C_p\left(\bar{\varepsilon}_p, \dot{\bar{\varepsilon}}_p, T\left(\bar{\varepsilon}_p\right)\right) d\bar{\varepsilon}_p \qquad \textit{Eq. 3-4'}$$

An interesting conclusion can be obtained from previous formulation; the **CIV** is only dependent on elastic and plastic wave propagation. Therefore, if the addition of the viscous drag term influences the **CIV** value, the addition of the viscous drag term influences the material strain hardening *(plastic wave speed)* in the necking zone. Since for an imposed

strain rate value the strain hardening is not affected by the viscous drag *(as previously demonstrated)*, then in the necking zone the strain rate level must be different for original and *Extended RK* models.

Previous expectations are confirmed in Fig. 3-18-a where the evolution of strain rate in the necking is depicted as a function of the strain for original and *Extended RK* models. If the dislocations drag term is not applied the strain rate is clearly larger and the material reaches early instability. Increasing rate sensitivity reduces the strain rate level in the necking spreading plasticity along the specimen. In addition, relevant differences are observed in the stress level taking place in the necking, Fig. 3-18-b.

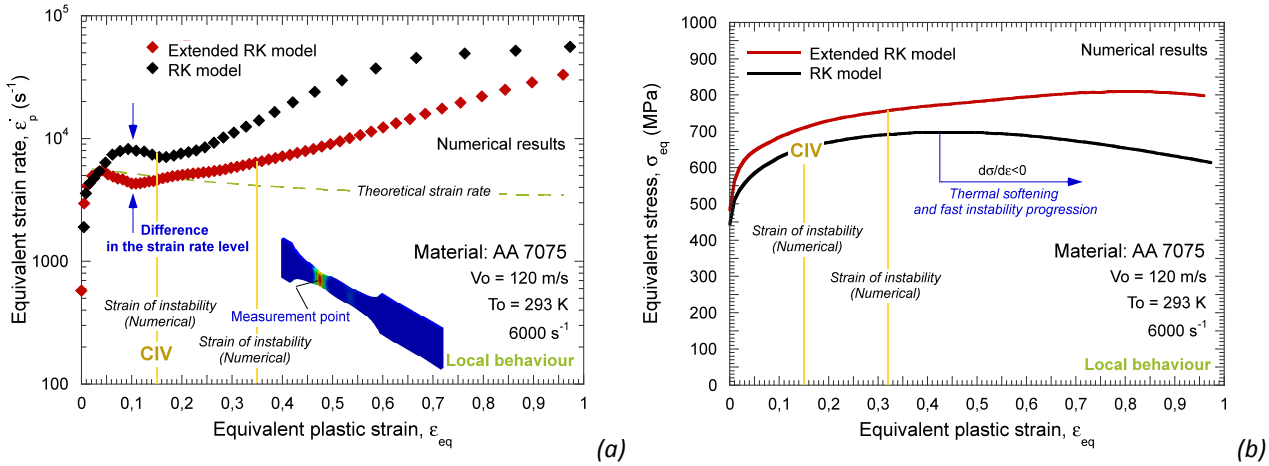

Fig. 3-18. Evolution (a) of strain rate and (b) of stress versus plastic deformation in the necking zone for original and Extended RK models, Vo=120 m/s.

Thus, in the necking, the strain hardening is modified by the application of the viscous drag term, Fig. 3-19. The celerity of the plastic waves is affected. This behaviour is responsible of the **CIV** variation between original and *Extended RK* models.

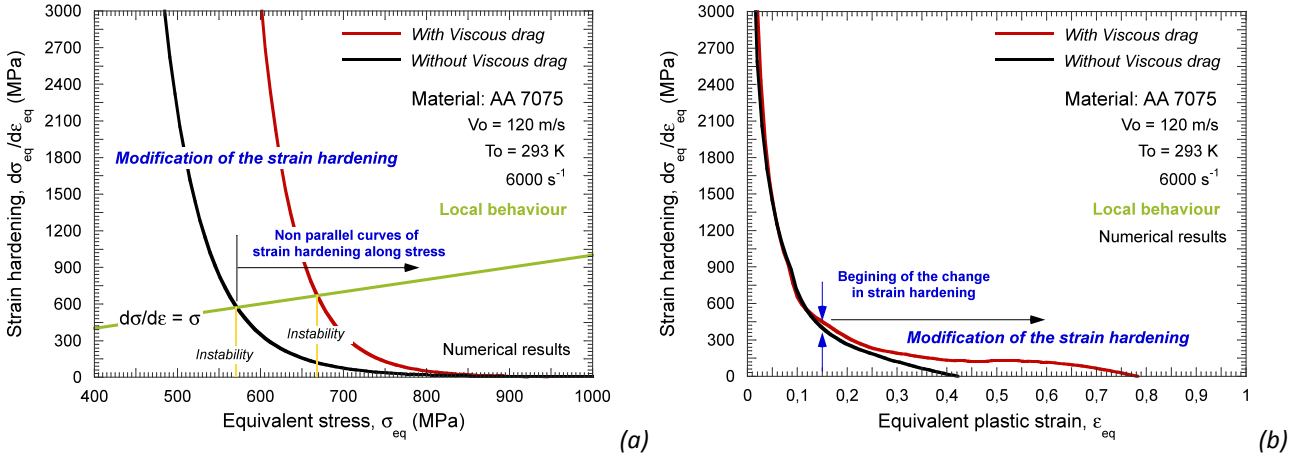

Fig. 3-19. Strain hardening evolution versus (a) flow stress plastic strain and versus (b) plastic strain for original and Extended RK models, V_0 = 120 m/s.

But not only the local behaviour of the material is affected by the viscous drag stress term, the specimen elongation is strongly influenced too, Fig. 3-20. In this figure, Fig. 3-20, plastic strain contours of the active part of the specimen for three different velocities and

both models *(original and Extended RK)* are shown once the plastic strain value of $\bar{\varepsilon}^{p} = 1$ is reached in the specimen *(remember that the failure criteria used has been the selection of a constant critical value for the strain –See Chapter 3.2-)*. This view of the specimens shows how the addition of the viscous-drag component tends to spread the plasticity through the active part of the sample. For the original *RK* formulation, the necking is much more localized than in case of using the *Extended RK* formulation, Fig. 3-20. Furthermore, the lengths of the active parts when this strain value *($\bar{\varepsilon}^{p} = 1$)* takes place are higher in case of using the *Extended RK* constitutive relation *(obviously, the time is different for each case)*. This is in agreement with the fact that the viscous-drag component tends to stabilize the material. Then, the predicted ductility of the material increases.

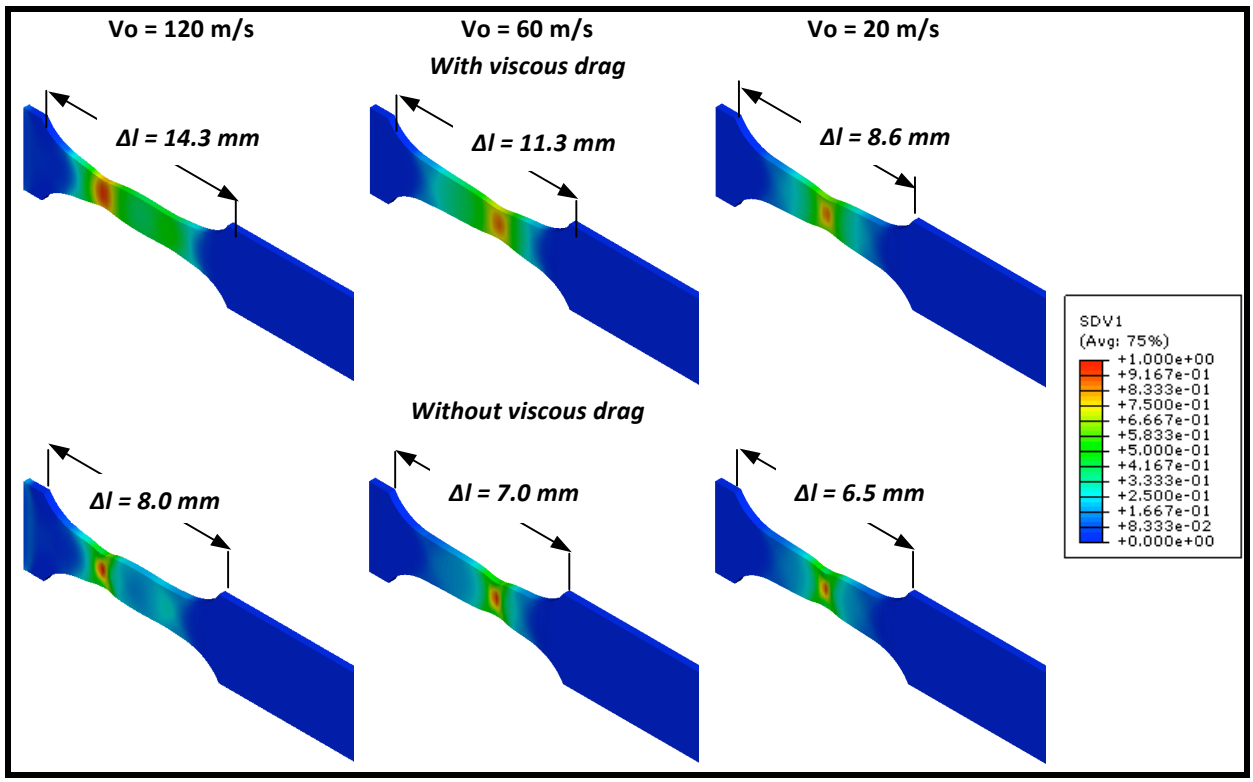

Fig. 3-20. Deformation contours of the specimen once the strain of instability appears for original and Extended RK models at different impact velocities.

In the next plots, Fig. 3-22, the transversal displacements of the points placed in the upper surface of the active part of the specimen are showed, Fig. 3-21.

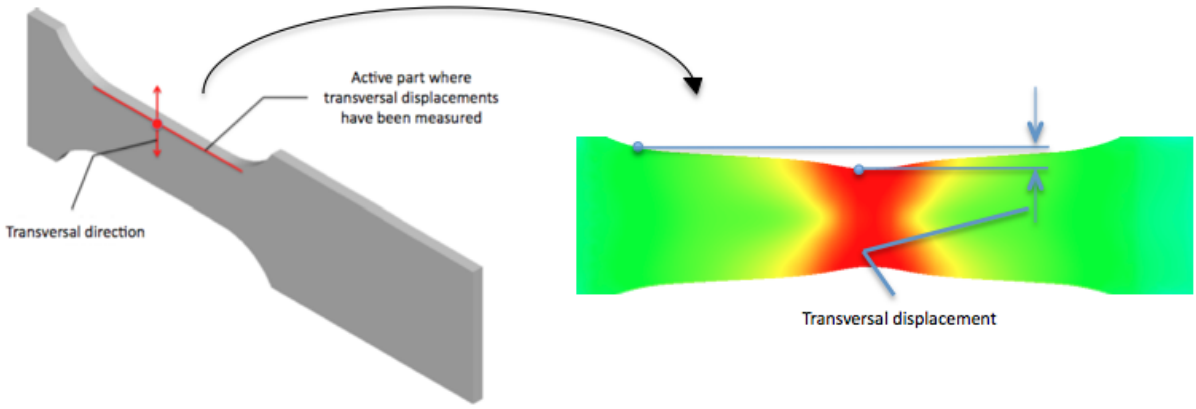

Fig. 3-21. Points and direction of measurement.

These displacements are higher for the case of using the *Extended RK* constitutive relation because of the increasing strain rate sensitivity, confirming the increase in the ductility of the material. The differences between both models are higher as impact velocity increases due to the increase in the strain rate of the sample, Fig. 3-22-a. Moreover, the place where necking appears is hardly influenced by the phonon drag stress term, Fig. 3-22. In addition, plasticity gradients are higher in the zones where necking takes place as it was expected.

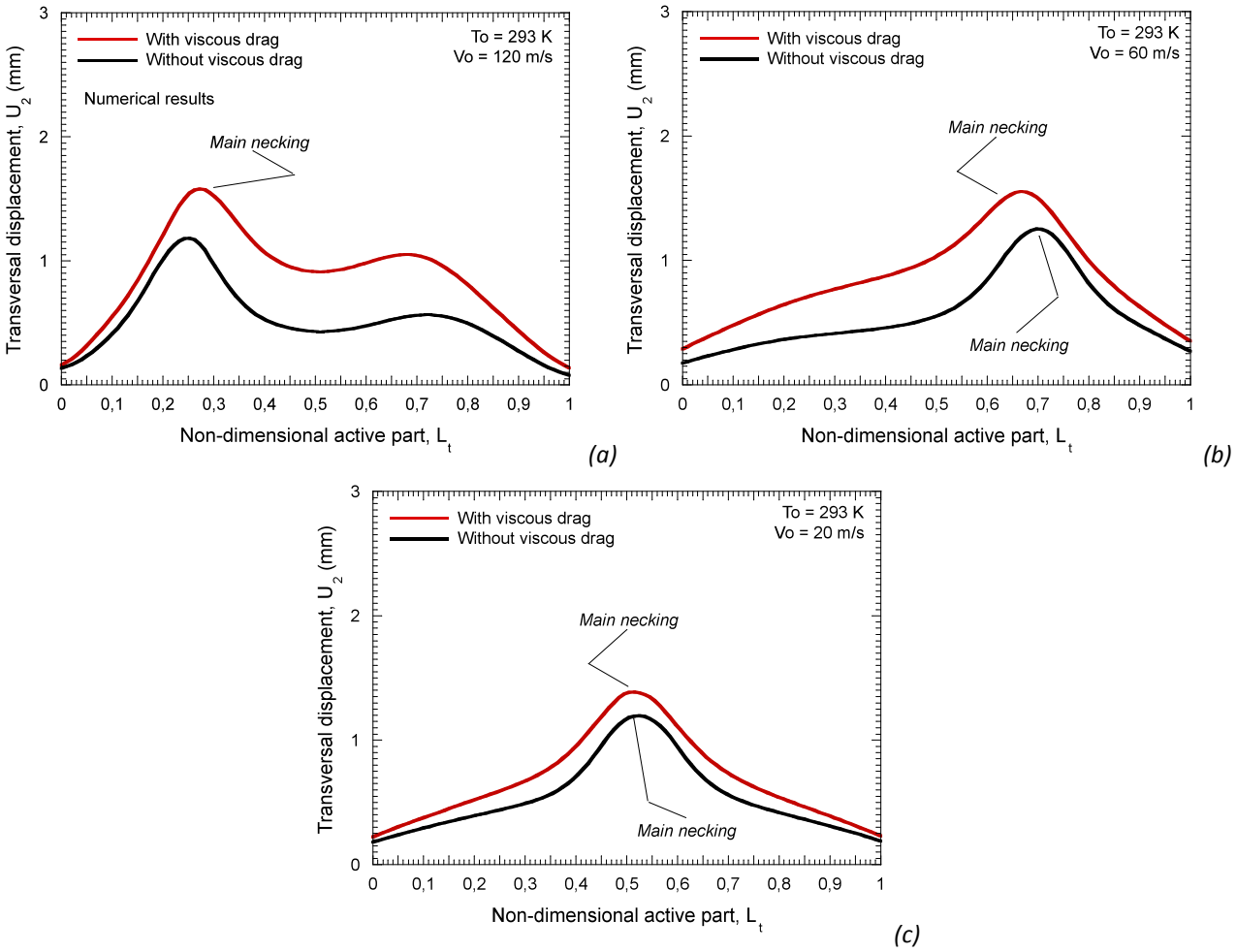

Fig. 3-22. Transversal displacement in the active part of the specimen for three different velocities using original and Extended RK models. (a) 120 m/s, (b) 60 m/s and (c) 20 m/s.

During homogeneous deformation the material strain hardening is not appreciably affected by the viscous drag application, Fig. 3-23. Out of the instability the deformation rate is the same for original and *Extended RK* models, Fig. 3-23. The wave propagation is not altered, neither the necking position. Only in the necking the application of the viscous drag term causes substantial differences in the deformation rate level, Fig. 3-23.

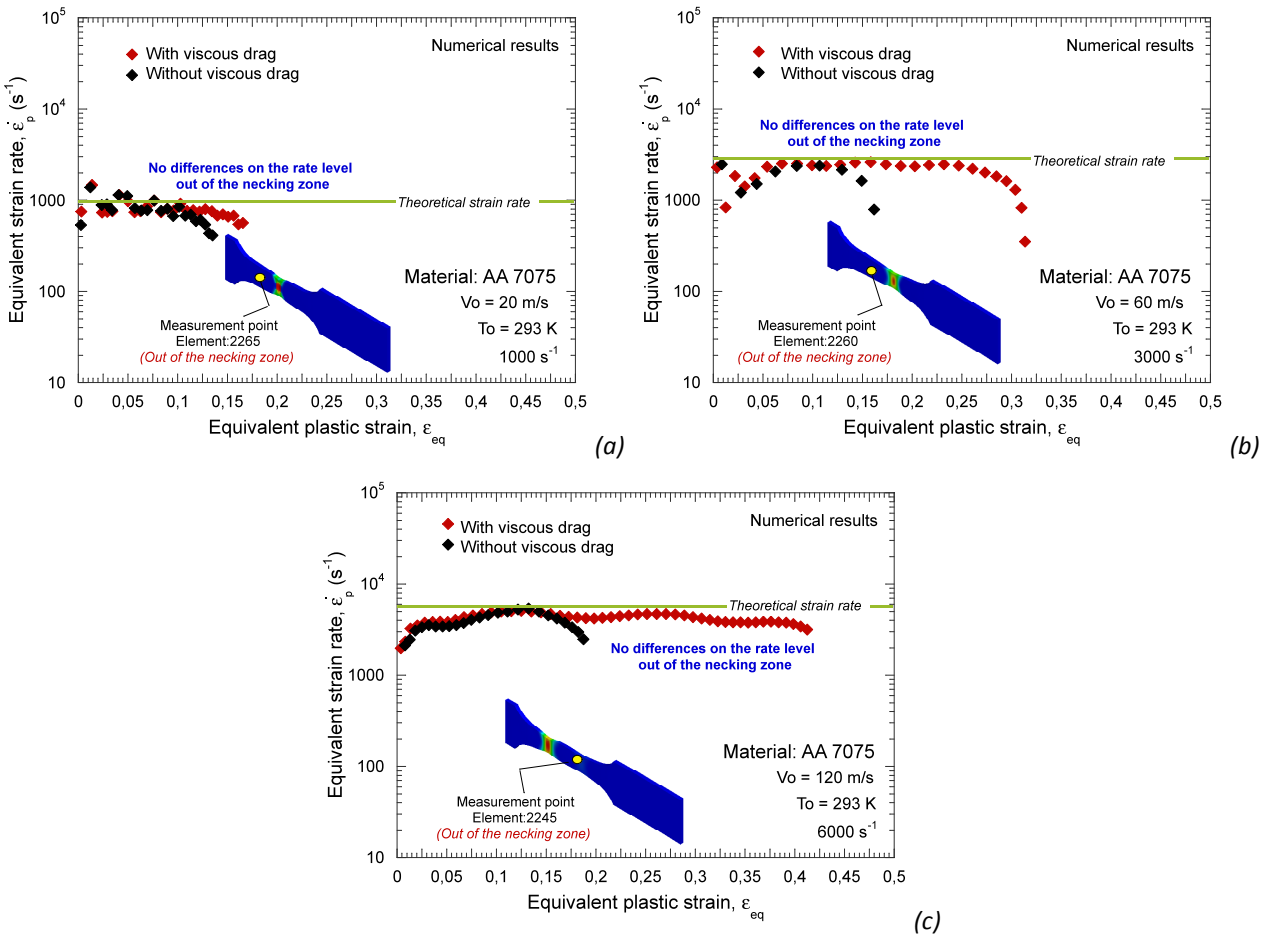

Fig. 3-23. Evolution of strain rate versus plastic deformation out of the necking zone for original and Extended RK models. (a) V_0=120 m/s, (b) V_0=60 m/s, (c) V_0=20 m/s.

When describing the constitutive behaviour of metallic alloys at high strain rates the dislocations drag phenomenon plays a fundamental role. A proper description of the rate sensitivity of **AA 7075** is indispensable in order to evaluate its suitability for constructing structures in charge of absorbing energy under dynamic solicitations. From an overview of the considerations reported in this section of the project can be concluded that the rate sensitivity of metals determines their ductility by homogenizing their behaviour under high loading rates.

In order to go further in this investigation, a parametric study on the influence of viscous drag formulation parameters on the material response when it is subjected to dynamic tension is conducted.

3.4.3 Influence of viscous drag formulation parameters on flow localization

To understand better the behaviour of the viscous-drag term and its relevance in the general behaviour of the material, a parametric study was carried out. Four different values for each one of the viscous-drag parameters were chosen. The parametric study has been developed choosing the values showed in Table 3-5 for each one of the material constants. The values in shady boxes are approximately the standard ones used for the **AA 7075**, Table 3-3, *(when varying one parameter the other one will take the value in bold)*.

χ (MPa)				α (-)			
100	200	**300**	400	0.00001	**0.00005**	0.0001	0.0005

Table 3-5. Value of the parameters present in the viscous-drag component

3.4.3.1 Influence of parameter χ

First of all, the influence of the parameter χ is studied. In Fig. 3-24-a is shown the value of the viscous-drag term as a function of the strain rate for the four different values of χ used. The increase of χ elevates the flow stress of the material but also the rate sensitivity provided by the dislocations drag component, Fig. 3-24-a. In Fig. 3-24-b is depicted the first derivate of the viscous-drag component with respect to the strain rate for the four different values of χ studied. It is important to notice that the maximum rate sensitivity *(maximum slope in* Fig. 3-24-*a)* corresponds to the same strain rate level for every value of χ considered. The parameter χ does not affect the point at which viscous-drag term starts to contribute, the strain rate at which the maximum rate of the viscous-drag term is reached *(plateau regime)* or the evolution of the slope with the strain rate, Fig. 3-24-a-b.

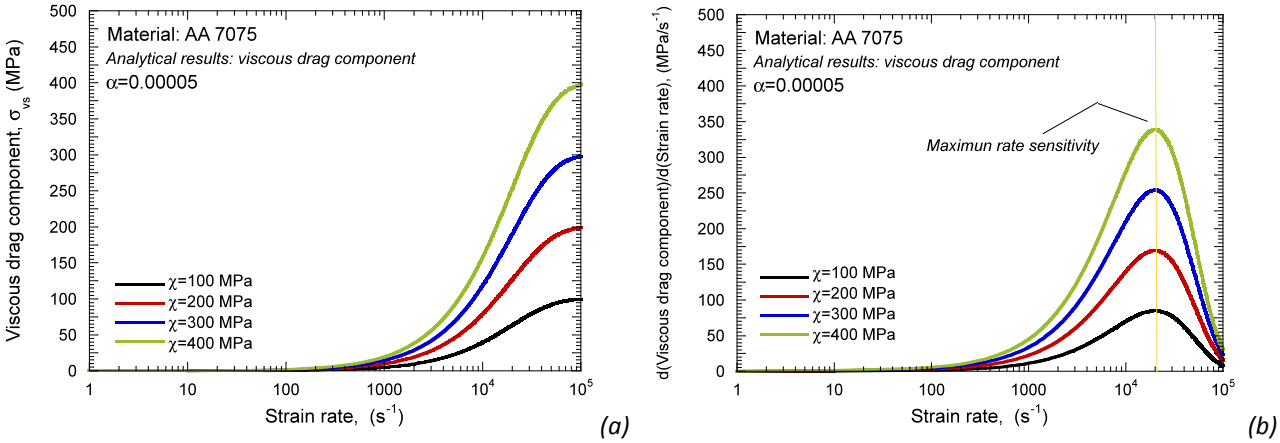

Fig. 3-24. (a) Viscous-drag component as a function of the strain rate. (b) First derivate of the viscous-drag component respect to the strain rate as a function of the strain rate.

As it has been discussed, the higher is the strain rate, the higher is the stress level due to the viscous-drag component for all possible values of the parameter χ. This is clearly seen in Fig. 3-25-a-b. Due to the high strain rates of both cases (1000 s^{-1} and 6000 s^{-1}) the importance of the viscous-drag term is notable. While the analytical predictions of the model at a strain rate of 1000 s^{-1} are similar both for χ = 400 MPa and χ = 100 MPa, the difference between both cases becomes essential at higher strain rates (for example at 6000 s^{-1}, Fig. 3-25-b). Nevertheless, the temperature increase caused by the augment on the flow stress with χ does not affect in a relevant way the material strain hardening *(plastic waves speed)*, Fig. 3-25-c-d. This observation has particular relevance since an important decrease of strain hardening may annihilate the expected beneficial effect on ductility caused by the rate sensitivity increase [Rodríguez-Martínez et al. 2009]. Again, a qualitative estimation of the plastic instabilities formation is obtained using the Considere's criterion, Fig. 3-25-c-d.

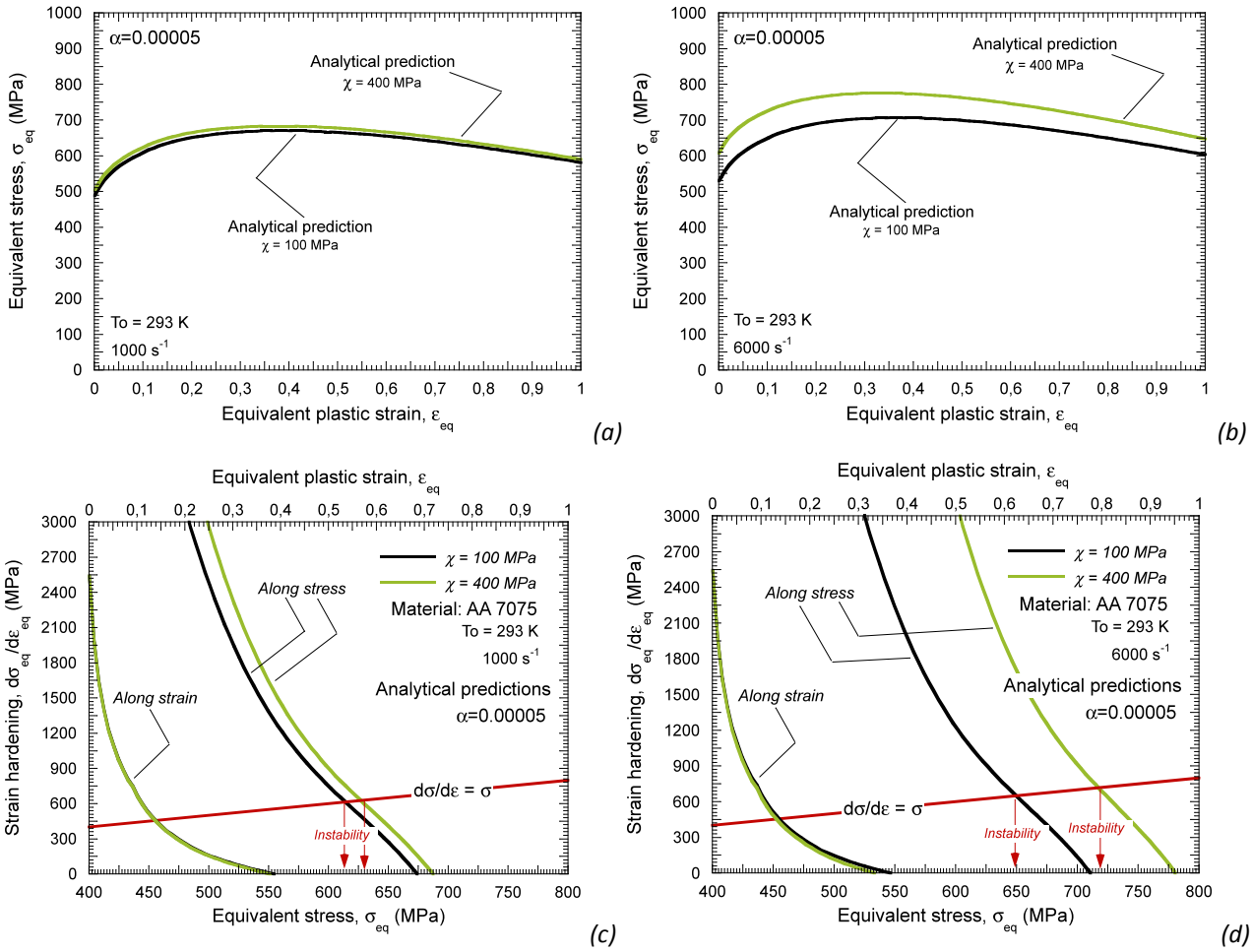

Fig. 3-25. (a)-(b) Flow stress evolution versus plastic strain for two values of the parameter χ. (c)-(d) Strain hardening evolution versus plastic strain and versus stress for two values of the parameter χ.

In order to study the influence of the parameter χ in the plastic instabilities formation of the material, the methodology based on the comparison between local and global plastic strain was again used. As it could be seen, for the three different velocities the plastic instability of the materials slightly depends on the value of the parameter χ.

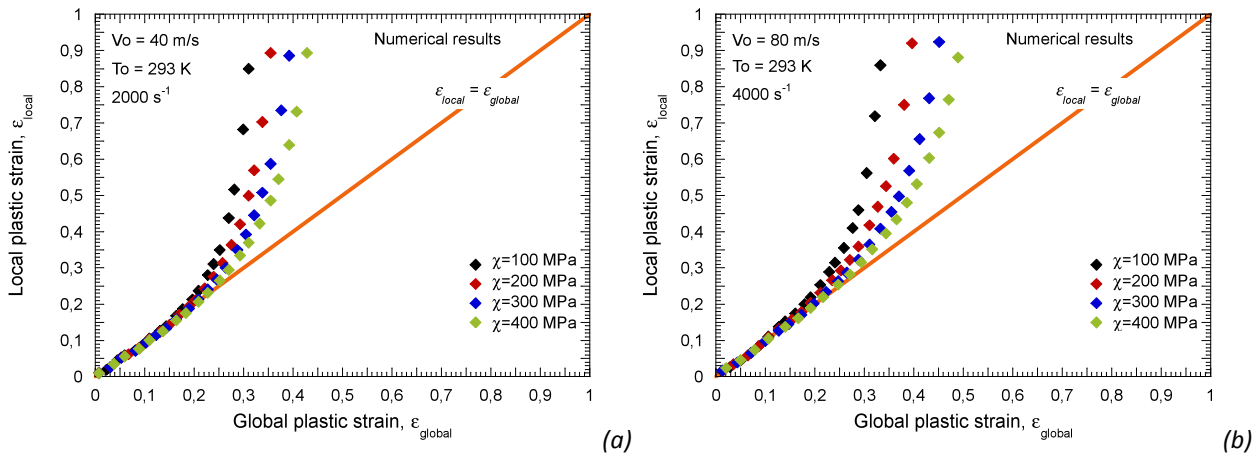

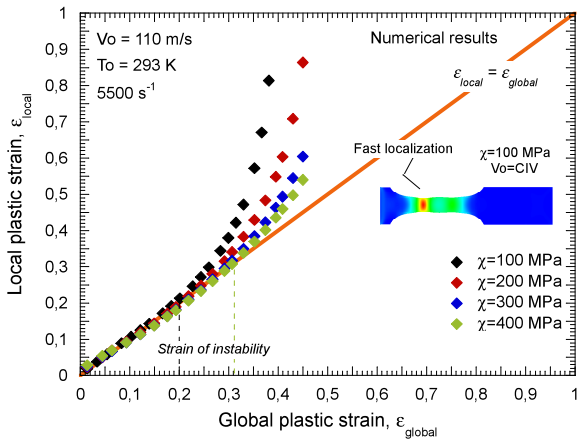

Fig. 3-26. Local plastic strain respect to the global plastic for different values of the parameter χ. (a) Vo=40 m/s, (b) Vo=80 m/s, (c) Vo=110 m/s.

In Fig. 3-27 is plotted the strain of instability respect to the impact velocity for the four different values of χ studied. The **CIV** value is also affected by the value of χ used, Fig. 3-27. In the necking zone the viscous drag term determines the strain rate level, affecting the plastic wave propagation.

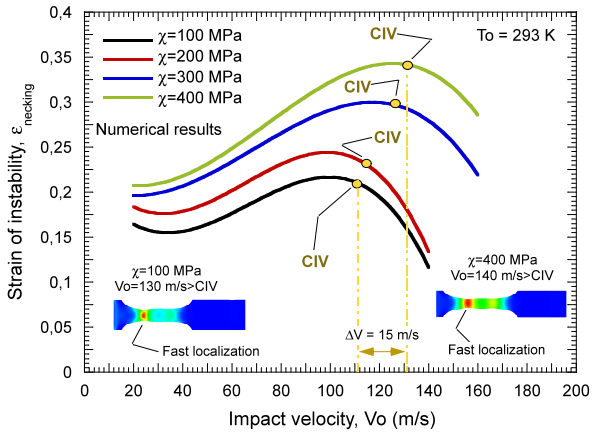

Fig. 3-27. Strain of instability respect to impact velocity for the four different values of χ.

Next, a macroscopic view of the effect of the viscous-drag component for the extreme values of the parameter χ (100 and 400 MPa) is shown, Fig. 3-28. As χ increases the plasticity is more spread along the active part of the specimen, Fig. 3-28. Notice that the length for the case of χ=400 MPa is higher than for χ=100 MPa. This is, higher values of the parameter χ tend to delay the strain localization process. The material augments its capability of absorbing energy.

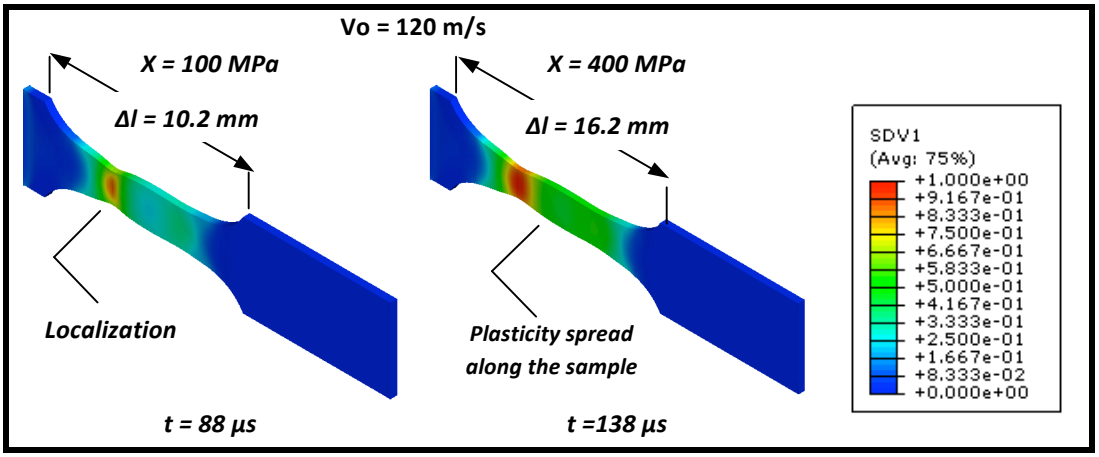

Fig. 3-28. Macroscopic view of the effect of the parameter χ in the specimen, V_0=120 m/s.

Next, the transversal displacements in the active part of the specimen are shown for two different impact velocities and the two extreme values of χ, Fig. 3-29. For the case of χ=400 MPa, the transversal displacements are higher for all impact velocities (this is the plasticity is more spread). Thus, stronger plasticity gradients are observed close to the necking zones as the value of χ decreases, Fig. 3-29. However, the place where necking appears is not modified by the viscous drag application. The rate level out of the necking is not conditioned by the viscous drag term; this is the plastic wave celerity is not modified.

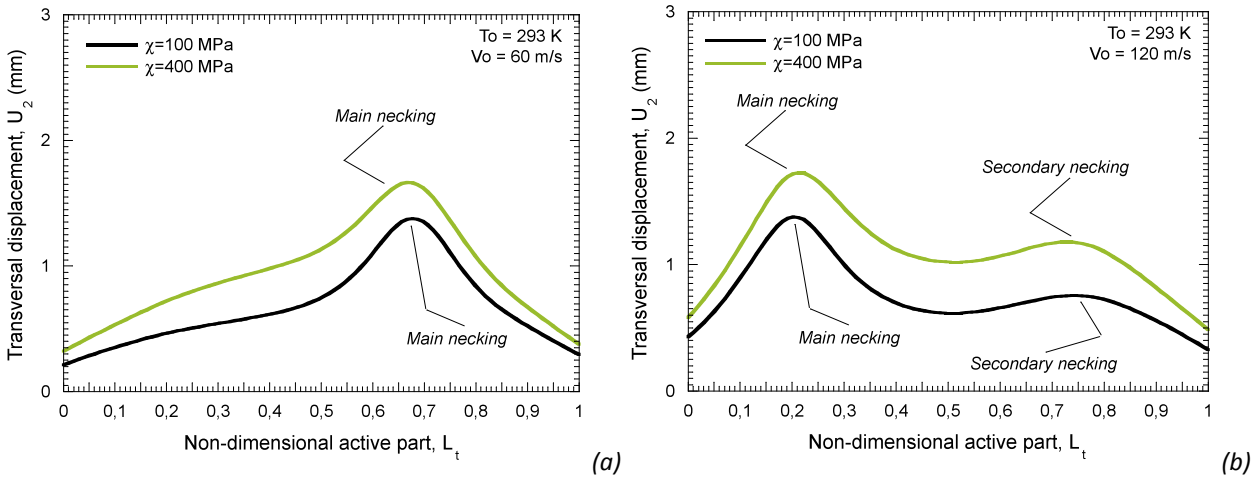

Fig. 3-29. Transversal displacements of the active part of the specimen for two different values of the parameter χ and two different impact velocities. (a) V_0 =60 m/s, (b) V_0 =120 m/s.

The greater effect of the parameter χ is the change in the strain rate sensitivity of the material *(the strain rate sensitivity due to the internal stress could be considered negligible in comparison with the one for the viscous-drag term)*. Moreover, higher values of χ increase the value of the viscous-drag stress component at high strain rates.

According with the calibration method described in [Rusinek and Rodríguez-Martínez 2009], the value of the parameter χ for a certain material comes from the value the viscous-drag term has for a particular strain rate.

3.4.3.2 Influence of parameter α

Four different values of α were taken covering the typical range reported for these constants [Nemat-Nasser et al. 2001, Rusinek and Rodríguez-Martínez 2009]. In Fig. 3-30-a is shown the evolution of the viscous-drag stress versus the strain rate for different values of α. In this case, the variation of this parameter does not shift the curve up and down but in the horizontal direction. The slope of the rate sensitivity remains constant but shifted with strain rate, Fig. 3-30. Higher values of the parameter α tend to move backward the $\dot{\bar{\varepsilon}}^{p}_{trans-drag}$, increasing the importance of the viscous-drag term at lower strain rates. Then, for a certain strain rate value *(within the value at which viscous drag starts to contribute and the strain rate at which the plateau regime is reached)* the higher is the parameter α, the higher is the strain rate sensitivity in the material. Then, the strain of instability of the material will be higher due to its higher strain rate sensitivity. Furthermore, not only the starting point where dislocations drag takes place is moved backward but also the strain rate at which the viscous-drag component reaches its maximum (*the plateau regime where no longer rate sensitivity is induced by the viscous drag term*). In Fig. 3-30-b is shown the first derivative of the viscous-drag stress component respect to the strain rate for the four cases. It is checked that the maximum rate sensitivity is shifted with strain rate, Fig. 3-30-b.

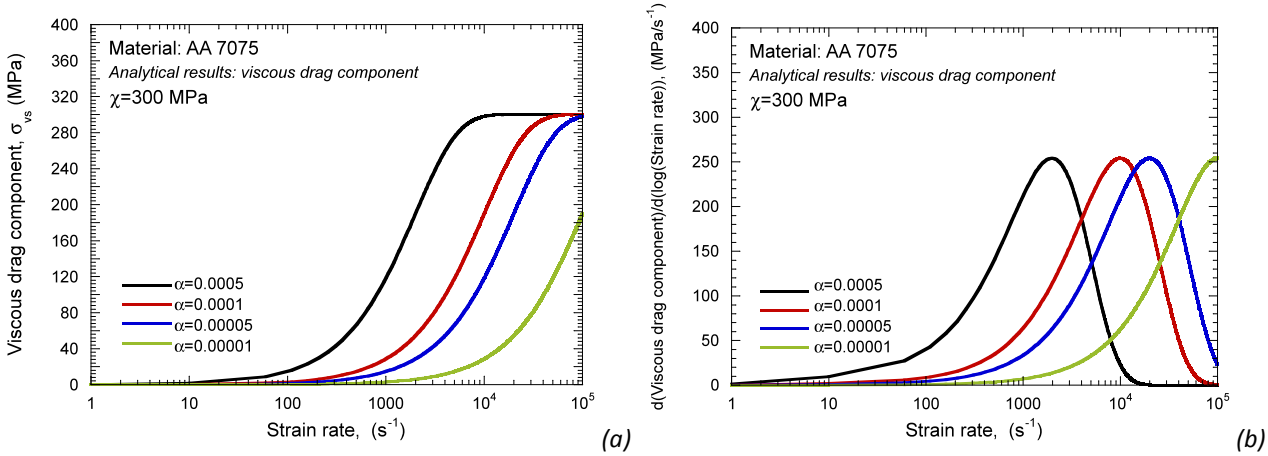

Fig. 3-30. (a) Viscous-drag stress component as a function of the strain rate for different values of α. (b) First derivate of the viscous-drag stress component respect to the strain rate for the same values of α.

In Fig. 3-31-a-b is depicted the flow stress evolution as a function of the plastic strain for two values of α and different strain rate levels. Although the variations of α conducted certainly modify the material flow stress level, its strain hardening *(plastic waves speed)* remains approximately invariable for the whole range of strain rates considered, Fig. 3-31-c-d. So, eventual differences in the adiabatic temperature increase due to variations of α will not change the analysis conducted subsequently.

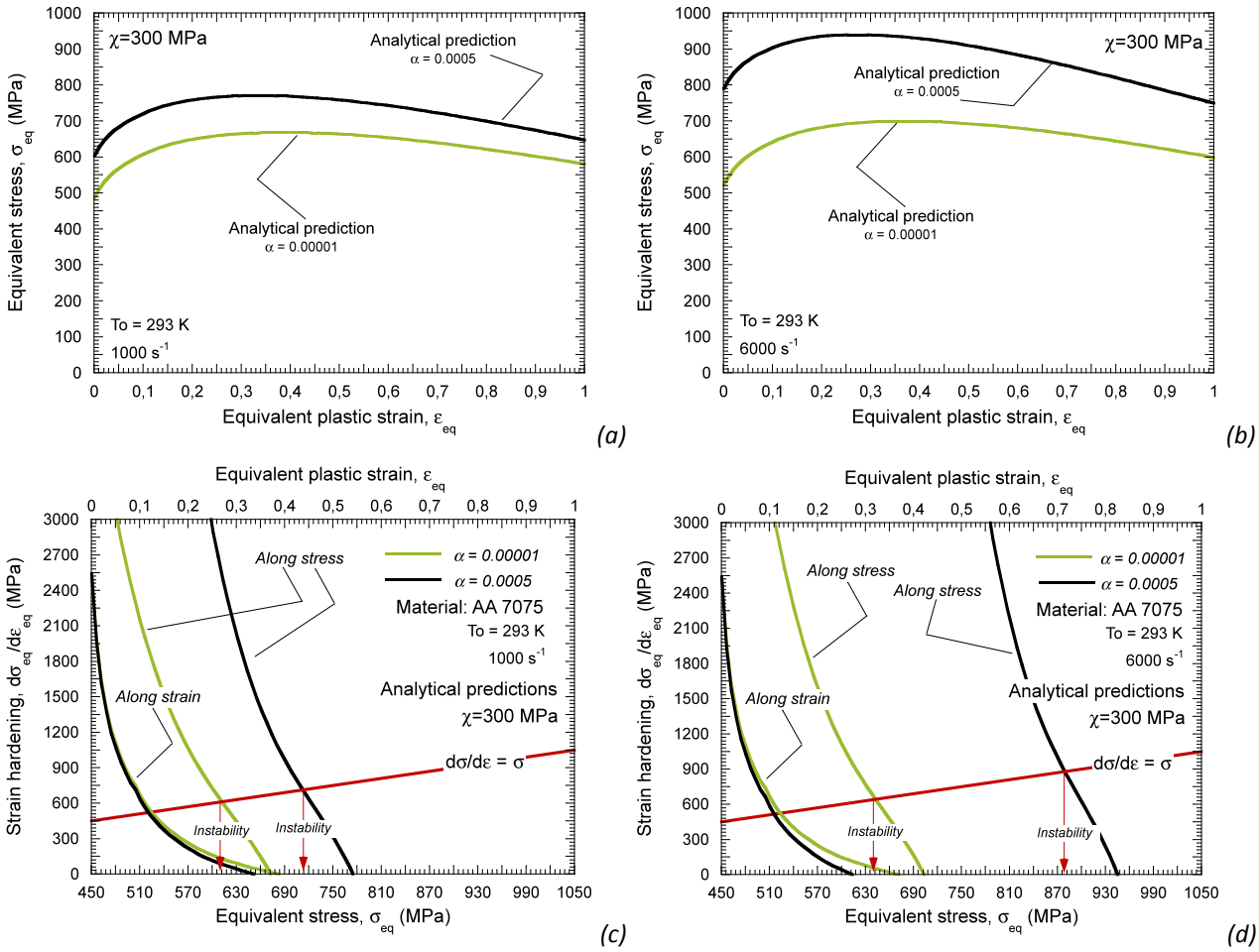

Fig. 3-31. (a)-(b) Flow stress evolution versus plastic strain for different values of α. (c)-(d) Strain hardening evolution versus plastic strain and versus stress for different values of α.

Next, it is analyzed the evolution of the local plastic strain *(in the necking)* with the global plastic strain *(of the whole specimen)* for all the values of α considered and different impact velocities. In the case of V_0 = 60 m/s, Fig. 3-32-a, as the value of α increases, the strain of instability value also does it *(in the case of α=0.00001 the viscous drag term is not even operative)*. However, different trend concerning the strain of instability evolution with α is observed for V_0 = 100 m/s, Fig. 3-32-b. In this case, the largest value of α does not match with the most stabilized material. Such behaviour is repeated for larger impact velocities, Fig. 3-32-c-d. This observation is of main interest. It occurs because the strain rate level for α=0.0005 *(homogeneous strain rate level)* is close to the starting point of the plateau regime of the viscous drag component, Fig. 3-32. Then, the rate sensitivity of the material only corresponds with the thermally activated mechanisms *(thermal stress component)* because of the strain rate applied to the sample has reached the one corresponding to the plateau regime, Fig. 3-30-a. In our particular case, that rate sensitivity is quite reduced *(before the viscous drag regime, most **FCC** metals show reduce rate sensitivity [Rusinek et al. 2009-a, Rusinek and Rodríguez-Martínez 2009])* and the material becomes prone to instabilities formation. The physical interpretation of such phenomenon is that the dislocations velocity is close to the limiting value given by the elastic shear wave propagation; the relativistic effects have already taken place.

Opposite behaviour is observed when the lowest value of α is applied to the viscous drag term. In this case, since the increase of rate sensitivity caused by the viscous drag term is considerably delayed, Fig. 3-32, the **CIV** of the material is reached before the drag regime played a relevant role. Then, and due to the particularities of the configuration analyzed in this work *(wave propagation affecting the strain localization)* the material does not get the benefits of the increasing strain rate provided by the viscous drag effect.

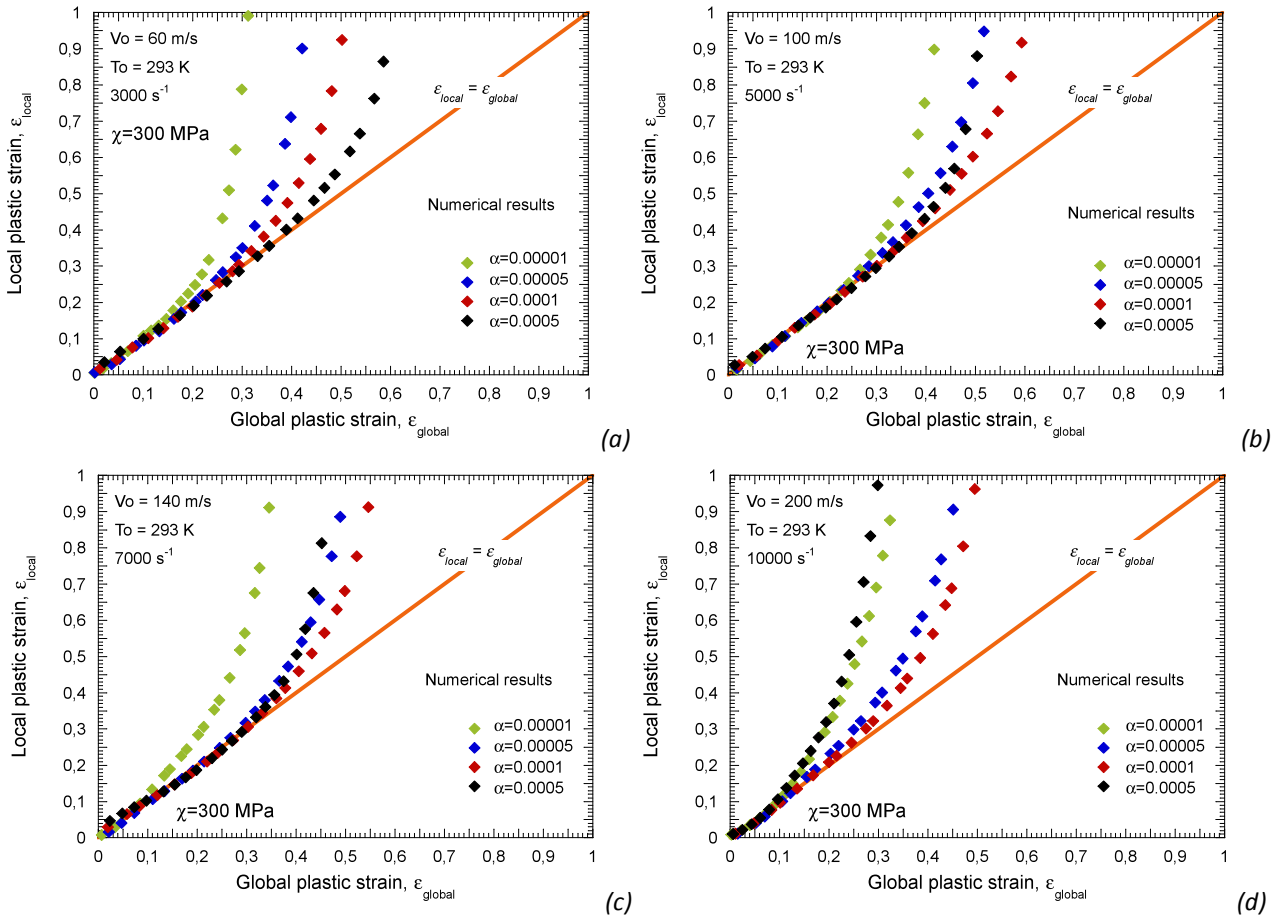

Fig. 3-32. Evolution of local plastic strain versus global plastic strain for different values of α. (a) Vo=60 m/s, (b) Vo=100 m/s, (c) Vo=140 m/s, (d) Vo=200 m/s.

New simulations have been performed in order to confirm that definitely previous conclusions related to the parameter α in the behaviour of the material are not caused due to different thermal softening in the material related to the different value of the viscous-drag stress term. In Fig. 3-33 are represented the results of three simulations in which isothermal conditions have been forced. This is achieved considering the value of the Taylor-Quinney coefficient equal to zero *($\beta = 0$)*. As it could be seen, Fig. 3-33, the material behaves similarly as depicted for adiabatic conditions, Fig. 3-32. Then, it is checked from the numerical results that the thermal softening of the material does not interfere considerably in the dependence of the strain of instability with the value of α.

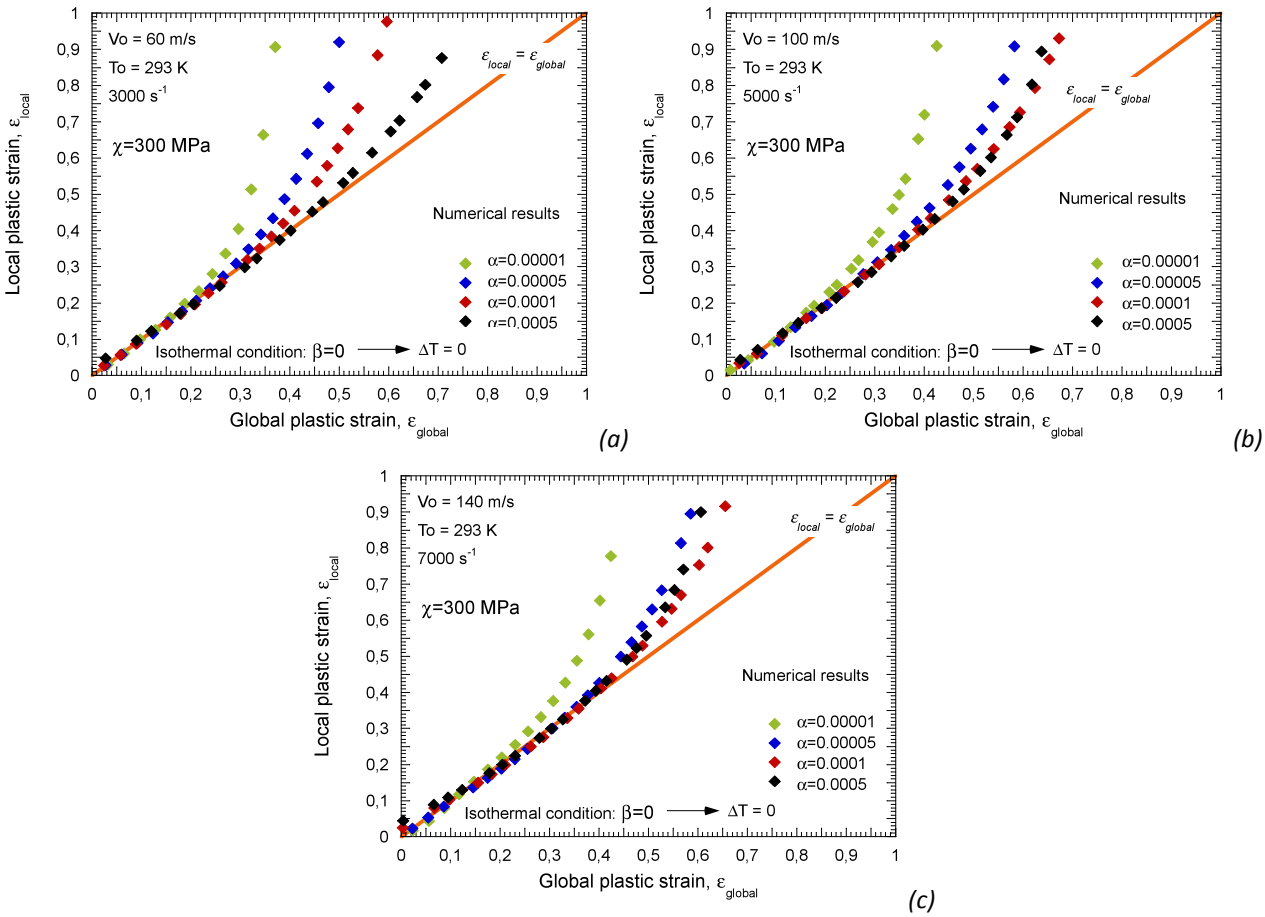

Fig. 3-33. Local plastic strain versus global plastic strain under isothermal conditions. (a) V_0=60 m/s, (b) V_0=100 m/s and (c) 140 m/s.

In Fig. 3-34 is plotted the relation between the strain of instability and the impact velocity for the four different values of α studied. It must be noticed that beyond a certain value of impact velocity, intermediate values of α are more effective in order to stabilize the material behaviour, Fig. 3-34. This fact is an important particularity of the tension test. For any other configuration free of waves disturbances *(and therefore free of **CIV** appearance)* [Hu and Daehn 1996, Mercier and Molinari 2004, Rusinek and Zaera 2007] no matter which value of α will be introduced into the viscous drag formulation, the strain of instability will suffer a decrease with increasing strain rate when the maximum rate sensitivity of the viscous drag component will be exceeded. In our particular case, for the intermediate values of α, the **CIV** phenomenon occurs before the maximum rate sensitivity of the material has been reached.

Moreover, achieving the **CIV** in the case of the largest value of α does not involve the reduction of the strain of instability reported in Fig. 3-34. Such reduction started for smaller values of impact velocity due to a sudden decrease of the material rate sensitivity *(maximum rate sensitivity is exceed)*. Variations on the **CIV** value depending on the value of α are reported. In the necking zone, the viscous drag term affects the plastic wave propagation.

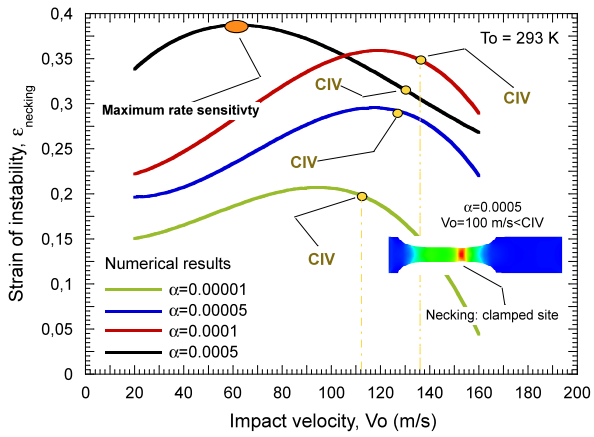

Fig. 3-34. Strain of instability evolution as a function of impact velocity for different values of α.

In Fig. 3-35, maps of plastic deformation in the specimens are shown. For an impact velocity low enough *(V_0=60 m/s)* the length of the active part of the specimen when the defined limit value for plastic strain *($\bar{\varepsilon}^p = 1$)* appears increases with the value of α, Fig. 3-35. For a higher velocity (V_0=140 m/s) the trend is exactly the same except for the highest value of α. In this case, both the length of the active part of the specimen and the time at which instability takes place are lower, Fig. 3-35. This is because of at this impact velocity the viscous-drag stress term has reached the *plateau regime*, Fig. 3-30. Thus, the strain rate sensitivity of the material is negligible and the plastic instability appears at a lower local plastic strain. Smallest elongation always corresponds to the lowest α value because of early **CIV** achieving, as previously discussed.

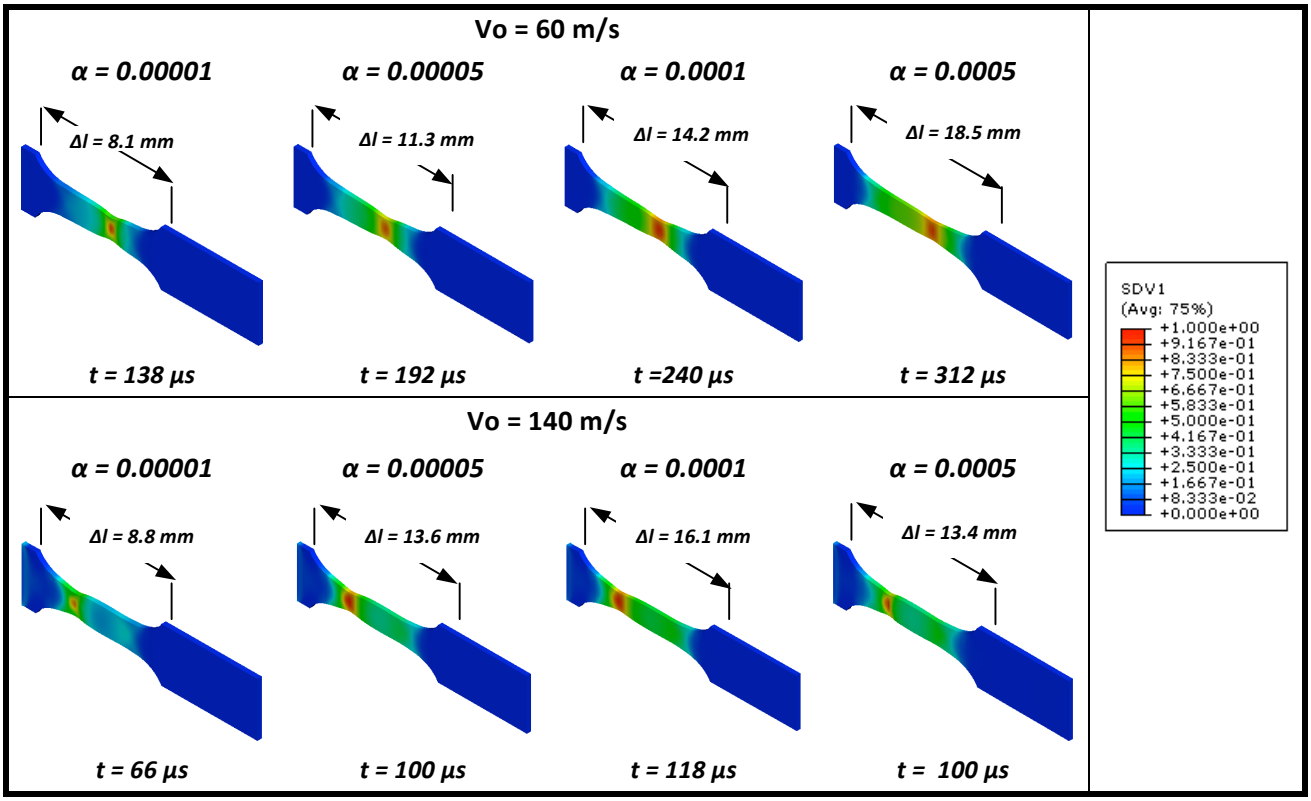

Fig. 3-35. Deformation maps in the specimens once the strain of instability appears for two velocities and the four different values of α.

In Fig. 3-36-a-b are plotted the transversal displacements of the points in the active part of the specimen. As it could be seen, the position of the necking does not depend on the value of α. The most uniform distribution of plastic strain along the active part of the specimen does not follow the increasing order of α value for the whole range of impact velocities analyzed.

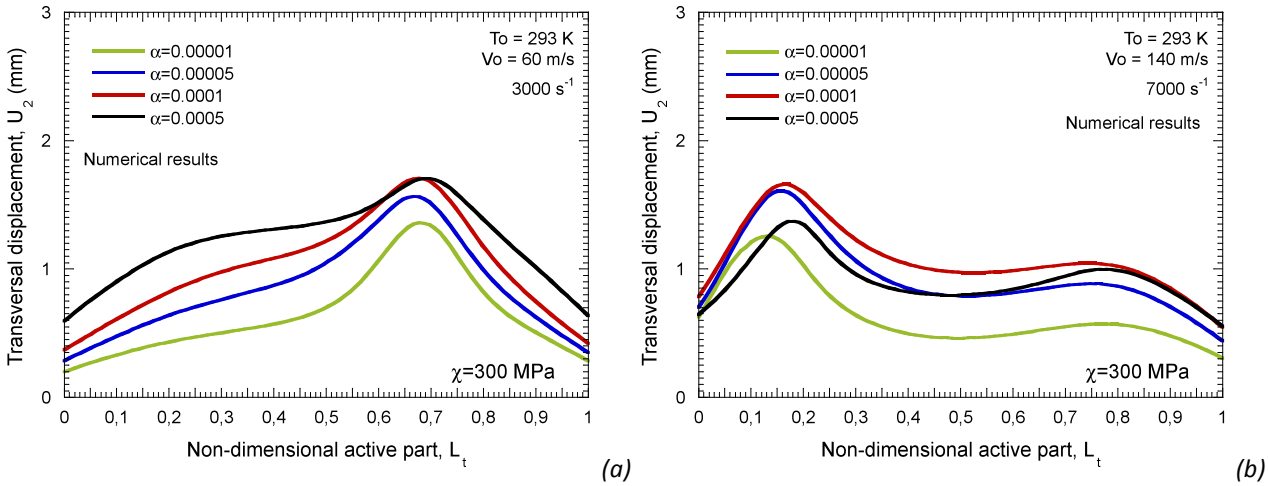

Fig. 3-36. Vertical displacements of the active part of the specimen for different values of α. (a) 60 m/s and (b) 140 m/s.

Then, vertical displacements are strongly dependent on impact velocity because of the formulation used to define the viscous drag term. As previously discussed, the strongest plasticity gradients are around the necking zone, Fig. 3-36.

In this chapter has been examined the influence of rate sensitivity on plastic instabilities formation under dynamic loading.

For that task, numerical simulations of dynamic tension test have been carried out. The material definition is conducted by application of the original Rusinek-Klepaczko (RK) and the Extended Rusinek-Klepaczko (Extended RK) model to viscous drag effects [Rusinek and Rodriguez-Martinez 2009]. A complete parametric study of the material constants involved in the viscous drag formulation is carried out.

In the case of metallic alloys used to build structural elements potentially subjected to fast loading during their service condition an accurate knowledge of their strain rate sensitivity is required, especially at high strain rates. It has been proven that the viscous drag regime, which is commonly neglected in constitutive modeling, determines the ductility of the material, retarding flow localization. The stabilizing effect of the increasing rate sensitivity acts an inductor for plasticity spreading during material loading. Viscous drag regime plays a fundamental role on the capability of metals for absorbing energy during crash or impacts. Finally, it has been found that maximum rate sensitivity corresponds with the maximum capability of a material for absorbing energy.

CHAPTER 4

INFLUENCE OF THE STRAIN HARDENING ON FLOW LOCALIZATION

ABSTRACT

Under determined loading conditions metallic alloys may exhibit a strong increase of strain hardening. In this chapter, the influence of strain hardening on flow localization is studied. For this purpose, an extension of the *RK* constitutive relation is used. This extension is able to predict the increase of the strain hardening in metallic alloys under certain loading conditions. This issue is developed by application of the ring expansion test configuration to the austenitic steel **301Ln2B** using ABAQUS/Explicit. This study is completed with a parametric analysis to check the effect each one of the parameters which define the increase in the strain hardening has on the flow localization of the material.

4 INFLUENCE OF THE STRAIN HARDENING ON THE FLOW LOCALIZATION

4.1 Introduction

Because of their excellent mechanical properties in terms of high hardening rate, large ductility and toughness, austenitic steels are quite used in many engineering fields, like naval structures or civil protections [Lebedev and Kosarchuk 2000, Nemat-Nasser et al. 2001, Larour et al. 2007]. Under well-defined conditions in term of stress, strain, strain rate and temperature, these steels reveal phase transformation from austenite to martensite, which induces an *extra strain hardening* in the material, Fig. 4-1-a. Nowadays there is a great industrial interest in the process known as TRIP (Transformation Induced by Plasticity). This is produced when phase transformation is induced by plastic deformation. This transformation phenomenon is desirable during loading since it increases the strength and the ductility of the material retarding plastic localization [Fischer et al. 2000, Crutze et al. 2009]. Because of that, *austenitic* steels are frequently applied to built structural elements responsible of absorbing energy during crash or impact. The structural relevance of austenitic steels components leads to the necessity of developing practical constitutive models allowing for a feasible use in the current industry, introducing them into **FE** codes with an accurate definition of the geometry and boundary conditions of the model.

In addition, in the case of metals having **FCC** and **HCP** crystal lattices twinning deformation mode usually takes place at high deformation rates. Crystal twinning occurs when two separate crystals share some of the same crystal lattice points in a symmetrical manner. The result is an intergrowth of two separate crystals in a variety of specific configurations. A twin boundary or composition surface separates the two crystals. Low stacking fault energy ***(SFE)*** of **FCC** and **HCP** crystallographic structures enhances twins appearance which leads to an increase in the material strain hardening, Fig. 4-1-b.

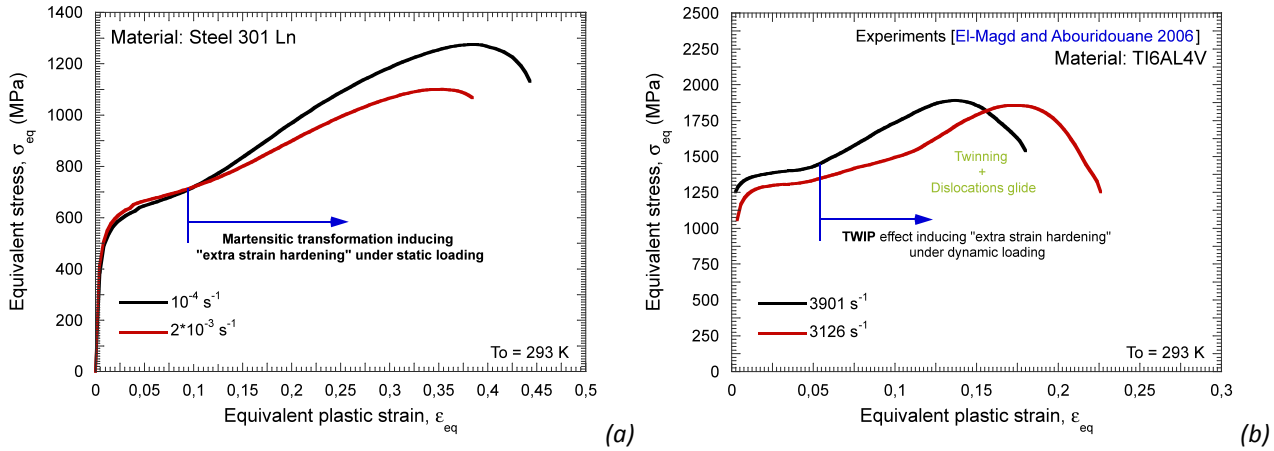

Fig. 4-1. (a) Extra strain hardening under static loading due to martensitic transformation [Rodríguez-Martínez 2010]. (b) Extra strain hardening under dynamic loading due to twinning [Rodríguez-Martínez 2010].

Thus, in order to examine the influence of strain hardening on the formation of instabilities under dynamic loading conditions the formulation reported in Chapter 2.5.2 has

been used, $\sigma_T = \sigma_T\left(\bar{\varepsilon}^p, \dot{\bar{\varepsilon}}^p\right)$. It was previously reported that such formulation allows for defining macroscopically *martensitic* transformation or *twinning* deformation mode effects *(sudden increase of material strain hardening)* on the material behaviour. The material model corresponding to steel **301 Ln2B** has been chosen for this study.

This extended model is suitable for a **FE** analysis due to the reasonable number of constants used *(only 12)* and the possibility to determine explicitly the mathematical forms of the first derivatives of each stress components, which is extremely useful for the implementation of the constitutive relation into a **FE** code.

In this work, the *Extended RK* model is implemented with the fully implicit algorithm [Zaera and Fernández-Sáez 2006] as it has been previously used for the study of viscous-drag effect in **AA**. The numerical tool selected to carry out this study is again ABAQUS/Explicit. Short computational time and simple formulation make the *Extended RK* constitutive relation very attractive for numerical applications in industry, where the *martensitic transformation* in austenitic steels or the *twinning effect* are usual (perforation, high speed machining, etc.).

4.2 Numerical model

The analysis developed in this chapter has been performed using the ring expansion test configuration built in ABAQUS/Explicit. From this configuration, numerical data has been analyzed in order to obtain conclusions about the effect of the strain hardening on the flow localization.

Next, the numerical model used in this chapter is detailed. First of all, a general overview of the ring expansion test is shown. Then, the numerical configuration used is described and the boundary conditions applied validated.

4.2.1 The ring expansion test

In this chapter, a non-conventional experiment that causes an uniaxial tension state in the material at high strain rates is utilized, the ring expansion test. This consists of loading a ring of radius R with a radial constant velocity V_0 varying within a wide range between 50 m/s $\leq V_0 \leq$ 300 m/s. It is important to notice that complications resulting from wave propagation are eliminated due to the symmetry of the problem. The strain rate applied to the material during the expansion is given by Eq. 4-1.

$$\dot{\bar{\varepsilon}}^p = \frac{V_0}{R(t)} \qquad \textit{Eq. 4-1}$$

where R(t) is the instantaneous radius of the ring as a function of the time.

Several experiment setups have been proposed in the literature, Fig. 4-2 [Triantafyllidis and Waldenmyer 2004]. In these proposals, the dynamic loading is provided by the use of explosives, Fig. 4-2-a or by the creation of a magnetic field, Fig. 4-2-b.

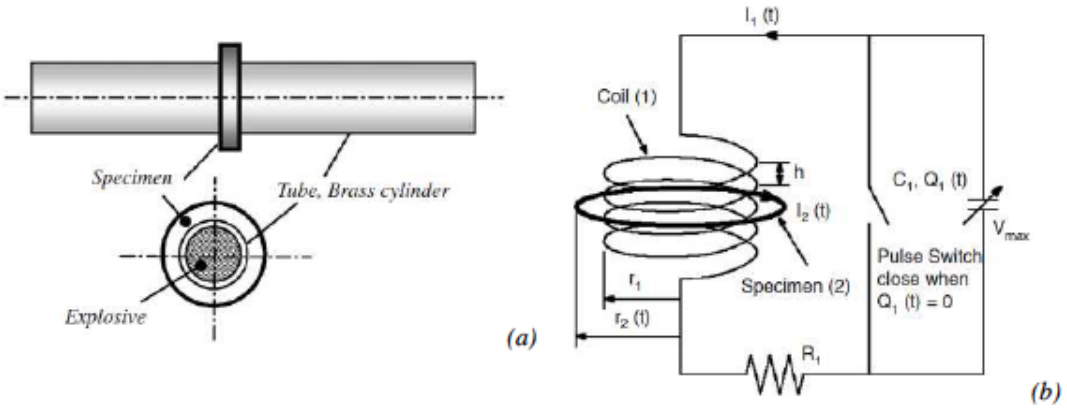

Fig. 4-2. Configuration of the loading conditions by explosive or by magnetic field in the ring expansion test [Rusinek and Zaera 2007].

When the uniform radial velocity is applied, the ring radius starts to increase with time. When the strain increases enough, some neckings are developed along the circumference of the ring. Some of these necks are arrested before failure and the others led to fracture of the specimen, resulting in a number of fragments, which depends on the initial velocity applied.

The fragmentation pattern is very difficult to predict. This depends on the competition between failure modes such as shear banding and those characteristics of static loading, for instance fracture nucleation and void growth [Rusinek and Zaera 2007].

As it has been previously discussed there are not waves effects in the ring expansion test. Thus, ductility is expected to increase with expansion velocity, Fig. 4-3. While for the dynamic tension test the ductility of the material reaches a maximum, for the ring expansion test the ductility increases with impact velocity with none theoretical maximum, Fig. 4-3. However, relativistic effects at very high impact velocities are expected to not make possible to fulfil previous statement.

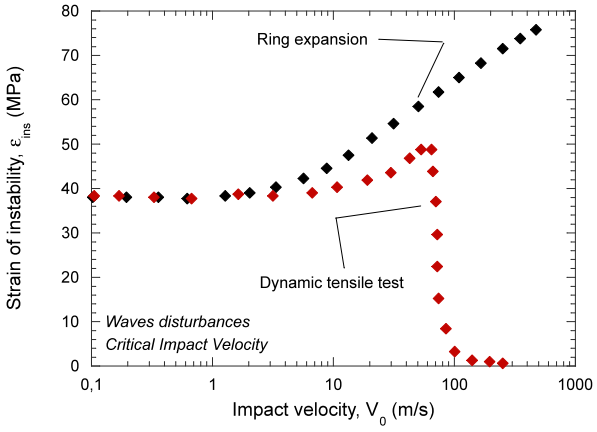

Fig. 4-3. Strain of instability as a function of the impact velocity for ring expansion problem and dynamic tension test [Hu and Daehn 1996].

Some researches could be found in the literature related to the mechanisms behind the plastic localization and instabilities progression during the ring expansion test [Sorensen and Freund 2000, Mercier and Molinari 2004]. These uses a perturbation analysis to study this problem. Due to these works are based on analytical studies, the material constitutive

relation used is usually simple, for instance a power-type equation. If advanced constitutive relations want to be used for defining the material behaviour, numerical methods are a suitable alternative [Rusinek and Zaera 2007].

4.2.2 Numerical configuration

The dimensions and geometry of the ring are based on a work of Rusinek and Zaera [Rusinek and Zaera 2007]. It consists in a ring with an inner diameter of 30 mm and a square cross section of 1x1 mm as it is shown in Fig. 4-4. The boundary condition that will be applied is a constant impact velocity in the inner diameter of the specimen that will remain constant during the whole simulation [Rusinek and Zaera 2007].

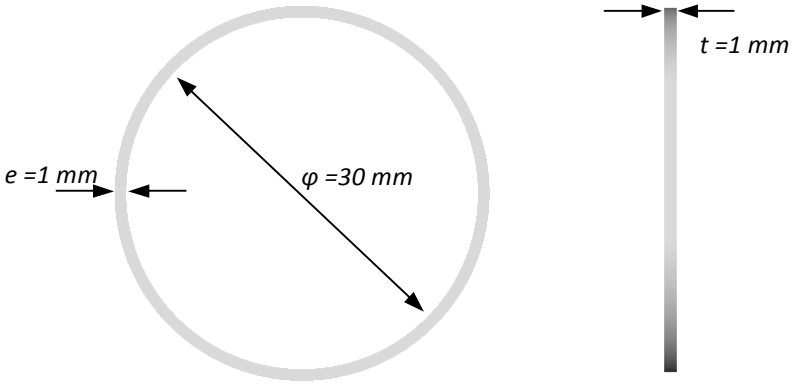

Fig. 4-4. Geometry and dimensions of the ring used in the simulations.

The mesh used for these ring simulations is depicted in Fig. 4-5. Due to the symmetry in the geometry and boundary conditions of the problem, the design of the mesh should be done in such a way that none potential point of plastic instabilities formation exists due to the mesh configuration. The strain localization will be caused by the numerical uncertainties through the integration process [Rusinek and Zaera 2007]. The final mesh used is presented in Fig. 4-5. There exist three elements along the thickness and the width of the specimen. Hexahedral elements have been used with an aspect ratio close to 1:1:1. The dimensions of each element are approximately $0.33 \cdot 0.33 \cdot 0.33\ \mathrm{mm}^3$.

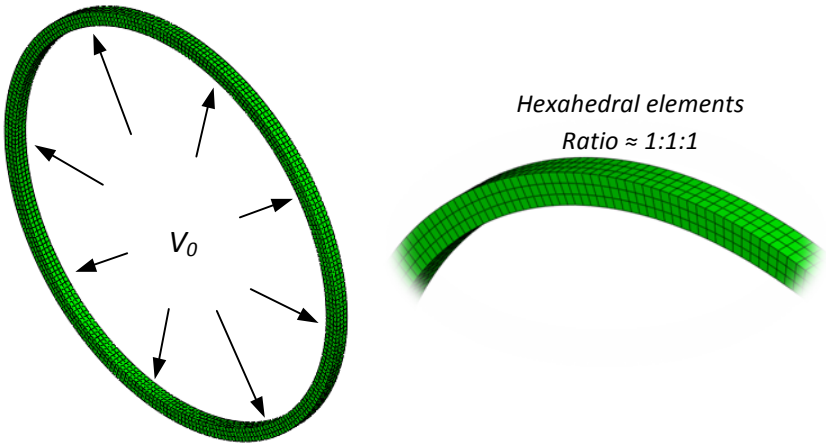

Fig. 4-5. Mesh configuration used for the ring expansion test

Another critical point during the numerical configuration of the test is ensuring that the boundary conditions applied guarantee an uniaxial tensile state in the sample. To

confirm this point, in the following figure, Fig. 4-6, can be observed the triaxiality of the specimen at different times during a numerical simulation. The triaxiality in all parts of the specimen remains close to 0.33 ($\sigma_{\text{triaxiality}} = 0.33$), which corresponds with an uniaxial tension state.

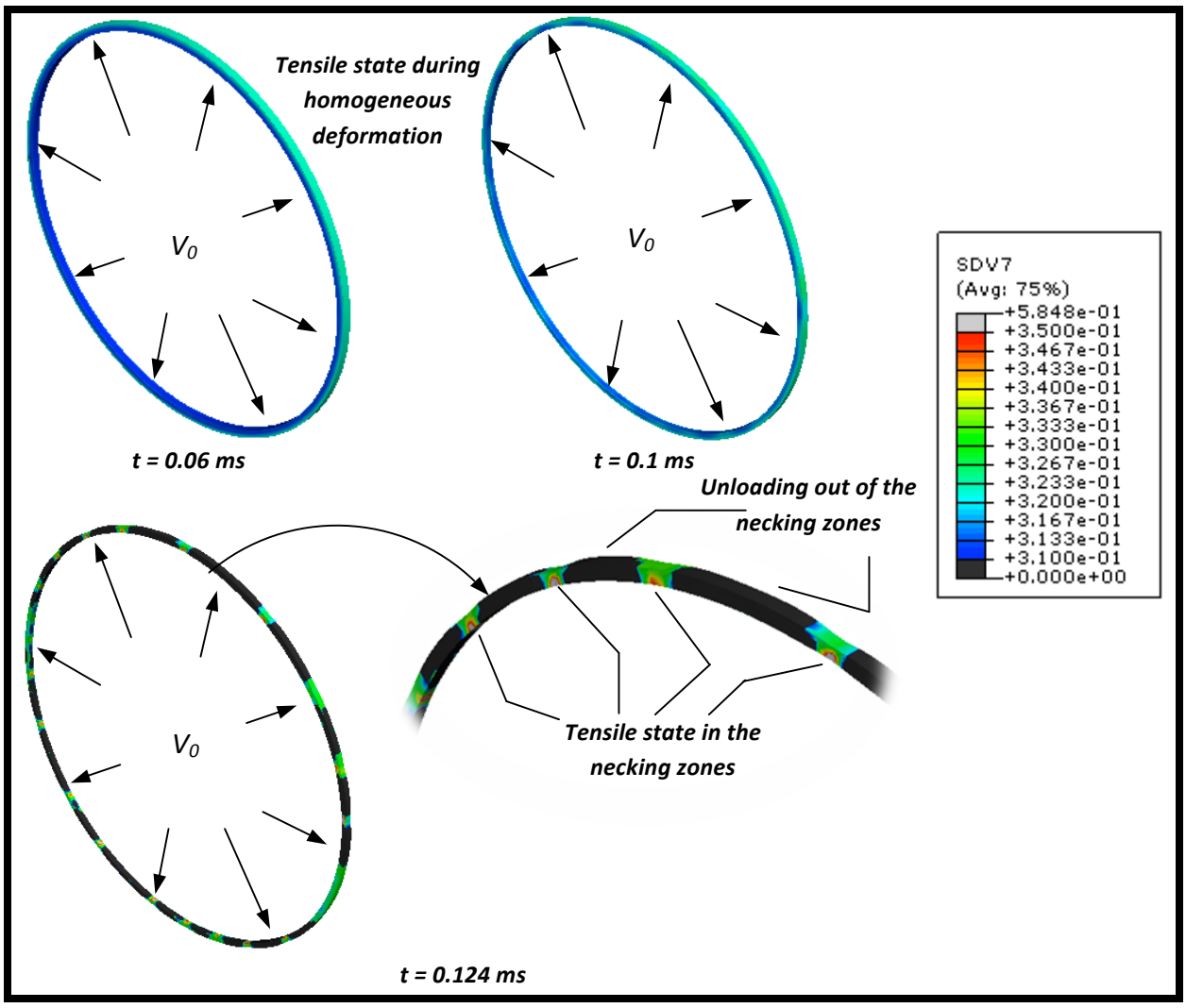

Fig. 4-6. Triaxiality contours during a numerical simulation.

It must be noticed that the strain of instability is intrinsically given by the definition of the homogenous material behaviour *(constitutive description used to define the material behavior)*. Thus, in agreement with [Rusinek and Zaera 2007], a constant critical failure strain has been used in the simulations *(erosive failure criterion involving element deletion)*. The condition that must be imposed to the failure strain is to be large enough to not disturb plastic localization and necking progression *(a constant failure strain is imposed* $\varepsilon_f^p = 1.5$ *)*. If such condition is fulfilled, strain of instability is not affected by the failure strain level, as it has been checked.

In the present work, the *Extended RK* constitutive description to phase transformation phenomena has been used to study the effect of strain hardening on flow localization.

4.3 Application to 301Ln2B

The main reason behind the selection of this austenitic steel **301Ln2B** is that it is one type of stainless steel in which the phase transformation is well observed during quasi-static loading inducing a strong increase of strain hardening rate during plastic deformation.

This steel has many properties in common with other stainless steels such as corrosion resistance, heat resistance, low life cycle cost, full recyclability, biological neutrality, ease of fabrication and cleaning or good strength-to-weight ratio.

It belongs to the 300 Series in the SAE steel grade (austenitic chromium-nickel alloys). As type 301 in this grade, it is remarkable due to its high ductility and its rapid hardenability during mechanical working. Furthermore, it has good weldability and better resistance and fatigue strength than other steels of the 300 series. The addition of the letters "Ln" in its nomenclature means that some percentage of carbon (C) has been substituted by nitrogen (N) in order to increase even more the weldability, ductility and corrosion resistance of this steel. Finally, the last two terms (2B) mean that the steel is cold rolled, heat treated, pickled and skinpassed before selling.

Using the procedure reported in [Klepaczko et al. 2009], the *Extended RK* model has been calibrated for **301Ln2B** using the experimental data reported in [Larour et al. 2006]. The following set of constants has been found, Table 4-1 and Table 4-2.

B_0 (MPa)	ν (-)	n_0 (-)	D_2 (-)	ε_0 (-)	σ_0^* (MPa)	m^* (-)	D_1 (-)
1380	0.1	0.41	0.05	0.018	488.33	1.66	0.52

Table 4-1. Values of material constants in the original RK constitutive relation for 301Ln2B steel.

σ_0 (MPa)	ξ (-)	λ_0 (-)	λ (-)
500	17	10	4

Table 4-2. Additional material constants defining phase transformation for 301Ln2B steel.

In this particular study, the parameter λ is made zero *(λ = 0)* for the whole analysis conducted in the following sections of this work *(the rate sensitivity of the strain hardening function is neglected by application of this procedure),* $\sigma_T = \sigma_T\left(\bar{\varepsilon}^p, \dot{\bar{\varepsilon}}^p\right)\Big|_{\lambda=0} \rightarrow \sigma_T = \sigma_T\left(\bar{\varepsilon}^p\right)$. It will allow us to isolate the effect of strain hardening.

Moreover, temperature effects have not been studied in the present work. All simulations have been carried out with same initial temperature of 298 K. It is important to notice that none of the proposed expressions to define the temperature effect in the phase transformation process have been used but the value for g(T) has been taken as 1 *(*$g(T)=1$*)*. This is due to for the material considered here there is absence of experimental data at different initial temperatures.

When this *Extended RK* constitutive relation is used for modeling the strain hardening effect, the overall stress is decomposed into three different stress components, the thermal stress, the athermal stress and the new term called *extra strain hardening* term. The *extra*

strain hardening operates beyond a certain value of plastic deformation. It increases drastically the material flow stress until saturation is reached, Fig. 4-7.

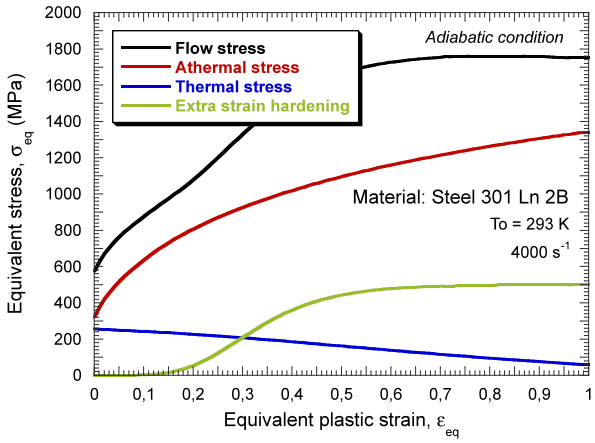

Fig. 4-7. Decomposition of the overall flow stress into its respective stress components.

The hardening function moves up the flow stress of the material from that predicted by the original *RK* formulation *(σ_T = 0 MPa is the lower limit for our material configuration)* up to that corresponding to the value of the material constant σ_0 *(σ_T = 500 MPa is the upper limit for our material configuration),* Fig. 4-8.

These three different material configurations will be used during the present analysis:

- ***Lower limit:*** *σ_T = 0 MPa (original **RK** formulation)*
- ***Strain hardening function:*** Table 4-2 *but with λ = 0*
- ***Upper limit:*** *σ_T = 500 MPa*

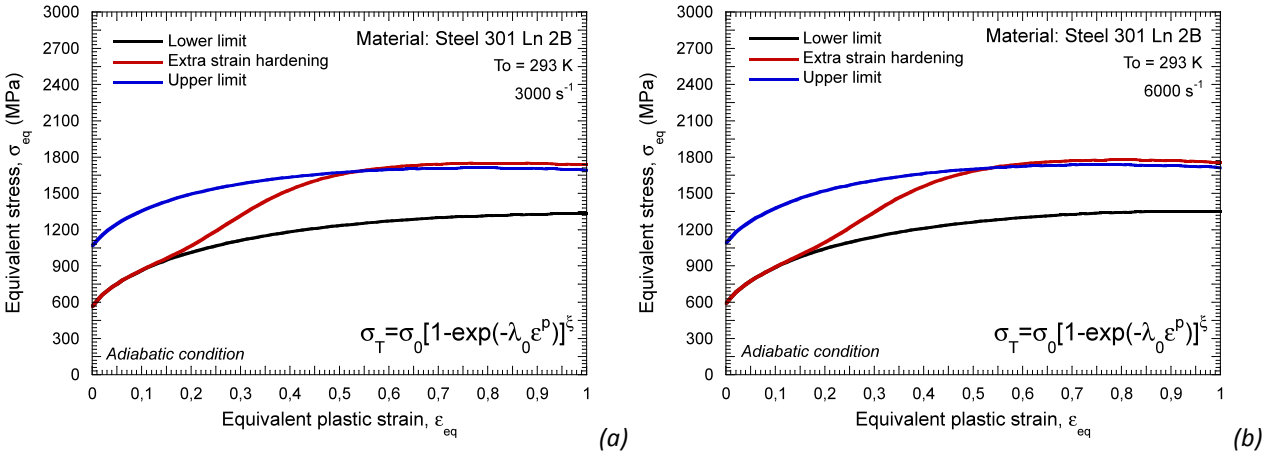

Fig. 4-8. Flow stress evolution versus plastic strain for the three material configurations analyzed and two strain rate levels, (a) 3000 s^{-1} and (b) 6000 s^{-1}.

It is important to notice that the strain hardening function slows down plastic waves celerity. It is expected that it will delay instabilities appearance in comparison with the lower and the upper limit configurations.

Considere's criterion could be applied to the three material models *($d\sigma / d\varepsilon = \sigma$),* Fig. 4-9. As it can be seen in the figure, the *upper limit* configuration will tend to cause instabilities formation. The Fig. 4-9 shows the same strain hardening *(certain differences are*

reported due to the adiabatic heating) than the *lower limit* configuration, but larger flow stress level. The strain hardening of the *Extended RK* constitutive relation changes due to the addition of the new term. This change causes the material behaviour is stabilized.

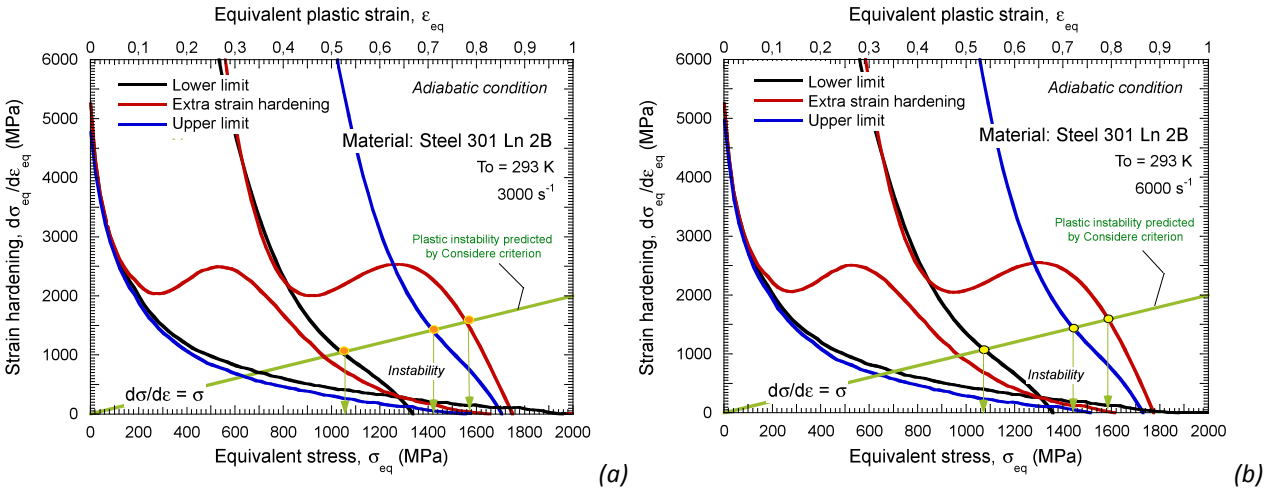

Fig. 4-9. Strain hardening evolution versus plastic strain and versus flow stress for the three material configurations considered and two different strain rate levels.

A key point in the present analysis is to notice the reduction in the strain rate sensitivity exhibited by all material configurations studied, Fig. 4-10. As it could be seen in the figure, Fig. 4-10, the strain rate sensitivity is not as important as it was in the analysis of the viscous drag effect *(See Chapter 3)*. As it will be studied in this project, this rate sensitivity does not influence the plastic instabilities formation. The reason is the strong influence of the strain hardening formulation on the material behavior. This will be subject of discussion during the following analysis.

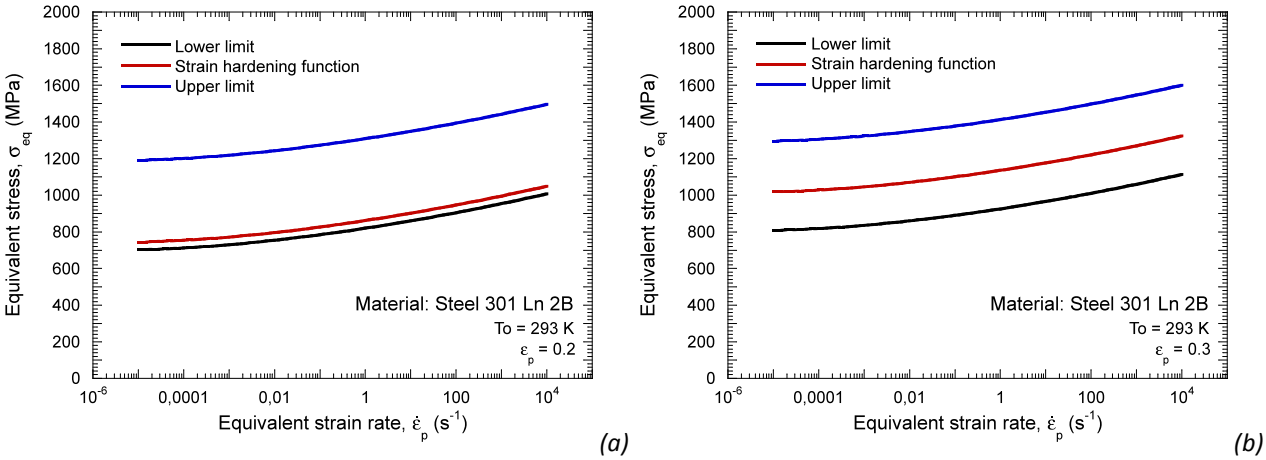

Fig. 4-10. Evolution of the flow stress versus strain rate for the three material configurations considered and different values of plastic deformation.

Finally it is very interesting to study the temperature during the loading of the material. The analytical temperature increment for the material configurations considered at two different strain rates is depicted in Fig. 4-11. As it was expected, the increase of temperature of the *lower limit* and the *strain hardening* configurations matches until the strain hardening function becomes active. When the hardening function becomes operative

the adiabatic temperature drastically augments looking for the temperature predicted by the *upper limit* model.

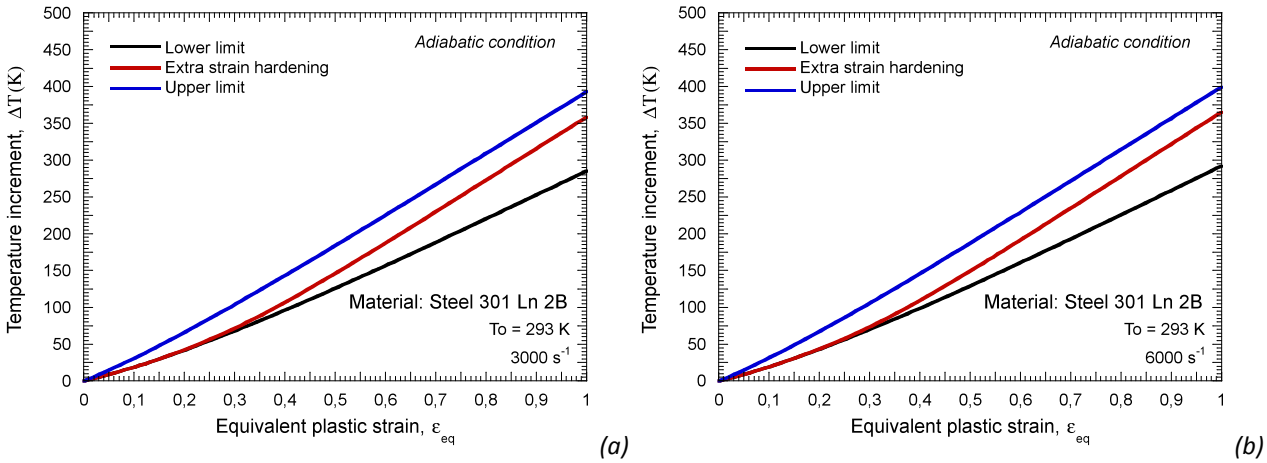

Fig. 4-11. Temperature evolution versus plastic strain for the three material configurations considered and two different strain rate levels.

During the analysis conducted in the following sections of this project, it will be checked that eventual changes in the material response will be tied to the strain hardening function and not to the differences in the adiabatic temperature increase predicted by each material model.

4.4 Analysis and results: the role of strain hardening

Next, the results and conclusions obtained from the numerical analysis developed in this chapter are described. First of all, a validation of the numerical model was performed. Once the model was validated, numerical simulations within wide range of impact velocities ($10\ \mathrm{m/s} \le V_0 \le 150\ \mathrm{m/s}$) were carried out in order to obtain conclusions about the role of strain hardening on flow localization under dynamic loading conditions.

4.4.1 Validation of the model

During the simulations carried out in this chapter, an extended constitutive relation of the *RK* has been used in order to take into account the extra strain hardening of the material. As for the rest of the constitutive relations used in this document, the implementation into ABAQUS/Explicit **FE** code has been conducted using the thermo-viscoplastic integration scheme for J2 plasticity proposed by Zaera and Fernández-Sáez [Zaera and Fernandez-Sáez 2006] *(See Appendix I)*.

In the same way as it was done for the viscous-drag effect study *(See Chapter 3)*, the validation of the model is based on the stress – strain curves obtained from simulations at different impact velocities. These curves are compared with the analytical predictions of the constitutive relation. The measurement is conducted on an integration point belonging to an element out of the necking zone, Fig. 4-12. There, the flow stress can be considered homogeneous.

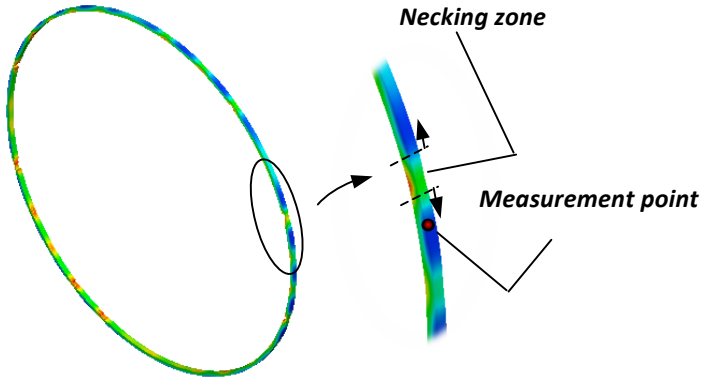

Fig. 4-12. Measurement point of strain-stress curves for model validation.

There is an important detail to take into account. In the case of the ring expansion test (as in the dynamic tension test), the strain rate does not remain constant during the test. However, since the reduction on the deformation rate during loading will be lower than a magnitude order, let us assume that a proper comparison between analytical predictions and simulations can be conducted. The analytical predictions will be obtained using the initial strain rate imposed to the test.

In order to compare the numerical results and the model predictions, some numerical simulations at different impact velocities were carried out. The range covered was $10\ \mathrm{m/s} \le V_0 \le 150\ \mathrm{m/s}$. Analytical results are obtained from that strain rate corresponding to Eq. 4-1 at the very beginning of the test. The results for an impact velocity of 100 m/s are shown in the following figure, Fig. 4-13. It can be observed a perfect matching for the *Extended RK* constitutive description, Fig. 4-13-c, and for the upper and lower limits of the model, Fig. 4-13-a-c. It validates the boundary conditions applied in the numerical configuration as well as the implementation of the constitutive relations into the **FE** code.

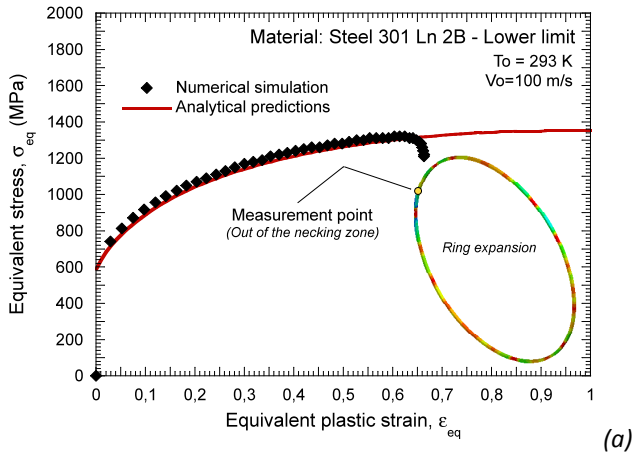

(a)

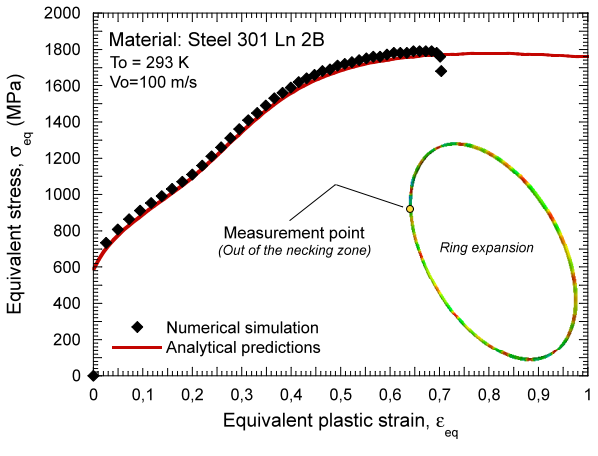

(b)

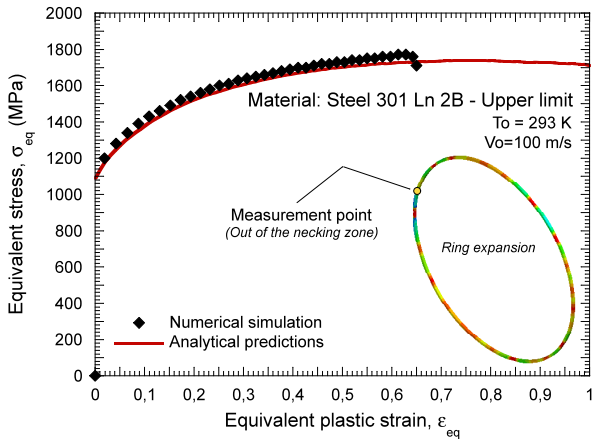

(c)

Fig. 4-13. Comparison between numerical results and analytical predictions for the constitutive relations used at Vo=100 m/s.

Once the numerical configuration is validated, an analysis on the influence of strain hardening on the flow stress localization of the austenitic steel **301Ln2B** is conducted.

4.4.2 Influence of strain hardening stress term on the dynamic behaviour of austenitic steel 301Ln2B

The main purpose of the present chapter is performing an analysis which allows the study of the effect of strain hardening on the flow localization for the ring expansion configuration. *Lower limit*, *upper limit* and *strain hardening function* configurations are used for this task.

Numerical simulations within the range of impact velocities $10\ \mathrm{m/s} \le V_0 \le 150\ \mathrm{m/s}$ have been carried out. As it was previously done in the analysis of the viscous drag effect (See Chapter 3), a study to relate the necking strain with the impact velocity of the test has been performed. Strain data was extracted from elements located in the necking zone. This data corresponds with the local strain of the elements in the integration point where maximum localization takes place *(middle point of necking),* Fig. 4-14. The data of the ring displacement was also extracted.

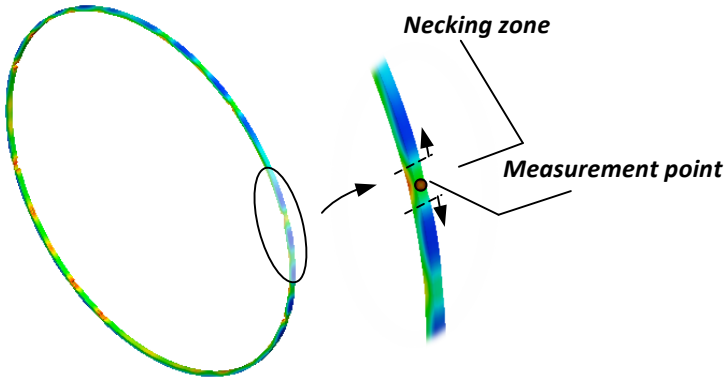

Fig. 4-14. Measurement point of local plastic strain.

In the following figures, Fig. 4-15, is shown the evolution of the local plastic strain versus the global *(theoretical one)* plastic strain for different impact velocities and the three material configurations considered. The plastic instability beginning corresponds with the

local strain at which local and global strains do not match [Triantafyllidis and Waldenmyer 2004]. The maximum strain of instability is reached by application of the *strain hardening function* within the whole range of impact velocities analyzed, Fig. 4-15. Furthermore, the upper limit configuration shows a quite reduced strain of instability along the whole range of impact velocities, Fig. 4-15. This is, it is prone to instabilities formation. Another interesting point is that the behaviour of these is very similar both for the *lower limit* and for the *Extended RK* constitutive relation, at least at low impact velocities.

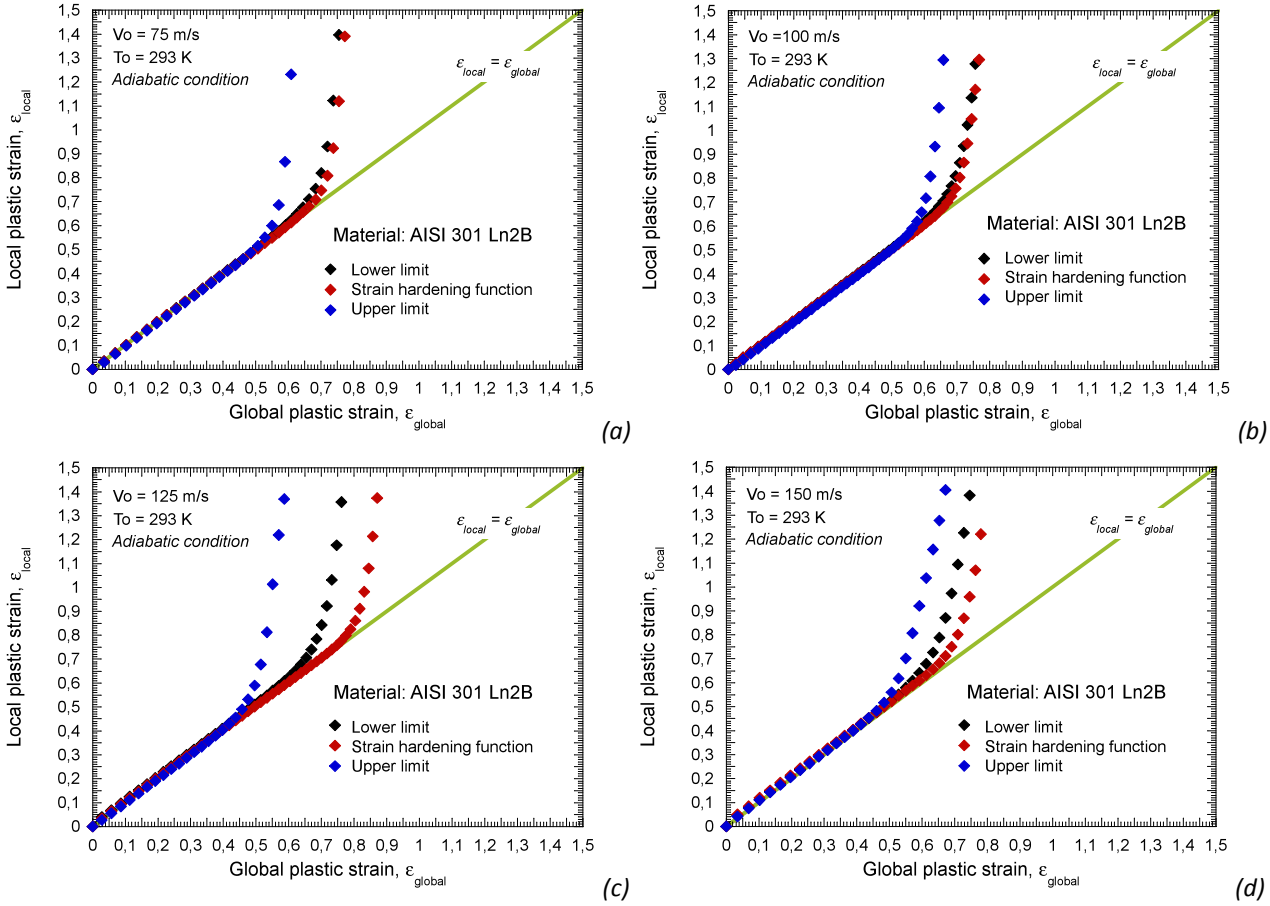

Fig. 4-15. Evolution of the local plastic strain with the global plastic strain for the configurations analyzed (a) Vo=75 m/s, (b) Vo=100 m/s, (c) Vo=125 m/s, (d) Vo=150 m/s.

In Fig. 4-16-a, the relation between the strain of instability and the impact velocity has been plotted for the three different material configurations. On the contrary as in the viscous-drag analysis, the strain of instability does not exhibit relevant changes with impact velocity *(so, rate sensitivity)*, even if the *strain hardening function* is applied, Fig. 4-16-a. Moreover, in Fig. 4-16-b is checked that such effect is neither related to temperature increase. For the *strain hardening* configuration, adiabatic heating does not influence the strain of instability. That behaviour is opposite to that observed for the *lower limit* and *upper limit* configurations. In these two cases, if isothermal conditions of deformation are applied the strain of instability is moved up for the whole range of impact velocities, Fig. 4-16-a-b.

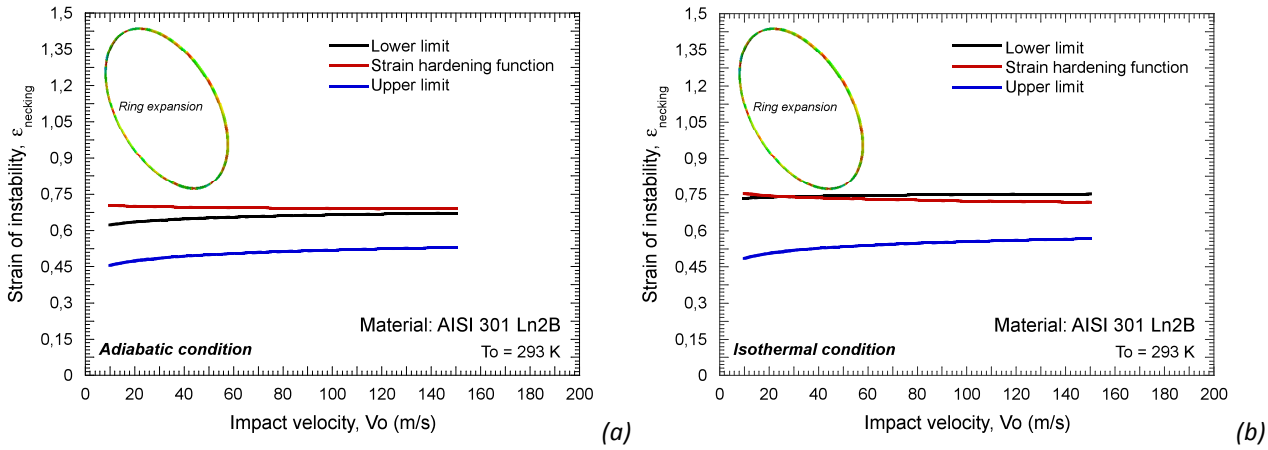

Fig. 4-16. Strain of instability versus impact velocity in (a) adiabatic conditions and (b) isothermal conditions

Some important comments can be done regarding to the previous considerations. If the Considere's criterion is used to qualitatively indicate the strain at which instability occurs, Fig. 4-17-a, it is easy to see that the strain of instability always happens once the maximum hardening rate is over passed, Fig. 4-17-b. Then, the strain hardening has such a big influence that the effect of rate sensitivity on the material ductility is hidden.

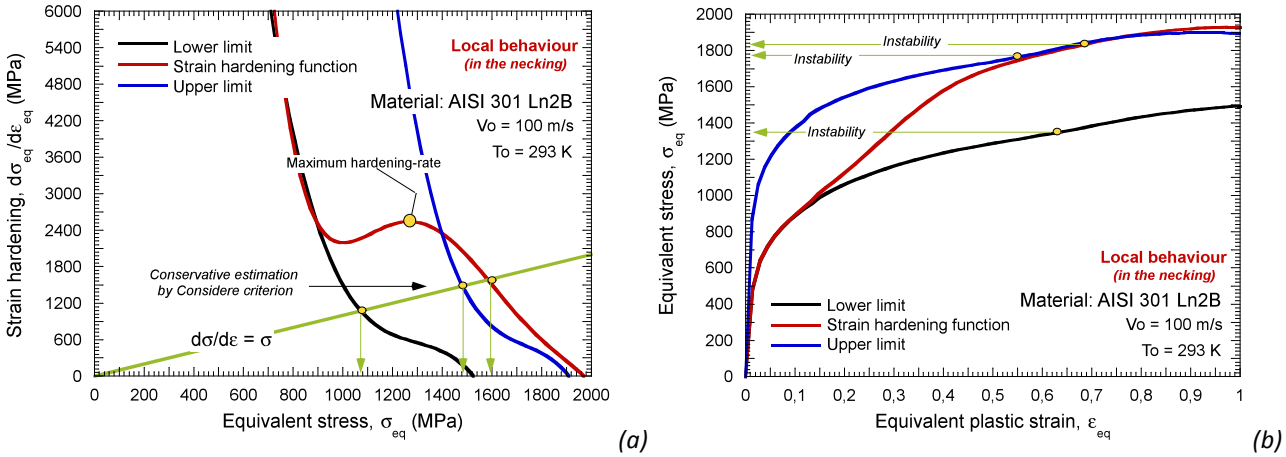

Fig. 4-17. (a) Evolution of the strain hardening versus stress in the necking for the three material configurations analyzed and (b) flow stress evolution versus plastic strain.

In Fig. 4-18 is depicted the evolution of the strain rate and stress in the necking as a function of the plastic strain. If the hardening function is applied the bifurcation of the local deformation rate from the theoretical one is delayed until the hardening rate of the material starts to decrease.

In case of applying the *lower* and *upper limit* models, previous consideration is not valid since the localization seems to the ruled by both the stress level and the rate sensitivity of the material *(that in this particular case is quite reduced),* Fig. 4-18.

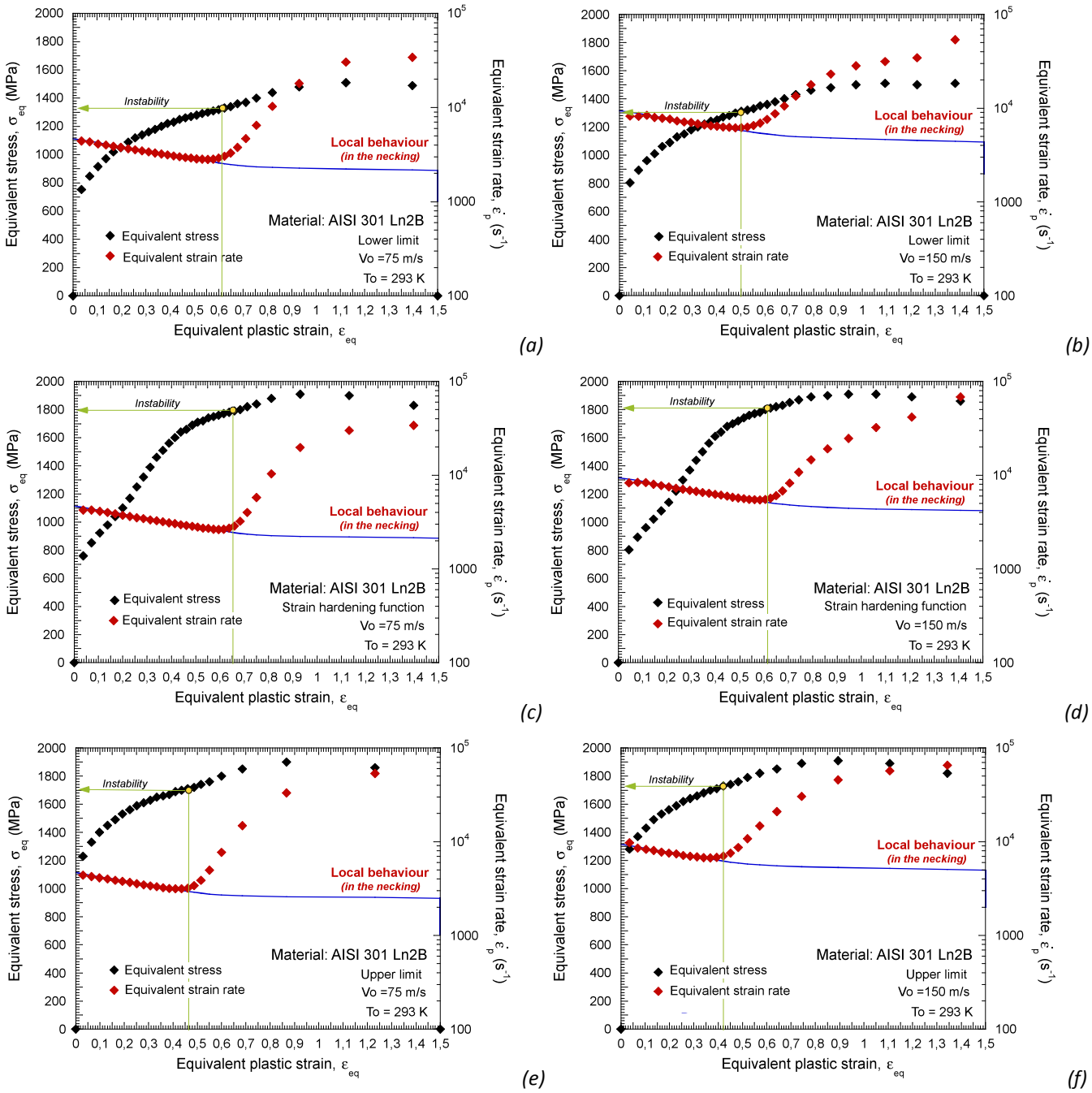

Fig. 4-18. Evolution of the strain rate in the necking as a function of plastic strain for the three material configurations considered and different impact velocities.

It seems that for a certain value of strain hardening rate *(in absence of material damage, wave propagation or any other disturbance mechanism)* strain localization never takes place. To extensively discuss this affirmation, a parametric study of the strain hardening function parameters is developed. This is performed in the following section in order to obtain some conclusions about this and some others points.

Finally it is necessary to check that the considerations reported for the local material behaviour are reflected in the global specimen response. At failure, the ring diameter is larger when the material configuration with the *strain hardening function* is applied due to the increase in the strain of instability of the material, Fig. 4-19, improving the capability of

the material for absorbing energy. Smallest specimen diameter corresponds to the *upper limit* configuration, Fig. 4-19.

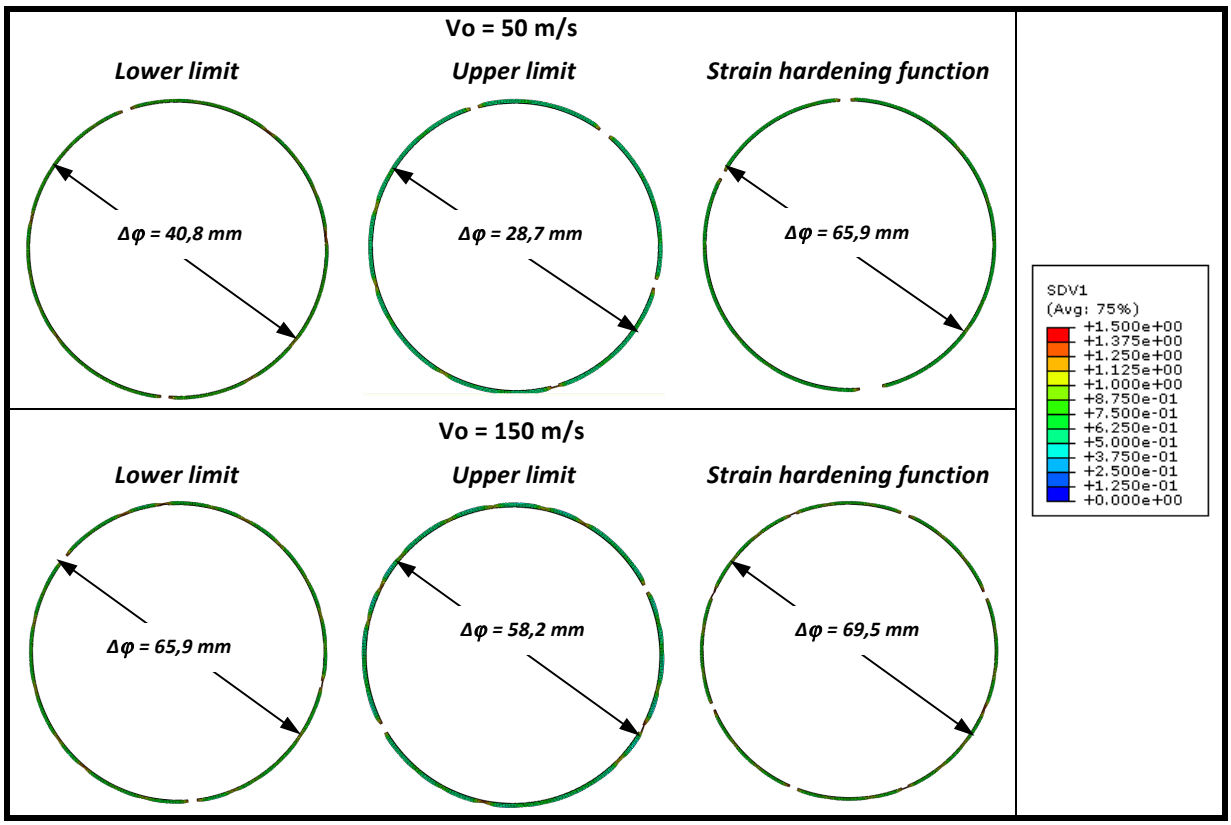

Fig. 4-19. Ring once the failure appears for the three different configurations at two impact velocities.

4.4.3 Influence of strain hardening formulation parameters on flow localization

In order to develop the current parametric analysis, the methodology will be the same as the one used for the viscous-drag study. All parameters of the *RK* model will remain constant as those corresponding to steel **301Ln2B**, Table 4-1. The material constants of the strain hardening function term will be varied using the values listed in Table 4-3. The values in bold numbers will be kept as the reference values *(when varying one parameter the other one will take the value in bold).* This methodology allows for a better understanding of the effect each parameter has on flow localization.

ξ (MPa)				λ_0 (-)			
10	*50*	*200*	*1000*	*3*	*5*	***10***	*15*

Table 4-3. Value of the strain hardening function constants used for the parametric study.

Next, the effect of parameter ξ on flow localization under dynamic tension is analyzed.

4.4.3.1 Influence of parameter ξ

First of all, the strain hardening component and its derivative is plotted in Fig. 4-20 for different values of the parameter ξ. As it could be seen, as the parameter ξ increases, both the plastic strain at which extra strain hardening becomes operative and at which this

extra strain hardening reaches saturation increase, Fig. 4-20-a. However, the hardening rate remains unaltered but shifted along strain, Fig. 4-20-b.

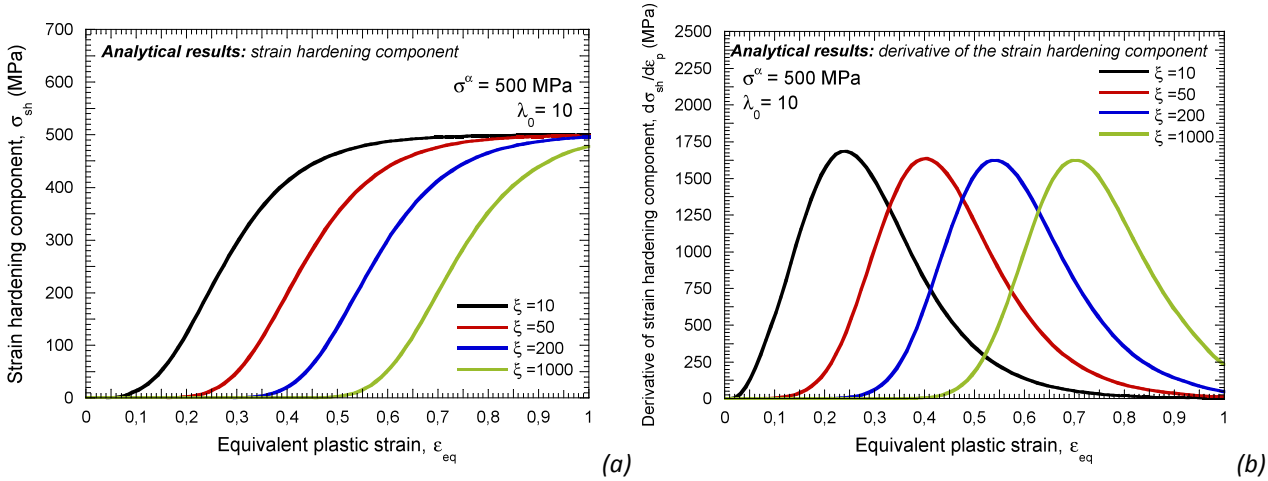

Fig. 4-20. (a) Flow stress predicted by the strain hardening function versus plastic strain. (b) Derivative of the strain hardening function versus plastic strain.

In the following figures, Fig. 4-21, the strain of instability is analyzed for different values of the impact velocity and the values of ξ proposed in Table 4-3. In all the cases considered, when the value of ξ increases the strain of instability also does it, Fig. 4-21. This behaviour means that as the value of the parameter ξ increases, the benefits the material obtains from the strain hardening function also increase *(it might have been possible that instability would have taken place before the strain hardening function becomes operative if larger values of ξ would have been considered, however this seems physically unlikely).* Moreover, as it is depicted in Fig. 4-22, the instability takes place close to the saturation stress condition, once the maximum rate hardening is overcome for all cases (the two extreme values used are plotted).

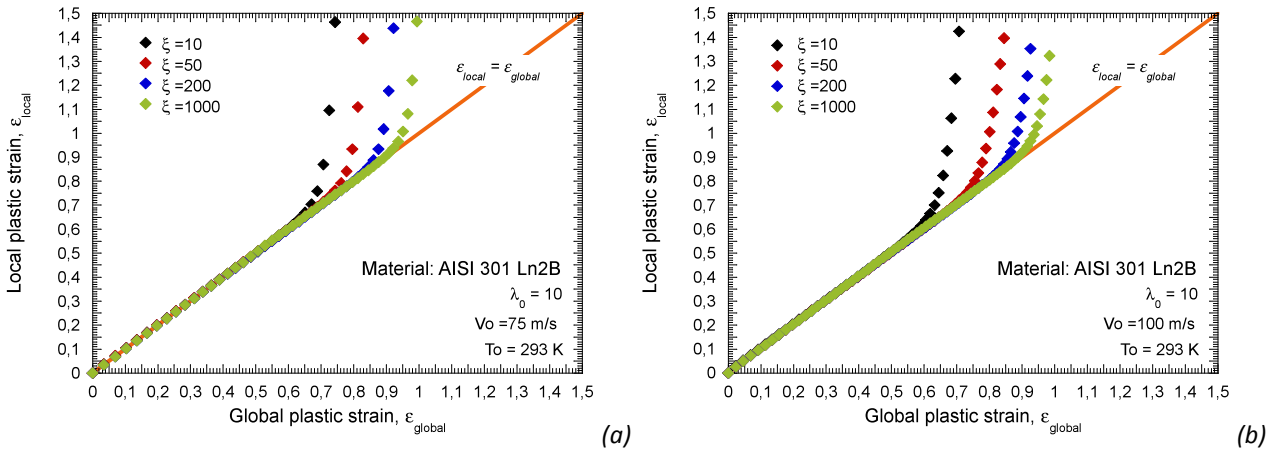

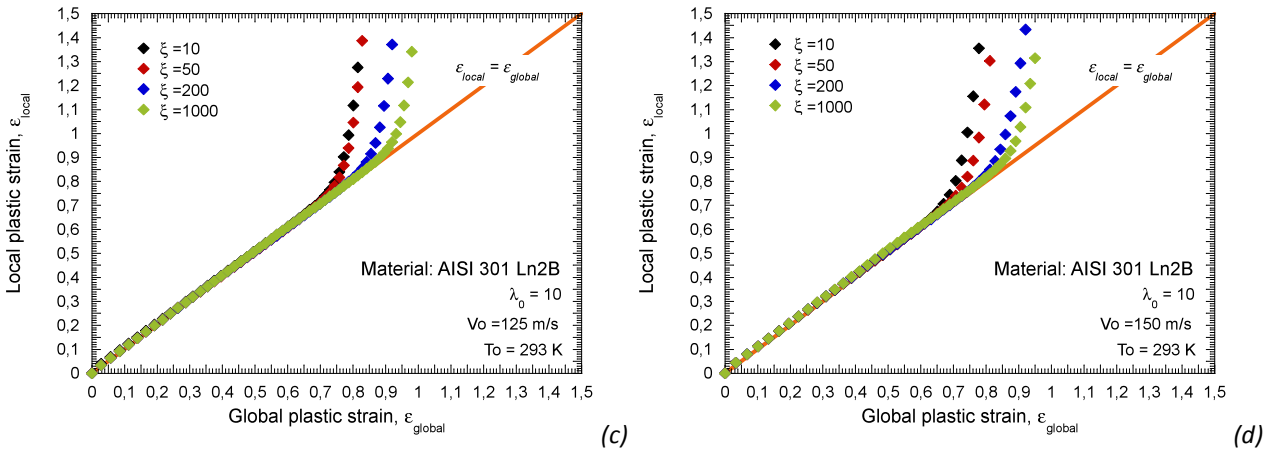

Fig. 4-21. Evolution of the local plastic strain with the global plastic strain for the configurations analyzed (a) Vo=75 m/s, (b) Vo=100 m/s, (c) Vo=125 m/s, (d) Vo=150 m/s.

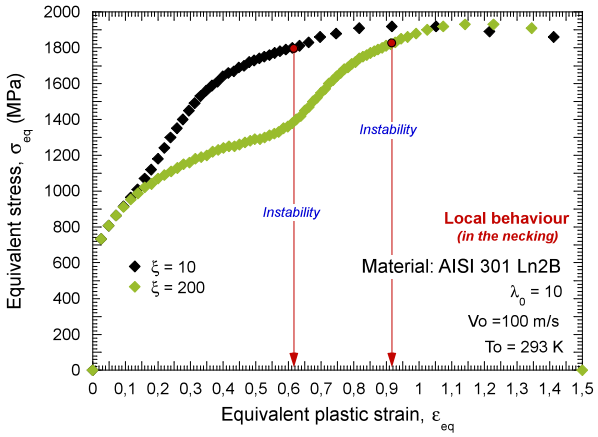

Fig. 4-22. Evolution of stress versus plastic strain in the necking for different values of ξ at Vo=100 m/s.

In Fig. 4-23 is plotted the strain of instability versus the impact velocity for the different values of ξ analyzed. The strain of instability remains approximately constant for the whole range of impact velocities considered both under adiabatic and isothermal conditions of deformation *(in the case of isothermal conditions of deformation the strain of instability is moved up in comparison with adiabatic conditions)*. This is because the material temperature increase under adiabatic conditions tends to diminish the strain of instability of the material.

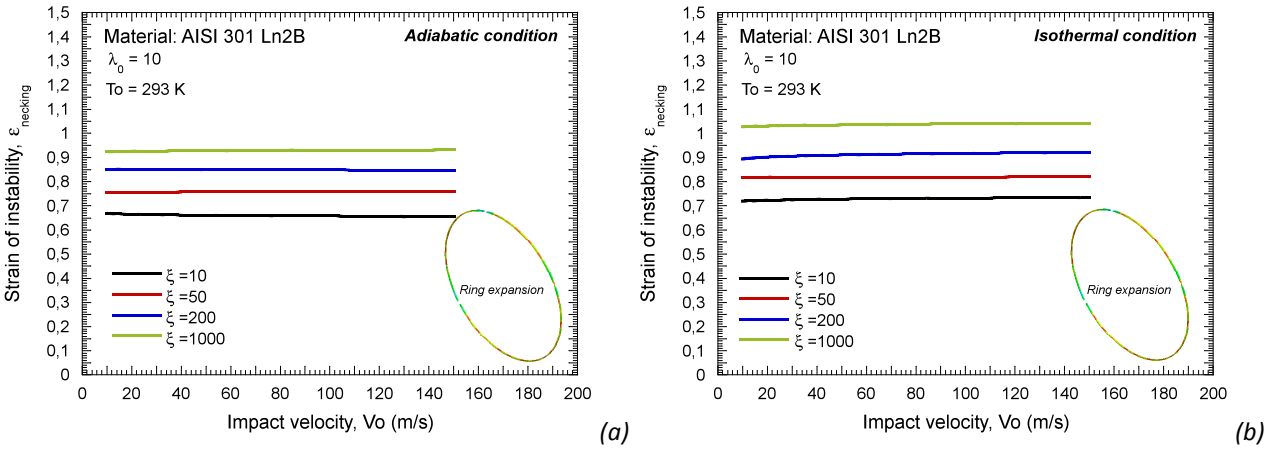

Fig. 4-23. Strain of instability versus impact velocity under (a) adiabatic and (b) isothermal conditions of deformation.

Next, it is shown the evolution of strain rate and stress in the necking for different impact velocities and all the values of ξ considered, Fig. 4-24. As it was previously commented, the equivalent strain rate in an element into the necking zone follows the theoretical one until the maximum hardening rate is overcome. Clearly, it seems that in a configuration free of waves disturbances there is certain value of strain hardening for which localization does not take place.

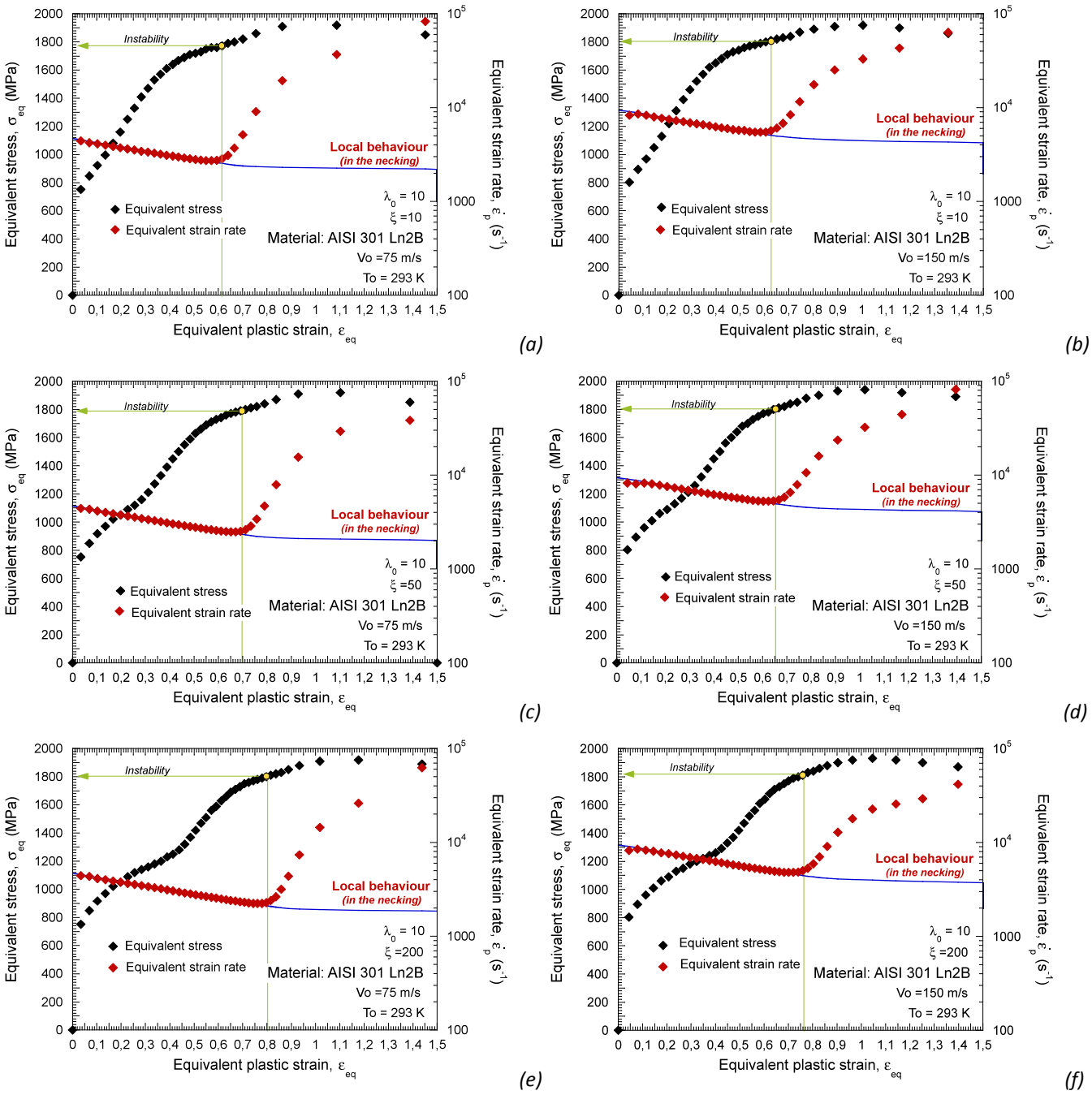

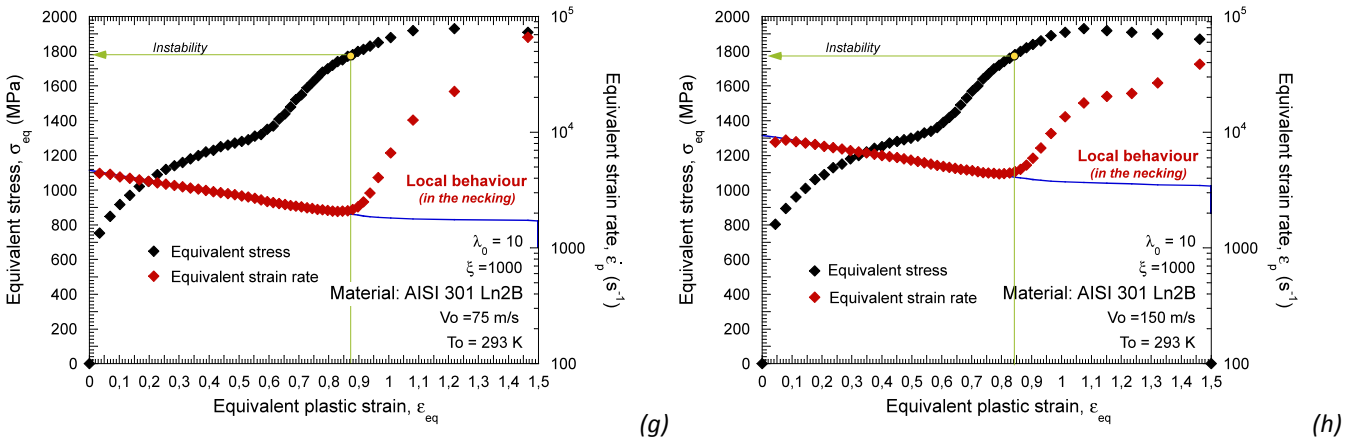

Fig. 4-24. Evolution of the strain rate and the flow stress in the necking as a function of the plastic strain for all the values of ξ considered and different impact velocities (75 m/s and 150 m/s).

It is reported in several studies [Altynova et al. 1996] that the number of fragments in a ring expansion test is highly related to the ductility of the material. Then, it is important to check that the number of fragments increases with the value of the parameter ξ as impact velocity increases. In Fig. 4-25, the number of fragments as a function of the impact velocity for the material configurations analyzed is shown. It seems that the increase of ξ leads to larger number of fragments as it was expected. However, it should be accounted that the number of pieces in which the material is fragmented is relatively low because of the low rate sensitivity of the material configuration used. Therefore, the influence of ξ in the number of fragments results difficult to evaluate with accuracy and future studies may be necessary.

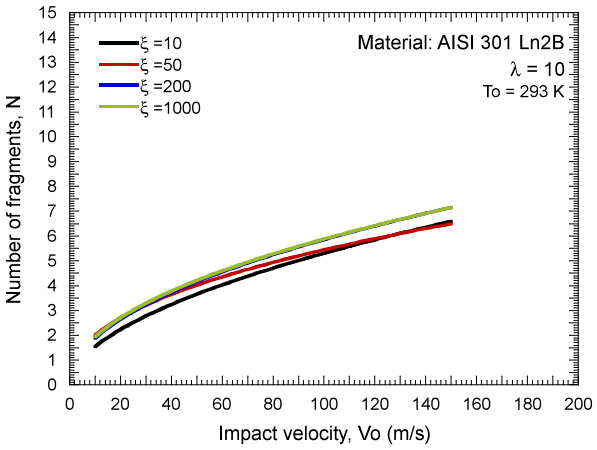

Fig. 4-25. Number of fragments as a function of impact velocity for different values of ξ

4.4.3.2 Influence of parameter λ_0

As it was previously done for the parameter ξ, in Fig. 4-26 is depicted the evolution of the strain hardening function versus strain for different values of λ_0 assuming a constant value for the parameter ξ (ξ = 10). In this case, an increase in the value of λ_0 augments the hardening rate of the material *(this is the slope of the strain hardening component,* Fig. 4-26-*a)*. In addition it delays the plastic strain at which the extra strain hardening becomes operative and the plastic strain where the extra strain hardening reaches saturation, Fig.

4-26-a. Finally, in Fig. 4-26-b is shown that in this case the maximum hardening rate is completely modified. An augment in the value of the parameter λ_0 tends to increase this maximum hardening rate and to moves it to lower plastic strains, Fig. 4-26-b.

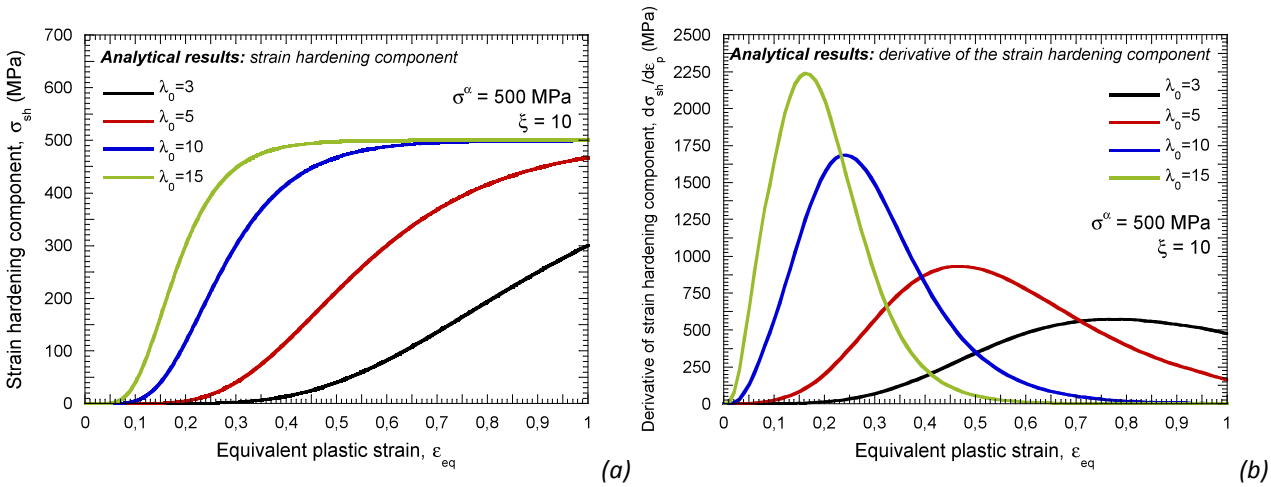

Fig. 4-26. (a) Flow stress predicted by the strain hardening function versus plastic strain. (b) Derivative of the strain hardening function versus plastic strain for different values of λ_0

As previously done, in Fig. 4-27 is plotted the evolution of the local plastic strain versus the global plastic strain of the ring for the different values of λ_0 studied within a wide range of impact velocities. In this case, low values of λ_0 delay flow localization increasing the ductility of the material. In the cases of λ_0=5, λ_0=10 and λ_0=15 the strain localization is induced close to the saturation of the hardening function, Fig. 4-26 and Fig. 4-27, which is in agreement with considerations previously discussed. It seems that a value of λ_0=3 is low enough to not play the strain hardening function a clear implication in the plastic instabilities formation.

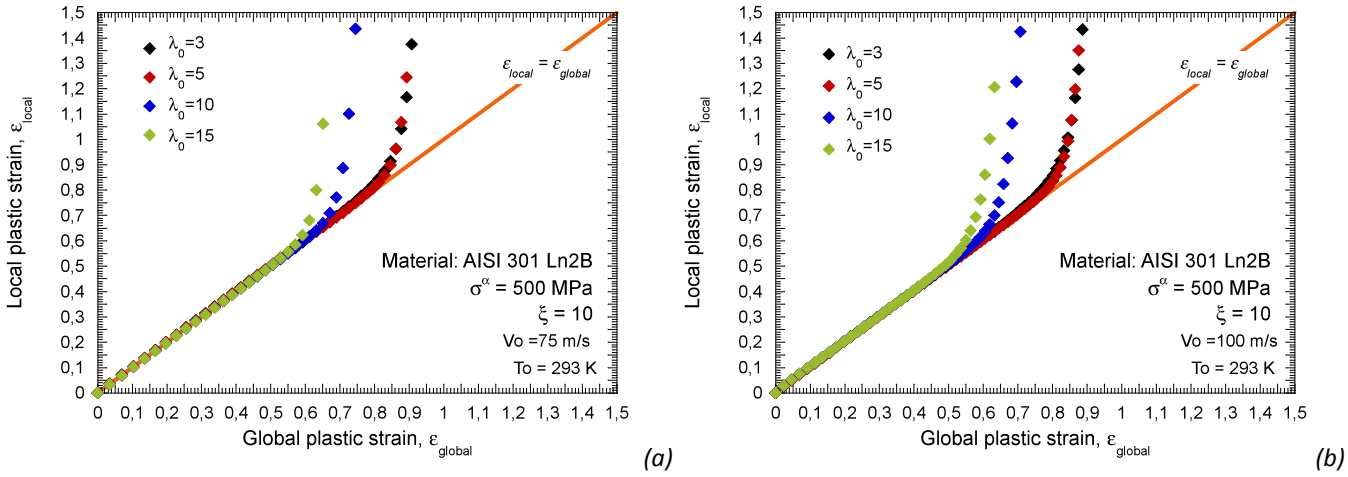

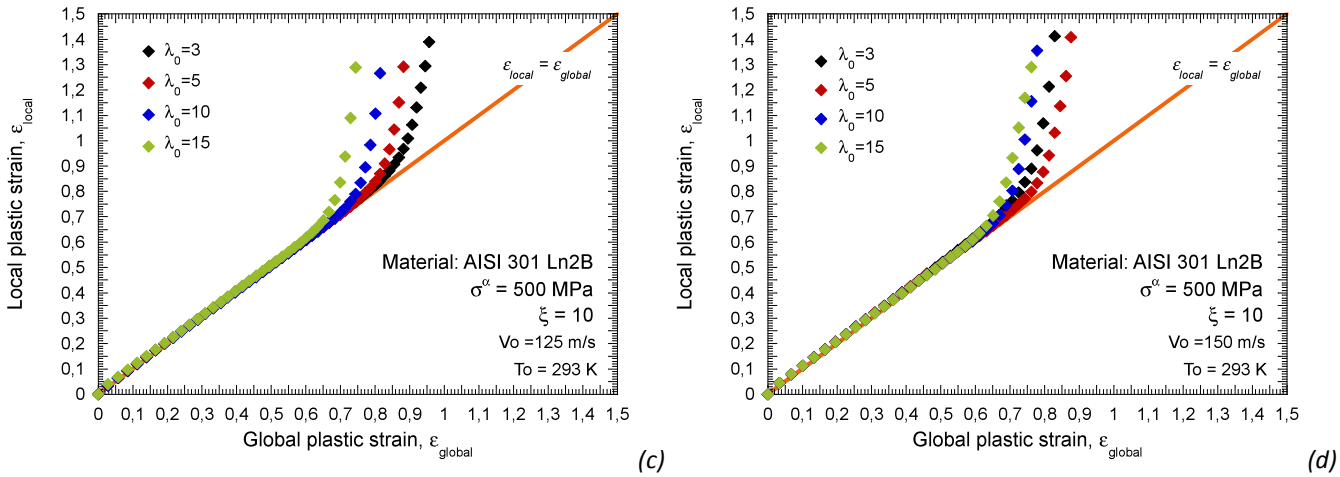

Fig. 4-27. Evolution of the local plastic strain with the global plastic strain the configurations analyzed (a) Vo=75 m/s, (b) Vo=100 m/s, (c) Vo=125 m/s, (d) Vo=150 m/s.

Previous considerations are studied in Fig. 4-28, in which two different velocities have been selected, V_0 = 50 m/s and V_0 = 100 m/s. It is clear, Fig. 4-28-a-b, that the instability in the case of λ_0 = 3 is formed considerably before the saturation of the extra strain hardening is reached. In the case of λ_0 = 5 the difference takes place just after the maximum hardening rate is overcome, far from the saturation stress level, Fig. 4-28-c-d. This also seems to happen for the case of λ_0 = 3, however, it is difficult to state it due to the low stress level of the material. This consideration reveals the role that the hardening rate plays by itself.

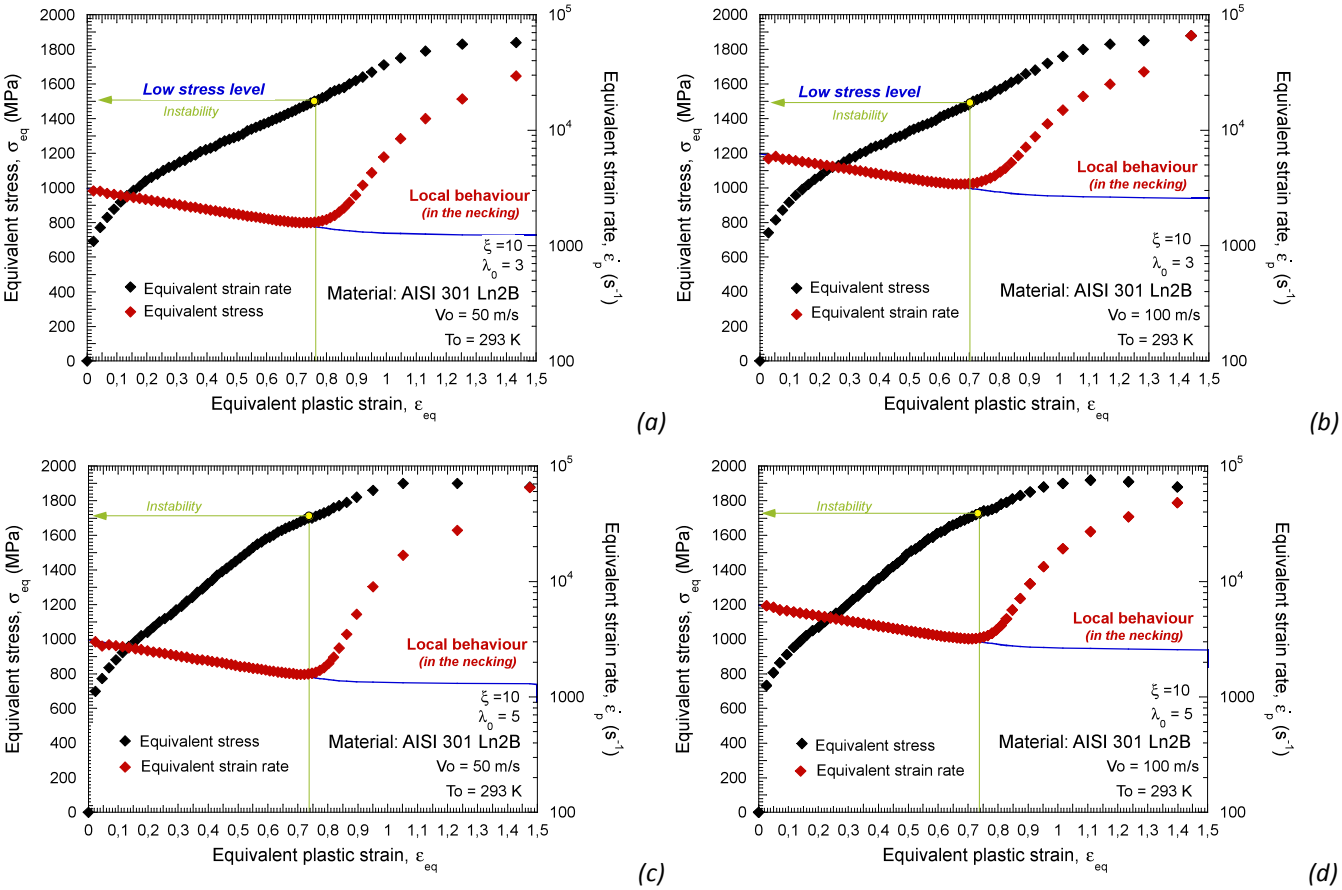

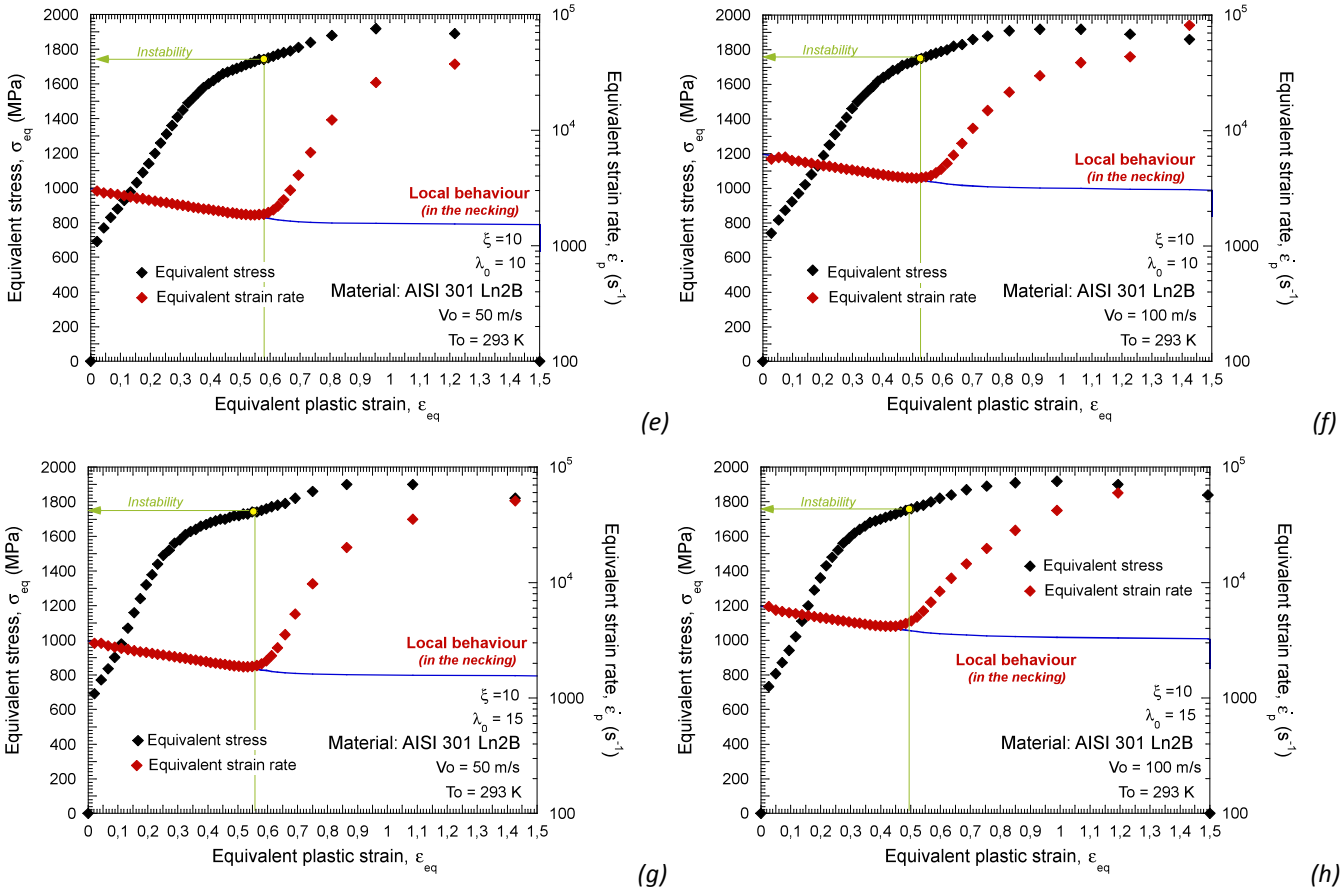

Fig. 4-28. Evolution of the strain rate and the flow stress in the necking as a function of plastic strain for all the values of λ_0 considered and different impact velocities.

In Fig. 4-29 is plotted the strain of instability of the material versus the impact velocity for the different values of the parameter λ_0. It can be seen, Fig. 4-29, that the strain of instability in case of λ_0 = 3 and λ_0 = 5 is quite similar for the whole range of impact velocities. This is the strain hardening presents an optimum value (close to these ones) which enhances ductility of the material and therefore improves its capability for absorbing energy under dynamic solicitations. In addition, as it was previously commented, the strain of instability does not depend on the impact velocity because of the strain hardening effect hides the effect of the strain rate sensitivity in the material.

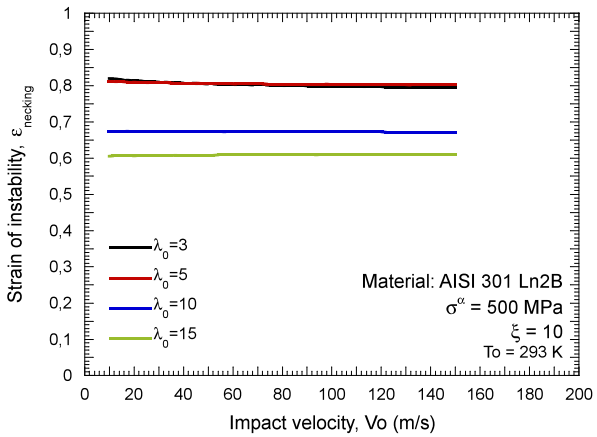

Fig. 4-29. Strain of instability as a function of the impact velocity for different values of the parameter λ_0.

Finally, the number of fragments as a function of the impact velocity is shown in Fig. 4-30 for the different values of the parameter λ_0. Again, it seems that the values of λ_0, which previously have shown higher ductility of the material *(lower values)*, produce higher number of ring fragments. However it must be pointed out that the differences reported in Fig. 4-30 are again quite reduced due to the low number of fragments produced that makes difficult to derive clear conclusions on this matter.

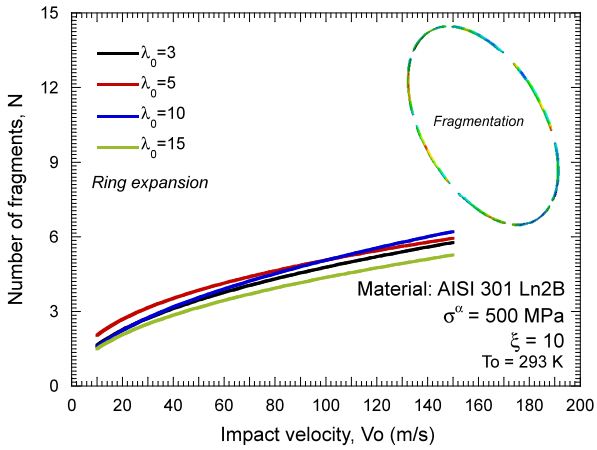

Fig. 4-30. Number of fragments as a function of the impact velocity for all the material configurations analyzed.

In this chapter has been examined the influence of strain sensitivity (strain hardening) on plastic instabilities formation under dynamic loading.

*For that task, numerical simulations of ring expansion test have been carried out. The material definition is conducted by application of the Extended Rusinek-Klepaczko (RK) model to martensitic transformation effects [Rodríguez-Martínez et al. 2008]. The material model corresponding to steel **301 Ln2B** has been chosen for this study.*

It has been found that the strain sensitivity of the material plays a fundamental role on the formation of plastic instabilities. In addition, it has been even proven that for certain value of strain hardening rate (in absence of material damage, wave propagation or any other disturbance mechanism) strain localization never takes place. It has been concluded that taking into account strain hardening effect reveals an increase in the material ductility. Then, strain sensitivity tends to stabilize the material.

Thus, it has been found that the suitability of a material for absorbing energy under dynamic loading is highly dependent on the boundary value problem approached. As reported in the literature [Rodríguez-Martínez 2010], wave interactions are able to annihilate the effect of the strain hardening function on the material ductility.

CHAPTER 5

INFLUENCE OF THE CONSTITUTIVE RELATION ON FLOW LOCALIZATION

ABSTRACT

In this chapter, the fundamental objective has been advancing in the understanding of the effects presented in previous chapters. For this purpose, the role of the constitutive relation on the material behavior predictions under impact solicitations has been studied. Three different physical-based constitutive relations (the Extended Modified Rusinek-Klepazcko -*EMRK-,* the Nemat-Nasser and Li -*NNL*- and the Voyiadjis and Almasri -*VA-)* have been used to model the behavior of **OFHC copper** specimens subjected to the dynamic tension and ring expansion tests. These three constitutive descriptions has been proven suitable to define the material behaviour under wide range of loading conditions. It has been concluded that even when constitutive descriptions with similar background are used, the predictions they provide regarding the capacity of the material for energy absorption under dynamic conditions are very different.

5 INFLUENCE OF THE CONSTITUTIVE RELATION ON FLOW LOCALIZATION

5.1 Introduction

Macroscopic plasticity in metals is the result of dislocations moving through the crystal lattice. Moreover, it is assumed that plastic deformation occurs by the motion of dislocations and that the resistance to this motion corresponds to the flow stress *(See Chapter 2)*. Following these premises, constitutive descriptions are defined to model the material behaviour under different loading conditions. Physical-based constitutive relations account for physical aspects of the material behaviour. All the constitutive descriptions studied in this project belong to this group. They are founded on the thermodynamics and kinetics of slip theory [Kocks et al. 1975].

In the present chapter, three different advanced constitutive relations to model **OFHC copper** will be analyzed and compared. These are the ***EMRK*** *(Extended Modified Rusinek-Klepaczko)* [Rusinek et al. 2010, Rodríguez-Martínez 2010], the ***NNL*** *(Nemat-Nasser and Li)* [Nemat-Nasser and Li 1998] and the ***VA*** *(Voyiadjis and Almasri)* [Voyiadjis and Almasri 2008]. These constitutive descriptions have been found suitable to define adequately the behaviour of the **OFHC copper.** However, the physical base used for each formulation is not the same in all cases, which has a great impact in some important points as the rate sensitivity predicted by the material. The purpose of this chapter is proving that even when this kind of advanced constitutive descriptions is used, different instabilities formation predictions are obtained when the material is subjected to dynamic loading conditions.

The relevance of metallic alloys in the current industry leads to the necessity of studying these predictions in order to obtain practical conclusions about the applicability of each model.

The final goal is having practical constitutive models allowing for a more feasible use in the current industry, introducing them in **FE** codes and using the results obtained from the software with high level of confidence in the numerical results.

5.2 Application to OFHC copper

Polycrystalline oxygen-free high conductivity copper ***(OFHC)*** is one of the most widely studied materials under a variety of deformation paths and over large strains, strain rates and temperatures. OF/OFE grade copper is used in plasma deposition *(sputtering)* processes, including the manufacture of semiconductors and superconductor components, as well as in high vacuum devices such as particle accelerators. Other common field where **OFHC copper** is used is in cryogenics. It also finds application for shaped-charges liner. This part of shaped charges is in charge of forming the jet which penetrates the target. Liner-material is required of excellent ductility and high density. Shaped charges are frequently used for military applications, although the most extensive use today of shaped charges is in the oil and gas industry to pierce metal, concrete, and other solid materials. Characteristics of copper are

high ductility, high electrical and thermal conductivity, high impact strength, good creep resistance, ease of welding, and low relative volatility under high vacuum.

Several constitutive relations to describe the characteristic behaviour of this type of face-centered cubic ***(FCC)*** metal under static and dynamic conditions are reported in the literature [Nemat-Nasser and Li 1998, Voyiadjis and Almasri 2008, Rusinek et al. 2010].

Conventional physical constants of **OFHC copper** can be obtained from material handbooks, Table 5-1.

E_0 (GPa)	C_p ($JkgK^{-1}$)	β (-)	ρ (kgm^{-3})
130	385	0.9	8960

Table 5-1. Physical constants for annealed OFHC copper.

5.3 Constitutive descriptions for modelling the thermo-viscoplastic behaviour of OFHC copper

Despite this metal *(OFHC copper)* has a **FCC** internal structure *(aluminium alloy AA7075 and austenitic steel **301Ln2B** also had it)*, this presents an important different characteristics. It has dependence of the plastic strain on the **VTA** *(Volume Thermally Activated)*. This involves that some constitutive relations such as the *original RK* do not represent correctly the material behaviour.

As it has been previously discussed *(See Chapter 2)* the definition *(and contribution to the overall flow stress)* of thermal and athermal terms is dependent on the crystal structure of the material. The causes are related to the available symmetries of the lattice, the nature of the dislocation cores and the available slip systems.

Next, an overview of the three constitutive descriptions that will be analyzed in this chapter is carried out.

5.3.1 The Extended MRK model

Taking into account previous considerations, a constitutive relation for **FCC** metals with application to **OFHC copper** was developed by Rusinek et al. [Rusinek et al. 2010], this is the *Extended MRK* constitutive relation. This adds an addend to the formulation of the *MRK* model *(See Chapter 2.5.1)*. The extension follows the purpose of representing correctly the change in the strain rate sensitivity of some metallic alloys when they are subjected to high strain rates of deformation (*viscous drag effect -See Chapter 3-).*

A complete discussion about this constitutive description and its specific formulation was reported in Chapter 2.4.

In order to perform this study, the numerical values of each one of the constants used to define the material behaviour should be known.

Using the procedure reported in [Rusinek et al. 2010], the *Extended MRK* model was calibrated for annealed **OFHC copper** using the experimental data collected from [Follansbee 1986, Nemat-Nasser and Li 1998]. The following set of constants was found, Table 5-2 and Table 5-3, [Rusinek et al. 2010].

Y (MPa)	B_0 (MPa)	ν (-)	n_0 (-)	D_2 (-)	ξ_2(-)	ξ_1(-)	T_m (K)	$\dot{\varepsilon}_{min}$ (s^{-1})	$\dot{\varepsilon}_{max}$ (s^{-1})	θ^* (-)
40	560.28	0.30447	0.492	0.0553	0.0131	0.0011932	1340	10^{-5}	10^{7}	0.9

*Table 5-2. Constants determined for annealed **OFHC copper** for thermal and athermal components of the MRK model [Rusinek et al. 2010].*

χ (MPa)	α (-)
249	0.0000122

*Table 5-3. Constants determined for annealed **OFHC copper** for the viscous drag component of the Extended MRK model [Rusinek et al. 2010].*

Next, the other constitutive descriptions used in this chapter are introduced.

5.3.2 The NNL model

According to the considerations reported for example in [Klepaczko 1975, Zerilli and Amstrong 1987, Rusinek et al. 2010], the *NNL* constitutive relation *(like the MRK model)* decomposes the equivalent Huber-Misses stress $\bar{\sigma}$ into thermal $\bar{\sigma}^*\left(\bar{\varepsilon}^p,\dot{\bar{\varepsilon}}^p,T\right)$ and athermal $\bar{\sigma}_\mu\left(\bar{\varepsilon}^p\right)$ components, Eq. 5-1.

$$\bar{\sigma}\left(\bar{\varepsilon}^p,\dot{\bar{\varepsilon}}^p,T\right)=\bar{\sigma}_\mu\left(\bar{\varepsilon}^p\right)+\bar{\sigma}^*\left(\bar{\varepsilon}^p,\dot{\bar{\varepsilon}}^p,T\right) \qquad \textit{Eq. 5-1}$$

The athermal stress term, which defines hardening of material, is only function of the plastic strain, Eq. 5-2.

$$\bar{\sigma}_\mu\left(\bar{\varepsilon}^p\right)=\sigma_a^0\cdot\left(\bar{\varepsilon}^p\right)^{n_1} \qquad \textit{Eq. 5-2}$$

where σ_a^0 and *n* are material constants describing the flow stress level and the strain hardening of the material.

On the other hand, the thermal stress is defined by Eq. 5-3. It depends not only on strain rate and temperature but also on plastic deformation. As it was previously discussed, such dependence is in agreement with the considerations reported in [Zerilli and Amstrong 1987, Nemat-Nasser and Li 1998] for determined **FCC** metals like **OFHC copper**.

$$\bar{\sigma}^*\left(\bar{\varepsilon}^p,\dot{\bar{\varepsilon}}^p,T\right)=\sigma^0\cdot\left(1-\left(-\frac{k\cdot T}{G_0}\cdot\left(\ln\left(\frac{\dot{\bar{\varepsilon}}^p}{\dot{\bar{\varepsilon}}_0}\right)+\ln\left(1+a\left(T\right)\cdot\left(\bar{\varepsilon}^p\right)^{n_0}\right)\right)\right)^{1/q}\right)^{1/p}\cdot\left(1+a\left(T\right)\cdot\left(\bar{\varepsilon}^p\right)^{n_0}\right) \qquad \textit{Eq. 5-3}$$

where σ^0 is a material constant, *k* is the Boltzmann constant, G_o is the reference Gibbs free energy at T=0 K *(it can be considered as an empirical parameter [Nemat-Nasser and Li 1998])*, $\dot{\varepsilon}_0$ is the reference strain rate, n_0 is a material constant defining strain hardening, *p*

and *q* are parameters describing the profile of the short range energy barrier to the motion of dislocations.

Moreover, a(T) is an empirical function depending on temperature and tied to the average dislocation spacing, Eq. 5-4. It contributes to the definition of the strain hardening of the material.

$$a\left(T\right) = a_0\left(1 - \left(\frac{T}{T_m}\right)^{n_2}\right) \qquad \textit{Eq. 5-4}$$

where a_0 and n_2 are material constants.

Some comments could be done concerning this constitutive relation [Rusinek et al. 2010]:

- Strain hardening is defined without taking into account the intrinsic effect of strain rate. The constancy of the strain hardening exponents n_i in the formulation is contrary to the observations frequently made and reported for metals in many publications, for example [Rusinek et al. 2007]. This fact may raise considerable relevance, especially in dynamic events susceptible for plastic instabilities, [Rusinek et al. 2009-a, Klepaczko et al. 2009].

- The model in its present form does not include definition of the electron and phonon drag effects *(viscous drag influence)* which may be of relevance at high strain rates and temperatures in **FCC** metals. However, in recent works [Kapoor and Nemat-Nasser 1999], Nemat-Nasser and co-workers gather such information for modeling these **FCC** materials.

- The constitutive relation does not account for the dependence of Young's modulus with temperature. It may lead to underestimation of the temperature sensitivity of the material.

More details concerning the formulation of the model and the calibration procedure can be found in [Nemat-Nasser and Li 1998].

Regarding the implementation of this model into a **FE** code, the material constants reported for annealed **OFHC copper** are shown in Table 5-4 [Nemat-Nasser and Li 1998].

p (-)	q (-)	k/G_0 (K^{-1})	$\dot{\varepsilon}_0$ (s^{-1})	a_0 (-)	σ^0 (MPa)	σ_a^0 (MPa)	n_0 (-)	n_1 (-)	n_2 (-)
2/3	2	0.000049	$2 \cdot 10^{10}$	20	46	220	0.5	0.3	2

*Table 5-4. Constants determined for annealed **OFHC copper** for NNL model [Nemat-Nasser and Li 1998].*

5.3.3 The VA model

Voyiadjis and Almasri [Voyiadjis and Almasri 2008] derived a physically-based model founded on the concept of thermal activation analysis. As for the previous constitutive descriptions introduced in this chapter, the equivalent Huber-Misses stress $\bar{\sigma}$ is split into

two parts, the equivalent thermal stress $\bar{\sigma}_\mu$ and the equivalent athermal stress $\bar{\sigma}^*\left(\bar{\varepsilon}^p, \dot{\bar{\varepsilon}}^p, T\right)$, Eq. 5-5.

$$\bar{\sigma}\left(\bar{\varepsilon}^p, \dot{\bar{\varepsilon}}^p, T\right) = \bar{\sigma}_\mu + \bar{\sigma}^*\left(\bar{\varepsilon}^p, \dot{\bar{\varepsilon}}^p, T\right) \qquad \textit{Eq. 5-5}$$

The athermal stress is defined without dependence on plastic strain which corresponds to ideal plasticity, Eq. 5-6.

$$\bar{\sigma}_\mu = Y_a \qquad \textit{Eq. 5-6}$$

where Ya is a material constant describing the stress component temperature and strain rate independent.

The thermal stress is defined as a function of plastic strain Eq. 5-7. It is derived from the concept of dislocation kinetics [Kocks et al. 1975].

$$\bar{\sigma}^*\left(\bar{\varepsilon}^p, \dot{\bar{\varepsilon}}^p, T\right) = \left(B \cdot \bar{\varepsilon}_p^n\right) \cdot \left(1 + B_1 \cdot T \cdot \left(\dot{\bar{\varepsilon}}_p\right)^{1/m} - B_2 \cdot T \cdot \exp\left(A\left(1 - \frac{T}{T_t}\right)\right)\right) \qquad \textit{Eq. 5-7}$$

In the previous expression *B* denotes the strain hardening modulus, *n* is the strain hardening exponent, B_1 and B_2 are material-constants tied, basically, to mobile dislocation-density evolution and to thermodynamic material-parameters [Voyiadjis and Almasri 2008], *m* defines the strain rate sensitivity and *A* is a material constant.

Some comments could be done concerning this constitutive relation [Rusinek et al. 2010]:

- As it was commented for *NNL* model, in the *VA* constitutive description strain hardening is defined without taking into account the intrinsic effect of strain rate.
- The expression used by the authors to define the velocity of dislocations derives in a formulation of the rate sensitivity of the form $\Delta\sigma\left(\dot{\bar{\varepsilon}}_i^p \rightarrow \dot{\bar{\varepsilon}}_{i+1}^p\right)\Big|_{\bar{\varepsilon}_p}^T \propto \left(\dot{\bar{\varepsilon}}^p\right)^{1/m}$. Such kind of expression neglects the rate sensitivity under quasi-static loading, overestimating it under dynamic loading, Fig. 5-1.

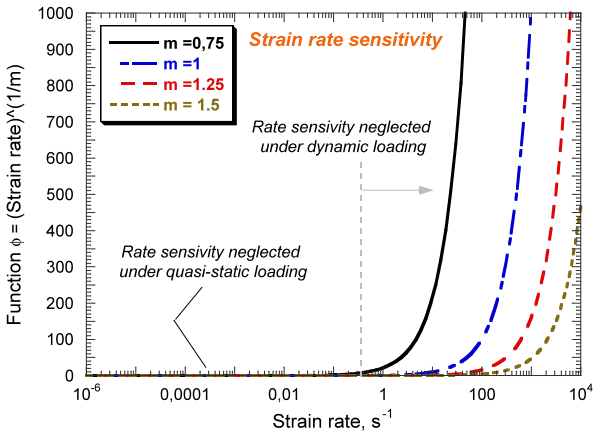

Fig. 5-1. Evolution of the function $\phi = \left(\dot{\bar{\varepsilon}}_p\right)^{1/m}$ *with increasing strain rate [Rusinek et al. 2010].*

- Temperature and rate sensitivities are decoupled in the formulation of the model. From the thermal activation analysis, and based on an Arrhénius-type equation, many researchers reported about the existence of reciprocity between strain rate and temperature [Kocks et al. 1975, Klepaczko 1975].

- As it was reported for *NNL* model, *VA* constitutive relation does not account for the dependence of Young's modulus with temperature.

More details concerning the formulation of the model and the calibration procedure can be found in [Voyiadjis and Almasri 2008].

Finally, for the *VA* constitutive relation the material constants reported for annealed **OFHC copper** are listed in Table 5-5 [Voyiadjis and Almasri 2008].

Y_a (MPa)	B_0 (MPa)	n (-)	B_1 (-)	B_2 (-)	m (-)	A (-)	T_t (K)
0	600	0.42	0.0000004	0.001	1.15	0.001	610

Table 5-5. Constants determined for annealed ***OFHC copper*** *for VA model [Voyiadjis and Almasri 2008].*

5.3.4 Direct consequences regarding the formulation of each constitutive description

The different definition of each one of the stress components leads to different strain rate sensitivities. In spite of under quasi-static loading conditions, the three constitutive relations fit quite reasonably the experimental results, Fig. 5-2-a, when dynamic conditions are applied, Fig. 5-2-b, considerable differences are found. In Fig. 5-2-b is depicted the flow stress evolution provided by each one of the models at a constant strain rate of 8000 s^{-1}. The constitutive relation which best fit experimental results seems to be the *Extended MRK*, Fig. 5-2-b.

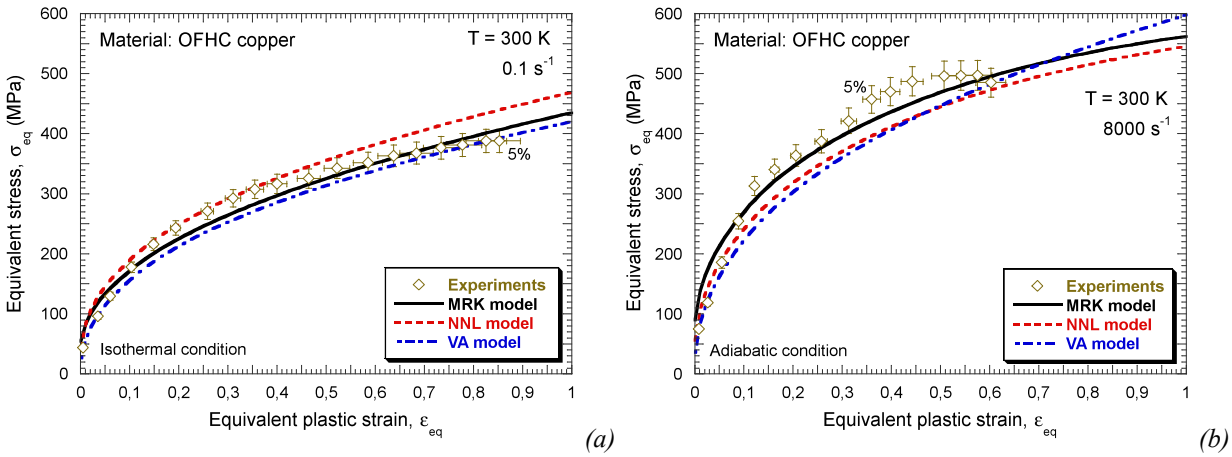

*Fig. 5-2. Description of the flow stress evolution versus plastic strain using Extended **MRK, NNL** and **VA** models and comparison with experiments at room temperature. (a) 0.1 s^{-1}, (b) 8000 s^{-1} [Rusinek et al. 2010].*

The differences observed above are highly related with the difference in the strain rate sensitivity definition of each model. This is one of the main important differences among the three models and must be taken into account in the following sections. As long as all the models provide similar value of the flow stress at low strain rates, when this strain rate increases, notable differences are observed, Fig. 5-3. The *NNL* defines slightly larger value of stress up to a certain strain rate level is reached. Beyond that point, *NNL* model underestimates the flow stress of the material since it does not account for the dislocations' drag effect, which takes place at high strain rates in annealed **OFHC copper** *(See Chapter 3)*. Moreover, *VA* model does not define properly the rate sensitivity of the material. As it was commented before, the *VA* constitutive relation neglects the rate sensitivity up to high strain rate level is achieved, $\dot{\bar{\varepsilon}}_p \approx 1000\ s^{-1}$, Fig. 5-3. In the case of $\dot{\bar{\varepsilon}}_p \geq 1000\ s^{-1}$, the rate sensitivity proposed is excessive, Fig. 5-3.

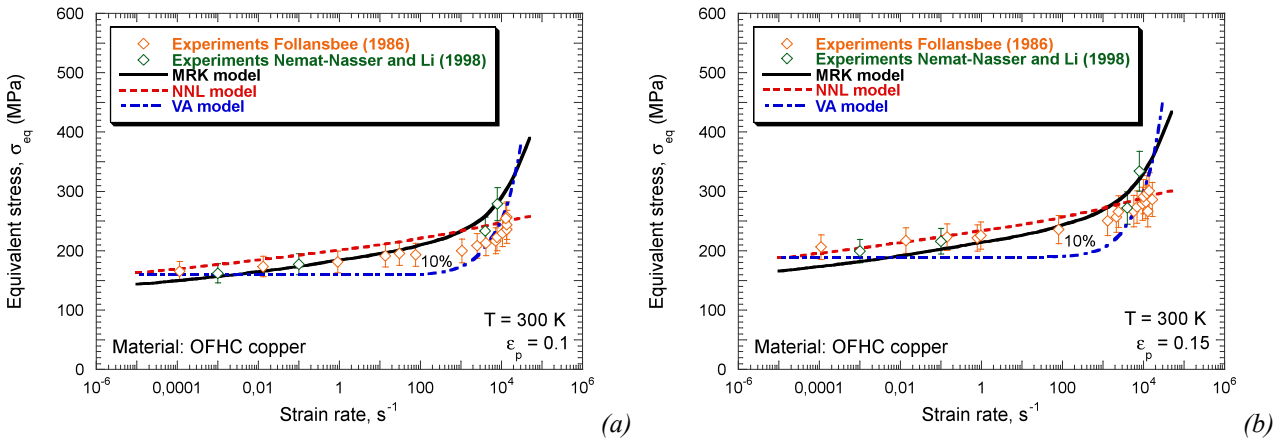

*Fig. 5-3. Description of the flow stress evolution as a function of strain rate using Extended **MRK, NNL** and **VA** models and comparison with experiments at room temperature. (a) ε_p=0.1, (b) ε_p=0.15 [Rusinek et al. 2010].*

In Fig. 5-4 is illustrated the rate sensitivity predicted by the constitutive relations considered for two values of plastic deformation, $\bar{\varepsilon}^p = 0.1$ and $\bar{\varepsilon}^p = 0.5$. The *NNL* model shows quite reduced rate sensitivity, lower than that provided by the *Extended MRK* formulation for the whole range of strain rates considered, Fig. 5-4. It has to be noted that for $\dot{\bar{\varepsilon}}^p \leq 10\ s^{-1}$ the rate sensitivity shown by the *VA* model is nil. Nevertheless, beyond that

point the rate sensitivity exhibited by this model sharply increases and it quickly exceeds the *Extended MRK* and *NNL* predictions.

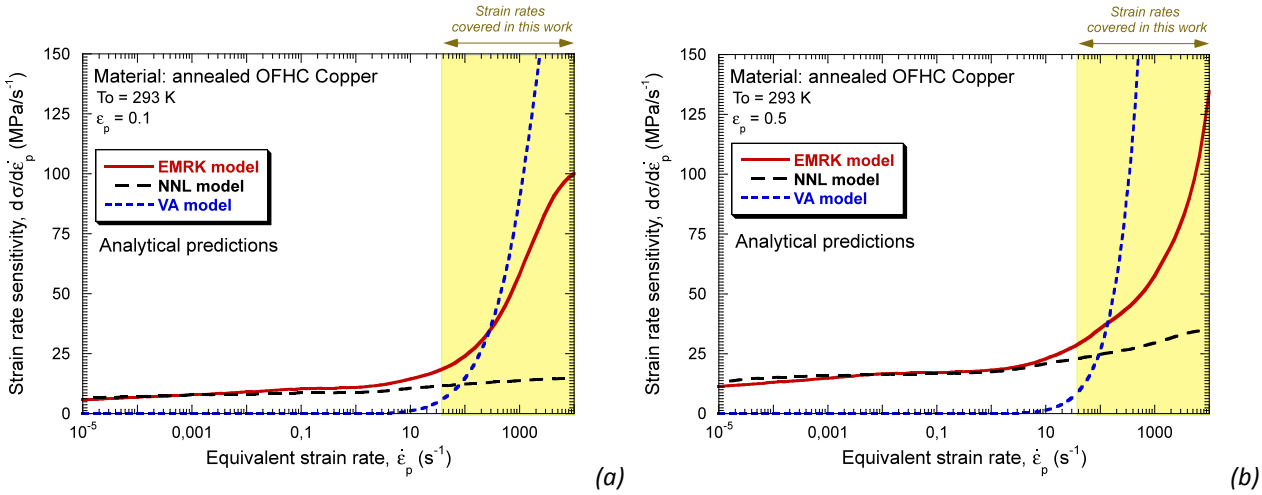

Fig. 5-4. Rate sensitivity predicted by the three models considered for different values of plastic deformation. (a) ε_p= 0.1, (b) ε_p= 0.5.

Related to the previous considerations, the flow stress estimated by each model under the same loading solicitations when different initial temperatures are used varies. The predictions of the models and their comparison with experiments are shown for different initial temperatures at high strain rate level, $\dot{\bar{\varepsilon}}_p \approx 4000\ s^{-1}$, Fig. 5-5 . For low temperatures, Fig. 5-5-a, the predictions of the *Extended MRK* and the *NN* model are quite similar, while the one provided by the *VA* model clearly underestimates the flow stress of the material. For the *Extended MRK* and *NNL* constitutive relations the difference with experiments only takes place at the beginning of loading. For larger value of initial temperature, T=600 K, Fig. 5-5-b, the three constitutive relations exhibit predictions in agreement with experiments. However, as the temperature increases, Fig. 5-5-c-d, the *VA* model starts to overestimate the flow stress.

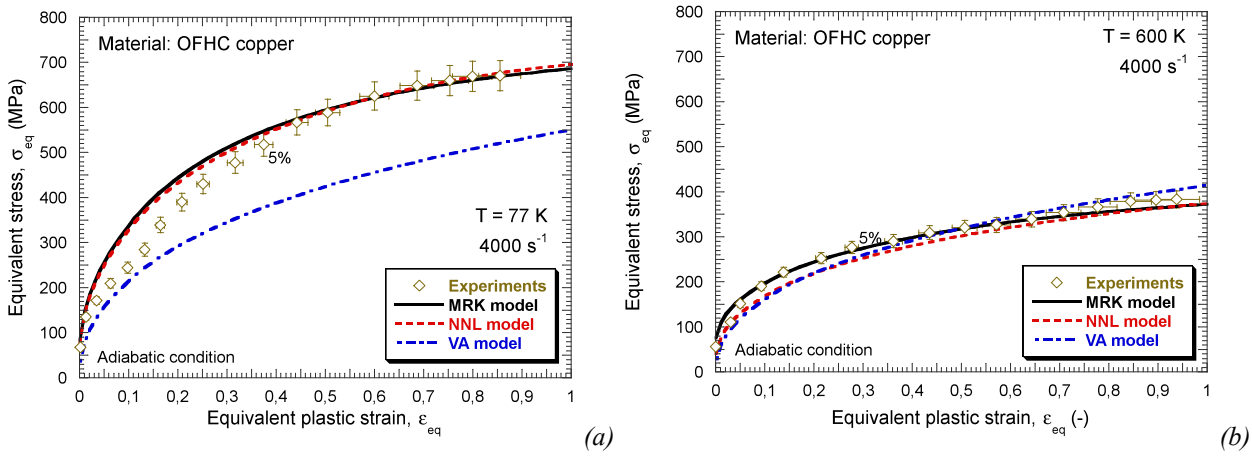

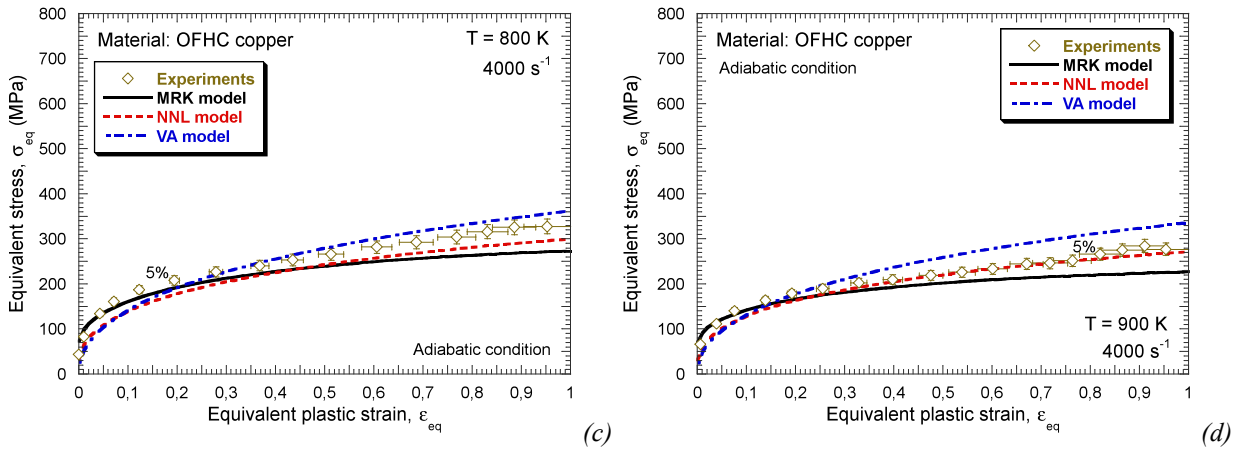

*Fig. 5-5. Description of the flow stress evolution as a function of plastic strain using Extended **MRK, NNL** and **VA** models and comparison with experiments at 4000 s^{-1}. (a) T_0=77 K, (b) T_0=600 K, (c) T_0=800 K, (d) T_0=900 K [Rusinek et al. 2010].*

The temperature sensitivity proposed by each model can be well observed in the following curves, Fig. 5-6. The *VA* relation shows temperature sensitivity lower than that observed in experiments. Moreover *Extended MRK* and *NNL* relations exhibit similar analytical predictions, close to experiments for the cases considered. However, the difference between these two models takes place at high temperature, $T_0 \geq 700\ \mathrm{K}$. Beyond that temperature level, the *Extended MRK* model predicts flow stress uniformly decreasing $\left(d\bar{\sigma}_{eq} / dT \approx cte\right)$ while *NNL* model predicts a decrease on the temperature sensitivity $\left(d\bar{\sigma}_{eq} / dT\big|_{T_0 \leq 700K} \geq d\bar{\sigma}_{eq} / dT\big|_{T_0 > 700K}\right)$, Fig. 5-6.

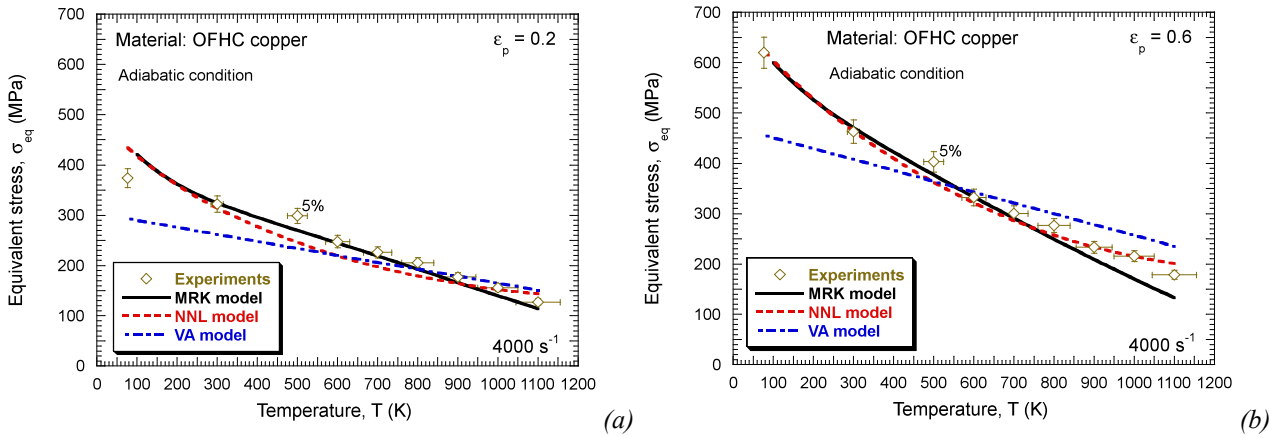

*Fig. 5-6. Temperature sensitivity description using Extended **MRK, NNL** and **VA** models and comparison with experiments at 4000 s^{-1}. (a) ε_p=0.2, (b) ε_p=0.6 [Rusinek et al. 2010].*

Next, the results obtained from numerical simulations of the three models are shown. The three constitutive relations have been implemented into ABAQUS/Explicit using the thermo-viscoplastic integration scheme for J2 plasticity proposed by Zaera and Fernández-Sáez [Zaera and Fernández-Sáez 2006] *(See Appendix I)*.

5.4 Analysis and results: the role played by the constitutive relation

Next, the results and conclusions obtained from the numerical analysis developed in this chapter are described. Firstly, a validation of the numerical models was performed. Once the models were validated, numerical simulations within wide range of impact velocities were carried out in order to obtain conclusions about the role of the constitutive relation on flow localization under dynamic loading conditions.

5.4.1 Numerical configuration and validation of the models

In this chapter, two different dynamical tests have been used. These are the same tests used before, the dynamic tension test and the ring expansion test.

Then, the information about the geometry, type of mesh used or boundary conditions applied, can be easily looked up in Chapter 3 *(for the case of the dynamic tension test)* and Chapter 4 *(for the case of the ring expansion test)*.

Next, the validation of both numerical models is carried out for the three constitutive descriptions. This ensures the implementation of the constitutive relation into ABAQUS/Explicit is correctly performed.

5.4.1.1 Dynamic tension test

Simulations at an impact velocity of V_0 = 5 m/s were carried out in order to validate this numerical configuration. Stress and strain data were extracted from an integration point belonging to an element out of the necking zone *(placed on the active part of the specimen),* Fig. 3-10. There, the flow stress can be considered homogeneous and the strain rate remains *(approximately)* constant along the test. Then, a proper comparison with analytical predictions for an imposed rate level can be carried out.

Next, in Fig. 5-7 are depicted stress-strain curves for the three models studied. The three models (*Extended MRK*, *NNL and VA)* provide quite well agreement between analytical and numerical results. As it is easily observed, numerical results match analytical curves during the whole simulation. Again, differences only appear once stress saturation has happened in the material *(*$\mathrm{d}\overline{\sigma}/\mathrm{d}\overline{\varepsilon}^{\mathrm{p}} = 0$*)*. It validates the boundary conditions applied in the numerical configuration as well as the implementation of the constitutive relations into the **FE** code.

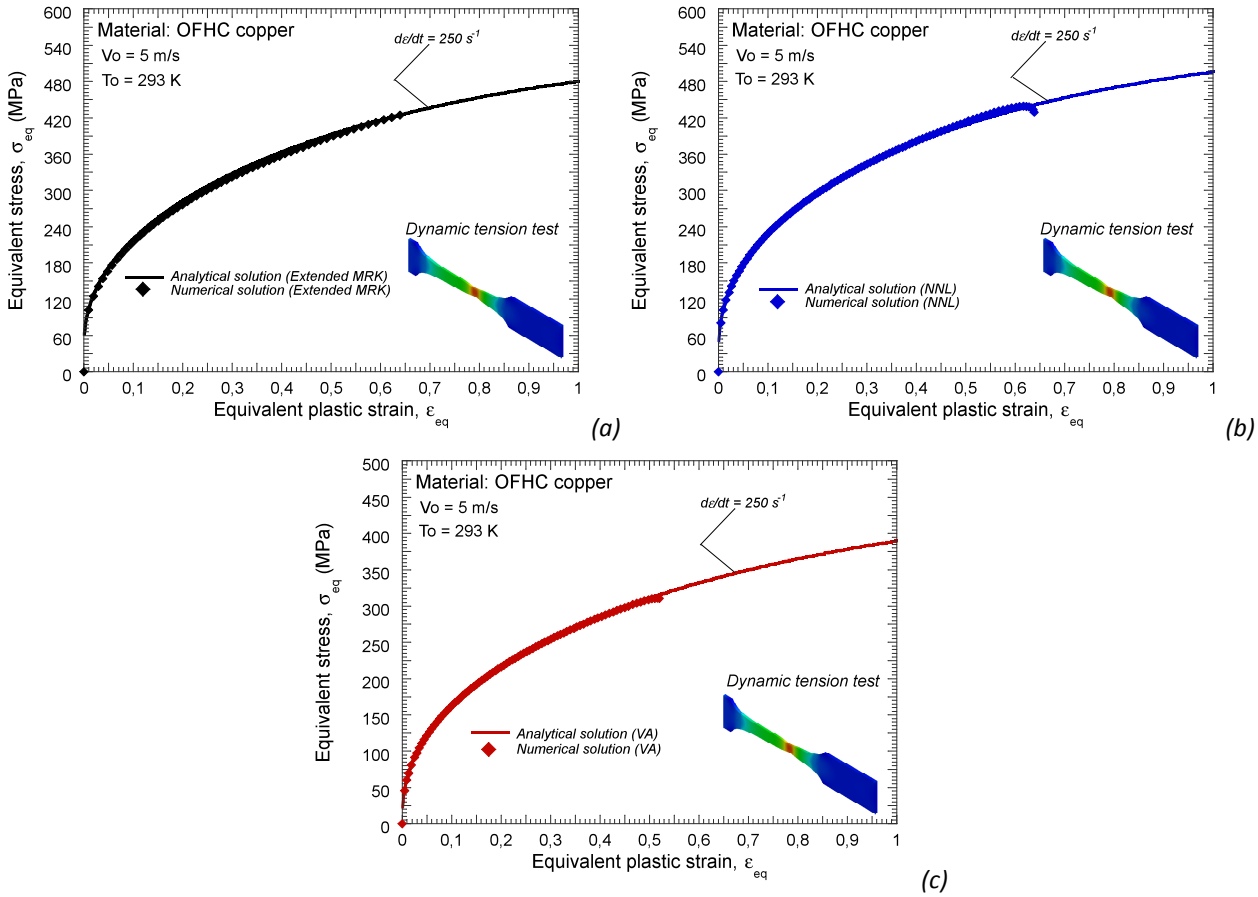

Fig. 5-7. Stress-strain curves (both simulation results and analytical predictions) at V_0 = 5 m/s and the three models. (a) Extended MRK model, (b) NNL model, (c) VA model.

5.4.1.2 Ring expansion test

Again, stress – strain curves obtained from simulations *(global deformation of the sample corresponding to the theoretical one)* for an input velocity of V_0 = 5 m/s are compared with the analytical predictions of the constitutive relation. During the simulations, the measurement is conducted on an integration point belonging to an element out of the necking zone *(placed on the active part of the specimen),* Fig. 4-12. There, the flow stress can be considered homogeneous.

Perfect matching is observed between analytical predictions and simulation results *(except for the **EMRK** model for which the decrease of the strain rate during the test is responsible for the small disagreement taking place at large deformation),* Fig. 5-8. The matching between analytical and numerical results validates both the boundary conditions applied in the numerical configuration of the ring and the implementation of the constitutive relations into the **FE** code.

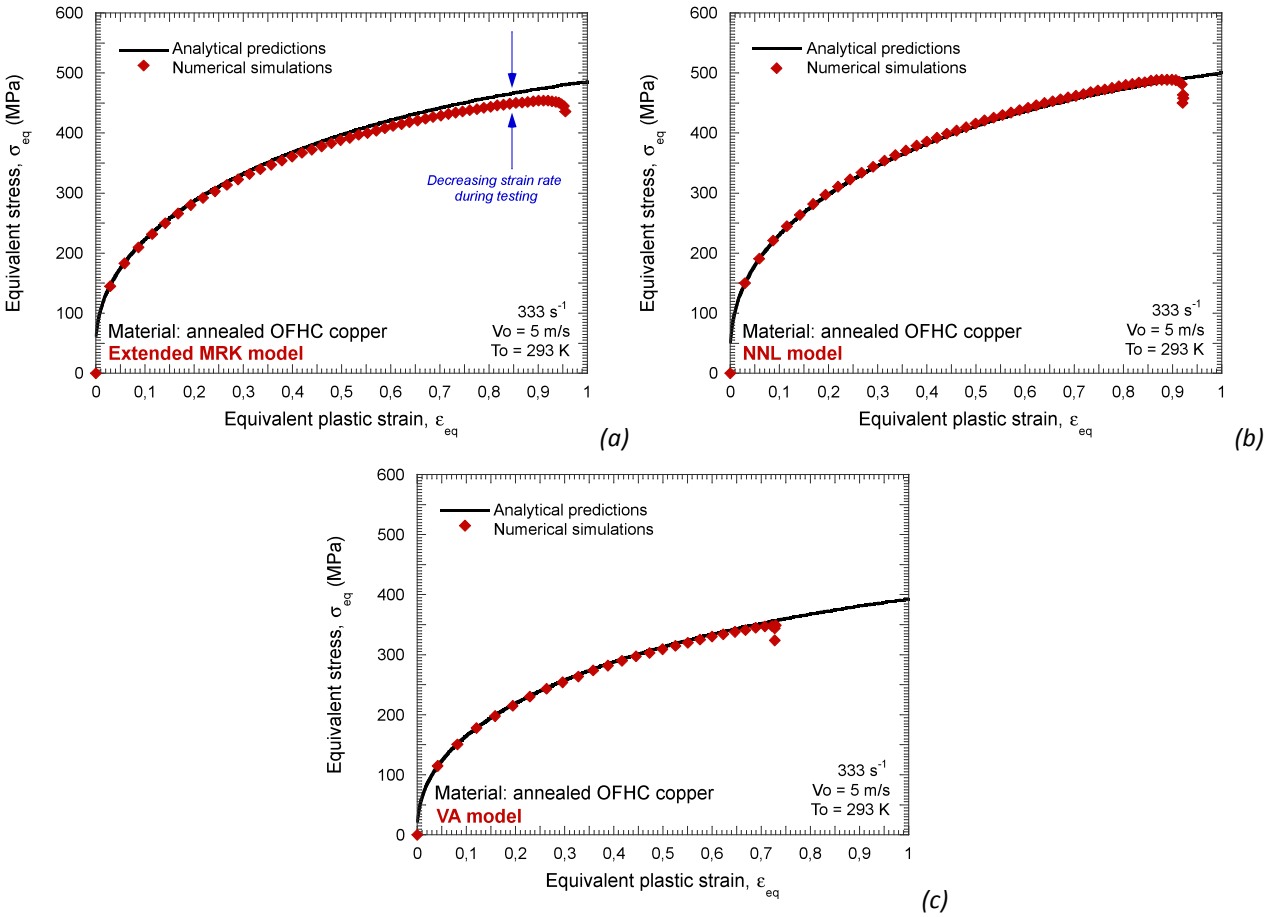

Fig. 5-8. Stress-strain curves (both simulation results and analytical predictions) for the three different models at 5 m/s. (a) Extended MRK model, (b) NNL model, (c) VA model.

Once the numerical configuration is validated, an analysis on the role played by the formulation on the flow localization in **OFHC copper** is conducted.

5.4.2 Remarks on the role played by the constitutive relation

In order to understand properly why the physical assumptions used in the formulation of the constitutive relation may have influence on plastic instabilities predictions in the sample, it is very important to bear in mind the relative importance each author gives for the thermal and the athermal stress components. In the following figure, Fig. 5-9, is depicted how the stress is decomposed in each one of the studied models for two different impact velocities. Very strong differences are found. Some important comments can be done regarding these results:

- Despite the fact that the *Extended MRK* is the only model that takes into account the viscous-drag effect, the contribution of this stress component to the overall stress is low. This aspect has already been studied in previous chapters *(See Chapter 3)*.

- While the *Extended MRK* and *VA* models consider that athermal stress as constant, the NNL consider this term dependent on plastic strain.

- Thus, the strain hardening of the *Extended MRK* and *VA* models only depends on the thermal stress.

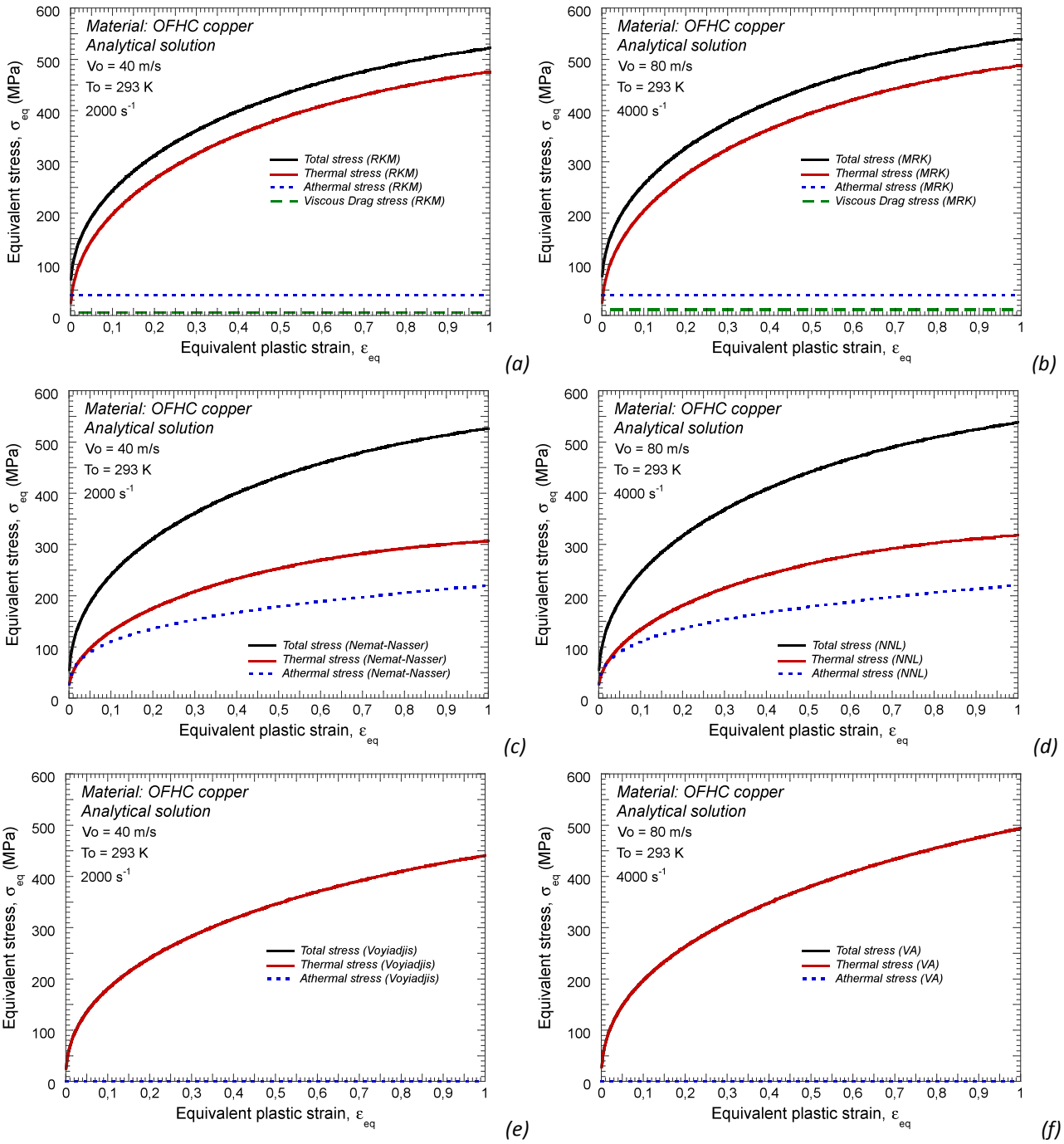

Fig. 5-9. Decomposition of the overall flow stress into its respective stress components for each one of the models analyzed at Vo = 40 m/s and Vo = 80 m/s. (a)-(b) Extended MRK model, (c)-(d) NNL model, (e)-(f) VA model.

However for strain rate levels between those analyzed in previous graphs, $0.1\ \mathrm{s}^{-1} < \dot{\bar{\varepsilon}}^{p} < 8000\ \mathrm{s}^{-1}$, the *VA* model provides predictions of material flow stress quite lower than those due to the Extended *MRK* and *NNL* formulations, Fig. 5-10.

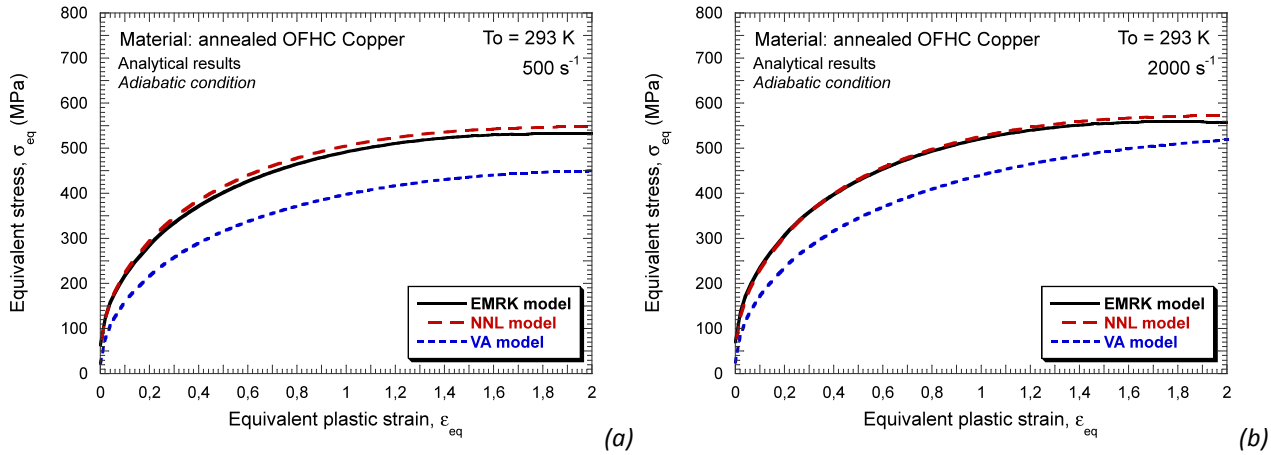

*Fig. 5-10. Description of the flow stress evolution as a function of plastic strain using Extended MRK, NNL and **VA** models at room temperature. (a) 500 s^{-1}, (b) 2000 s^{-1}.*

Nevertheless, it must be highlighted that the strain hardening definition provided by the three models is quite similar for the whole range of strain rates analyzed, Fig. 5-11.

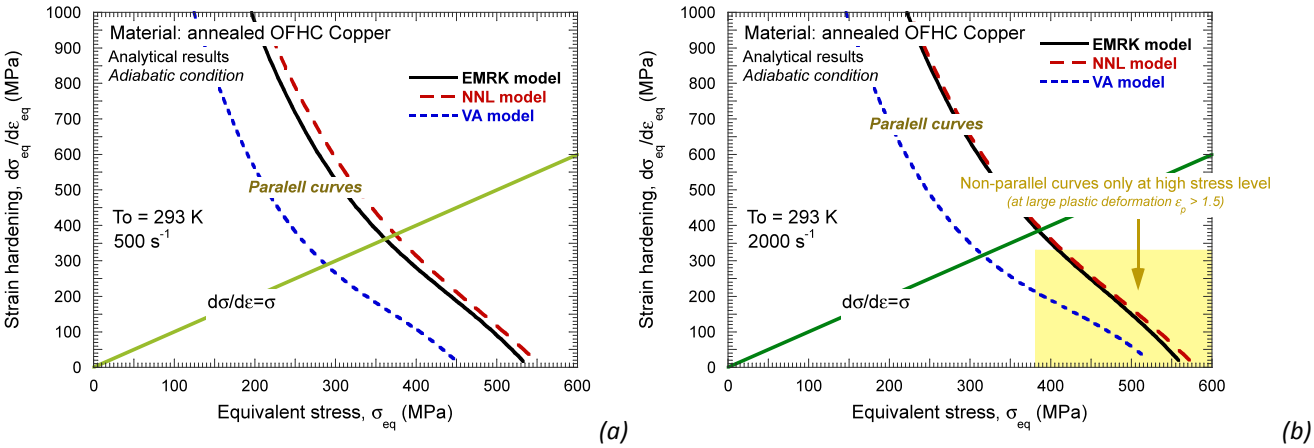

*Fig. 5-11. Description of the strain hardening evolution as a function of equivalent stress using Extended **MRK, NNL** and **VA** models at room temperature. (a) 500 s^{-1}, (b) 2000 s^{-1}.*

Next, the results obtained from the numerical simulations developed in ABAQUS/Explicit are analyzed. First, the ring expansion test results are discussed.

5.4.2.1 The ring expansion case

First step is to analyze the evolution of the local plastic strain with the global one *(theoretical deformation corresponding to homogeneous behaviour)* for the three constitutive descriptions and different impact velocities. The measurement of the local plastic strain evolution is conducted as depicted in Fig. 4-14'.

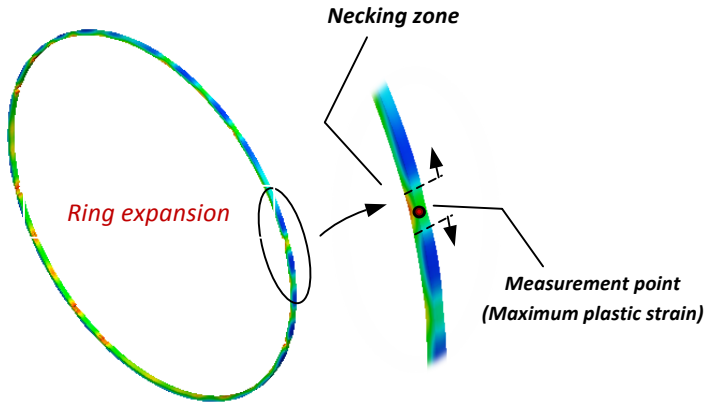

Fig 4-14'. Measurement point of local plastic strain in ring expansion configuration.

The method applied here, as it has been discussed in previous chapters, follows the considerations of Triantafyllidis and Waldenmyer [Triantafyllidis and Waldenmyer 2004]. The bifurcation point *(strain of instability)* is highly dependent on impact velocity as well as on the constitutive model applied.

In Fig. 5-12 are represented the results obtained at three different impact velocities within the range considered. For the three loading conditions, the *VA* model predicts higher strains of instability than the *Extended MRK* and *NNL*. Furthermore, the difference in the plastic strain of instability increases with the strain rate, Fig. 5-12-b-c. The results for the *NNL* and the *Extended MRK* model seem to be similar. However, when the strain rate level is high the *Extended MRK* model predicts a higher strain of instability because of the *NNL* does not take into consideration the effect of the dislocations-drag mechanism *(See conclusions of Chapter 3)*.

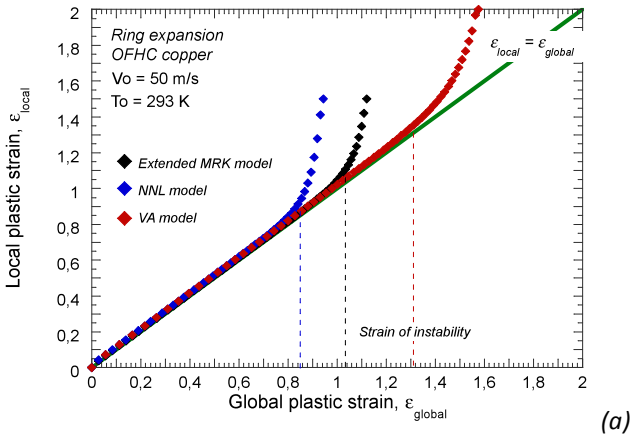

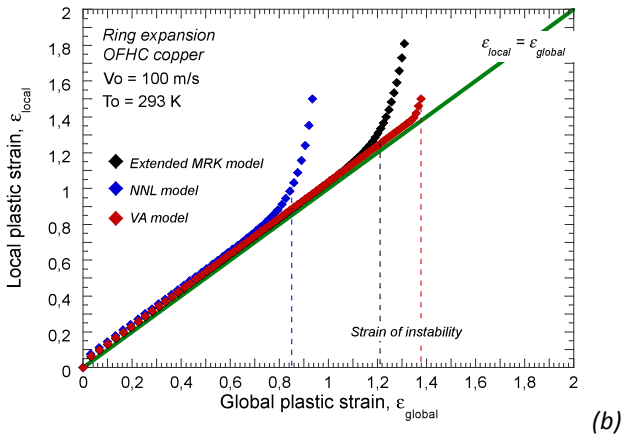

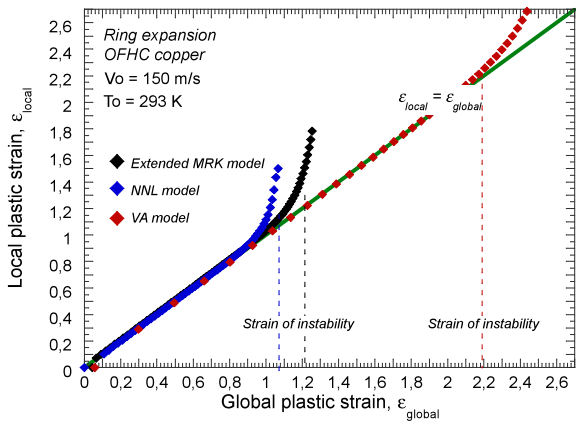

*Fig. 5-12. Evolution of the local plastic strain with the global plastic strain for Extended **MRK, NNL** and **VA** models. (a) Vo= 50 m/s, (b) Vo=100 m/s, (c) Vo=150 m/s.*

For the whole range of impact velocities the strain of instability predicted by the *Extended MRK* model is larger than that shown by the *NNL* formulation, Fig. 5-13. The difference between the predictions of both models increases with impact velocity, Fig. 5-13.

Moreover, the *VA* constitutive description shows the lowest strain of instability until V_0=10 m/s, Fig. 5-13. Then, it exceeds the predictions of the *NNL* model. Subsequently for V_0>10 m/s the strain of instability shown by the *VA* constitutive relation becomes the largest one, Fig. 5-13. The range of impact velocities V_0 < 10 m/s corresponds to initial strain rates of the test $\dot{\bar{\varepsilon}}^p \leq 650\ s^{-1}$ *(the strain rate applied to the material will decrease during loading from this value)*. It has to be noted that within that range of strain rates the rate sensitivity predicted by the *VA* model is the lowest one, Fig. 5-13. The range of impact velocities V_0>10 m/s corresponds to initial strain rates of the test $\dot{\bar{\varepsilon}}^p \geq 650\ s^{-1}$. It has to be noted that within that range of strain rates the rate sensitivity predicted by the *VA* model becomes the largest one, Fig. 5-13. It becomes clear that rate sensitivity and strain of instability are closely related.

As larger the rate sensitivity as larger the strain of instability *(it has to be taken into account that the strain hardening predictions of all the models are very similar. Strain hardening is not responsible for the differences on the strain of instability shown in* Fig. 5-13*)*. This consideration explains the increasing strain of instability with impact velocity exhibited by the three constitutive relations, Fig. 5-13. Since all constitutive models show increasing rate sensitivity with strain rate augment *(within the range of impact velocities considered in this investigation)*, the strain of instability is always increasing with impact velocity augment.

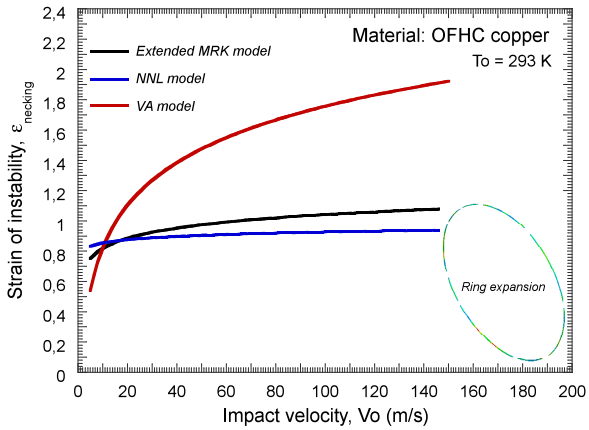

*Fig. 5-13. Strain of instability as a function of impact velocity for Extended **MRK, NNL** and **VA** models.*

Such trends are confirmed analyzing the evolution of the local plastic strain rate in the necking as a function of the global plastic strain, Fig. 5-14. In such a case the strain of instability is determined by the bifurcation point of the local strain rate from the theoretical one, Fig. 5-14. Necking formation involves a sharp augment of the local strain rate and flow stress. This process increases material temperature leading to subsequent fragmentation of the ring.

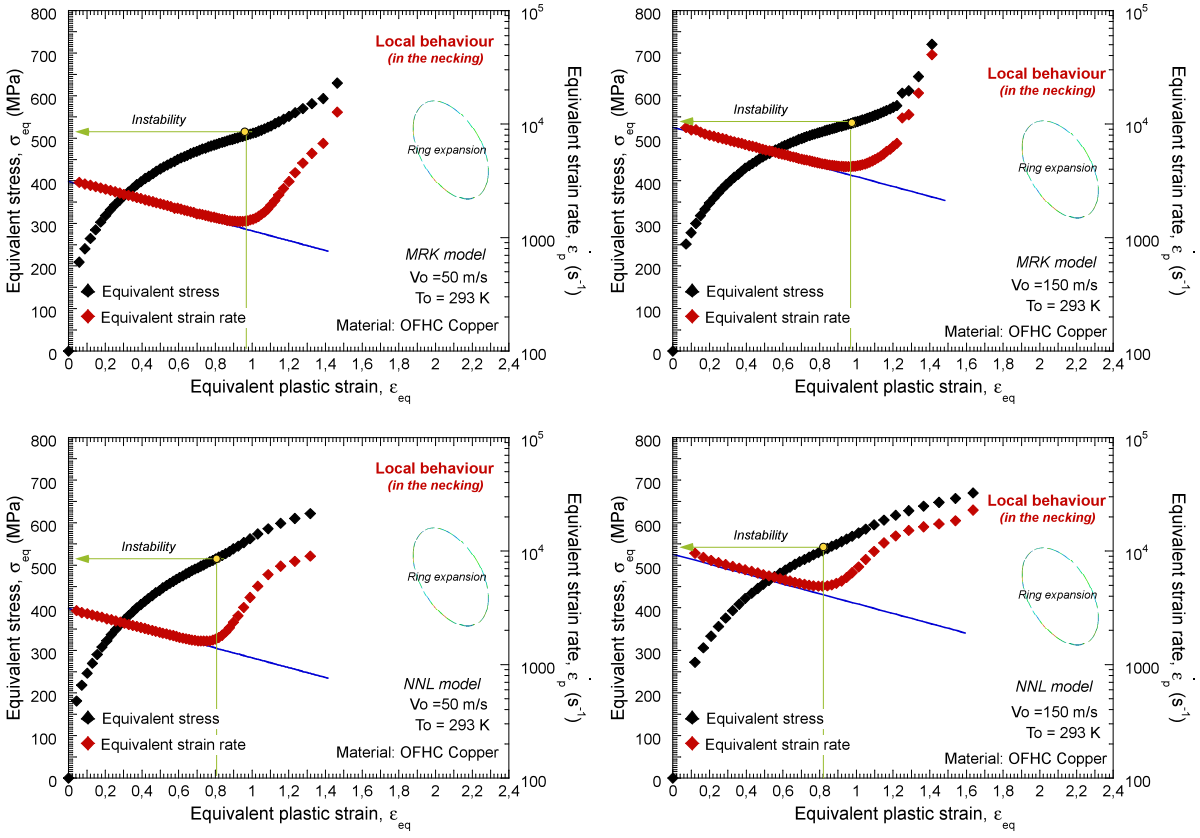

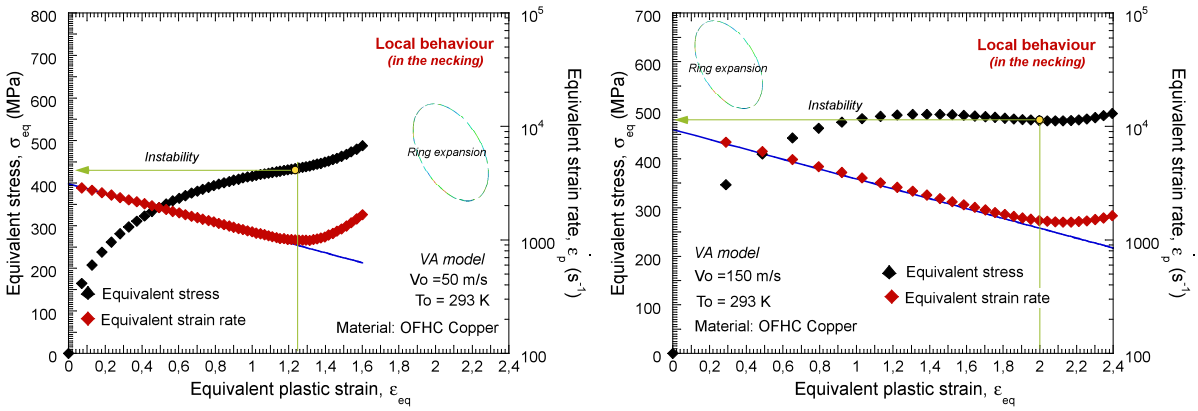

Fig. 5-14. Evolution of the strain rate in the necking as a function of plastic strain for the three material configurations considered and different impact velocities.

In Fig. 5-15 is illustrated, for the three constitutive descriptions, the evolution of the time of instability with impact velocity. Within the range of impact velocities into which the *VA* model shows the lowest rate sensitivity, it predicts the smallest time of instability, Fig. 5-15. Opposite behaviour is observed within the range of impact velocities into which the *VA* formulation predicts the largest rate sensitivity, Fig. 5-15.

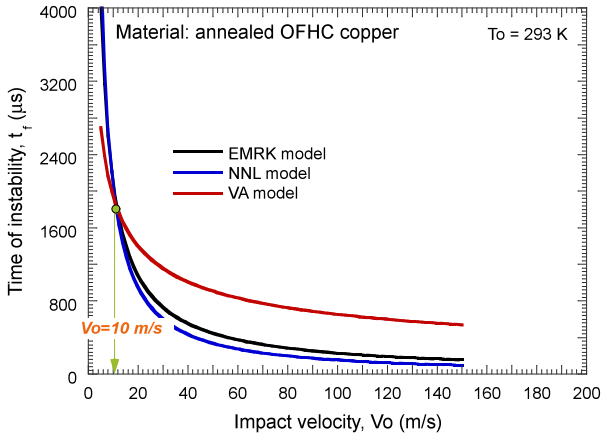

Fig. 5-15. Time of instability as a function of the impact velocity for the three constitutive descriptions considered.

Such relation between rate sensitivity and instabilities formation is patently clear analyzing the number of necks taking place in the sample *(as previously discussed the number of necks is independent of the failure strain applied in the simulation if this is large enough to not disturb the strain localization process)*, Fig. 5-16. The largest rate sensitivity leads to the largest number of necks. Therefore increasing impact velocity leads to increasing number of necks for all the models analyzed [Mercier and Molinari 2004, Rusinek and Zaera 2007].

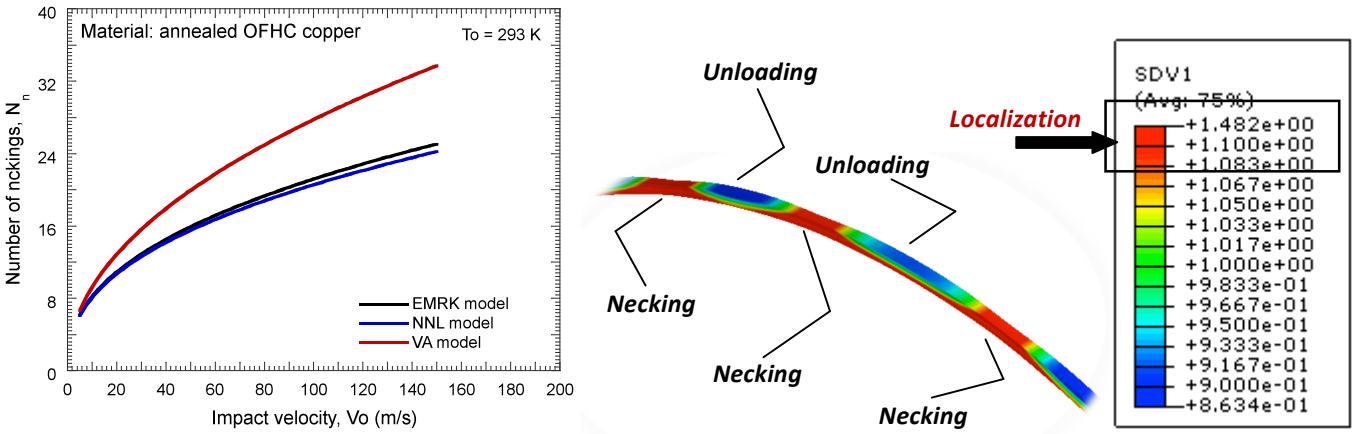

Fig. 5-16. Number of necks as a function of the impact velocity for the three constitutive descriptions considered. Plastic strain contours of the ring during loading for determination of the number of necks.

Analogous analysis can be done for explaining the relation between the number of fragments and the strain rate sensitivity *(and the impact velocity [Hu and Daehn 1996, Mercier and Molinari 2004, Rusinek and Zaera 2007])*, Fig. 5-17. Rate sensitivity retards flow localization; a large number of fragments is related to materials suitable for absorbing energy under high loading rates.

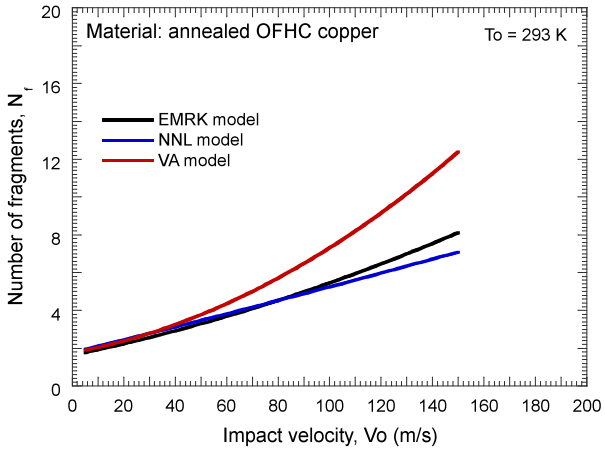

Fig. 5-17. Number of fragments as a function of the impact velocity for the three constitutive descriptions considered.

These considerations can be clearly observed in the following plots, Fig. 5-18 and Fig. 5-19. First of all, in Fig. 5-18, the plastic strain contours of the ring are shown just after instability appears for two different impact velocities. Moreover, the ring diameter variation is indicated. It is clear that this variation increases with strain of instability. Thus, for the case of the most stable model *(VA)*, the ring diameter variation predicted is considerable larger than for the case of the *Extended MRK* and *NNL*. In Fig. 5-19 are represented strain contours after failure indicating the number of fragments in each case. Higher number of fragments is predicted with the *VA* model due to the high strain rate sensitivity of the model at high strain rates, which indicates that the plasticity is spread along the ring.

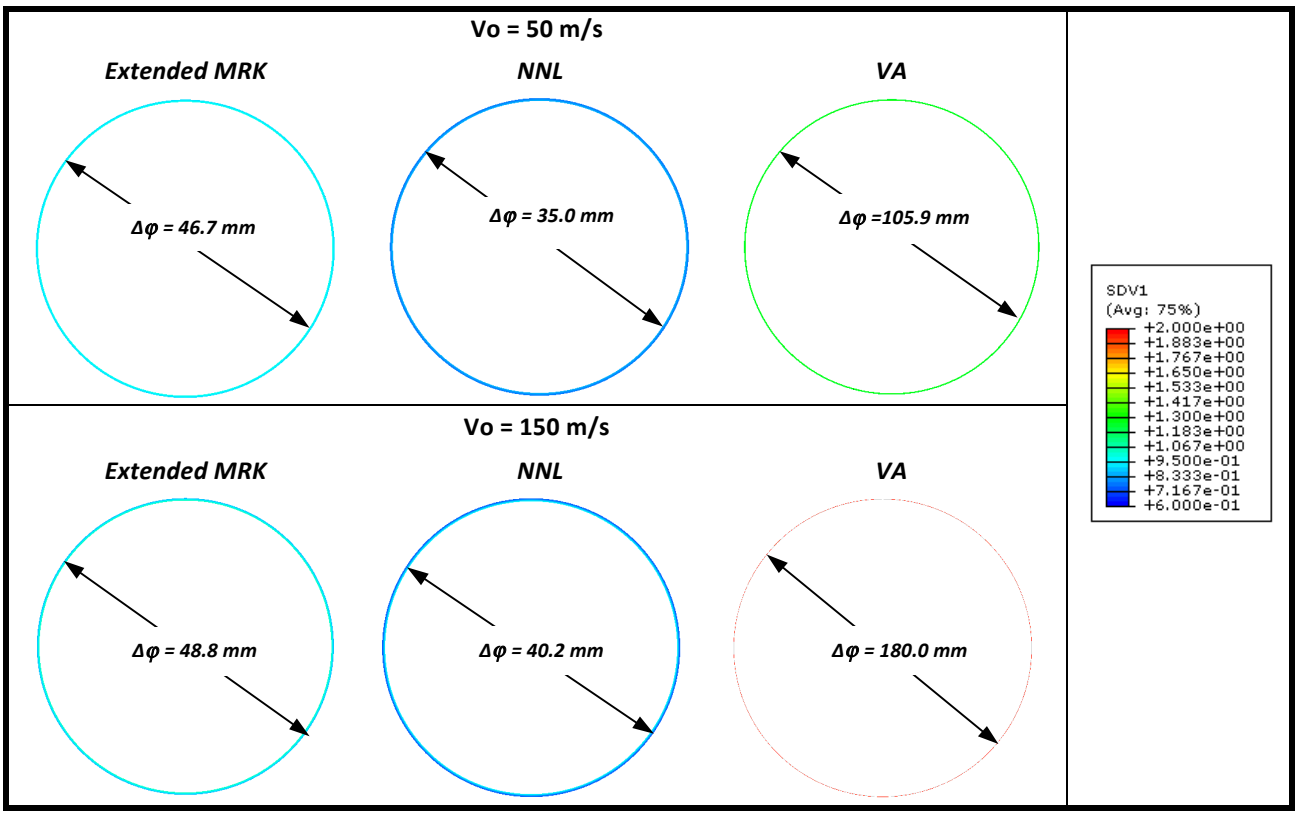

Fig. 5-18. Ring diameter variations just after plastic instability is produced at two different impact velocities, 50 m/s and 100 m/s.

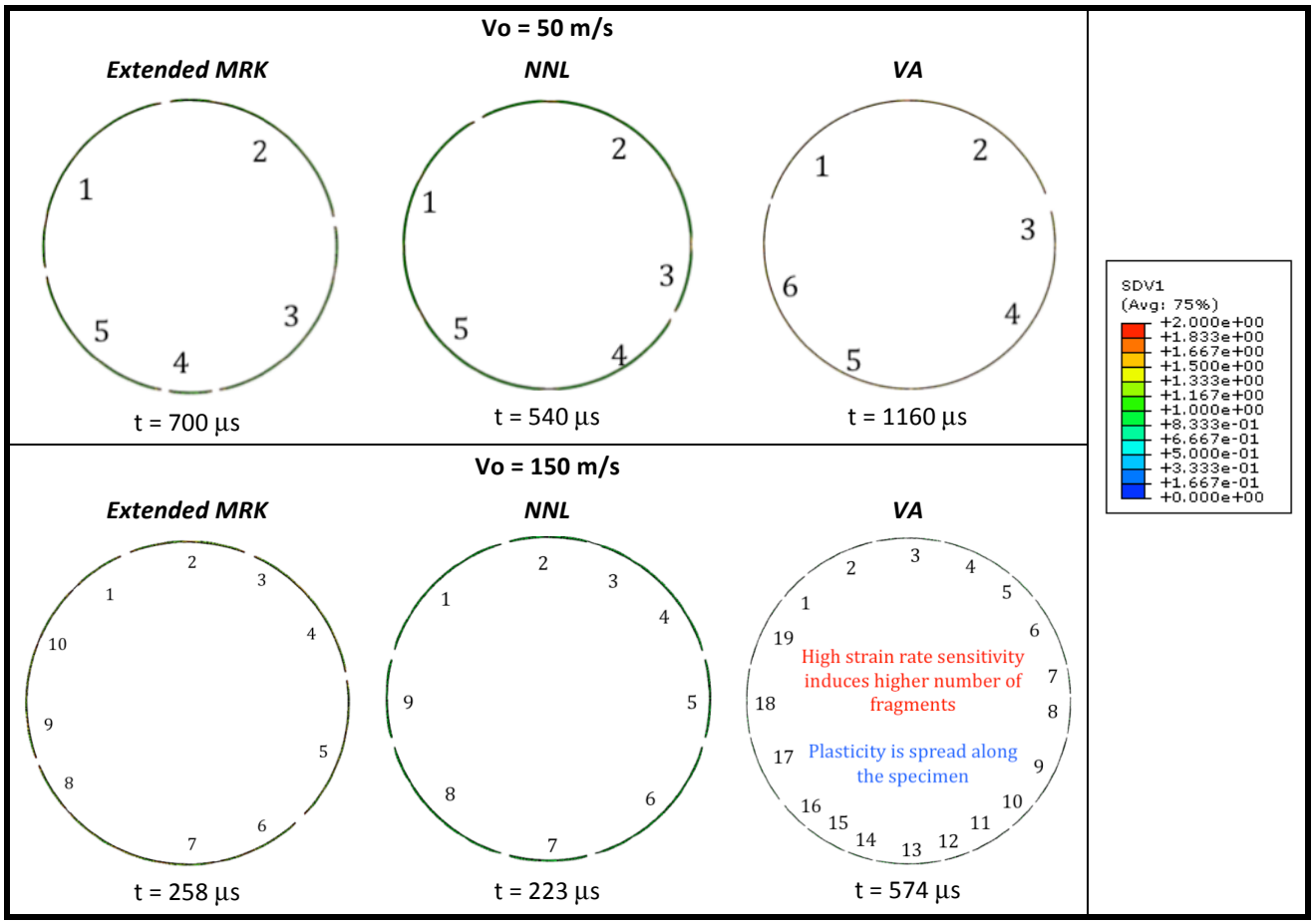

Fig. 5-19. Strain contours just after the failure is produced ($\varepsilon_f = 2.5$) and number of fragments in each case for two different impact velocities, 50 m/s and 100 m/s.

Next, the results extracted from the simulations carried out using the dynamic tension test are analyzed.

5.4.2.2 The dynamic tension case

As it was reported for the ring expansion case, first step is analyzing the evolution of the local plastic strain with the global one for the three constitutive descriptions and different impact velocities. The measurement technique for the local plastic strain is depicted in Fig. 3-14'.

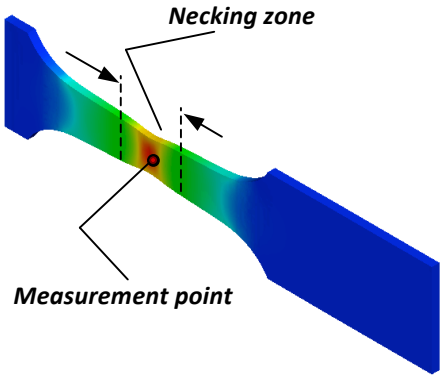

Fig. 3-14'. Measurement point of local plastic strain in dynamic tension test configuration.

In Fig. 5-20-a can be observed that for an impact velocity of $V_0 = 40\ m/s$, the plastic strain of instability is approximately the same for the three models. However, a slightly lower value for this plastic strain of instability is found in case of considering the *NNL* model. The difference between the instability predicted by the *MRK* and the *NNL* model is hardly observed in the range 90 - 120 m/s *(within this range of velocities, **CIV** has been exceeded for both models)*. Furthermore, as the impact velocity increases the difference between estimations of the *VA* model and the *MRK* and *NNL* models increases in a very notable way due to the overestimation of the strain rate sensitivity of the *VA* model, Fig. 5-20-d.

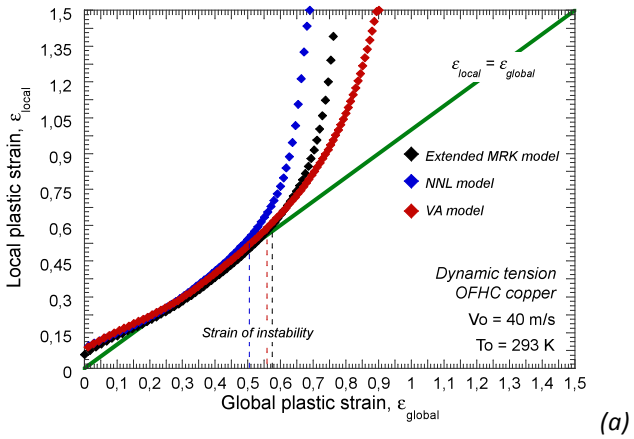

(a)

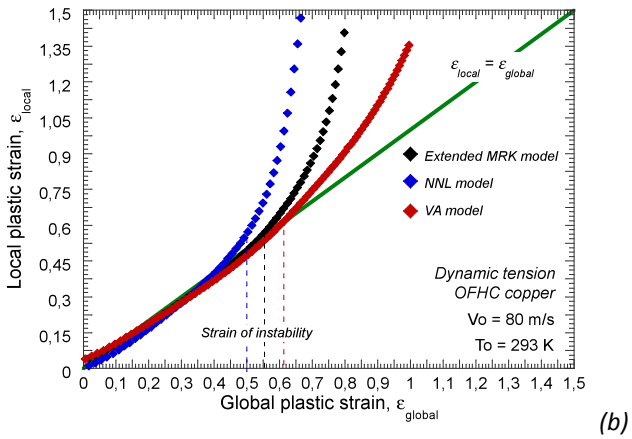

(b)

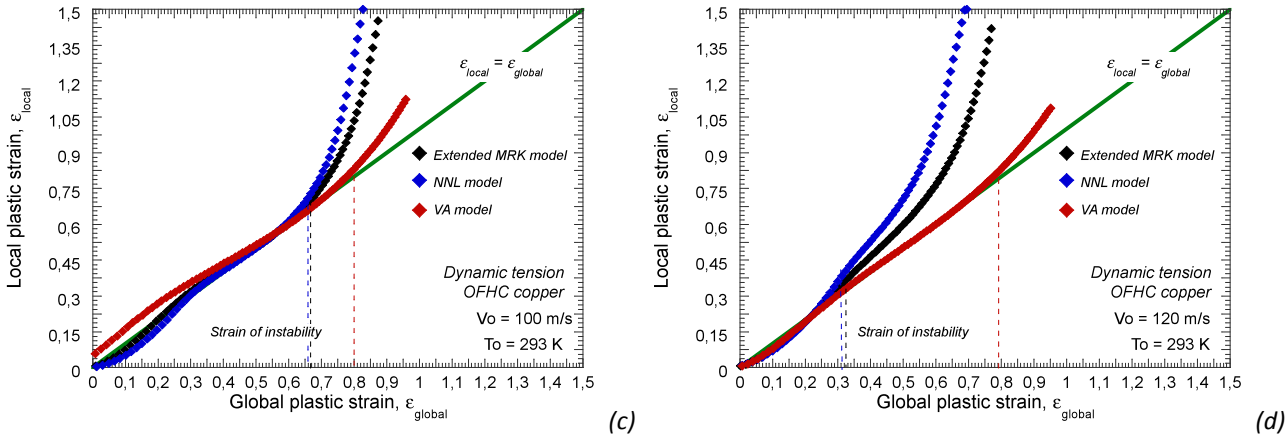

*Fig. 5-20. Evolution of the local plastic strain with the global plastic strain for Extended **MRK, NNL** and **VA** models. (a) Vo=40 m/s, (b) Vo=80 m/s, (c) Vo=100 m/s, (d) Vo=120 m/s.*

Next, it is showed the evolution of the strain of instability with impact velocity for *Extended MRK, NNL* and *VA* models, Fig. 5-21. It must be noticed that the strain of instability for the dynamic tension tests is much more reduced than that observed for the ring expansion case, Fig. 5-13.

As it is shown in Fig. 5-21, at low impact velocities the strain of instability predicted by Extended *MRK* and *VA* matches while the one predicted by the *NNL* is lower. The trend predicted by the three models is similar until the **CIV** of Extended *MRK* and *NNL* is reached. Then, due to the high strain rate sensitivity predicted by the *VA* model at high strain rates, the **CIV** is higher than in case of Extended *MRK* and *NNL*.

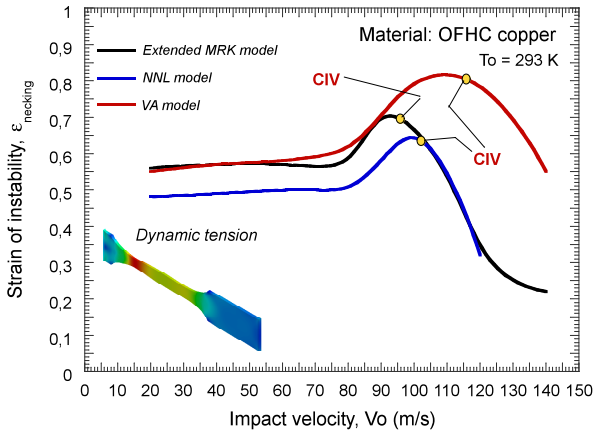

Fig. 5-21. Strain of instability as a function of impact velocity for the three models.

The **CIV** showed in previous figure, Fig. 5-21, has been estimated by comparison of input (at the impacted site, Fig. 3-4) and output (at the clamped site, Fig. 3-4) forces, Fig. 5-22. The **CIV** is supposed to be the impact velocity at which both forces do not reach equilibrium as reported in [Rusinek et al. 2005, Rodríguez-Martínez et al. 2009].

Both input and output forces for *Extended MRK* and *NNL* models are very similar in all cases. Moreover, at an impact velocity of 100 m/s, the behaviour for the *Extended MRK* and *NNL* model is unstable, while for the *VA* model is still stable *(the equilibrium is obtained at the end of the simulation)*. Then, the **CIV** is increased in case of considering the *VA* model mainly because of the high strain rate sensitivity of the model at high strain rates of

deformation. Notice that when an impact velocity higher than the **CIV** is studied, the plasticity is localized, Fig. 5-22-b-d-g.

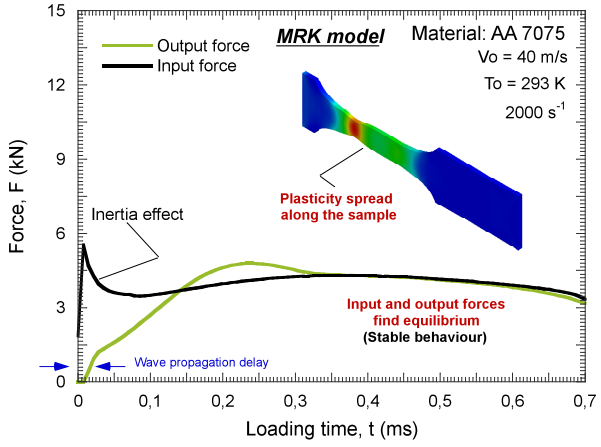

(a)

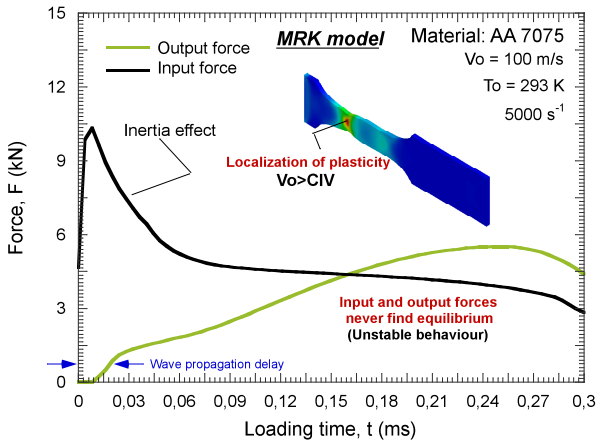

(b)

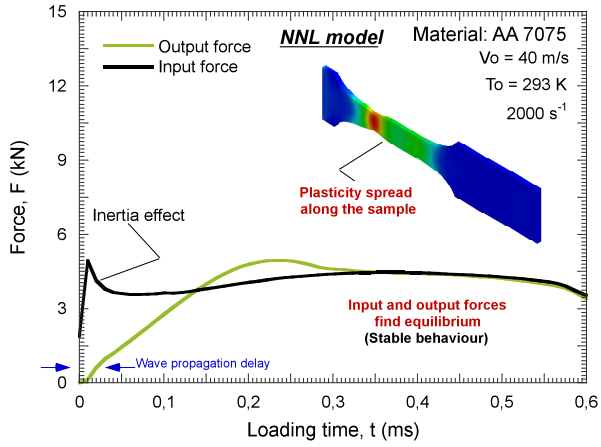

(c)

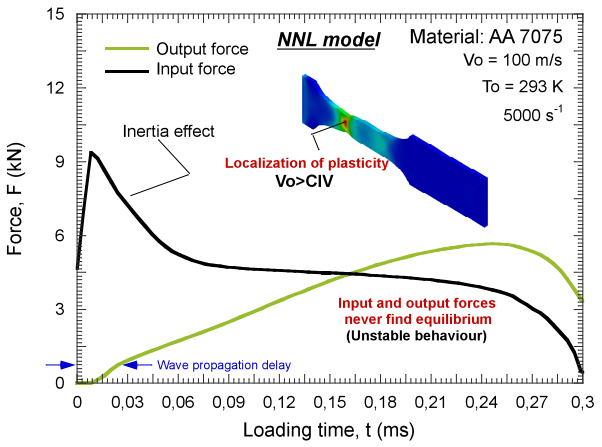

(d)

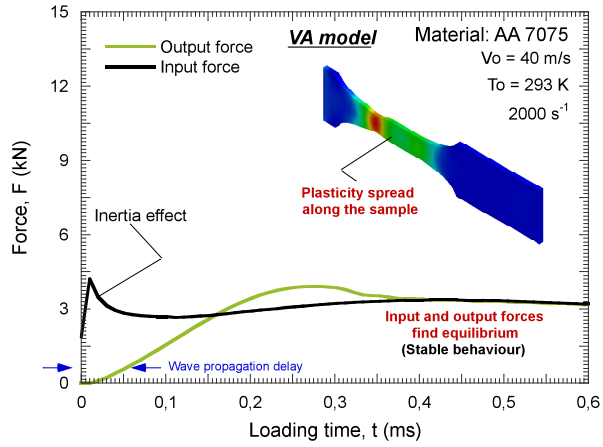

(e)

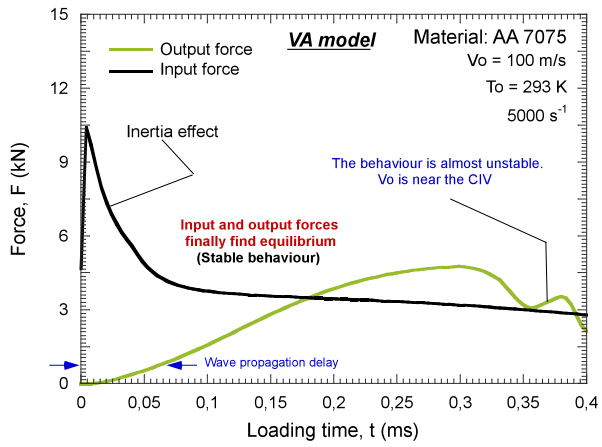

(f)

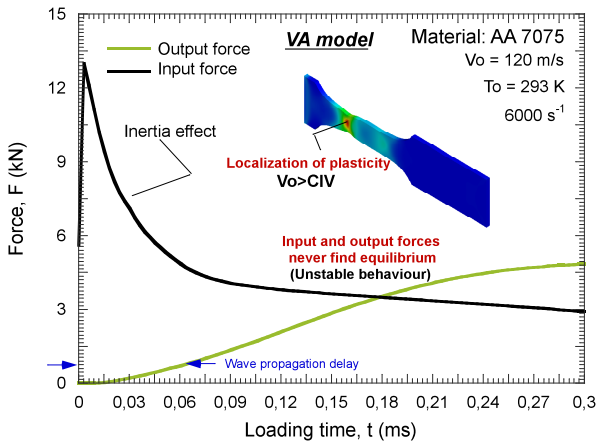

*Fig. 5-22. Output and input forces for Extended **MRK, NNL** and **VA** models at different impact velocities.*

Next, it is interesenting to study the local behaviour of the three models when the **CIV** of the *Extended MRK* and *NNL* models have been reached. As it is depicted in Fig. 5-23-a, the strain rate level does not vary until instability appears in *Extended MRK* and *NNL* models. Despite the equivalent strain rate is similar for the three models, the flow stress is completely different, Fig. 5-23-b. At this impact velocity the curves of the flow stress for the *Extended MRK* and *NNL* match. However, the *VA* constitutive relation predicts lower stress level in the necking zone, Fig. 5-23-b. This aspect contributes to increase the plastic strain of instability of the material, Fig. 5-21.

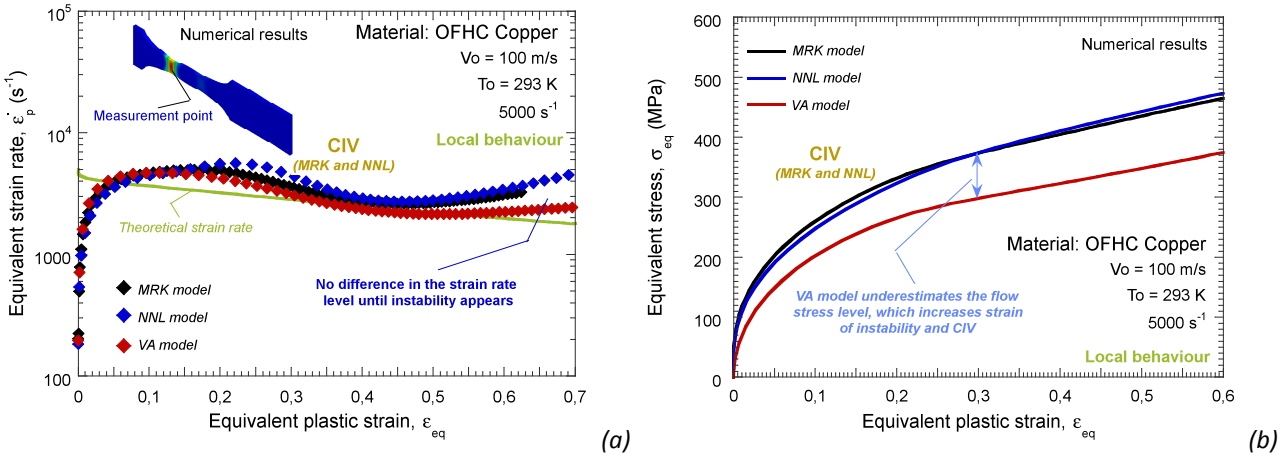

*Fig. 5-23. Evolution of (a) strain rate and of (b) stress as a function of plastic deformation in the necking zone for Extended **MRK, NNL** and **VA** models, Vo=100 m/s.*

But not only the local plastic behaviour of the material is affected by the type of constitutive relation used, the specimen elongation at failure *(an imposed critical failure strain* $\bar{\varepsilon}_f^p = 1.5$ *has been imposed for this particular problem)* is strongly influenced too, Fig. 5-24 and Fig. 5-25. Considering the *VA* constitutive description, Fig. 5-24 and Fig. 5-25 show that plasticity is more spread along the active part of the sample. These considerations agree with previous observations conducted for the ring expansion case. In addition, it seems that the ductility of the material is slightly higher in case of considering the Extended *MRK* model than for the *NNL* constitutive description. Because of the constant impact velocity, as the elongation of the active part of the sample increases, the failure time also does it. Then, in

case of considering an impact velocity of 40 m/s, the failure time for the *VA* model is approximately a 37% higher than considering the *NNL* model. Furthermore, it is important to notice that the necking point is near for the three constitutive models. However, the exact position does not match and varies depending the model used.

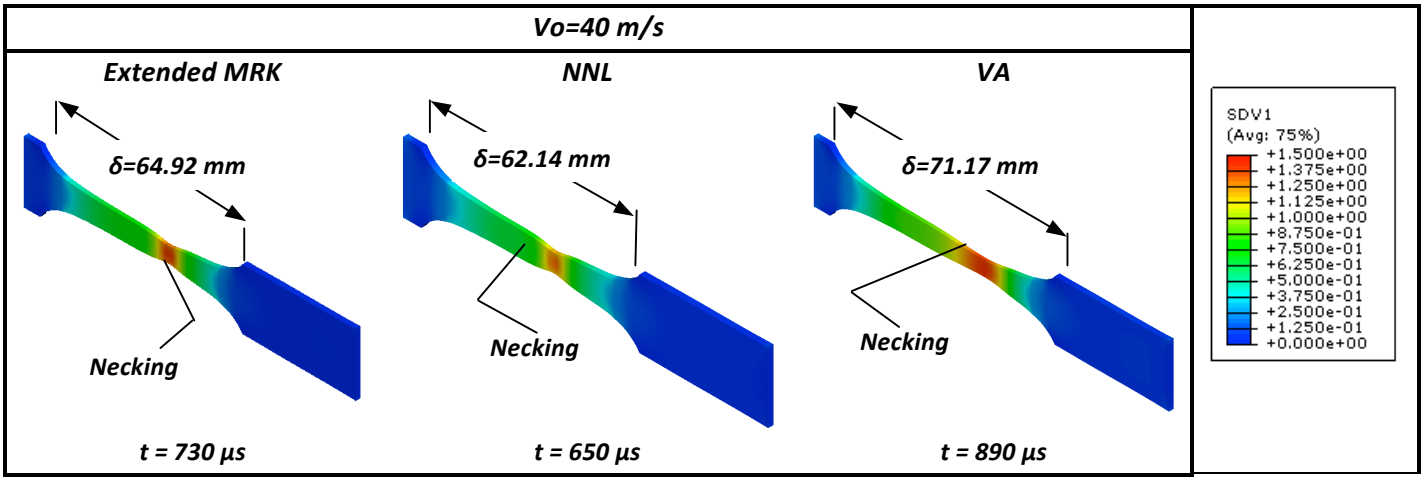

*Fig. 5-24. Plastic strain contours at failure time for Extended **MRK, NNL** and **VA** models at specimen failure at an impact velocity of 40 m/s.*

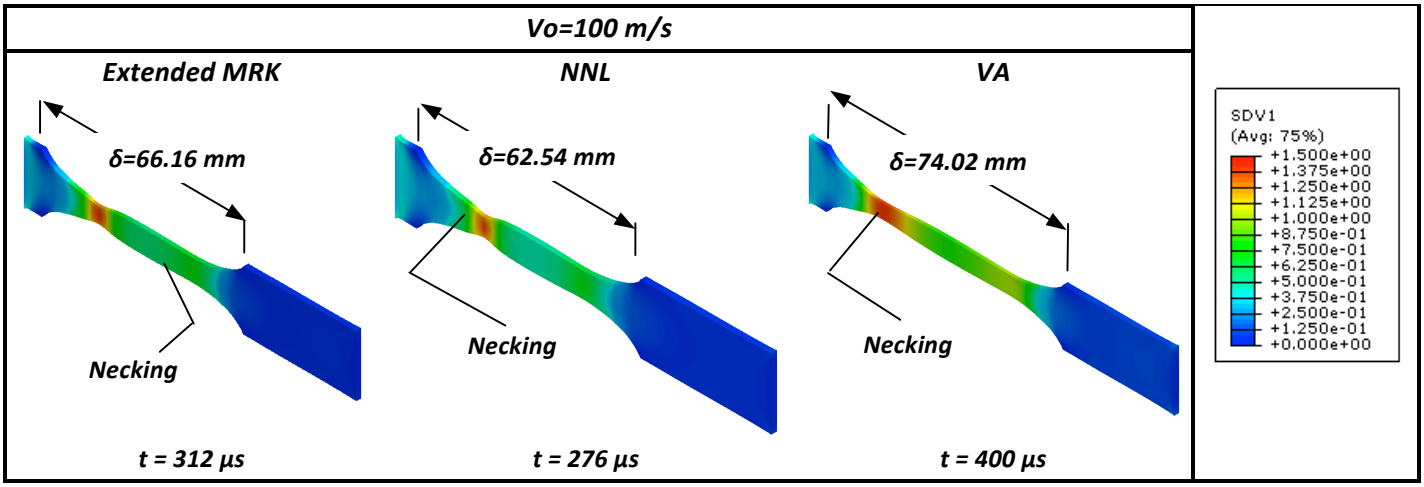

*Fig. 5-25. Plastic strain contours at failure time for Extended **MRK, NNL** and **VA** models at specimen failure at an impact velocity of 100 m/s.*

In Fig. 5-26 are plotted the vertical displacements of the active part of the sample for three different impact velocities. In previous chapters *(See Chapter 3)* have been discussed that with increasing rate sensitivity, the transversal displacement of the specimen at failure is larger. Then, vertical displacements are higher for the *VA* model. It delays necking appearance, especially for high impact velocities, Fig. 5-26-c. Moreover, from Fig. 5-26 can be concluded that the plasticity is more localized in case of using the *NNL* constitutive model. The plasticity gradients in the necking zones are higher. Moreover, the point of the sample where the necking is produced is nearer among the different models as the impact velocity increases, Fig. 5-26-a-c. This is due to the fact that as the impact velocity increases, this is nearer the **CIV**. In such conditions, the necking takes place in the impacted side for the specimen due to the stress wave induced by the impact provokes the fast trapping of plastic deformation.

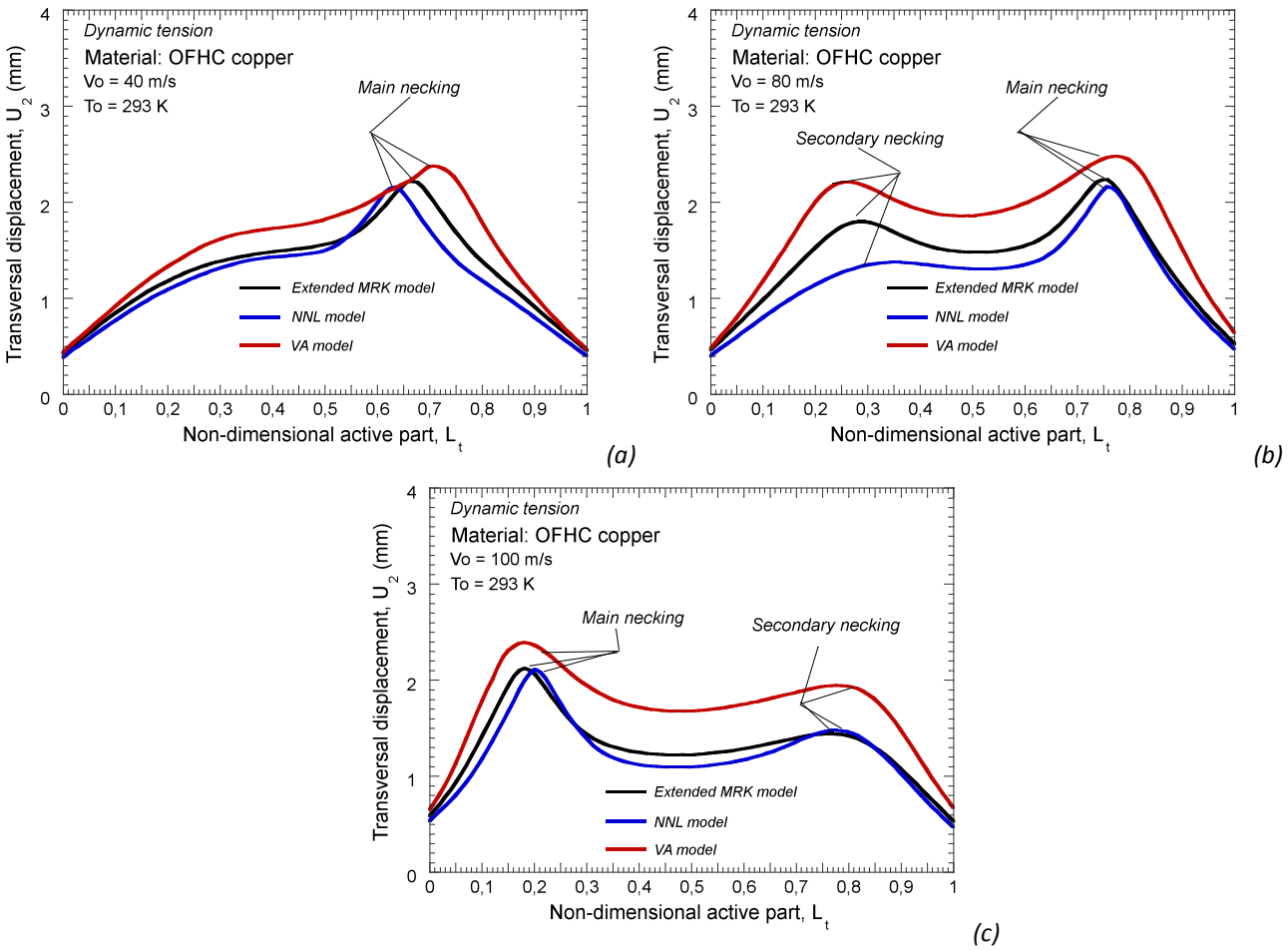

Fig. 5-26. Transversal displacement of the active part of the specimen for the three models. (a) Vo=40 m/s, (b) Vo=80 m/s, (c) Vo=100 m/s.

Next, in Fig. 5-27 the stress contours of the sample at an impact velocity of $V_0 = 100\ \mathrm{m/s}$ are depicted for the three different models. In spite of the behaviour of both the *Extended MRK* and *NNL* constitutive descritions seems to be very similar *(similar stress-strain curve, plastic strain of instability, local strain rate…)* at this impact velocity, Fig. 5-23, the macroscopic behaviour of the specimen is different. As it could be seen in Fig. 5-27, from the very beginning of the numerical simulation the stress level of the sample in each position differs in some dozens of MPa. Then, even when two constitutive relations show a stress-strain law very similar at a certain strain rate, the definition of the strain rate sensitivity, temperature sensitivity and strain sensitivity has a stronge influence on the macroscopic behaviour of the sample, Fig. 5-27.

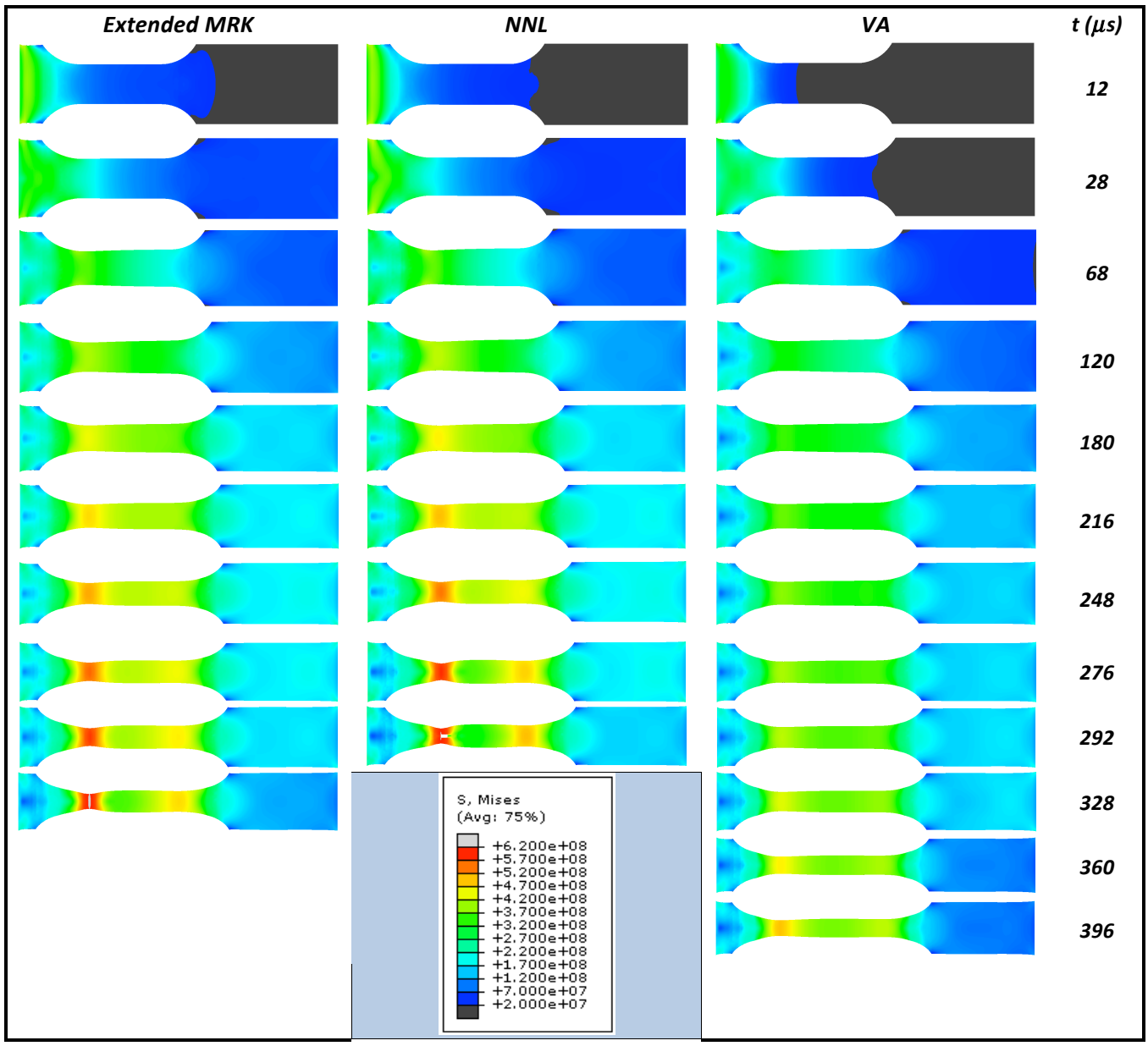

Fig. 5-27. Stress contours of the specimen at different simulation times at an impact velocity of Vo = 100 m/s.

It is concluded that if a constitutive description is applied for predicting the thermo-viscoplastic response of a metallic alloy subjected to impact loading, it has to procure an accurate description of the material strain hardening and rate sensitivity, Fig. 5-27. Otherwise the confidence on the results obtained from such analysis should be questioned.

In this chapter has been examined the influence of the constitutive descriptions on plastic instabilities formation under dynamic loading.

For that task, numerical simulations of dynamic tension test and ring expansion test have been carried out within a wide range of impact velocities. The material definition is conducted by application of three different constitutive descriptions, the Extended Modified Rusinek-Klepaczko (MRK) model [Rusinek and Rodriguez-Martinez

2009], the Nemat-Nasser and Li (NNL) model and the Voyiadjis and Almasri (VA) model. The OFHC copper has been the material selected to carry out this analysis.

Comparing the numerical results obtained, it has been concluded that in the modelling of metallic alloys used to build structural elements potentially subjected to fast loading during their service conditions, it is necessary an accurate knowledge of their strain rate and strain sensitivity. It has been proven that even when these advanced constitutive descriptions reproduce correctly the material behaviour under wide range of strain rates and temperature, the predictions for the plastic instabilities formation at high strain rates are different.

Then, the selection of a certain constitutive description plays a fundamental role on the estimated capability of metals for absorbing energy during crash or impacts. This aspect is of main interest in the industrial field (See Chapter 1).

CHAPTER 6

CONCLUSIONS AND FUTURE WORKS

ABSTRACT

Next, the main conclusions obtained along the different chapters of this document are summarized. In addition, future lines of work are proposed in order to go further into this topic.

6 CONCLUSIONS AND FUTURE WORKS

6.1 Conclusions

This work presents a numerical analysis on the formation of plastic instabilities under dynamic tension using advanced constitutive relations. Two different numerical configurations have been utilized: the dynamic tension test and the ring expansion test.

Main conclusions extracted from the project are:

- Material modelling plays an important role on the predicted capability of metallic alloys for absorbing energy.
- The strain of instability has been proven a good variable to determine the suitability of metals for absorbing energy.
- Ring expansion test and dynamic tension test have been proven good dynamic tests to determine the formation of plastic instabilities under a dynamic tension state.

Next, conclusions obtained along the different chapters of the project are discussed.

First of all, the influence of strain rate sensitivity on plastic instabilities formation under dynamic loading has been analyzed performing numerical simulations of the dynamic tension test. **AA 7075** has been the material chosen to develop this study. With this analysis, it has been concluded that:

- The strain rate sensitivity determines the ductility of metallic alloys.
- The stabilizing effect of the increasing rate sensitivity acts as an inductor for plasticity spreading during material loading.
- An accurate knowledge of the strain rate sensitivity is required for metallic alloys used to build structural elements potentially subjected to fast loading during their service conditions. This is especially important at high strain rates.
- Maximum strain rate sensitivity corresponds with the maximum predicted capability for energy absortion in the material.

Later on, the influence of strain hardening on plastic instabilities formation under dynamic loading has been studied. In this case, the ring expansion test has been the numerical configuration used. The austenitic steel **301Ln2B** has been the material utilized. In this study, it has been proven that:

- The strain hardening of the material plays a fundamental role on the formation of plastic instabilities.

- Beyond certain value of strain hardening rate *(in absence of material damage, wave propagation or any other disturbance mechanism)* strain localization never takes place.

- Increasing strain hardening effect reveals an increase in the material ductility. Then, strain hardening tends to homogenize the material behaviour.

Finally, with the fundamental objective of advancing in the understanding of the effects previously presented, the role of the constitutive relation on the material behavior predictions under dynamic solicitations has been studied. For that task, three physical-based constitutive relations have been used to model **OFHC copper**. The analysis revealed that:

- The processes of strain localization and fragmentation occurring in the sample during loading are strongly influenced by the material modelling.

- The rate sensitivity and strain hardening definition determine the model predictions for instabilities formation.

- The assumptions used to develop physical-based constitutive descriptions play a crucial role on the models' predictions for the flow localization.

6.2 Future works

Next, possible future works are suggested in order to go further into the present study of plastic instabilities formation.

- The advanced constitutive relations studied in this project only take into account the instantaneous rate sensitivity of the material. Instantaneous strain rate sensitivity describes the rate dependent behaviour of metals during continuous loading condition. However, it is known that strain rate history effects are present in the material deformation behaviour. Historical effects may be of relevance for modeling the material behaviour when it is subjected to an abrupt increase of the applied deformation rate or to a cycling loading process. It would be very interesting developing and implementing a constitutive model that took these historical effects into account.

- The J2 plasticity theory has been used as yield criterion during the whole study. A future line of work could be the implementation of these advanced constitutive descriptions with another different plasticity criterion, for example, the Burzynski or the Hill models.

- The analysis carried out here could be repeated using other kind of loading conditions. Numerical configurations of a pure shear test or simulating the copper jet fragmentation with these constitutive relations would contribute to extend the conclusions obtained in this work.

APPENDIX I

INTEGRATION SCHEME FOR J2 PLASTICITY

A APPENDIX I. INTEGRATION SCHEME FOR J2 PLASTICITY

As reported, for example, in [Lubarda and Benson 2003] particular relevance has the generalization of constitutive relations to three dimensional states of stress and strain. For it, constitutive descriptions may be extended to 3D modelling and implemented into **FE** code by means, for example, of the integration scheme proposed in [Zaera and Fernández-Sáez 2006]. Thus, the main features of the algorithm proposed by Zaera and Fernández-Sáez are described below.

The yield condition is defined by Eq. A-1:

$$f = \bar{\sigma} - \sigma_y\left(\bar{\varepsilon}^p, \dot{\bar{\varepsilon}}^p, T\right) = 0 \qquad \textit{Eq. A-1}$$

where $\bar{\sigma}$ is the equivalent stress, σ_y is the yield stress defined by the used constitutive description, $\bar{\varepsilon}^p$ is the equivalent plastic strain, Eq. A-2, $\dot{\bar{\varepsilon}}^p$ is the equivalent plastic strain rate, Eq. A-3, and T is the temperature:

$$\dot{\bar{\varepsilon}}^p = \sqrt{\frac{2}{3}\cdot\dot{\varepsilon}_{ij}^p\cdot\dot{\varepsilon}_{ij}^p} \qquad \textit{Eq. A-2}$$

$$\bar{\varepsilon}^p = \int \dot{\bar{\varepsilon}}^p \cdot dt \qquad \textit{Eq. A-3}$$

Assuming additive decomposition of the deformation tensor *(hypoelastic-plastic approach)*, the tensor of total strain rate $\dot{\varepsilon}_{ij}$ is written as a sum of the elastic strain rate tensor $\dot{\varepsilon}_{ij}^e$, the plastic strain rate tensor $\dot{\varepsilon}_{ij}^p$ and the thermal strain rate tensor $\dot{\varepsilon}_{ij}^T$, Eq. A-4.

$$\dot{\varepsilon}_{ij} = \dot{\varepsilon}_{ij}^e + \dot{\varepsilon}_{ij}^p + \dot{\varepsilon}_{ij}^T \qquad \textit{Eq. A-4}$$

Elastic strains are related to stress through an isotropic hypoelastic law, Eq. A-5:

$$\dot{\sigma}_{ij} = C_{ijkl}\cdot\varepsilon_{kl}^e \qquad \textit{Eq. A-5}$$

where C_{ijkl} is the stiffness tensor.

The thermal strains tensor is defined as follows, Eq. A-6:

$$\varepsilon_{ij}^T = \alpha\cdot\dot{T}\cdot\delta_{ij} \qquad \textit{Eq. A-6}$$

where α is the coefficient of thermal expansion and δ_{ij} is the unit matrix $\left(\delta_{ij} = 1 \quad \text{if} \quad i = j\right)$.

To define the plastic flow, the normality rule is used, Eq. A-7.

$$\varepsilon_{ij}^p = \dot{\lambda}\cdot\frac{\partial f}{\partial\sigma_{ij}} \qquad \textit{Eq. A-7}$$

where $\dot{\lambda}$ is the rate plastic multiplier that, in J2 plasticity, can be defined by Eq. A-8:

$$\dot{\lambda} = \frac{\Delta\lambda}{\Delta t} = \dot{\bar{\varepsilon}}^{p} \qquad \textit{Eq. A-8}$$

And hence, the equivalency of the plastic multiplier and the equivalent plastic strain, Eq. A-9:

$$\bar{\varepsilon}^{p} = \lambda \qquad \textit{Eq. A-9}$$

Adiabatic conditions of deformation are assumed, Eq. 2-9.

The consistency model is used to integrate the thermo-viscoplastic rate equations, via the equality of equivalent stress and yield stress for updated values of plastic strain, plastic strain rate and temperature. In the frame of the return-mapping algorithms, the consistency condition, Eq. A-10, could be written in terms of the equivalent plastic strain increment corresponding to a time step, Eq. A-11:

$$\dot{\lambda} \cdot f = 0 \qquad \textit{Eq. A-10}$$

$$f\left(\Delta\bar{\varepsilon}^{p}\right) = 0 \qquad \textit{Eq. A-11}$$

Linearising the consistency condition, the following equation is found which allows us to iteratively obtain $\Delta\bar{\varepsilon}^{p}$, Eq. A-12:

$$f_{(k+1)} \approx f_{(k)} + \frac{\partial f}{\partial \sigma_{ij}}\left(-\delta\bar{\varepsilon}^{p}_{(k)} 2G \left.\frac{\partial f}{\partial \sigma_{ij}}\right|_{(k)}\right) + \left.\frac{\partial f}{\partial \bar{\varepsilon}^{p}}\right|_{(k)} \delta\bar{\varepsilon}^{p}_{(k)} + \left.\frac{\partial f}{\partial \dot{\bar{\varepsilon}}^{p}}\right|_{(k)} \frac{\delta\bar{\varepsilon}^{p}_{(k)}}{\Delta t} + \left.\frac{\partial f}{\partial T}\right|_{(k)} \frac{\beta}{\rho C_{p}}\left(\delta\bar{\varepsilon}^{p}_{(k)} \bar{\sigma}^{trial}_{n+1} - 6G\Delta\bar{\varepsilon}^{p}_{(k)} \delta\bar{\varepsilon}^{p}_{(k)}\right) = 0 \qquad \textit{Eq. A-12}$$

where *k* is an iterative index. From the previous expression $\delta\bar{\varepsilon}^{p}_{(k)}$ can be calculated, Eq. A-13.

$$\delta\bar{\varepsilon}^{p}_{(k)} \approx \frac{f_{(k)}}{3G - \left.\frac{\partial f}{\partial \bar{\varepsilon}^{p}}\right|_{(k)} - \frac{1}{\Delta t}\left.\frac{\partial f}{\partial \dot{\bar{\varepsilon}}^{p}}\right|_{(k)} - \left.\frac{\partial f}{\partial T}\right|_{(k)} \frac{\beta}{\rho C_{p}}\left(\bar{\sigma}^{trial}_{n+1} - 6G\Delta\bar{\varepsilon}^{p}_{(k)}\right)} \qquad \textit{Eq. A-13}$$

Then, $\Delta\lambda$ is updated after every iteration, Eq. A-14:

$$\Delta\lambda_{(k+1)} = \Delta\lambda_{(k)} + \delta\lambda_{(k)} \qquad \textit{Eq. A-14}$$

All the variables could be determined from the final value of $\Delta\lambda$. A more detailed explanation of the integration procedure can be found in [Zaera and Fernández-Sáez 2006].

REFERENCES

REFERENCES

ABAQUS Explicit Version 6.4, User's manual, ABAQUS Inc., Richmond, USA, 2004.

Altynova M, Hu X, Daehn GS. Increased ductility in high velocity electromagnetic ring expansion. Metall Trans A 1996; 27:1837–1844.

Aravas N. On the numerical integration of a class of pressure-dependent plasticity models. Int J Numer Methods Eng 1987; 24:1395-416.

Campbell, J. D., Ferguson, W. G. (1970) The temperature and strain-rate dependence of the shear strength of mild steel, Phil. Mag. 81, 63-82.

Clark D. S., Wood D. S. The influence of specimen dimension and shpae on the results in tension impact testing. T Am Soc Mech Eng 1957:577-85.

Cowper GR, Symonds PS. Strain hardening and strain rate effects in the impact loading of cantilever beams. Brown Univ., Div. of Appl. Mech., report no. 28; 1952.

Curtze S., Kuokkala V. T., Hokka M., Peura P. Deformation behaviour of TRIP and DP steels in tension at different temperatures over a wide range of strain rates. Materials Science and Engineering A. 508 (2009) 195-199.

El-Magd E. Mechanical properties at high strain rates. J Phys IV 1994; C8(4): 149-70.

El-Magd E., M. Abouridouane M. Characterization, modelling and simulation of deformation and fracture behaviour of the light-weight wrought alloys under high strain rate loading. Int J Impact Eng32 (2006) 741-758.

Fischer F.D. A micromechanical model for transformation plasticity in steels. Acta Metall Mater 1990; 38:1535-46.

Fischer F.D., Reisner G., Werner E., Tanaka K., Cailletaud G., Antretter T. A new view on transformation induced plasticity (TRIP) Int J of Plasticity 16 (2000) 723-748.

Follansbee P.S. High-Strain-Rate Deformation of FCC Metals and Alloys**.** Metallurgical Applications of Shock-Wave and High-Strain-Rate Phenomena, (1986) 451-479.

Follansbee P.S., Kocks U.F. A constitutive description of the deformation of copper based on the use of the mechanical threshold stress as an internal state variable. Acta Metall 1988; 1:81–93.

Hu X., Daehn G.S., 1996, Effect of velocity on flow localization in tension. Acta Mater. 1996; 44, 1021-1033.

Johnson G.R., Cook W. H. A constitutive model and data for metals subjected to large strains, high strain rates and high temperatures. In: Proceedings of Seventh International Symposium on Ballistics, (1983) pp. 541-547.

Kapoor R., Nemat-Nasser S., 1999. Comparison between high strain-rate and low strain-rate deformation of tantalum. Metall.&Mater. Trans. 31A, 815-823.

Klepaczko J. R. Thermally activated flow and strain rate history effects for some polycrystalline FCC metals. Mater Sci Eng. 18 (1975) 121-135.

Klepaczko J. R. Review on critical impact velocities in tension and shear, Int. J. Impact Eng. 2005; 32, 188-209.

Klepaczko J. R., Rusinek A., Rodríguez-Martínez J. A., Pęcherski R. B., Arias A., Modeling of thermo-viscoplastic behaviour of DH-36 and Weldox 460-E structural steels at wide ranges of strain rates and temperatures, comparison of constituve relations for impact problems. Mech. Mater. 41 (2009) 599-621.

Kocks. U. F. Argon, A. S. Ashby, M.F., 1975. Thermodynamics and kinetics of slip. In: Chalmers, B., Christian, J.W., Massalski, T.B. (Eds.), Progress in Materials Science, vol. 19. Pergamon Press, Oxford.

Larour P, Verleysen P, Bleck W. Influence of uniaxial, biaxial and plane strain pre-straining on the dynamic tensile properties of high strength sheet steels. J Phys IV 2006; 134:1085-90.

Larour P, Rusinek A, Klepaczko JR, Beck W. Effects of strain rate and identification of material constants for three automotive steels. Steel Res Int 2007; 78:348-58.

Lebedev AA, Kosarchuk V. Influence of phase transformation on the mechanical properties of austenitic stainless steels. Int J Plasticity 2000; 16:749-67.

Lennon A. M, Ramesh K. T. The influence of crystal structure on the dynamic behavior of materials at high temperatures. International Journal of Plasticity 20 (2004) 269-290.

Lubarda, V.A., Benson, D.J., Meyers, M.A., 2003. Strain-rate effects in rheological models of inelastic response. Int. J. Plast. 19, 1097–1118.

Macdougall D. Determination of the plastic work converted to heat using radiometry. Exp. Mech 2000; 40:298-306.

Mahnken R, Schneidt A, Antretter T. Macro modelling and homogenization for transformation induced plasticity of a low-alloy steel. Int J Plasticity, in press. doi:10.1016/j.ijplas.2008.03.005.

Mercier S., Molinari A. Analysis of multiple necking in rings under rapid radial expansion Int J Impact Eng, 2004;4:403-419.

Nemat-Nasser S., Li Y., Flow stress of FCC polycrystals with application to OFHC Copper. Acta Mater. 1998; 46, 565-577.

Nemat-Nasser S., Guo W. G., Kihl D. P. Thermomechanical response of AL-6XN stainless steel over a wide range of strain rates and temperatures. Journal of the Mechanics and Physics of Solids 49 (2001) 1823-1846.

Olson GB, Cohen M. Kinematics of strain-induced martensitic nucleation. Metall Trans A 1975; 6:791-5.

Oussouaddi O, Klepaczko JR. An analysis of transition from isothermal to adiabatic deformation in the case of a tube under torsion. Proceedings. Conf. DYMAT 91. Journal de Physique IV 1991; Coll. C3 (Suppl. III): C3-323 [in French].

Papatriantafillou I, Agoras M, Aravas N, Haidemenopoulos G. Constitutive modelling and finite element methods for TRIP steels. Comput Methods Appl Mech Eng 2006; 195:5094-114.

Pęcherski RB. Macroscopic effect of micro-shear banding in plasticity of metals. Acta Mech 1998; 131:203-24.

Perzyna P. Application of the thermodynamical theory of elasto-viscoplasticity in modern manufacturing processes. Course notes: Damage mechanics and micromechanics of localized fracture phenomena in inelastic solids. CISM. Udine, July 7-11, 2008.

Regazzoni G., Kocks U. F., Follansbee P. S. Dislocation kinetics at high strains rates. Acta Metallurgica 1987; (35) 12, 2865-2875.

Rodríguez-Martínez J. A., Rusinek A., Klepaczko J. R., Pęcherski R. B. Extension of R-k constitutive relation to phase transformation phenomena. J Mater Design, 2008, doi:10.1016/j.matdes.2008.09.043.

Rodríguez-Martínez J. A., Advanced constitutive relations for modelling thermo-viscoplastic behaviour of metallic alloys subjected to impact loading. Doctoral Thesis. 2010.

Rusinek A., Klepaczko J. R. Shear testing of sheet steel at wide range of strain rates and a constitutive relation with strain-rate and temperature dependence of the flow stress. Int J Plasticity. 2001; 17, 87-115.

Rusinek A., Zaera R., 2007. Finite element simulation of steel ring fragmentation under radial expansion. Int. J. Impact Eng. 34, 799-822.

Rusinek A., Zaera R., Klepaczko J. R., Constitutive relations in 3-D for a wide range of strain rates and temperatures – Application to mild steels. Int J Solids Struct. 2007; 44:5611-5634.

Rusinek A., Rodríguez-Martínez J. A., Zaera R., Klepaczko J. R., Arias A., Sauvelet C. Experimental and numerical analysis of failure process of mild steel sheets subjected to perpendicular impact by hemispherical projectiles. Int. J. Impact Eng. 36;4 (2009), 565-587.

Rusinek A., Rodríguez-Martínez J. A., Klepaczko J. R., Pęchersky R. B. Analysis of thermo-visco-plastic behaviour of six high strength steels. J. Mater. Design 30 (2009) 1748-1761.

Rusinek A., Klepaczko J.R. Experiments on heat generated during plastic deformation and stored energy for TRIP steels. Mater Design 2009; 30:35-48.

Rusinek A., Rodriguez-Martinez J. A. Thermo-viscoplastic constitutive relation for AA alloys, modeling of negative strain rate sensitivity and viscous drag effects. MaterDes2009; 30:4377–90.

Rusinek A., Rodríguez-Martínez J. A., Arias A. A thermo-viscoplastic constitutive model for FCC metals with application to OFHC Copper. 2010. International Journal of Mechanical Sciences.

Sorensen N.J., Freund L.B. Unstable necking formation in a ductile ring subjected to impulsive radial loading. Int. J Solids Struct. 2000; 37_2265-83.

Taylor GI. Plastic wave in a wire extended by an impact load. Scientific papers, vol. 1 mechanics of solids. Cambridge: Cambridge University Press; 1958. p. 456.

Tomita Y., Iwamoto T. Constitutive modelling of TRIP steel and its application to the improvement of mechanical properties. Int J Mech Sci 1995; 37:1295-305.

Triantafyllidis N., Waldenmyer JR. Onset of necking in electro-magnetically formed rings. J Mech Phys Solids 2004; 52:2127–2148.

Varas D., Zaera R., Lopez-Puente J. Numerical modelling of the hydrodynamic ram phenomenon. Int J Impact Eng 36 (2009) 362-374.

Voyiadjis G.Z., Abed F.H. Microstructural based models for bcc and fcc metals with temperature and strain rate dependency. Mech Mater 2005; 37:355–78.

Voyiadjis G.Z., Almasri A.H., A physically based constituve model for fcc metals with applications to dynamic hardness. Mech. mat. 2008; 40, 549-563.

Zaera R., Fernández-Sáez J. An implicit consistent algorithm for the integration of thermoviscoplastic constitutive equations in adiabatic conditions and finite deformations. Int J Solids Struct 2006; 43:1594-612.

Zerilli F.J., Amstrong R.W., 1987. Dislocation-mechanics-based constitutive relations for material. Dynamics calculations. J Appl Phys. 1987; 61:1816-1825.

Zhang S., McCormick P.G, Estrin Y. The morphology of Portevin–Le chatelier bands: finite element simulation for Al–Mg–Si. Acta Mater 2001; 49:1087–94.

Zukas J.A., Scheffler D.R. Practical aspects of numerical simulations of dynamic events: effects of meshing, Int. J. Impact Eng. 2000; 24: 925-945.